Wetting and CO Oxidation on Transition Metal and Bimetallic Surfaces

Thesis submitted in accordance with the requirements of the University of Liverpool for the degree of Doctor in Philosophy

by

Mark Stewart Taylor

Surface Science Research Centre, Department of Chemistry

September 2015

Dedication

This thesis is dedicated to my beloved parents Zephania “Relton” and Eugene Taylor, whose early inspiration during my formative years has sustain me throughout and laid the path for the life I have today.

Abstract

The oxidation of carbon monoxide has been investigated in two different systems, Au alloyed with Pd(111) at room temperature and Cu(110) at 90 to 170 K. All experiments were conducted under UHV conditions using mass spectrometry and temperature-programmed desorption to follow the reaction.

For the Au/Pd(111) system the intention was to improve the catalytic activity of the pure Pd(111) crystal by alloying with Au, as bimetallic alloys often display enhanced catalytic activities compared to that of the pure metal due to a combination of both ensemble and ligand effects. The ensemble effects being the arrangement of the active atoms and the ligand effects the electronic modifications or charge transfer associated with these active atoms. This was carried out by vapour deposition of various amounts Au on the Pd(111) crystal and annealing to form a surface alloy. Enhanced catalytic activities of up to 27 % was achieved by alloying with Au coverages of 0.2 - 0.4 ML on the Pd(111) substrate followed by annealing to temperatures 650 – 750 K compared to that of the pure Pd(111) surface.

For the Cu(110) system we aimed to assess the catalytic activity of Cu, the objective being to determine the exact kinetic mechanism of the oxidation reaction at 90 to 170 K. This was done initially by pre-adsorbing O_2 on the Cu(110) substrate surface at various coverage, followed by CO and monitoring for CO_2 production. The experiment was then reversed with CO pre-dosed followed by O_2. The catalytic oxidation reaction was found to proceed by a hot-precursor mechanism when O_2 was dosed on a CO pre-covered surface above 130 K. Below this temperature any O_2 dosed prior to or after the CO uptake would tend to physisorb molecularly and only reacted during dissociation while the O atom remained in a reactive transient. Here, the atomic O reacted directly with adsorbed molecule CO transiently prior to adsorption to the Cu substrate a catalytic reaction akin to that of an Eley-Rideal mechanism.

We have studied the wetting properties, autocatalytic dissociative adsorption and the reactivity of the hydroxyl species originating from the co-adsorption of water and oxygen on Cu(110) at 200 to 300 K. Experiments were conducted by two separate methods; using molecular beam uptakes and by varying the static H_2O pressures from 1.0×10^{-11} up to 5.0×10^{-7} mbar in conjunction with LEED and TPD.

It has been hypothesized that the strong attractive interaction between mixed OH and H_2O slows down the desorption kinetics of H_2O sufficiently to produce H_2O-OH structures that are stable up to RT. As a result the main focal point of the research was to gain some insight into the bonding mechanisms at elevated water pressures and ambient temperatures, whilst assessing the stability of the H_2O-OH species.

In addition to the $1H_2O$:1OH chains structures and dimers observed previous at these temperatures we also observed an additional stable structure during the TPD experiments. This structure appeared particularly when H_2O was adsorbed with low (0.06 ML) atomic O coverages and became increasingly prominent when the uptake temperature was increased from 200 up to 240 K. The origin of this structure is discussed in the context of the structure proposed by earlier investigators.

Acknowledgements

First and foremost I would like to express my deepest gratitude to my supervisor Prof. Andrew Hodgson for his unwavering support and mentorship throughout this project. His guidance helped me throughout the research and the writing of thesis. I would like to thank Dr Alan Massey for his valuable advice throughout the time he spent with me in the laboratory and Dr Fiona McBride during the start of the project.

I wish to express my sincere gratitude to Dr Sam Haq for his constructive guidance, being a fantastic mentor and keeping me sane when things were going haywire. His knowledge in the laboratory is incomparable.

Very special thanks also to Dr Martin Volk and Dr Heike Arnolds for their productive advice in both of my first and second year viva and Nikki Fowler patiently proofread my chapters and tolerating my anecdotes during the start of her PhD studies. I wish her well in her studies.

I thank David Hesp for all the stimulating discussions we always had, particular in relation to the art of pugilism which very few people seem to appreciate. And finally I want to express my appreciation to Dr George Darling and Katariina Pussi for their DFT calculations associated with the papers that are in preparation, not featured in these chapters.

The work was carried out within the Surface Science Research Centre, School of Physical Sciences, University of Liverpool funded by the Engineering and Physical Sciences Research Council. So, I would like to thank everyone associated with the centre and EPSRC for the funding.

Mark Stewart Taylor 2015

Contents

Chapter 1

1 Introduction

Surface science in general and surface chemistry in particular can be defined as the study of chemical reactions at the interface of two phases. This includes the solid-liquid, solid-gas and liquid-gas interfaces. These interfaces exhibit some remarkable physical and chemical properties. The chemical behaviour of the solid-gas and solid-liquid interfaces is responsible for heterogeneous catalysis, electrochemistry and corrosion. Although studying interfacial chemistry in Ultra High Vacuum (UHV) conditions (10^{-9} mbar) and low temperatures can provide detailed information at the molecular level, most chemical processes in reality occur at much higher or ambient pressures and elevated temperatures. As a result there remains a degree of controversy as to the validity of data when extrapolating over as many as 10 orders of magnitude. To surmount this barrier we have combined our studies at UHV conditions with studies at higher pressures and temperature. This thesis focuses on the catalytic oxidation of carbon monoxide (CO) and the interaction of water (H_2O) on copper (Cu) and bimetallic gold/palladium (Au/Pd) metal surfaces.

In chemistry bimetallic surfaces play a crucial role in a number of technologically important areas including heterogeneous catalysis. The Au/Pd surface alloy system has received a significant amount of attention due to its enhanced activity in a number of catalytic reactions. However, with this being the case, to our knowledge no CO oxidation research has been completed on the Au/Pd(111) system to date. All of the previous research carried out for CO oxidation was focused on Au/Pd(100) and Pd-Au nanoparticles on TiO_2[1–3]. In addition, a previous DFT study by Yuan et al.[4] showed that Au(111) decorated with Pd adatoms is highly active for CO oxidation. All of the information obtained from these researchers will be

presented in detail later in Chapter 3, together with our results obtained for the catalytic oxidation of CO on the Au/Pd(111) alloy.

Although Cu is commonly used as an industrial catalyst essentially in methanol production from CO and H_2, it is very rarely used for the catalytic oxidation of CO. On most transition metals including Cu it is generally assumed that the heterogeneous catalytic oxidation of CO takes place by way of the Langmuir-Hinshelwood (L-H) mechanism. In brief this is when both the reactants adsorb, migrate on the substrate surface and then collide to form products. This along with the Eley-Rideal (E-R) and Hot Atom (HA) mechanisms will be expanded on in Chapter 4.

There is a need to extend the research already conducted on the reactivity of O_2 with CO on Cu(110), particularly at low temperatures due to the lack of consistency in the results published previous. In addition, most of the previous work is centred specifically on the reactions of pre-adsorbed O_2 with CO, with no straightforward interpretation of the type of intermediate species preceding desorption of CO_2. It has been suggested in early work that pre-adsorbed O_2 at low temperatures ~ 85 to 150 K does not oxidise CO[5,6], in contrast to later work that suggests oxidation does take place at similar temperatures[7]. However, in addition to these inconsistencies very little research has been focused on the oxidation of pre-adsorbed CO. Chapter 4 details the kinetic study of the catalytic oxidation of CO on the Cu(110) substrate focused on reversing the order of the pre-adsorbed reactants O_2 and CO at 90 to 170 K.

Only recently have researchers been able to establish a clear picture of the structures formed by H_2O at molecular level on well-defined metal surfaces including Cu. The structures at low temperature are determined by the interplay between the intermolecular H_2O-H_2O and H_2O–substrate interactions. At higher temperatures the structures are determined by the barriers towards both diffusion and partial dissociation, with partial dissociation giving rise to a variety of H_2O-OH structures depending on temperature and pressure[8,9].

It has been hypothesized that the strong attractive interactions between mixed OH and H_2O slows down the desorption kinetics dramatically stabilizing H_2O structures near ambient conditions of 1.33 mbar and 295 K[10].

Recent work suggests OH species stabilize H_2O structures up to RT even at pressures as low as 7.5×10^{-9} mbar[11]. However, these latter structures studied by STM bear no resemblance to anything observed previously at UHV or ambient pressures. The results presented in Chapter 5 detail the wetting properties H_2O and the reactivity of the OH species at pressured 1.0×10^{-11} – 5.0×10^{-7} mbar and temperatures 200 - 300 K.

1.1 Catalysis

A catalyst is a substance that speeds up a reaction by allowing the reaction to take place through an alternative mechanism that requires lower activation energies. However, the catalyst is not consumed in the reaction and therefore does not appear in the net reaction equation. In addition a catalyst will have an effect on the forward and reverse rates equally, which means it has no effect on the equilibrium constant and thus on the composition of the equilibrium state.

Catalysis can be divided into two categories, homogeneous and heterogeneous catalysis. Homogeneous catalysis is when the catalyst exists in the same phase as the reactants, gas or liquid, and enters directly into the chemical reaction by means of forming a new compound or complex with a reactant. However, after the reaction is complete the catalyst is released in its initial form and therefore does not appear in the net reaction equation. Heterogeneous catalysis, on the other hand, is when the catalyst exists in a different phase to the reactants. Here typically the catalyst is almost always a solid and the reactants gases or liquids.

The catalytic affect in heterogeneous catalysis typically arises from disruption (often dissociation) of the reactant molecules brought about by their interaction with the surface of the catalyst. An example of this is the oxidation of carbon monoxide which requires the dissociation of oxygen (O_2) prior to reaction with carbon monoxide (CO). O_2 typically does not react in its gaseous diatomic state due to the high activation energy required to dissociate the diatomic O_2 molecule, which is typically in the region of 1.2 eV (117 $kJmol^{-1}$). On transition metals O_2 can be dissociated with zero activation

energy producing atomic oxygen (O) which is then able to react with CO to produce CO_2[12–14].

An important factor that determines how adsorbates interact on the substrate surface is whether they behave as relative electron donors or acceptors. The CO molecules for example when adsorbed on the metal substrate C end down will behave as a relative electron acceptor in comparison to adsorbates like H_2 and atomic O. This will inevitably determine whether there is an attraction or repulsion between co-adsorbates based on the dipole or charge associated with that specific adsorbate[15]. Consequently in terms of the oxidation mechanism, the C atom the electron acceptor or electrophile will react with the atomic O the electron donor or nucleophile. In addition, this donor-acceptor synergism, as will be expanded upon later determines the relative binding energies of the adsorbates to the substrate surface[16].

The existence of electron transfer and exchange properties between surface and adsorbate enable neutral molecules to yield a dipole, positive ions, negative ions or radicals depending on the electronegativity of the surface. This spontaneous production of a surface dipole during adsorption occurs when a normally full electron level lies above a normally empty level. If the donating level lies below the acceptor level then activation energy is required. There are a number of preconditions in order for electron transfer changes to occur. Namely, the free energy change of the overall process must be negative, the catalyst should possess vacant or occupied levels capable of accepting or donating electrons and the potential barrier between the catalyst and adsorbate must be permeable to electrons[17].

1.1.1 Enzyme catalysis

Electron donors and acceptors are also important in enzymatic catalysis where for example the $–NH_2$ and COOH groups act as proton donors or acceptors existing as $-NH_3^+$ and $–COO^-$ in their ionic form. The fundamental role that enzymes play in enzymatic catalysis is to increase the rate of the biochemical reaction. These include assisting the transport of protons in

acid/base catalysis such as the keto-enol tautomerization reaction as shown in Mechanism 1.1. They also act as electron carriers in covalent catalysis such as the decarboxylation reaction where the carboxyl-lyases aids the removal of the COOH group and releases CO_2 as shown in Mechanism 1.2[18–21].

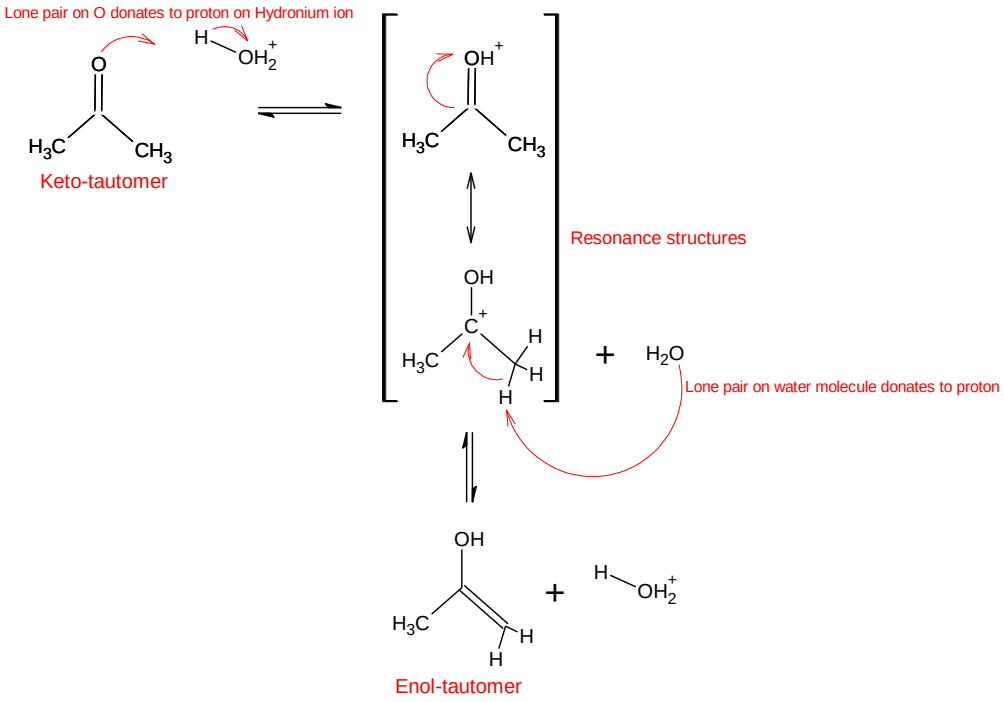

Mechanism 1.1. The acid/base catalysed conversion of keto-tautomer to the enol-tautomer by way of proton transfer and the shifting of bonding electrons. (Source Structure: Drawn – using Advanced Chemistry Development ACD/ChemSketch Product Version 12.01)

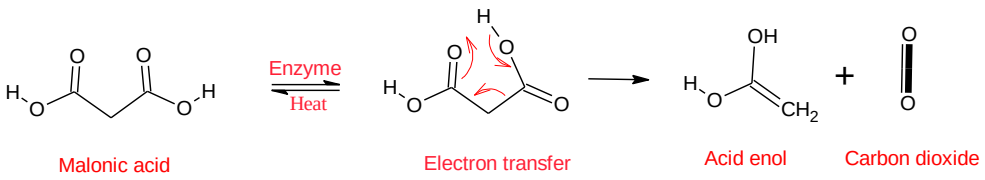

Mechanism 1.2. The catalysed decarboxylation of malonic acid to the acid enol by the removal of CO_2, catalysed with carboxyl-lyases. (Source Structure: Drawn – using Advanced Chemistry Development ACD/ChemSketch Product Version 12.01)

1.2 Catalytic oxidation of carbon monoxide

The heterogeneous catalytic oxidation of carbon monoxide (CO) has been studied extensively for the last fifty years for a number of reasons. Primarily CO is an extremely toxic molecule and must therefore be removed from anthropogenic sources e.g. transportation exhaust, industrial emissions and stationary sources. In the three way catalytic converter for example, CO is removed as CO_2 from the auto-mobile exhaust by reacting with O_2 or nitrogen on noble metals[22–24]. CO, along with nitrogen oxides (NO_x) and volatile organic compounds (VOC) are the main precursors involved in the photochemical production of tropospheric ground level ozone, a major constituent of photochemical smog[25–27]. In addition to this, the catalytic reaction between atomic oxygen (O_a) and CO is commonly used to evaluate the catalytic activity of other closely related reactions. Specifically, it is believed that the intermediates involving O_a are similar in both the water-gas-shift reaction (Equation 1.1) and the synthesis of methanol (Equation 1.2)[28,9,29,30].

$$H_2O + CO \rightarrow H_2 + CO_2 \tag{1.1}$$

$$CO + 2H_2 \rightarrow CH_3OH \tag{1.2}$$

Although carbon monoxide is a flammable gas, it's combustion in air can only occur between 12 and 75 vol%[31]. In most cases tropospheric concentration levels are typically in the region of 50 – 50,000 ppm, making combustion virtually impossible, which means abatement can only be carried out by way of catalysis. Historically catalytic oxidation of CO was initially carried out over metal oxides (hopcalites)[32] and later by way of noble metal catalysts, especially Pt, Pd and Rh[33]. However, due to the increasing price of these metals and significant progress in oxide synthesis, catalytic oxidation of CO over alternative cheaper metals i.e Cu has gathered interest in recent years. This was one of the contributing factors for studying the catalytic properties of Cu in this thesis.

1.2.1 Chemisorption of carbon monoxide and oxygen on metal surfaces

1.2.1.1 Carbon monoxide

Blyholder first proposed the electronic model of CO chemisorbed on metal surfaces explaining the different vibrational spectra according to the alignment and location on the metal substrate[34]. Five IR spectral vibration ranges of CO adsorption bands can be detected, 1700–1800 cm^{-1}, where the CO is bonded to 4 metal atoms, 1800–1920 cm^{-1}, 3 metal atoms, 1860-2000 cm^{-1}, 2 metal atoms, and 2000–2130 cm^{-1}, when the CO is bonded to the linear or atop position.

The highest occupied molecular orbital (HOMO), which is the 5σ molecular orbital (MO), and lowest unoccupied molecular orbital (LUMO), which is the 2π* MO are both involved when CO bonds to metal substrates. In addition to this the alignment of both of the MOs with respect to the Fermi level is also important in determining the bonding. The primary interactions when CO adsorbs to metal surfaces are the forward and back donations of the orbitals between the substrate surface atoms and those associated with the C end of the CO molecule, described by Blyholder as the donor-acceptor synergism. As shown in Figure 1.1, the 5σ MO located on the C end of the CO molecule acts as the electron donor, and interacts with the d_z^2 states on the substrate. The more dominant interactions occur between the 2π* MO also located on the C end of the CO molecule; this acts as the electron acceptor interacting with the $d_{xz,yz}$ states on the substrate. As shown in Figure 1.2, when adsorbed to the Cu(110) surface, C end towards the substrate, the 5σ MO is completely occupied as it lies below the Fermi level and interacts strongly with the metal d_z^2 electronic states. The 2π* MO on the other hand accepts electrons from the metals $d_{xz,yz}$ bands by back donation and is only partially occupied[35].

Due to the fact that the 2π* MO is antibonding with respect to the C-O bond, increased occupation by back donation from the metal $d_{xz,yz}$ bands leads to weakening of the C-O bond and therefore an increase in its reactivity. Not only do surfaces provide a meeting place for reactants, but also they lead to weakening of the adsorbate bonds, which in turn leads to a

decrease in the activation barrier for the overall reaction. This weakening of the C-O is also dependent on the adsorption site, with the higher coordination sites creating a greater weakening due to increased back donation. In contrast, as stated earlier the IR vibration will decrease with an increase in the back donation from the substrate[13,33].

It is also important to note that moving across the transition metal series from right to left gives rise to both an increase in the Fermi level in addition to the diffusiveness of the d orbitals. In combination, this leads to dissociation of the CO molecule on the earlier transition elements as a result of increased electron density from the $d_{xz,yz}$ states interacting with the 2π* MO[35,36].

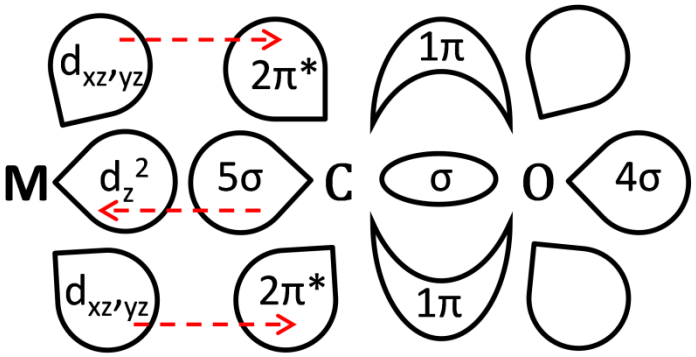

Fig 1.1. The Blyholder model for the non-dissociative chemisorption of CO to metal surfaces where the 5σ MO located on the C end of the CO molecule and interacts with the d_z^2 states of the metal substrate M and more dominant interactions between the 2π* MO located on the C end interacting with the $d_{xz,yz}$ states.

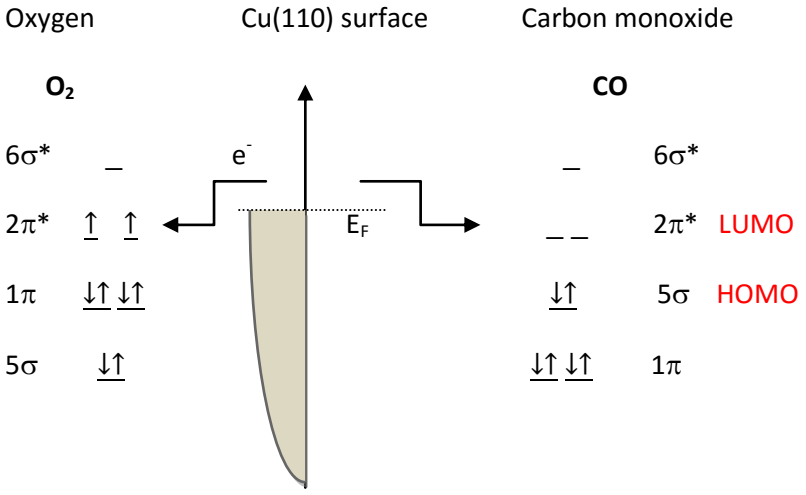

Fig 1.2. The non-dissociative chemisorption of CO and dissociative chemisorption of O_2, by way of the HOMO and the LUMO to the Cu(110) surface.

1.2.1.2 Oxygen

In comparison to CO the interaction of O_2 with metal surfaces is more complicated, adsorbing dissociatively on metal surfaces at ambient temperatures. However, when adsorbed at low temperature, depending on the metal, it will first enter a physisorbed state and will only dissociate when heated, requiring adjacent metal substrate atom for dissociation. A few of the transition metal surfaces where chemisorbed molecular oxygen species have been detected at temperatures below ~150 K include Pt(111), Pd(111), Ni(111), Ag(110) and Cu(110). As shown in Figure 1.2, this dissociation occurs as a result of filling of the 2π* MO that is half filled and degenerate in the gaseous state. Significant charge transfer from the substrate to the 2π MO orbital weakens the O-O bond, which makes them likely precursors to O_2 dissociation[15,37].

1.2.2 The Mechanism of CO oxidation over metal surfaces

It is generally accepted that the oxidation of CO over metal substrates proceeds according to a Langmuir-Hinshelwood (LH) mechanism, which will be discussed in detail in Chapter 4, in which the rate determining steps occur in the adsorbed phase. The initial step of the reaction involves the adsorption of both the reactants as detailed earlier. Depending on the reactivity of the metal, the CO may adsorb dissociatively or non-dissociatively according to Equation 1.3 and 1.4 respectively with the O_2 adsorbing dissociatively according to Equation 1.5.

$$CO_{(g)} \rightarrow C_{(ads)} + O_{(ads)} \tag{1.3}$$

$$CO_{(g)} \underset{k_2}{\overset{k_1}{\rightleftharpoons}} CO_{(ads)} \tag{1.4}$$

$$O_{2(g)} \underset{k_4}{\overset{k_3}{\rightleftharpoons}} 2O_{(ads)} \tag{1.5}$$

Adsorption energies for atomic O on late transition elements tend to range from 1.6 to 5 eV, much higher than that of the CO molecule[38]. Consequently, O_2 desorption will generally occur at much higher temperatures than CO and is also a lot less mobile on the surface. Saturated atomic O coverages tends to be a lot lower in comparison to CO on the same metal surface due to strong repulsive interactions between the negatively charged O atoms.

As stated for dissociative adsorption on any metal substrate O_2 requires pairs of adjacent adsorption sites. Therefore with CO adsorbed first, this will make dissociation difficult, whereas to when the O_2 is adsorbed first CO will be able to find vacant sites between the atomically adsorbed O.

If oxidation is to occur by way of the Langmuir-Hinshelwood mechanism, which will be expanded on later in Chaper 4, an important step in the oxidation rate and subsequent CO_2 production (Equation 1.6) is the mobility of both the CO and atomic O on the surface. An alternative mechanism that will be discussed also in Chapter 4, is the Eley-Rideal mechanism, where as shown in Equation 1.7, the CO molecules reacts direct with the adsorbed atomic O to produce CO_2 [12–15].

$$CO_{(ads)} + O_{(ads)} \xrightarrow{k_5} CO_{2(g)} \tag{1.6}$$

$$CO + O_{(ads)} \xrightarrow{k_6} CO_{2(g)} \tag{1.7}$$

1.2.3 Heterogeneous catalysis on bimetallic surface alloys catalysts vs pure metallic catalysts

An alloy of two metals can change the activity or the selectivity of the catalyst in comparison to a pure metallic catalyst. These effects can be termed as poisoning or promotion of the pure metallic catalyst. Poisoning is where the added metal is able to attenuate or prevent the formation of undesirable side reactions by blocking the active sites associated with these reactions,

otherwise known as ensemble effects. Promotion occurs when the added metal changes the electronic perturbations of the pure metal structure by charge transfer between the two metals. This has the effect of changing the binding energies and likewise the activation energies associated with the reactants of catalytic reactions. These electronic perturbations, otherwise known as ligand effects, are most likely to occur when the two metals are alloyed, either randomly or in an ordered fashion. That is when one metal is dispersed into the other as opposed to being dispersed as islands, which would otherwise leave each metal with virtually the activity of the pure metals[39–41].

1.3 Studies of H_2O on clean and atomic O metal substrates

The interfacial molecular properties of H_2O on well-defined metal surfaces under ultra-high vacuum (UHV) conditions has been studied extensively over the past two decades, primarily because H_2O-metal interactions play an important role in many chemical processes throughout a range of fields beyond academia. These fields include meteorology where studies on epitaxial ice nucleation on metal crystal surfaces can be utilized to aid the process of cloud-seeding to bring about precipitation[42,43]. Also in the field of electrochemistry, where the characteristics of the molecules at the surface of the electrode play a key role in the electrochemical reactions as opposed to those of the bulk solution[44].

In addition to offering a cheaper alternative to more expensive transition elements in the oxidation of CO reaction, Cu plays an important role in a number of catalytic reactions. This includes the water-gas shift reaction (WGSR) as shown in Equation 1.8, with assumed redox mechanism, Equation 1.9. with Rate-controlling steps (RCS)

$$H_2O_{(g)} + CO_{(g)} \rightleftharpoons H_{2(g)} + CO_{2(g)} \quad (1.8)$$

$$Redox\ Mechanism: \quad (1.9)$$

1. $H_2O_{(g)} \rightleftharpoons H_2O_{(ads)}$
2. $H_2O_{(ads)} \rightarrow H_{(ads)} + OH_{(ads)}$ (RCS)
3. $2OH_{(ads)} \rightleftharpoons H_2O_{(g)} + O_{(ads)}$
4. $OH_{(ads)} \rightarrow O_{(ads)} + H_{(ads)}$ (RCS)
5. $2H_{(ads)} \rightleftharpoons H_{2(g)}$
6. $CO_{(g)} \rightleftharpoons CO_{(ads)}$
7. $CO_{(ads)} + O_{(ads)} \rightarrow CO_{2(ads)}$ (RCS)
8. $CO_{2(ads)} \rightleftharpoons CO_{2(g)}$
9. $H_{(ads)} + CO_{2(ads)} \rightleftharpoons HCOO_{(ads)}$

In recent years there has been renewed interest in the WGSR the interest being largely in connection with fuel cells and fuel cell powered vehicles with a view to reducing greenhouse gas emissions[29,30]. Given that the hydroxyl molecule is a key rate-controlling intermediate in this and many other redox reactions, including proton transfer in enzymatic catalysis[45], a thorough comprehension of its behaviour on the surface is necessary. It is also important in terms of developing a more active catalyst at conditions close to those likely to be encountered for fuel cell applications.

Whilst stable water/hydroxyl (H_2O-OH) structures can be produced by means of pre-adsorption of O followed by adsorption with H_2O, there is still a

high degree of uncertainty with regards to the exact composition and structures formed at higher temperatures. As most chemical processes take place at ambient conditions, there is a need to bridge the gap between the studies conducted at low temperatures, under UHV conditions, with those carried out at elevated temperatures and higher pressures. In addition, under ambient conditions the majority of solid surfaces are covered with H_2O, particularly at high humidity, which can adversely affect the rate of corrosive oxidation[46]. Now, whilst H_2O adsorption on all metal surfaces can be extremely complex due to the number of reactions occurring, the basic questions one needs to consider are; under ambient conditions what are the products? Does H_2O adsorb, and if so does it remain intact molecularly in clusters or dissociate and what conditions will have an influence on the reaction pathway? It has been suggested that well-ordered H_2O-OH structures are thermally stable up to room temperature[46], which is the main theme of this study later in the thesis[47].

The molecularly intact and partially dissociated H_2O overlayers are stabilized by the cooperative effect of the surface bound O non-bonding lone pair, interacting with the electron-poor cationic sites, together with intermolecular H-bonding. H-bonding is the dynamic electrostatic attraction that occurs between a pair of typically electronegative atoms involving an H atom located between them. As shown in Figure 1.3 for pure H_2O not bound to any substrate, H-bonding occurs where the partially positively charged H atom lies between partially negatively charged oxygen atoms. With the formation of H-bonds between H_2O molecules there is a redistribution of electrons which enhances the formation of further H-bonding. This occurs when the H_2O molecule donating the H-bonds subsequently experiences an increase in electron density on the O lone pair which subsequently encourages the formation of further H-bonds from other H_2O molecules. This effect of electron redistribution followed by the acceptance of H-bonds is known as the cooperative effect. There is also an anti-cooperative effect where the acceptance of a single H-bond marginally discourages the acceptance and formation of further H-bonds. This also occurs between both

H_2O-H_2O and H_2O-OH structures on the substrate surface with the partially dissociated H_2O-OH structures having the greater stability.

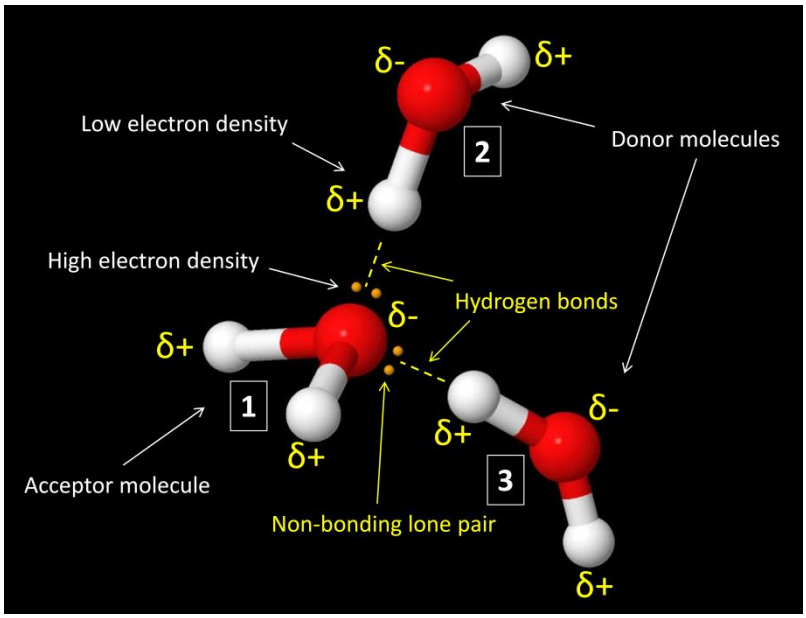

Fig 1.3. H-bonding occurring in H_2O molecules between the partially positively charged H atom (white) and the partially negatively charged O atom (red). The non-bonding lone pairs are only shown on the accepting O atom attached to the H_2O molecule labelled 1 with the participating H atoms covalently attached to the two donor H_2O molecules labelled 2 and 3.

For the intact monomer, the non-bonding lone pairs are made up of contributions from the $2p_x$ (b_1), $2p_z$ ($3a_1$) and 2s ($2a_1$) MO as shown in Figure 1.4 with the accompanying molecular orbital diagram Figure 1.5. These symmetry labels a_1 and b_1 are based on the classification of the H_2O molecule into the C_{2v} point group as shown in Figure 1.6.

There is a general tendency for H_2O, when binding to metal surfaces, to lie almost parallel to the surface. As a result the surface bonding will favour the non-bonding $2p_x$ (b_1) orbital interacting with the vacant d orbital. This is in combination with the filled d orbital interacting with the vacant anti-bonding ($3a_1$) MO (Figure 1.7). H-bonding occurs directionally between the lone pair of the electronegative O and the net positive charge on the H atom, which is produced by intra-molecular polarisation, giving rise to cluster formation on the surface[48].

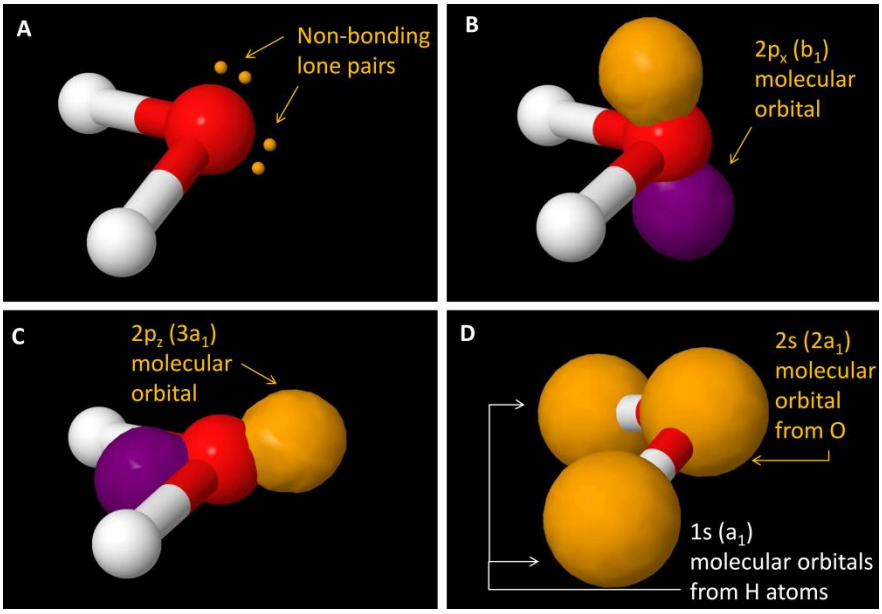

Fig 1.4. The intact H_2O monomer, showing (A) the non-bonding lone pairs which are made up of contributions from (B) the $2p_x$ (b_1), (C) the $2p_z$ ($3a_1$) and (D) the 2s ($2a_1$) molecular orbitals.

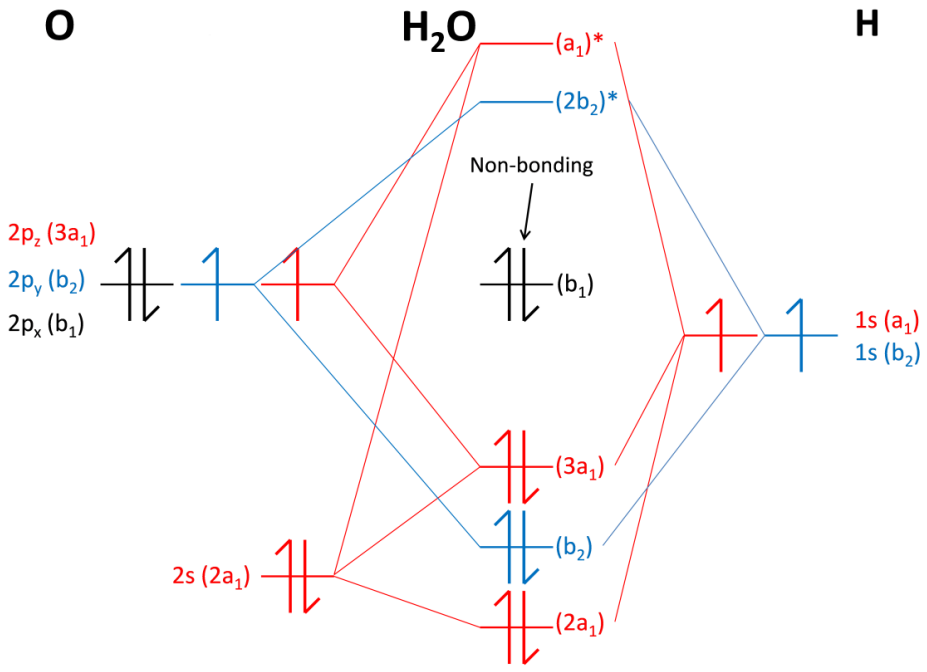

Fig 1.5. Molecular orbital diagram for H_2O molecule with the a_1 and b_2 overlap symmetries highlighted in red and blue respectively. The $2p_x$ non-bonding orbital has b_1 symmetry with no overlap and there has the same energy as the original atomic orbital.

C_{2v}		Symmetry Elements E	C_2	σ_v	σ'_v	Spectroscopic active component Microwave	IR	Raman
Symmetry Label	a_1	1	1	1	1		z	x^2, y^2, z^2
	a_2	1	1	-1	-1	R_z		xy
	b_1	1	-1	1	-1	R_y	x	xz
	b_2	1	-1	-1	1	R_x	y	yz

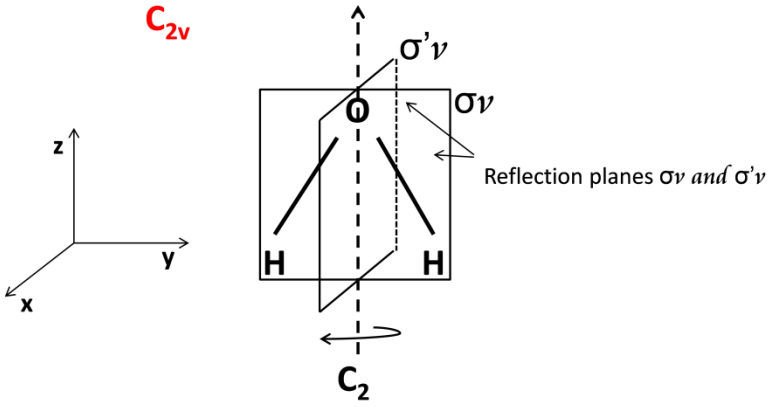

Fig 1.6. C_{2v} symmetry of the H_2O molecule, indicating the C_2 operation and combination of reflections σ'_v in the y,z plane and σ_v in the x,z plane with the a_1 and b_1 symmetry labels highlighted.

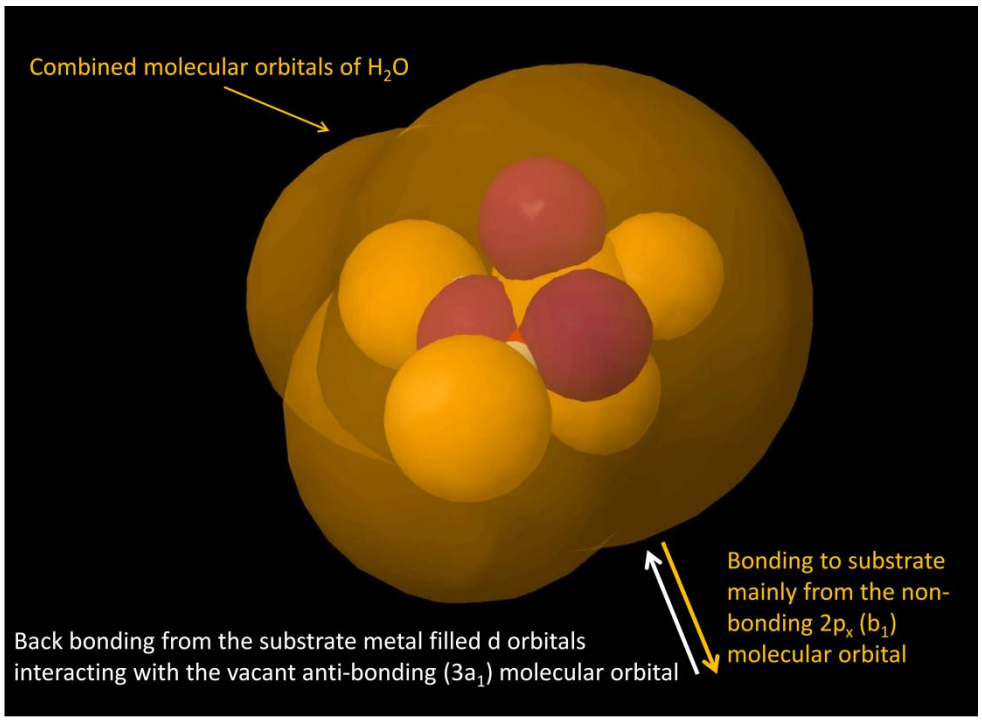

Fig 1.7. Bonding of the molecular H_2O monomer to the substrate, mainly from the non-bonding $2p_x$ (b_1) molecular orbital in combination with the filled d orbital from the substrate interacting with the vacant anti-bonding ($3a_1$) molecular orbital.

The basis of the dissociated structure is the strong Cu-OH chemical bond where stabilization takes place by charge transfer from the substrate to the partially occupied 1π lone pair orbital of the OH as shown in the molecular orbital diagram Figure 1.8. As a result the dissociated H-bonded structure where H-bonding is directional from the H_2O to the OH is far stronger than that of the H-bonded H_2O to H_2O bonded structure. This leads to asymmetry between the O-O distances, very similar to hydroxyl ions in solution. The significance of the charge transfer from the metal substrate to the partially occupied 1π lone pair orbital of the OH is important in that it stabilizes long-range lateral order for mixed H_2O-OH complexes. This was detailed as the cooperative effect which in turn also has a dramatic effect on the reactivity of the surface. This reactivity is evident in the relative bond strengths for the different interactions of mixed H_2O + OH complexes on metal surfaces. In decreasing relative bond strength order Metal-OH >> H_2O-OH > Metal- H_2O ≈ H_2O-H_2O > OH-H_2O[9,49–51].

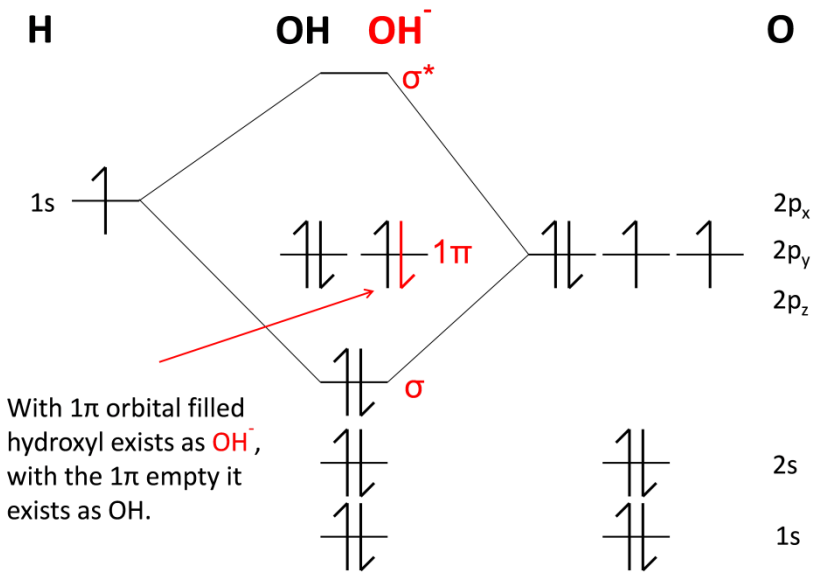

Fig 1.8. Molecular orbital diagram for the hydroxyl and hydroxyl ion, where stabilization takes place by charge transfer from the substrate to the partially occupied 1π lone pair orbital.

1.3.1 Electron transfer, redox and corrosion

As detailed electron transfer occurs when an electron transfers from an atom or molecule to another chemical entity. Another example of this is in a reduction-oxidation (redox) reaction where the oxidation state of the reactants and products changes. In humid gases, a thin layer of moisture is present on metal surfaces. This can give rise to the deterioration of the metal by way of a galvanic process called corrosion. Although the deterioration takes place by way of an overall redox reaction involving the oxidation of the metal, it does not necessarily result in the production of the metal oxide as shown in Equations 1.10 - 1.12 for the redox corrosion of copper. Under ambient conditions, the oxidation of most metals excluding gold and platinum is thermodynamically spontaneous; as a result knowledge of the adsorbed aqueous phase is important in order to develop a model of atmospheric corrosion[52].

Cu corrosion process

Oxidation reaction at the anode:

$$Cu_{(s)} \rightarrow Cu^{2+} + 2e^{-} \tag{1.10}$$

Reduction reaction at the cathode:

$$H_2O_{(ads)} + \frac{1}{2}O_{2(g)} + 2e^{-} \rightarrow 2OH^{-}{}_{(ads)} \tag{1.11}$$

and/or

$$2H^{+} + 2e^{-} \rightarrow H_{2(g)} \tag{1.12}$$

1.4 Thesis Outline

This Thesis consists of six chapters. This chapter, **Chapter 1**, presented a brief introduction to catalysis, the heterogeneous catalytic oxidation of CO on single and bimetallics surfaces in addition to an introduction to the studies of H_2O on clean and atomic O covered surfaces. **Chapter 2** gives a thorough description of the experimental setup used throughout. This includes a description of both UHV chambers, the crystal types used, and a breakdown of all the instruments and analytical techniques used, including LEED, MCP-LEED, QMS, TPD and PVD. **Chapter 3** outlines the catalytic oxidation of CO on the Au/Pd(111) alloy in comparison with the pure Pd(111) crystal where **Chapter 4** focusses on the kinetic mechanism of the oxidation reaction at 90 to 150 K on Cu(110). In **Chapter 5** the wetting properties, the formation of the H_2O-OH phases and the reactivity of the hydroxyl species on Cu(110) were studied at 200 to 300 K. **Chapter 6** gives a brief summary of the significance of all the findings with suggestions for further work, publications and conference contributions.

Chapter 2

2 Experimental

In order to achieve useful information from surface science studies, almost all studies are carried out under Ultra High Vacuum (UHV) conditions, that is, at pressures at or below 10^{-9} mbar. This enables atomically clean surfaces to be prepared and maintained in a contamination-free state for the duration of the proposed experiment. Additionally, this permits molecular beam and sublimation dosing, low energy electron and ion based experimental techniques, with limited interference from gas phase scattering. This chapter starts with a detailed explanation of each technique in full, since these are used throughout the experiments detailed in the latter parts of the thesis.

2.1 Ultra-high vacuum Chambers

All of the experiments presented in this thesis were performed in one of the two ultra-high vacuum (UHV) chambers 1 & 2 as shown in Figures 2.1 & 2.2 respectively.

Chamber 1 consisted of three stages and the main chamber, each differentially pumped by water cooled oil diffusion pumps (each backed by rotary vane pumps) in addition to two turbo pumps and an ion pump, to maintain an operating base pressure of $< 10^{-10}$ mbar. The main chamber was also equipped with a second two stage molecular beam, differentially pumped independently by separate turbo pumps as shown in Figure 2.1.

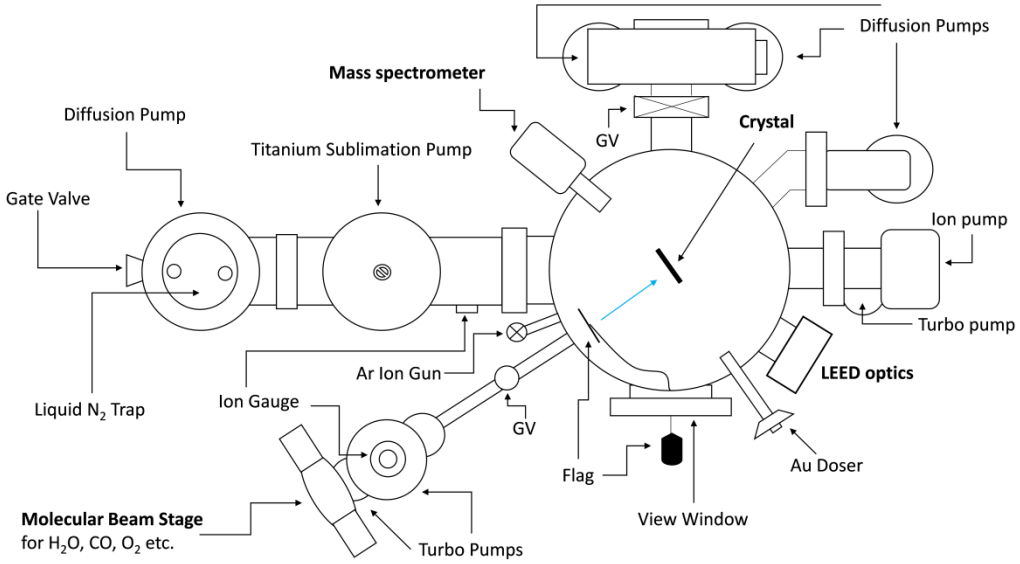

Fig. 2.1. Schematic of vacuum chamber 1, with the LEED optics, Au doser, and Quadrupole Mass spectrometer (QMS) attached to the main chamber which is equipped with an independently pumped two stage molecular beam arm.

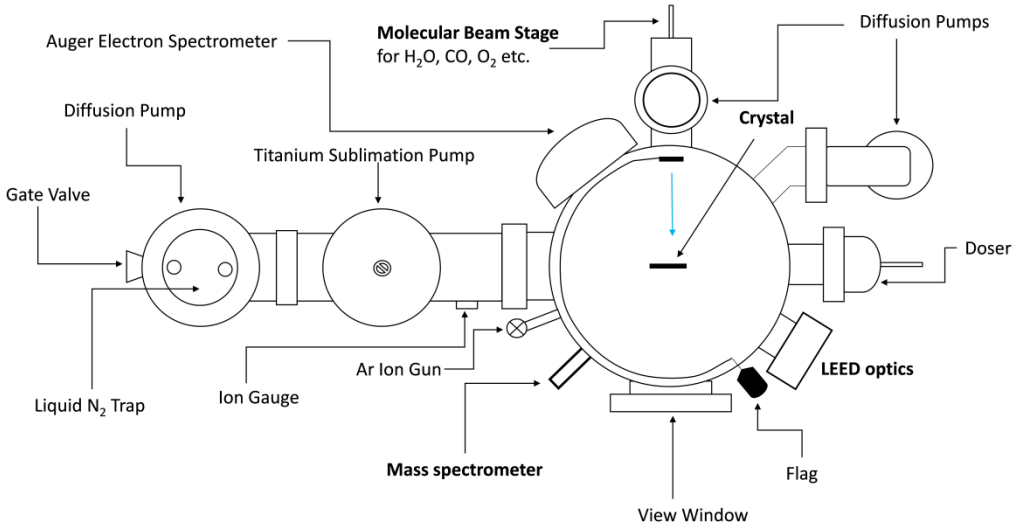

Fig. 2.2. Schematic of vacuum chamber 2, with the LEED optics, Auger Electron spectrometer, Quadrupole Mass spectrometer (QMS) and two stage molecular beam arm attached to the main chamber.

Chamber 2 consisted of a two stage beam source and the main chamber, each differentially pumped by water cooled oil diffusion pumps, (each backed by rotary vane pumps) again to maintain operating base pressures of $< 10^{-10}$ mbar. Here the molecular beam arm is positioned directly inside the primary stage as illustrated in Figure 2.3. In addition both chambers were equipped with a liquid nitrogen LN_2 cold trap mounted directly above the diffusion pump to the main chamber. This was filled daily with LN_2 in order to prevent any unwanted gases and oil vapours back-streaming into the main chamber by condensation. This section of the chamber was also pumped by a titanium sublimation pump (TSP) section, containing a titanium/molybdenum alloy filament which when heated produced a titanium vapour, coating the surrounding chamber walls. This layer would subsequently react with any active gases to form stable compounds such as titanium oxide, hence removing them from the chamber.

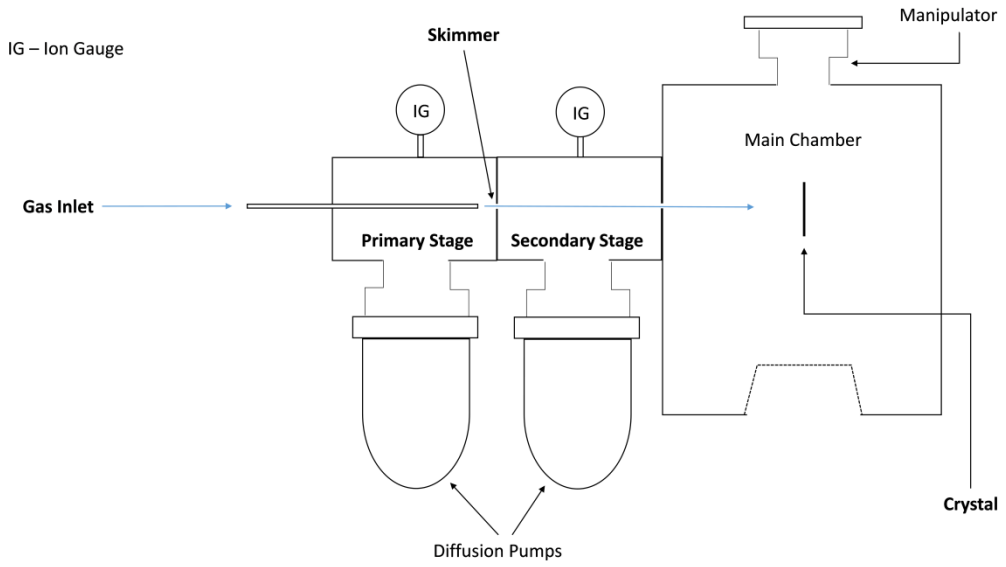

Fig. 2.3. Schematic of the two stage molecular beam stage linked to the rear of the main chamber 2

At UHV pressures of 10^{-10} mbar, the mean free path of the gas molecule is circa 700 km, consequently the gas molecules will collide with the chamber walls many times before colliding with each other. To put it another way, with ultra-high vacuum pressures of $< 10^{-10}$ mbar, assuming at worst, a sticking

coefficient of S (θ) = 1; a typical gaseous contaminant such as carbon monoxide will require approximately 11 hrs to form a monolayer on a Cu(110) crystal at 300 K. For reliable studies of systems that are extremely sensitive to contamination, this is a precondition.

In order to achieve and maintain UHV conditions, some of the following conditions are required: the use of materials that exhibit very low rates of out-gassing under vacuum and where applicable, tolerate bake-out temperatures up to 150 °C. This is achieved by the use of special stainless steels, the use of low vapour pressure materials such as glass and ceramics and high pumping speeds. The process of baking the chambers up to temperatures of 150 °C for periods of 12 hours or more with continuous pumping greatly accelerates all thermally activated processes. Both the surface and bulk adsorbed gases are removed at a much greater rate than at room temperature, drastically reducing the out-gassing when cooled back to room temperature[53,54,15].

Both of the chambers are equipped with a sample manipulator which enables cooling of the crystal down to temperatures of 90 K by filling with liquid nitrogen along with heating up to temperatures of 1000 K by resistive heating by way of an electrical feed-through. Sample temperatures are monitored by the use of a thermocouple mounted to the side of the crystal. All crystals were mounted (by the use of 0.2 – 0.5 mm Tantalum (Ta) wires on Ta rods) on the 360° rotatable manipulator which could also be moved horizontally in the x, y-plane and vertically along the z-axis.

2.2 Crystal types and Preparation

The crystals used for this study were Cu(110) and Pd(111), with surface areas of 100 mm^2 and 80 mm^2, both cut and polished to within an accuracy of 0.25° and 0.1° of the crystallographic plane respectively. The Cu(110) crystal was mounted using 0.25 mm Ta wire suspended in grooves milled at the top and base on the crystal, whereas the Pd(111) was mounted by spot

welding 0.125 mm Ta wires directly around the circumference of the crystal (Figure 2.4). The ends of the wires were spot welded to two Ta rods attached to the Cu feed-through. As stated earlier, the sample temperature was monitored by means of a 90%Ni/10%Cr (T1) Chromel – 95%Ni/2%Mn/2%Al/1%Si (T2) Alumel K-type thermocouple spot welded directly to the side of the Pd(111) crystal or inserted into an aperture on the side of the Cu(110) crystal.

Both crystals underwent extensive Ar^+ ion sputtering cleaning cycles for 15-20 minutes at a drain current of 2 - 5μA (500 eV) at room temperature after mounting and prior to each experiment in order to remove surface contaminants such as carbon, oxygen and sulphur. This was followed by post-irradiation flash annealing to 823 K for Cu(110) and 1023 K for the Pd(111) to remove any lattice defects produced from the impinging ions and to remove any shallow implanted argon. The surface ordering prior to analysis was assessed by Low Energy Electron Diffraction (LEED) and Temperature-programmed desorption (TPD)[53,55].

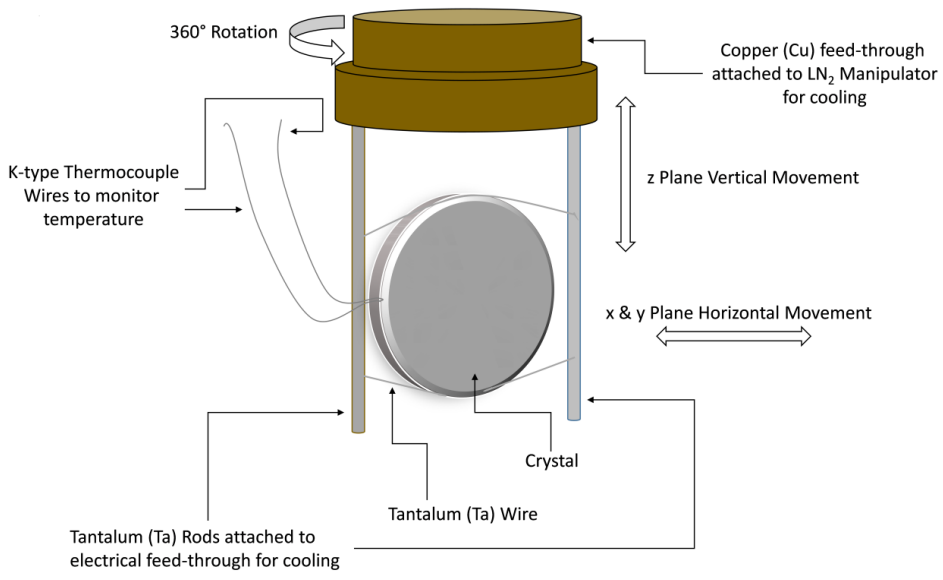

Fig. 2.4 Sample crystal mounted on the Cu feed-through Ta rods at the base of the manipulator. The K-type thermocouple is spot welded or inserted into the side of the crystal to monitor the temperature.

2.3 Low Energy Electron Diffraction (LEED)

Low energy electron diffraction (LEED) was used both qualitatively and quantitatively for the determination of the surface structures formed. Qualitative analysis involved analysing the spot positions produced by the diffraction image in order to obtain the size, symmetry and rotational alignment of the adsorbate unit cell with respect to the substrate unit cell. Quantitative analysis involved analysing the intensities of the spot positions across a succession of electron beam energies to obtain I-V curves, and comparing with theoretical curves to determine the complete surface structure (i.e. the positions and identities of all the atoms within the unit cell)[56].

Figure 2.5 shows the experimental setup for direct observation of the LEED patterns. The apparatus consists of an electron gun which emits an electron beam (from the cathode set at a negative potential – V) of well-defined low energy electrons (typically in range 20 – 200 eV) incident normal on the surface. These electrons undergo diffraction on striking the surface, due to their wave characteristics, and are only diffracted back if the crystal has a well ordered surface structure. As shown, the apparatus consists of four grids and a fluorescent screen. The first grid and the sample are grounded, creating a field free environment for any diffracted electrons. The second and third grids are set at a potential slightly lower than the cathode potential (V – ΔV) to cut off any inelastically scattered electrons, with the fourth grid grounded to shield the other grids from the fluorescent screen, which is set at a potential ≈ +5 kV. At such a high positive potential any elastically scattered electrons passing through the retarding second and thirds grids are accelerated giving rise to fluorescence when striking the screen to produce the desired diffraction pattern[56]. This diffraction pattern is a reflection of the symmetry and crystalline order of the surface.

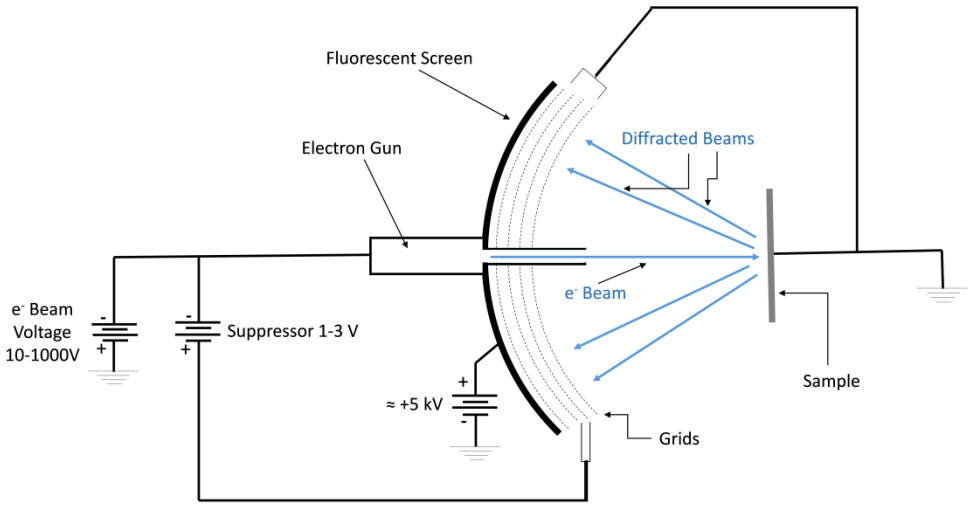

Fig. 2.5. The schematic setup of the LEED apparatus with the electrons (blue) diffracting from the crystal sample. The various grids ensure only the elastically scattered electrons reach the fluorescent screen.

2.3.1 Principles of LEED & Multichannel Plate (MCP) LEED

There are two principle reasons why low energy electrons are used for the determination of surface structures on crystal surfaces. The de Broglie wavelength of electrons in the range 20 – 200 eV is approximately 0.1 - 0.3 nm. This satisfies the condition of diffraction on atomic structures, i.e. this wavelength is equal or smaller than the inter-atomic distances of both the adsorbate and substrate. Additionally, the mean free path length of these low energy electrons equates to only a few angstroms (a few atomic layers) in a crystal substrate. Consequently, most of the elastic scattering occurs in the uppermost layers of the sample, which will therefore make the maximum contribution to the diffraction pattern thus keeping any contribution from the deeper atoms to a bare minimum.

One of the disadvantages of using LEED to determine weakly bound or inherently sensitive structures is the intrinsic problem of electron beam damage destroying the adsorbate prior to obtaining an image. This was minimised by the use of a dual channel electron multiplier array LEED often called a microchannel plate (MCP) LEED. Whereas the standard LEED instruments are normally operated with beam currents in the microampere

range, the MCP-LEED is specifically designed to be operated with beam currents ranging from pico to nanoamperes.

The MCP is a device placed in front of the fluorescent screen, a fraction of mm in thickness, consisting of millions of 25 µm pore channels. Each microchannel is coated with a high-resistance semiconductor which serves as a secondary electron multiplier, as shown in Figure 2.6. These microchannels are electrically connected in parallel by metal electrodes on the opposite faces of the plate for high voltage operation in ultra-high vacuum conditions. With the application of a voltage there is a continuous potential gradient along the length of each microchannel, therefore as soon as a charged particle i.e. an electron with sufficient energy falls on the front surface of the MCP, it typically produces 2 to 3 electrons. These electrons are accelerated down the microchannel by a positive bias voltage. Striking the mocrochannel walls they subsequently produce additional electrons which get accelerated further down the microchannel and collide with the wall producing more secondary electrons. This process of amplification of the electron cloud continues till the end of the microchannel producing a pulse with a gain as high as ~10^3 in one plate or ~10^6 across two plates. Consequently with these high gains, the MCP-LEED permits analysis of inherently sensitive structures at much lower beam currents.

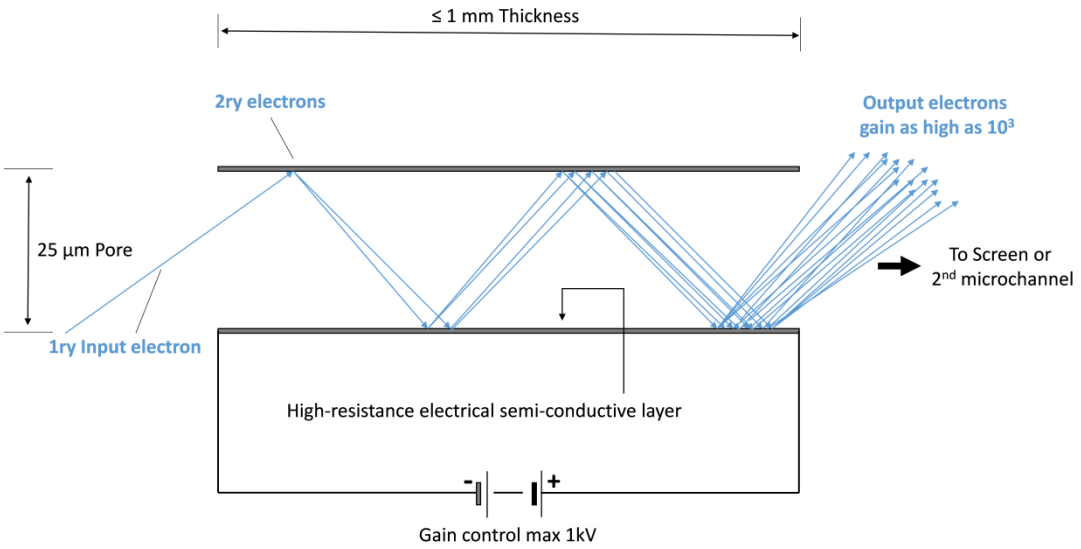

Fig. 2.6. An Illustration of a single microchannel with electron multiplication taking place from the primary input (blue) giving rise to a gain as high as 10^3.

2.3.2 Diffraction from periodic array

2.3.2.1 One Dimensional

Figure 2.7 illustrates the diffraction of electrons from a one-dimensional periodic array with lattice constant a at an angle θ.

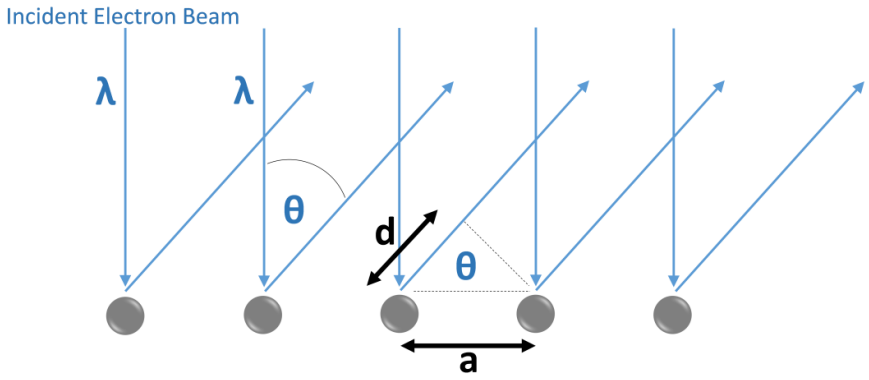

Fig. 2.7. The schematic representation of the back scattering of electrons (blue) with a path difference 'd' from a one dimensional plane of atoms (grey circles) with atomic spacing 'a'.

As shown with path difference d;

$$\sin\theta_a = \frac{d}{a}$$

$$\therefore d = a.\sin\theta_a \qquad (2.1)$$

The interference is constructive when the path difference is in multiples of 2π or integers of n, a condition known as Bragg's diffraction;

$$d = n\lambda \qquad (2.2)$$

Where; $n =$ Integer or Integral Number (0, ±1, ±2, ±3, ±4 etc) and $\lambda =$ the de Broglie Wavelength of electrons.

∴ Combining Equations 2.1 & 2.2;

$$n\lambda = a.\sin\theta$$

$$\therefore \sin\theta_a = \frac{n.\lambda}{a} \tag{2.3}$$

On observation of Equation 2.3, one can see that for a fixed wavelength λ, an increase in the lattice constant a will inevitably give rise to a decrease in the diffraction angle θ and likewise $\sin\theta$, giving rise to narrower diffraction patterns. Similarly, for a fixed lattice constant a, a decrease in the wavelength λ, (increase kinetic energy) will give rise to a decrease in the diffraction angle, again giving rise to narrower diffraction pattern.

Given that the electron beam has a periodic (sinusoidal) oscillation in space, its spatial frequency, or wave number, can be defined as the number of waves that exits over a specified distance;

$$\bar{v} = \frac{1}{\lambda}$$

In multidimensional systems where there are several independent variables, diffraction is usually described using the wave vector. The wave vector of the electron $|k_0|$ can be defined as;

$$|k_0| = \frac{2.\pi}{\lambda} \tag{2.4}$$

The de Broglie wavelength λ, is related to its' momentum p, through Planck's constant[57];

$$\lambda = \frac{h}{p} \tag{2.5}$$

With momentum;

$$p = mv \tag{2.6}$$

Combining Equation 2.4 with the de Broglie relationship Equation 2.5 (incorporating Equation 2.6) to eliminate wavelength λ gives;

$$|k_0| = \left(\frac{2.\pi}{n}\right) m.v \tag{2.7}$$

Additionally combining Equation 2.4 with Equation 2.3 to eliminate wavelength λ gives;

$$|k_0| = \left(\frac{2.\pi}{a.\sin\theta_a}\right) n$$

$$\therefore\ |k_0|.\sin\theta_a = \left(\frac{2.\pi}{a}\right) n \tag{2.8}$$

From Figure 2.8;

$$\sin\theta = \frac{k^{\parallel}}{k_0}$$

$$\therefore\ \underline{k^{\parallel}} = \underline{k_0}.\sin\theta \tag{2.9}$$

$$\cos\theta = \frac{k^{\perp}}{k_0}$$

$$\therefore k^{\perp} = k_0.\cos\theta \tag{2.10}$$

On observation of Figure 2.8 and Equation 2.8 with Equation 2.9, clearly $|k_0|.\sin\theta_a$ is a component of the parallel wave vector $k^{\parallel}$, with the quantized unit $2\pi\ /\ a$ being the magnitude of the one dimensional reciprocal lattice vector;

$$\therefore \Delta k^{\parallel} = |k_0|.\sin\theta_a = \left(\frac{2\pi}{a}\right)n \tag{2.11}$$

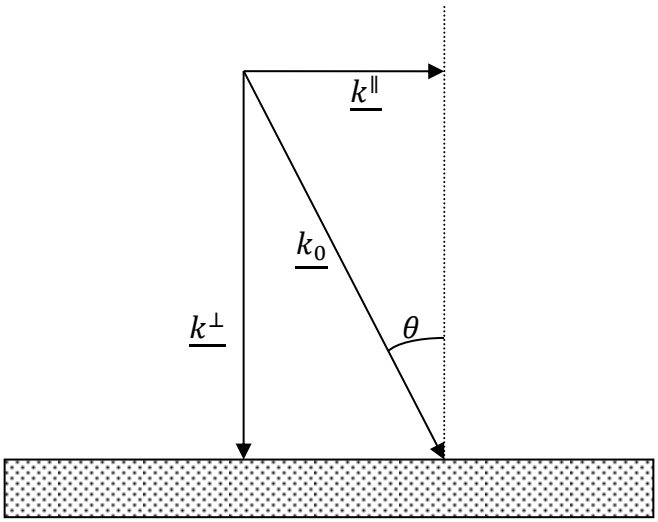

Fig. 2.8. The resolution of incident electron beam wave vector $\underline{k_0}$ into parallel $\underline{k^{\parallel}}$ and perpendicular $\underline{k^{\perp}}$ components.

2.3.2.2 Two Dimensional

The introduction of periodicity in a second dimension 'y' orthogonal to the first, simply leads to second diffraction condition. Therefore using a lattice parameter of b and an integer or integral number m; along 'y'

$$\therefore \sin\theta_b = \frac{m.\lambda}{b} \tag{2.12}$$

$$\& \ \Delta k^{\parallel} = |k_0|.\sin\theta_b = \left(\frac{2\pi}{b}\right)m \tag{2.13}$$

The point of interception of both independent one-dimensional reciprocal lattice vectors gives rise to a corresponding two-dimensional reciprocal lattice vector G, resulting in a two-dimensional LEED diffraction pattern.

$$\therefore G = \Delta k^{\parallel} = \left(\frac{2\pi}{a}\right)n + \left(\frac{2\pi}{b}\right)m \tag{2.14}$$

More generally for a 2D surface net of arbitrary symmetry, the LEED pattern is a scaled representation of the reciprocal surface net. The relationships between the real space lattice vectors (a, b) and the reciprocal lattice vectors (a^*, b^*) are;

$$|a^*| = \frac{2\pi}{|a|} \tag{2.15}$$

$$|b^*| = \frac{2\pi}{|b|} \tag{2.16}$$

With $|a^*|$ perpendicular to $|b|$ and with $|b^*|$ perpendicular to $|a|$ therefore;

$$a.b^* = a^*.b = 0 \tag{2.17}$$

$$a.a^* = b^*.b = 1 \tag{2.18}$$

And with $\frac{2\pi}{|a|}$ and $\frac{2\pi}{|b|}$ the magnitude of the reciprocal lattice vector, Equation 2.14 can be generalised to;

$$G = \Delta k^{\parallel} = (a^*)n + (b^*)m \tag{2.19}$$

There is an inverse relationship between the real space lattice vectors (a, b) and the reciprocal lattice vectors (a^*, b^*). This means that a long vector in real space corresponds to a short vector in reciprocal space according to Equation 2.20 and 2.21.

$$|a| = \frac{1}{|a^*| \cos\theta} \tag{2.20}$$

$$|b| = \frac{1}{|b^*| \cos\theta} \tag{2.21}$$

Where θ is the angle between the vectors (a, a^*) and (b, b^*).

For specific surfaces as shown in the example (Figure 2.9) the angle between the vectors (a, a^*) and (b, b^*) equates to zero, therefore Equation 2.20 and 2.21 simplifies to a simple reciprocal relationship between the lengths.

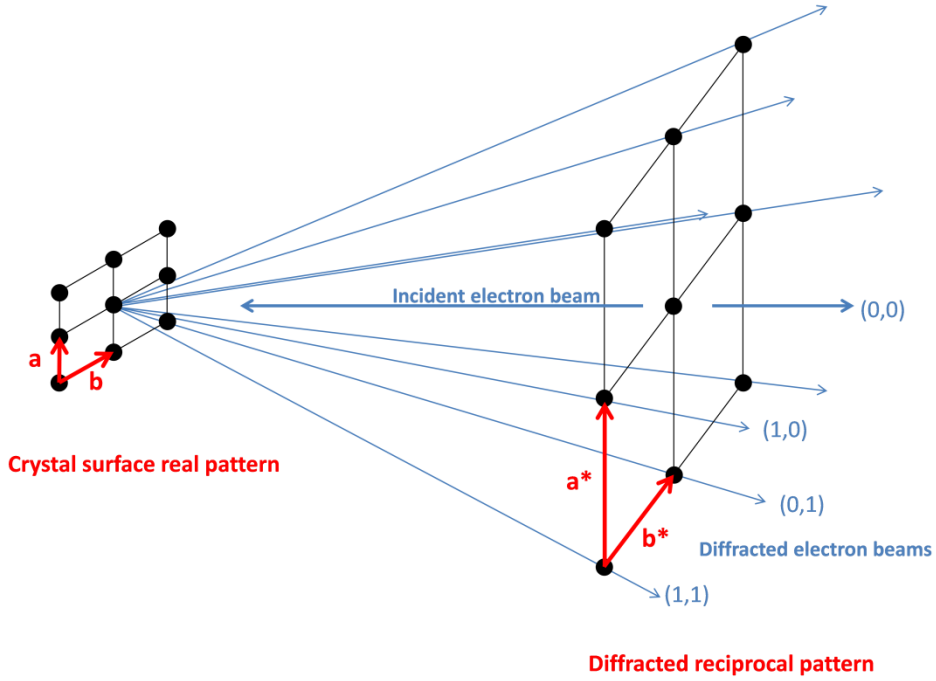

Fig. 2.9. Diffracted LEED pattern for real space lattice vectors perpendicular to the reciprocal lattice vectors.

It is possible to interpret all LEED patterns by applying the following set of rules;

- a must be perpendicular to b^* and b must be perpendicular to a^*.
- a must be parallel to a^* and b must be parallel to b^*.
- Lengths of vectors $|a| = \frac{1}{|a^*| \cos\theta}$ and $|b| = \frac{1}{|b^*| \cos\theta}$.

Applying the above for a (111) hexagonal surface of a simple face centred cubic lattice; Figure 2.10 shows the real and reciprocal lattice vectors.

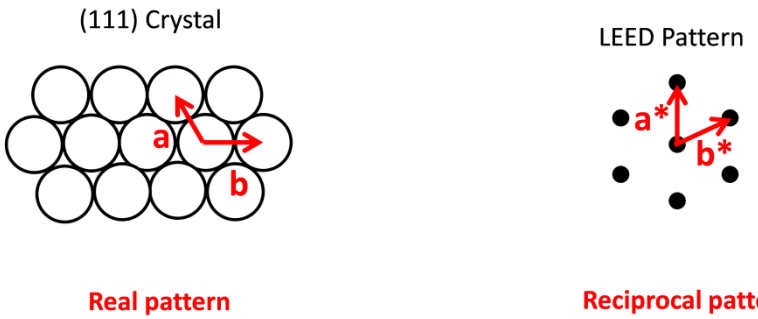

Fig. 2.10. Lattice vectors defining the surface unit cell of a (111) crystal and the corresponding reciprocal lattice vector.

2.4 Quadrupole Mass Spectrometer (QMS)

A Quadrupole Mass Spectrometer (QMS) was used for qualitative or quantitative analysis of gasses within the UHV chamber on the basis of their partial pressure. The distinction among the individual gases is fundamentally on the basis of their individual molar masses. Therefore the primary purpose is to register qualitatively the proportions of gas within the system with regards to the individual molar masses and subsequently determine quantitatively the amount of the individual gases on the basis of various atomic numbers. In brief the measurement devices comprise of a sensor, quadrupole separator and an ion trap (Figure 2.11). The separation of charged particles differing in masses and charges is done by utilizing electrical and magnetic fields which causes only those particles with a certain mass-to-charge to move along a stable track (distance < r_0 between the rods) and reach the detector. The remaining particles move along an unstable path (distance > r_0 between the rods) colliding with the rods where they are discharged (neutralized) thus becoming unavailable to the detector. The detectors can be in the form of an ion trap Faraday cage (Faraday cup) or secondary electron multiplier SEM. Channeltrons or channeltron plates can be used as SEMs to achieve greater sensitivity with gains up to 10^6.

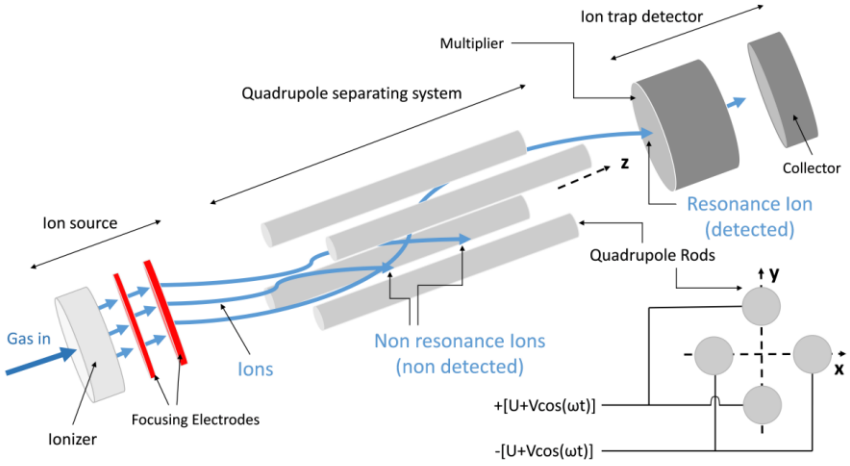

Fig. 2.11. A schematic of a quadrupole mass spectrometer with the ion source, quadrupole separating system and ion trap detector illustrated. Certain ions of a specific mass-charge-ratio passing through the quadrupole separating system are separated when given a set of conditions (U, V, ω and t).

2.5 Temperature-Programmed Desorption (TPD), Thermal Desorption Spectroscopy (TDS)

One of the most sensitive techniques used to determine both the surface kinetics and thermodynamic parameters of desorption/decomposition reactions on surfaces is Temperature-programmed desorption (TPD). This is particularly important in determination of the binding energy (strength of the interaction) between the substrate and the adsorbate and to obtain a measure of the actual coverage.

When the substrate is heated there will be a point at which the thermal energy of the adsorbate is such that the molecular species decomposes to yield either gaseous products or other adsorbate species, the atomic/molecular species reacts with the substrate to yield specific surface compounds or diffuse into the bulk, or alternatively the adsorbate may have enough energy to undergo desorption prior to or after decomposition.

Basically the sample (crystal) is exposed to the desired gas either by back-filling the UHV chamber or by molecular beam. After exposure the sample is rotated to face the quadrupole mass spectrometer and heated at a steady controlled rate $\frac{dT}{dt}$ (a temperature program where the Temperature T is

a linear function of the time t, see Equation 2.22) and the partial pressures of any atoms or molecules desorbing from the surface monitored. For all of the experiments in this thesis the heating rates $\frac{dT}{dt}$ were set between 1 – 3 Ks^{-1}. This experimental technique is also often referred to as thermal desorption spectroscopy (TDS) when the experiments are performed specifically using well-defined surfaces of single-crystalline samples in a continuous pumped UHV chamber.

According to the following Equation 2.22 during a TPD the sample (crystal) is heated in a fashion where the heating rate is linear in time;

$$T_t = T_0 + \frac{dT}{dt}t \tag{2.22}$$

$$\therefore \qquad T_t = T_0 + \beta t \tag{2.23}$$

Where; T_t = Sample temperature at time t, T_0 = Initial sample temperature (Temperature at t = 0), β = Heating rate (Ks^{-1}) at time t.

2.5.1 Theoretical analysis

2.5.1.1 Polanyi-Wigner equation

The shape of the TPD/TDS curve contains information about the desorption kinetics of the adsorbate/substrate interaction. Only a portion of the desorbed ionized adsorbates are collected by the mass spectrometer therefore the TPD curve (or partial pressure) is only proportional to the atomic/molecular coverage (number of adsorbed molecules N) and not equal to it. It is also therefore proportional to rate of desorption of the adsobate ($\frac{dN}{dt}$) which equates to the rate of change/loss of coverage ($\frac{d\theta}{dt}$). The rate of chemical

desorption process often follows Arrhenius-type behaviour and can be described by the Polanyi-Wigner equation in its most general form:

$$\frac{dN}{dt} = -\frac{d\theta}{dt} = v\theta^n . exp\left(-\frac{E_{des}}{RT}\right) \quad (2.24)$$

Where; $N =$ Number of Adsorbed Molecules, $t =$ time (s), $\theta =$ Coverage (ML), $v =$ Frequency or Pre-exponential factor (s^{-1}), $n =$ Kinetic or Desorption order, $E_{des} =$ Activation energy to desorption ($kJmol^{-1}$), $T =$ Temperature (K) and $R =$ Universal Gas constant (8.314 $Jmol^{-1}K^{-1}$)

The rate of desorption (change of coverage) may also be expressed as:

$$-\frac{d\theta}{dt} = k_{des}\theta^n \quad (2.25)$$

Where; $k_{des} =$ rate constant (for desorption), and if this obeys an Arrhenius dependency, it can be written:

$$k_{des} = v_n exp\left(-\frac{E_{des}}{RT}\right) \quad (2.26)$$

The desorption process (change/loss of coverage) can be written as:

$$\frac{d\theta}{dt} = \frac{d\theta}{dT} \times \frac{dT}{dt} = \frac{d\theta}{dT}\,\beta \quad (2.27)$$

With heating rate;

$$\beta = \frac{dT}{dt} \quad (2.28)$$

Substituting into Equation 2.25:

$$-\frac{d\theta}{dT}\beta = k_{des}\theta^n$$

$$\therefore -\frac{d\theta}{dT} = \frac{k_{des}\theta^n}{\beta}$$

Combining with Equation 2.26:

$$-\frac{d\theta}{dT} = \frac{v\theta^n}{\beta}.exp\left(-\frac{E_{des}}{RT}\right) \quad (2.29)$$

The rate of the desorption process contains a term for the coverage θ^n and activation term $exp\left(-\frac{E_{des}}{RT}\right)$. If the activation energy to desorption E_{des} is much greater than RT, little or no desorption occurs. As the temperature is increased the activation term increases exponentially until desorption occurs.

2.5.1.2 Desorption order

Zero-order desorption kinetics

With $n = 0$

$$-\frac{d\theta}{dt} = v.exp\left(-\frac{E_{des}}{RT}\right) \quad (2.30)$$

Zero-order kinetics occurs when an adsorbate forms a thick adsorbate layer (multilayer). In this case all of the TPDs share a common leading edge, with a rapid drop when all of the adsorbates have desorbed. The peak maximum moves to higher temperatures with increasing coverage. Whilst the rate of desorption increases exponentially with temperature it is independent of coverage (Figure 2.12).

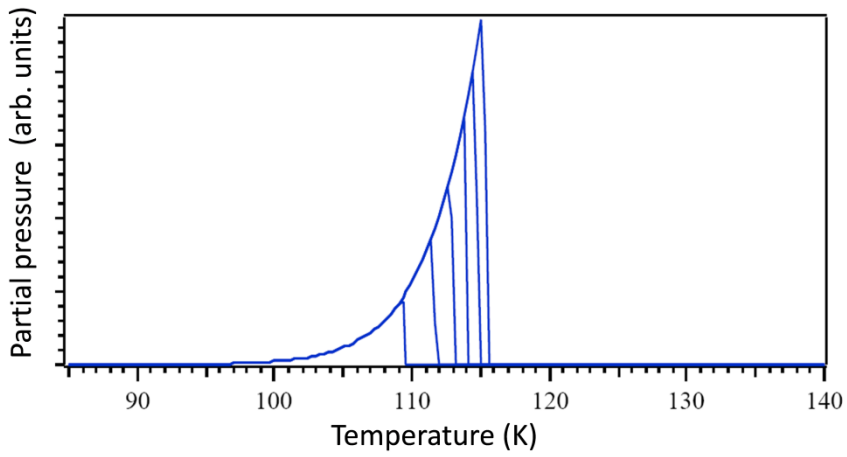

Fig. 2.12. Zero-order desorption of adsorbates at various coverages θ from the substrate surface all sharing a common leading edge.

First-order desorption kinetics

With $n = 1$

$$-\frac{d\theta}{dt} = v\theta . exp\left(-\frac{E_{des}}{RT}\right) \tag{2.31}$$

First-order kinetics occurs during non-dissociative atomic or molecular desorption. Here the peaks have a characteristic asymmetric peak shape with a constant peak maximum regardless of coverage θ (Figure 2.13), which means the rate of desorption is directly proportional to θ.

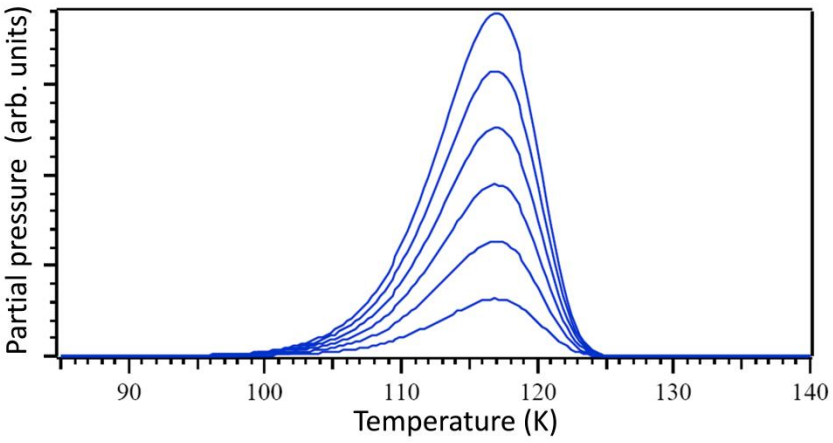

Fig. 2.13. First-order desorption of adsorbates at various coverages from the substrate surface all have a characteristic asymmetric peak shape with a constant peak maximum regardless of coverage.

Second-order desorption kinetics

With $n = 2$

$$-\frac{d\theta}{dt} = v\theta^2 . exp\left(-\frac{E_{des}}{RT}\right) \quad (2.32)$$

Second-order desorption kinetics is only strictly observed during recombinative desorption:

$$A_{(ads)} + B_{(ads)} \rightarrow AB_{(ads)} \rightarrow AB_{(g)}$$

The peaks have a characteristic almost symmetrical shape with a common trailing edge with the peak maximum moving to lower temperatures with increasing θ (Figure 2.14).

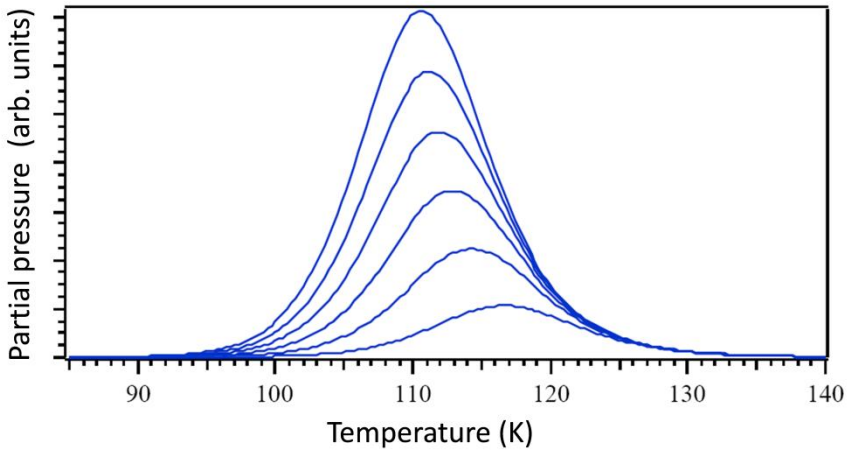

Fig. 2.14. Second-order desorption of adsorbates at various coverages θ from the substrate surface all have an almost characteristic symmetric peak shape with a common trailing edge.

2.6 Dosing of Gases & Molecular Uptake

Dosing of the gases for analysis was achieved either by leaking directly into the chamber and monitoring the pressure on the ion gauge, or by using a molecular beam and monitoring the individual partial pressure by the quadruple mass spectrometer (QMS). The advantage of background dosing is that one is able to replicate experiments more in line with those taking place at ambient conditions as there is more often than not a need to bridge the gap between the studies conducted at low temperatures, under UHV conditions, with those carried out at elevated temperatures and higher pressures. However, the disadvantage is, being non directional the gases have a tendency to stick to all areas of the sample and chamber making it difficult to obtain accurate results, particularly when performing quantitative TPD experiments, mainly due to interfering desorption from other sections of the manipulator and to the background pressure remaining high for extended periods as desorption occurs from the chamber walls. When using a molecular beam the gas source is collimated with a well-defined flux, allowing greater control on both the direction and quantity of gases being dosed. Additionally, as surface reactions are dependent also on the translational, vibrational and rotational states of the incident molecules, all of these factors can be controlled by using a modified molecular beam source, but not by background dosing.

2.6.1 Sticking probability and kinetics of adsorption

The sticking probability S or the adsorption rate is a measure of the ability of a surface to adsorb incident atomic or molecular particles. Adsorption may be intact or dissociative, by either physisorption or chemisorption, depending on the surface temperature. The value of the sticking probability is dependent on surface temperature, adsorbate coverage and the extent of excitation of internal degrees of freedom of the incident particle.

As illustrated in Figure 2.15, sticking probability molecular beam uptake experiments for reactive species were carried out by the well-established beam reflectivity technique[58]. At the beginning of the experiment the base

pressure is at a minimum prior to the introduction of any gases. At $t = t_0$ the shutter to the chamber is opened and the particles are incident on the flag which is positioned between the shutter and the crystal, resulting in the reflection of all particles. At $t = t_1$ the flag is removed and there is an immediate drop in partial pressure due to the uptake/sticking of the particles incident on the crystal surface. After a period of time the pressure begins to rise again due to filling of vacant adsorption sites. After closing the shutter the pressure goes back up to P_0. When the beam is blocked there is a slow drop in the pressure as any gases introduced into the chamber are pumped away.

The sticking probability can be calculated at any time during the uptake period using the formula;

$$S_t = \frac{P_0 - P_t}{P_0} \tag{2.33}$$

Where; $P_0 =$ Base chamber pressure – Partial pressure (from molecular beam introduction) and $P_t =$ Base chamber pressure – Partial pressure (during uptake)

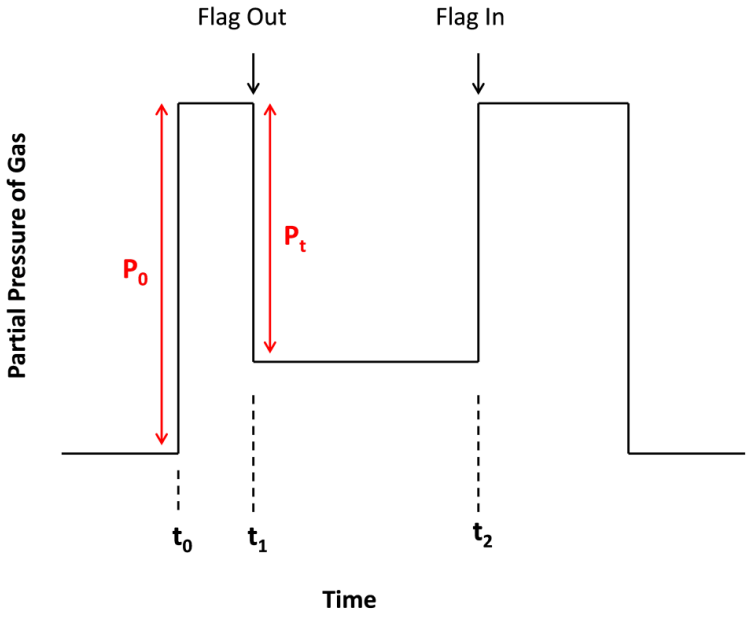

Fig. 2.15. A representation of the King and Wells method for measuring the sticking probability based on an uptake with sticking probability (0 < S < 1).

In Langmuir adsorption the uptake is proportional to the number of vacant sites, $S \propto (1-\theta)$. However, very rarely does the sticking probability S behave according to this Langmuir associative adsorption model where it is assumed that S is directly proportional to the fraction of vacant sites. More often than not it is not as simple as this, as S can drop off significantly at the start of the uptake. In other cases S behaves monotonically where the adsorbate forms cluster multilayers or even increases at the start of the uptake process only to drop off significantly as the coverage approaches a monolayer. In the latter case the molecules are physisorbed into an extrinsic precursor state where the rates of migration and desorption above occupied sites are significantly different to those rates associated with unoccupied sites[54,59].

2.7 Physical Vapour Deposition PVD

One of the most common ways to form surface metal alloys is by vapour deposition. This is carried out by the thermal evaporation (sublimation) of the source metal by resistive heating where the vacuum allows the vapour particles to travel directly to the substrate where they condense and form the surface alloy. Under UHV conditions the mean free path is extremely long, therefore during sublimation the atomic metal is able to travel directly to the substrate without colliding with the background gases.

Resistive sublimation was achieved by attachment of the source materials; for this research gold to a filament made from a refractory metal. During the sublimation process the filament is heated by passing a large enough current to deposit the source metal.

The sublimated source metal is condensed on the substrate and the sublimation time varied according to the coverage required. Deposition was followed by annealing of the substrate to obtain a uniform layer and subsequently assessed by LEED. Tungsten wire was used as the refractory metal due it having a vapour pressure of zero at the sublimation temperatures of gold.

Chapter 3

3 Oxidation of CO on Pd(111) and Au/Pd(111)

3.1 Introduction

Bimetallic surface chemistry plays a crucial role in a number of technologically important areas, including heterogeneous catalysis, microelectronics fabrication, electrochemistry, and corrosion. With the advent of UHV surface analytical techniques and the development of efficient methods for surface preparation, it has been possible for the last 45 years to prepare well-defined bimetallic surfaces. One of the main goals of studying bimetallic surfaces is to better understand the unique function of mixed-metal alloys in heterogeneous catalysis. The ability to prepare well-defined bimetallic surfaces presents us with the opportunity to not only correlate the chemical reactivity of the surface with that of the bimetallic mix, but to also tailor the bimetallic to possess desirable reactive properties[39].

Among bimetallic catalysts, the Au/Pd surface alloy system has received significant attention due to its enhanced activity in a number of reactions. Whilst Au/Pd bimetallic alloys have been found to provide both active and selective catalysts for a number of reactions, including CO oxidation, no catalytic measurements have been carried out on the Au/Pd(111) system, only on Au/Pd(100). Hence the aim of the research in this chapter is to produce a bimetallic Au/Pd(111) alloy with a view to enhance the activity of CO oxidation with CO pre-dosed on the surface.

Before proceeding it is important that we define the terms alloy, multi-metallic and bimetallic, as these terms have a tendency to be used incorrectly or interchangeably. Irrespective of intimacy or precise manner of mixing, an alloy is most conveniently defined as a metallic system containing two or more components. When an alloy contains two metallic components it is often referred to as either a bimetallic or multi-metallic. For clarification,

with regards to our research we shall employ the term bimetallic when the two elements are segregated and only use the term alloy when they are intimately mixed.

Surface composition and local order at the surface are both key properties for all heterogeneous catalytic applications. As a result, a detailed knowledge of the atomic surface compositions and lateral distribution of Au on the Pd(111) crystal surface is necessary to obtain any real fundamental understanding of the effects, if any, on any enhanced catalytic reactions. The following sections detail the characterisation of the Au/Pd surface alloy and whether or not it is possible for the Au to form an ordered structure on the Pd(111) surface.

3.1.1 Au Film deposition and structure on Pd(111)

Baddeley et al.[60] used LEED and Auger Electron Spectroscopy (AES) to characterise a Au/Pd surface alloy whilst investigating ensemble effects in the coupling of acetylene to benzene on a bimetallic Au/Pd(111) surface. Calaza et al.[61] also used similar techniques in their research to study the adsorption of ethylene on Au/Pd(111) alloy surfaces. Their research showed that progressive annealing of Au overlayers, pre-dosed by vapour deposition on Pd(111) at RT, led to the formation of a series of random surface alloys with continuously varying composition. They found that the most efficient catalyst corresponds to a surface composition of 85 % Pd and 15 % Au. They also found it difficult to obtain ordered surface alloys, instead a range of disordered Au/Pd solid solutions were produced throughout.

Based on their results the Au coverages were estimated from AES and LEED, where Figure 3.1 shows the variation in Au (69 eV) and Pd (330 eV) peak intensities as a function of the sample annealing temperature, for an approximate 4 monolayer (ML) Au film. It is clear that the Au overlayers begin to intermix with the Pd substrate at about 600 K, with the alloy forming at ca. 800 K. This was evident by the sharp rise in the Pd AES signal, concomitant with a precipitous drop in the Au signal at 600 K, indicating the intermixing of the surface Au with the Pd substrate. At 700 K both signals balance out with

the surface alloy forming above at 800 K. Above 1050 K the Au signal drops off completely, simultaneously with the Pd signal levelling off, indicating diffusion of the Au into the bulk Pd. Similarly there is a decrease in the lattice parameter in line with that of the pure Pd surface with increasing annealing temperature, levelling off above 1050 K.

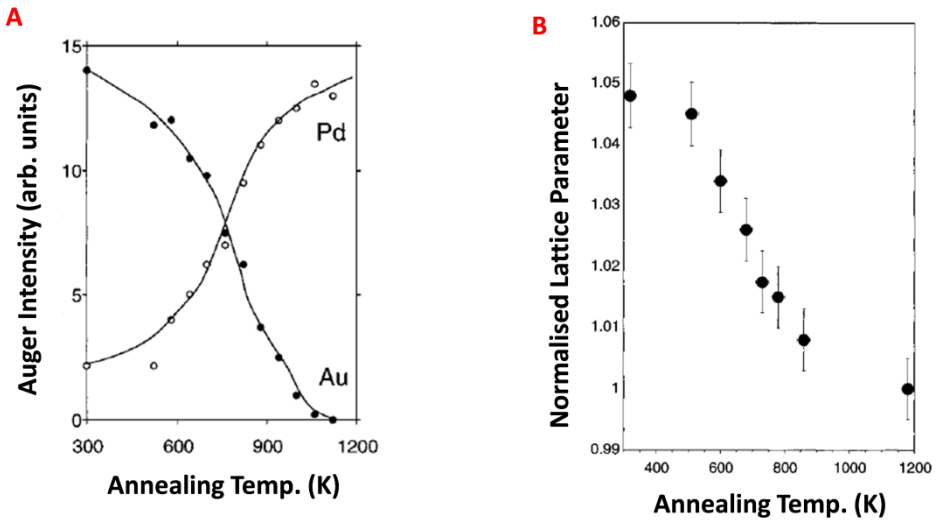

Fig. 3.1. (A) Au 69 eV and Pd 330 eV AES peak intensities for 4.5 ML Au on Pd(111) as a function of annealing temperature. (B) Variation in measured lattice parameter (from LEED data) as a function of annealing temperature for a 4 ML Au film on Pd(111). Reproduced (Adapted) from Baddeley et al. Ensemble effects in the coupling of acetylene to benzene on a bimetallic surface: A study with Pd(111)/Au. J. Phys. Chem. 100, 2189–2194 (1996). Copyright 2015 American Chemical Society."

Similar results were also obtained by Li et al.[62] when researching the formation and characterization of Au/Pd surface alloys on Pd(111). Using X-ray Photoelectron Spectroscopy (XPS) to determine the Au/Pd alloy, they found that Au grew in a layer-by-layer fashion on the Pd(111) surface at 300 K, and started to diffuse into the bulk after annealing to above ca. 600 K, resulting in a decrease in the Au signal intensity and a simultaneous increase in the Pd signal intensity with increasing temperature. As shown in Figure 3.2, it is clear that the Au film starts to intermix with the Pd substrate at ca. 500 K. Extensive intermixing of Au and Pd is found at temperatures above 700 K, with Au moving into the bulk of the metal, whilst annealing the sample

to 1110 K, resulted in almost no Au being detected. After assessing the LEED data Li et al. found the lattice spacing of the alloy varied linearly with alloy composition, yet they were unable to establish an ordered pattern between the Au and Pd surface atoms. Hence it was concluded that the Au and Pd atoms were likely randomly distributed on the surface.

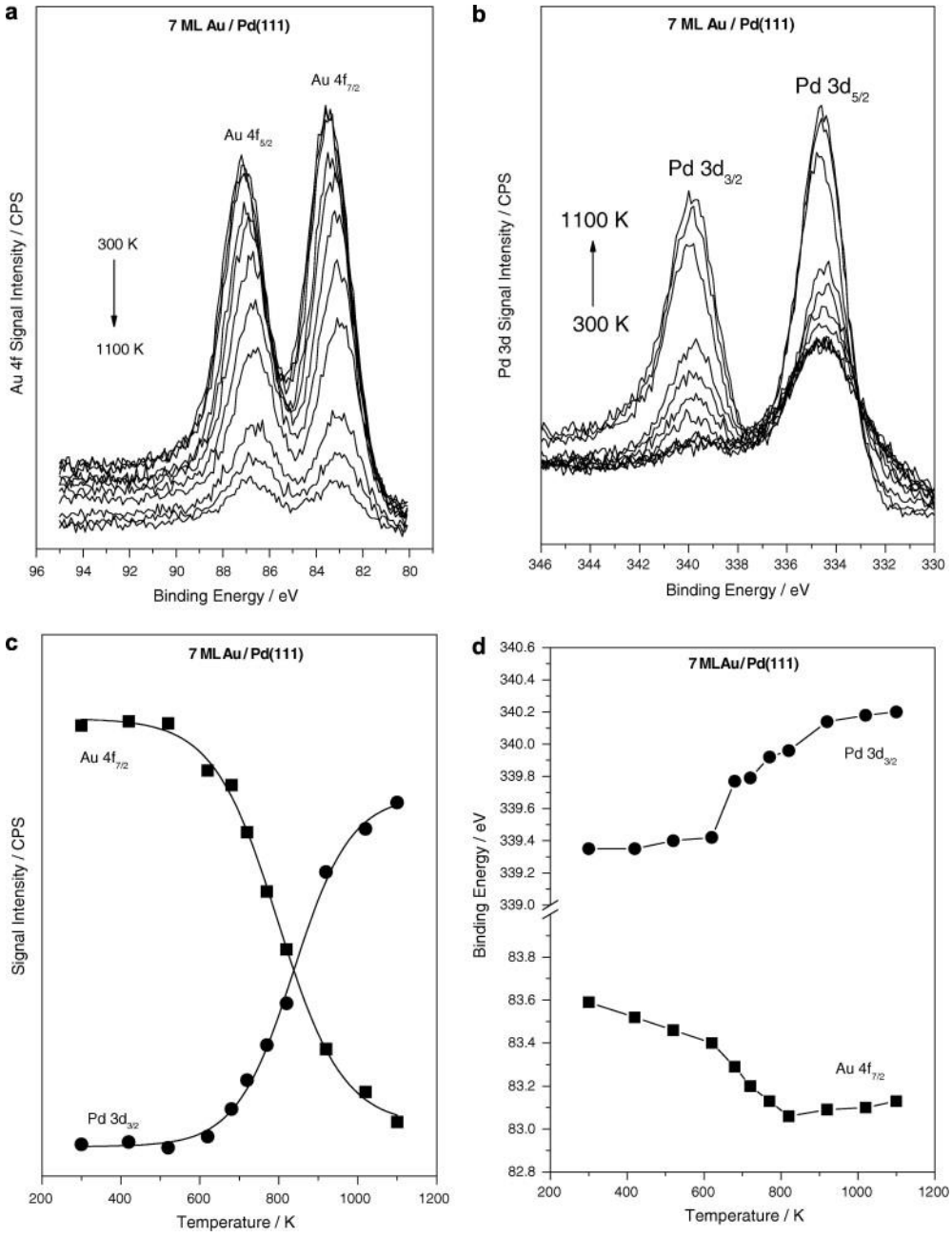

Fig. 3.2. (a) and (b) display the Au 4f and Pd 3d XPS regions as a function of annealing temperature following the deposition of 7 monolayers of Au on a Pd(111) surface at 300 K. Graph (c) plots the Au $4f_{7/2}$ and Pd $3d_{3/2}$ signals intensities and graph (d) their binding energies as a function of annealing temperature. "Reprinted from *Surf. Sci.* **601,** (2007), Li, Z. *et al.* Formation and characterization of Au/Pd surface alloys on Pd(111), 1898–1908, Copyright (2015), with permission from Elsevier

3.1.2 Thermodynamic enthalpy of mixing (Gibbs free energy) and the atomic radii

Several factors determine the formation of a well-defined bimetallic surface, namely the size and sign of the mixing enthalpy change (Gibbs free energy), whereas the particle size in terms of the atomic radii influences the enthalpy of mixing. A reaction that is spontaneous either gives off energy in the form of heat and therefore has a negative enthalpy $(\Delta H < 0)$, or there is an increase in the disorder of the system leading to an increase in the entropy $(\Delta S > 0)$. The Gibbs free energy (G) of the system is defined as the enthalpy of the system minus the product of the temperature times the entropy of the system (Equation 3.1).

$$\Delta G = \Delta H - T.\Delta S \qquad (3.1)$$

Where: ΔG = Gibbs free energy change, ΔH = change in enthalpy, T = (absolute) temperature and ΔS = change in entropy.

When alloying (mixing) two or more metals the Gibbs free energy or enthalpy change determines whether mixing at constant temperature T (and pressure P) is a spontaneous process. The mixing of an ideal system has zero enthalpy of mixing meaning that the Gibbs free energy is always negative, hence mixing of ideal solutions are always spontaneous. However, the mixing of a Au/Pd system has been found to have a small negative enthalpy, which means the system tends to form spontaneous solid solutions which behave almost ideally or as regular solutions. Conversely, when the enthalpy is large and negative for metal alloying, the system tends to favour the formation of inter-metallic compounds or ordered solutions. In contrast, when the enthalpy is large and positive only surface bimetallic clusters are formed.

In addition the Au/Pd system has also proved to be ideal for fundamental studies due to the fact that the lattice mismatch with regards to each element separately is only 4.86 %, based on the atomic radii of 1.37 and 1.44 Å for Pd and Au respectively[62,63].

3.1.3 Catalytic activity, charge transfer and density of states (DOS)

For the late transition metals such as Pd and Au both their catalytic and chemisorption properties are determined by the valence d electrons, as opposed to the s and p electrons. The position of the Fermi level (E_f) is dependent upon the valence electronic configuration of the respective metals. For Pd the electronic configuration is such that E_f lies within the partially filled d band, whereas for Au, the d band is complete filled and the E_f lies within the sp band. The high catalytic activity of Pd is associated with the high density of electrons at the E_f, whereas Au has a much lower relative catalytic activity due to its lower density of electrons as illustrated in Figures 3.3 and 3.4[41,64,65].

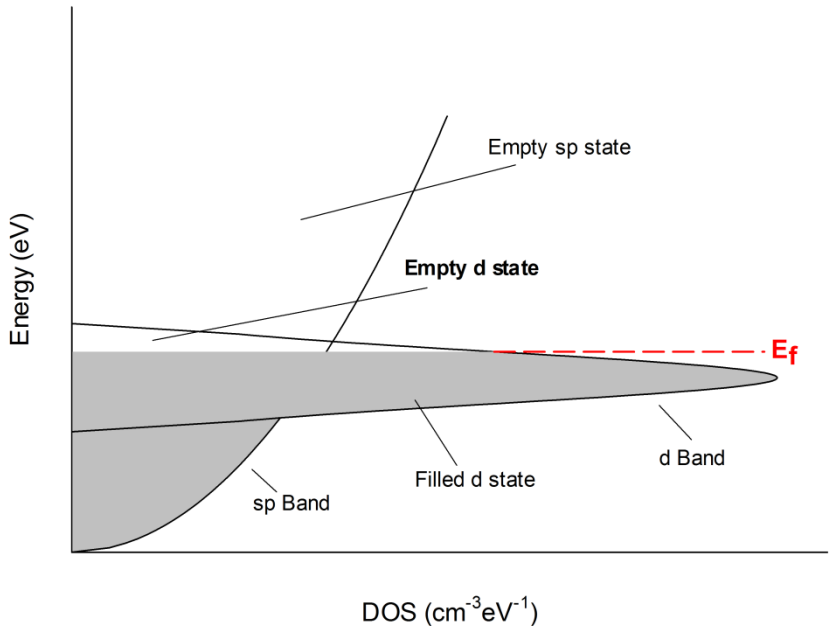

Fig 3.3. High density electronic state at the Fermi level E_f for Pd which has a partially filled (or open) d-band.

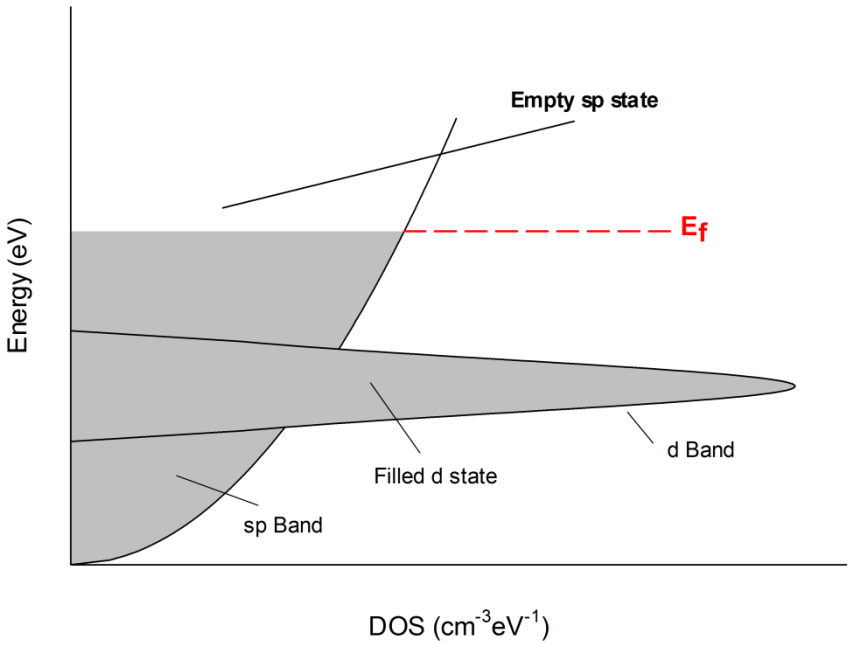

Fig 3.4. Low density electronic state at the Fermi level E_f which lies in the sp band for Au and has a filled d-band.

In theory alloying Au with Pd will result in a transfer of electrons from the Au to the Pd due to the fact the electrons associated with the Au are at a higher Fermi energy level than the electrons associated the Pd. This might result in a decrease in the reactivity of the bimetallic Au/Pd surface in comparison with the pure Pd(111) surface. This change is directly associated with the surface electronic structure, manifested as a shifting of the d-band centre away from the E_f, which in turn leads to a weaker interaction between the adsorbates and the surface[66]. This transfer will also decrease the repulsion of the electrons within the 4d band of Pd, resulting in a shift of the Fermi level within the Pd with an overall lower DOS[54]. In addition, one would expect re-hybridisation of one or both of the metals[67]. According to Lee et al.[65] and later Sárkány et al.[68], Pd has been found in certain cases to adopt the lattice constant of Au during alloying which also causes a rise in E_f within the Pd d band. This enhances the atomic-like character of the Pd atoms with a corresponding weakening towards the reactants i.e. CO or O.

The high catalytic activity of Pd is directly associated with its higher DOS when compared to the lower catalytic activity of Au which has a much lower DOS. Now one may assume based on these facts that alloying with Au will inevitably result in a reduction of catalytic activity. This is not necessarily the case for Au/Pd bimetallics, where enhanced catalytic activity is often found due to both ensemble and ligand effects. It may also be tempting to speculate that alloying two metals that are active for a given reaction may augment with enhanced reactivity. Unfortunately, bimetallics of this nature have been found to only exhibit the maximum activity of the individual metal[69].

3.1.4 Ensemble and ligand effects

Ensemble effects are associated with the dilution of surface atoms, in this case the dilution of Pd(111) surface atoms by Au atoms. For certain reactions this gives rise to an enhanced catalytic reaction rate due to the formation of isolated highly reactive surface sites, in addition to the switching off of undesirable side reactions. Ligand effects on the other hand are associated with the change in the electronic structure i.e. the change in the DOS of the valence electrons of Pd(111) surface atoms by incorporating Au atoms and vice versa. However, predicting the direction of the ligand effect is extremely difficult without experimental data.

Numerous studies have shown that it is not possible to alter ensemble effects through alloying without also altering the ligands around the adsorption sites[66,69]. Hence, making a clear distinction as to whether these effects are primarily associated with ensemble effects, or a combination of both, is difficult.

Enhanced activity for the oxidation of CO on Au-Pd bimetallic surfaces has been found by Gao et. al[1–3], for Pd-Au nanoparticles grown on a thin TiO_2 layer deposited on both Mo(110) and AuPd(100). Their investigation showed that alloying Pd with Au formed isolated Pd sites that were incapable of dissociating O_2, a pre-requisite for CO oxidation. Only at elevated CO

pressures did the surface become active due to chemisorption induced segregation. In this case, the Pd segregated to the surface due to it having a much higher CO binding site energy of 84 $kJmol^{-1}$ as opposed to only 69 $kJmol^{-1}$ on Au[41]. For the pure single crystal surfaces, these values are much different, 150 $kJmol^{-1}$ on Pd and 40 – 50 $kJmol^{-1}$ on Au. Only under stoichiometric conditions $\left(\frac{1}{2}O_2 + CO \rightarrow CO_2\right)$ did the Au-Pd alloy show a degree of superior activity due to the weakening of the CO-substrate interaction, caused by ligand effects.

Under O_2 rich conditions the activity was much superior on the clean Pd(111) surface due to facile dissociation of the O_2 molecules. An earlier theoretical study conducted by Liu and Norskov used DFT to assess the interaction of CO, O_2 and N_2 on the Au/Pd(111) bimetallic surface. They found a linear relationship between the binding energy of CO and both atomic O & N weakening with an increase in Au coverage. In addition, their study showed the main weakening in binding energy was mostly attributed to ensemble effects. This weakening of the CO binding energy should prove significant in terms of increasing oxidation on the CO pre-dosed surface.

3.2 Experimental

A single Pd(111) crystal with surface area 80 mm^2, cut and polished with an accuracy to ~ 0.1° of the crystallographic plane was used throughout this study. All experiments were performed in an UHV chamber, operated at base pressures < 10^{-10} mbar as detailed in Chapter 2. The polished Pd(111) crystal was cleaned by prolonged Ar^+ ion sputtering cycles of 15-20 minutes at a drain current of 2 - 5μA (500 eV) at room temperature. This was performed prior to each experiment to remove surface contaminants such as carbon, oxygen and sulphur. This was followed by post-irradiation flash annealing to 1023 K to remove any lattice defects produced from the impinging ions and to remove any shallow implanted argon. The surface ordering was then assessed by LEED to obtain a sharp (1 x 1) pattern.

All Temperature-Programmed Desorption (TPD) and uptake experiments were measured by a VG Smart IQ^+ Thermo QMS. A heating rate (dT/dt) of 2.4 Ks^{-1} was used throughout for the TPD measurements. Oxygen (99.5 % high purity supplied by BOC, CAS No: 7782-44-7), carbon monoxide (99.0 % CO, supplied by Aldrich, CAS 680-08-0) and water (deionised Milli-Q) were all dosed by means of a molecular beam.

Sublimation was achieved as detailed in Chapter 2 by attachment of Au wire (0.25 mm) to a Tungsten wire filament. During sublimation, the filament was heated by passing a current of ~ 4.0 A through the filament to evaporate the Au. Deposition was then followed by flash annealing of the substrate to various temperatures according to methods of Baddeley et al.[60], Calaza et al.[61] and Li et al.[62], to order up the Au layer, which would otherwise remain in a quasi-random lattice arrangement[39]. After annealing, the substrate was saturated with ca. a monolayer of H_2O, followed by a post deposition TPD in order to characterize the Au/Pd surface alloy. This was done in order to determine the exact temperature the deposited Au started to diffuse into the Pd(111) substrate, and, therefore, the exact temperature required to form the alloy. Due to the relative inertness of Au and hence its resistance to wetting[70], H_2O was also dosed on the surface to estimate the relative Au coverage prior to formation of the alloy. This was done by equating the

fraction of the peak with a corresponding multilayer binding energy during TPD to the amount of Au on the surface.

The activation energy for H_2O desorption E_d was estimated using the following equation 3.1, as shown in the Results and Discussion 3.1.1, Figure 3.7;

$$E_d = R.T_p\left[In\left(\frac{A.T_p}{\beta}\right) - 3.46\right] \quad (3.1)$$

where R = the universal gas constant (8.314 $Jmol^{-1}K^{-1}$), T_p = desorption peak max, A = pre-exponential factor (assumed 10^{13} s^{-1}) and β= heating rate (dT/dt) = 2.4 Ks^{-1}.

The value of the pre-exponential factor A specifically relates to temperature dependent molecular collisions. In addition, it is an indication of the floppiness of the adsorbate H_2O molecules and provides a correction through the conventional transition state theory. As a result a value of 10^{13} s^{-1} can only be assumed based on the fact that no dynamic corrections through the conventional transition state theory occur. That is, the H_2O adsorbate molecules are not interacting on the surface with no change in the vibrational, rotational and translational degrees of freedom. Values for pre-exponential factor A can actually range from 10^{11} - 10^{19} s^{-1}, however, for these experiments the E_d for H_2O is used purely to assess the gold coverage. As a result we can assume a value of 10^{13} s^{-1} which is a common value for simple non-dissociative first order desorption. To be concise we are assuming a simple molecular first order desorption from the substrate surface to the gaseous phase, neglecting any coverage dependence and kinetic parameters[15,9,71–73].

3.3 Results and Discussion

3.3.1 Formation & Characterisation of the Au/Pd(111)-alloy by deposition of Au on the Pd(111) surface.

This section gives a brief outline of the methods used in order to characterise and form the Au/Pd(111) alloy. Although it might have been more accurate to use AES or XPS to estimate the exact Au coverage, these techniques were not available for us to use. We were able to make use of the QMS alongside the molecular beam doser to obtain an estimate of the Au coverage. As this research is centred on enhancing the catalytic oxidation of CO, an exact coverage of Au was not of paramount importance.

Figure 3.5 shows the TPD of 1 ML H_2O desorbing from the clean Pd(111) surface calculated by a timed uptake. The timed uptake was calculated by repeated uptakes followed by TPDs up to the point the monolayer transferred to produce an additional multilayer peak with lower binding energy. Figure 3.6 shows the TPD of a 1 ML of H_2O from the surface after vapour deposition of a single monolayer of Au annealed to various temperatures. As shown in Figure 3.7, the amount of Au deposited was estimated by dosing a single monolayer of H_2O onto the Au/Pd(111) surface after a flash anneal to 500 K. A flash anneal was required to order up the Au on the Pd(111) surface prior to formation of the alloy. The grey area corresponds to the peak associated with adsorption on Au, which in this case corresponds to 0.67 ML of Au. As stated, with the Au being inert to the H_2O the peak has shifted to a binding energy similar to that of a multilayer peak desorbing from Pd(111).

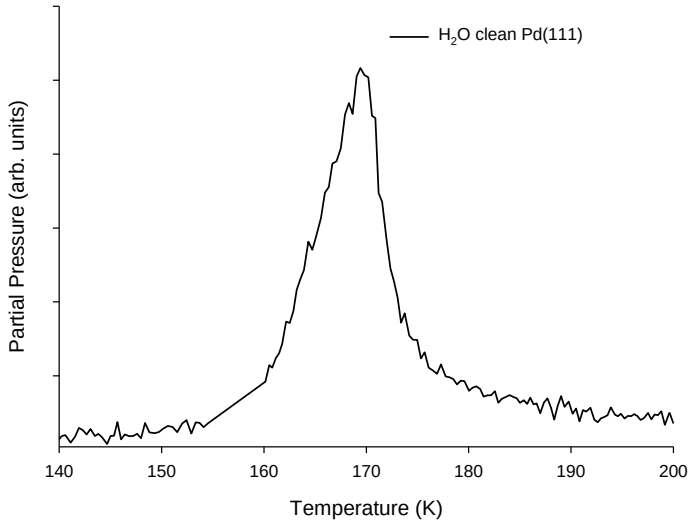

Fig 3.5. TPD of H_2O from clean Pd(111) (dT/dt) of 2.4 Ks^{-1}. The activation energy for H_2O desorption = 0.45 eV (43 $kJmol^{-1}$)

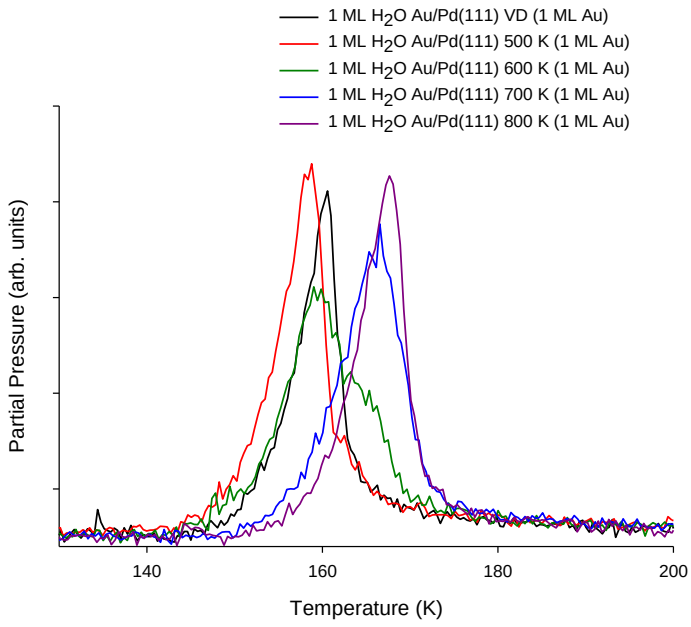

Fig 3.6. TPD of H_2O from the Au/Pd(111)-Alloy surface (dT/dt) of 2.4 Ks^{-1} following 1 ML vapour deposition of Au (black) and subsequently annealed to 500 K (red), 600 K (green), 700 K (blue) and 800 K (purple). Alloying occurring at 700 K (blue), with a H_2O activation energy of desorption = 0.442 eV (42.6 $kJmol^{-1}$), with the Au defusing into the bulk Pd at 800 K (Purple), with a slightly higher H_2O activation energy of desorption = 0.443 eV (42.83 $kJmol^{-1}$).

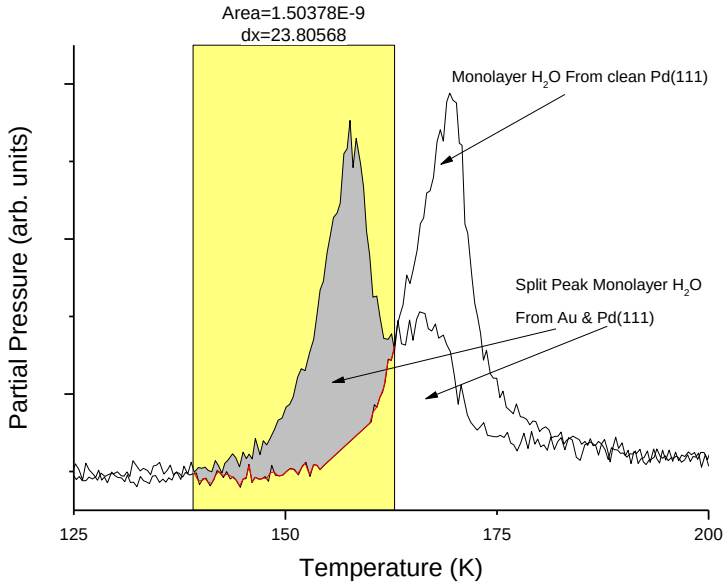

Fig 3.7. The coverage estimation of Au/Pd(111) based on TPD of a single monolayer of H_2O from the Au/Pd(111)-bimetallic surface (dT/dt) of 2.4 Ks^{-1} vapour dosed with Au and subsequently annealed to 500 K. The shaded (Grey) area corresponds to H_2O desorbing from the Au covered part of the Pd(111) crystal with an activation energy of desorption = 0.42 eV (40.54 $kJmol^{-1}$) with H_2O desorbing from the uncovered Pd(111) with an activation energy of desorption = 0.45 eV (43.44 $kJmol^{-1}$)

In order to investigate the diffusion of Au into the Pd(111) substrate and the resulting formation of the Au/Pd(111) alloy, a single monolayer of Au was first deposited on the clean Pd(111) at 90 K. A single monolayer of H_2O was then dosed on the surface at 90 K, followed by a TPD resulting in the black peak seen in Figure 3.6. The crystal was then flash annealed to 500 K, and then allowed to cool back to 90 K. This was followed by a single monolayer dose of H_2O and a TPD as shown by the red peak. Repeat anneal cycles were carried out increasing the temperature by 50 K each time followed by a H_2O monolayer uptake and TPD after each cycle. For the sole purpose of clarification only the temperatures from 500 to 800 K are plotted in Figure 3.6 omitting the 50 K increments in between. It is clear that Au begins to intermix with the Pd(111) surface at 600 K (green peak) finally forming the Au/Pd(111) alloy at 700 K (blue peak). At 800 K, the Au appears to diffuse into the bulk Pd at which point the TPD of the H_2O has an activation energy of desorption,

0.443 eV (42.8 kJmol^{-1}) very close to that of the uncovered Pd(111), surface 0.45 eV (43.4 kJmol^{-1}).

3.3.2 LEED of Au/Pd(111)-alloy

LEED patterns were taken throughout the characterisation process of the Au/Pd(111)-alloy in order to access the growth and lateral adatom-adatom arrangement of Au on the Pd(111) substrate. Alloying of metals that have the same bulk structures as the parent substrate and a similar lattice parameter usually results in 2D pseudomorphic growth of the admetal[39]. Here the adatoms tend to assume the same position as the atoms in the next layer of the substrate. This was evident during the characterisation of the Au/Pd alloy by the observation of a sharp $p(1 \times 1)$ LEED pattern as shown in Figure 3.8. Similar LEED observations were found by Paffett et al.[74,75] whilst researching surface chemical properties of Ag/Pt(111) and the adsorption of Cu on Pt(111). It has been documented that alloy metals with a lattice mismatch ≤ 9 % will display this kind of 2D pseudomorphic growth[39]. Just to reiterate the lattice mismatch between Au and Pd is 4.86 %; likewise in the research conducted by Paffett et al. the lattice mismatch was 3.47 % for Ag/Pt and 7.91 % Cu/Pt.

It is clearly visible that the LEED image of the AuPd(111) is much sharper and brighter than that of the clean Pd(111). This is possibly due to an improvement in the surface crystallinity concomitant with a decrease in the surface roughness at the atomic scale. The enhancement in sharpness is typically related to an increased surface area of well-ordered domains, whereas the increased intensity in brightness is directly associated with the number of well-ordered domains. An increase in the number of well-ordered domains would effectively produce significantly greater coherent interference. It is therefore possible that all of the aforementioned effects are a combination of the surface alloy forming along with the annealing of the crystal to 700 K.

The majority of research and characterisation of the Au/Pd(111)-alloy has been performed using XPS, LEED and AES[60–62], with very little STM results

obtained. With this, researchers have yet to establish anything other than a random distribution for the Au when alloyed with the Pd(111) substrate. With our LEED observations, we have not been able to find anything suggesting any ordered structure of the Au on Pd(111) either, and therefore we can only assume a quasi-random alloy structure is most likely.

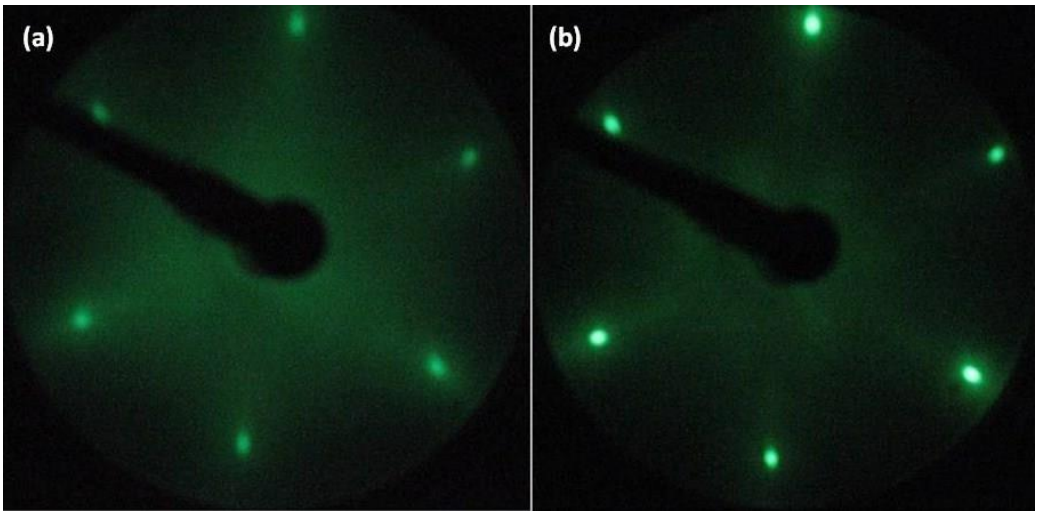

Fig 3.8. LEED images of (a) clean Pd(111), and (b) AuPd(111)-alloy annealed to 700 K, both taken at 88.9 eV. Patterns appear very similar due to pseudomorphic heteroepitaxial growth where the inter-atomic spacing is the same.

3.3.3 Adsorption of CO and atomic oxygen on the Pd(111) surface

This section details the adsorption of CO and atomic O on the Pd(111) done before investigating any catalysis reactions. CO usually adsorbs carbon end down, at either the atop, bridge or three-fold bridge configurations on pure (111) metal surfaces. It is also possible for the CO molecule to adsorb flat, dissociating to produce $C_{(ads)}$ + $O_{(ads)}$, however this is only likely to occur on the early transition metals and less frequently on the later ones, including Pd and Au. Whilst the traditional adsorption model for CO introduced 50 years ago by Blyholder[76] serves well as a theoretical pedagogy, previous studies of the CO/Pd(111) system by Kuhn et al.[77] have shown that there are

multiple adsorption sites for CO depending on the coverage and adsorption conditions, as confirmed in our study conducted at 150 K.

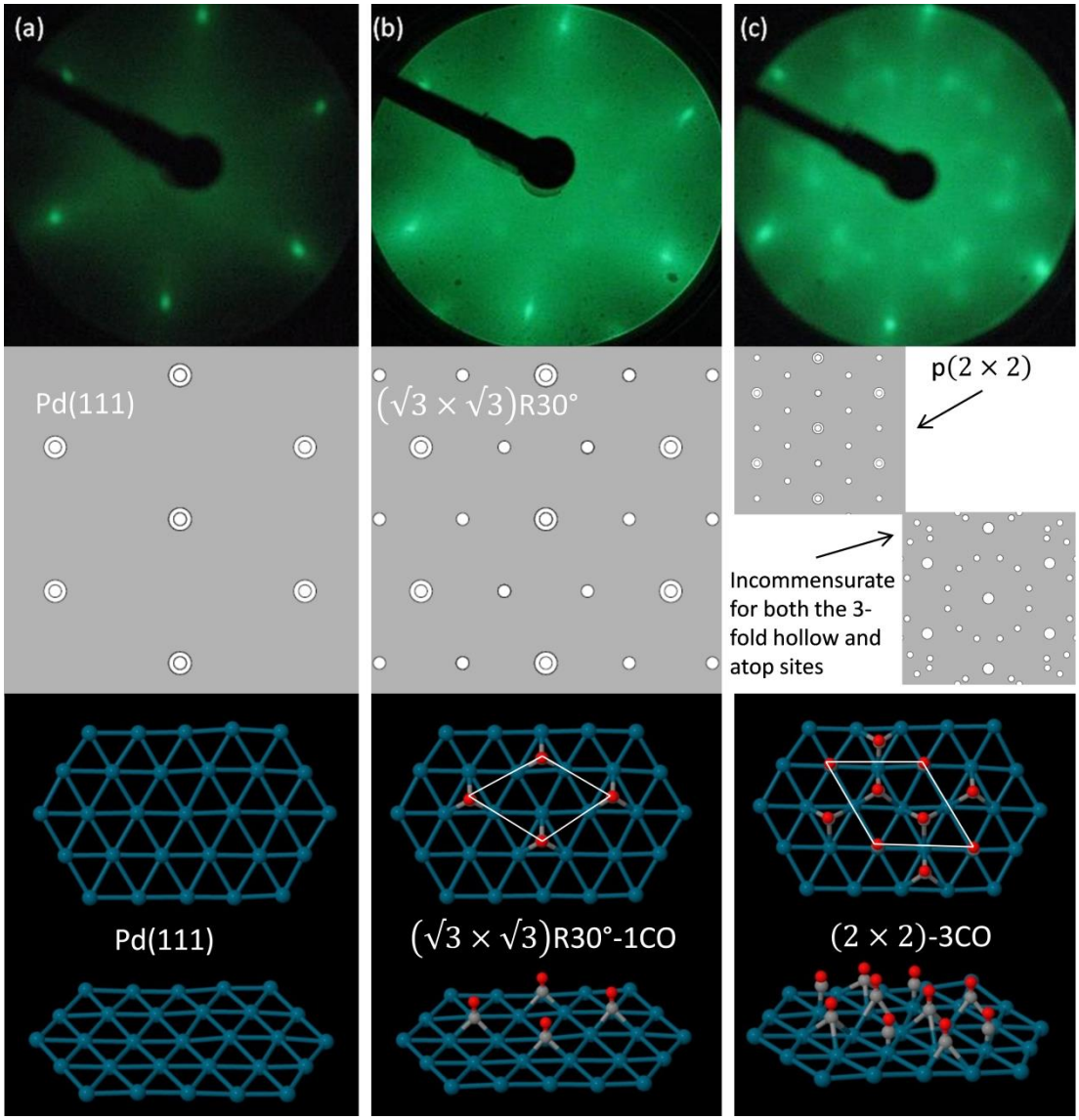

Fig 3.9. LEED images for (a) clean Pd(111) at 88.9 eV, with schematic representation for the Pd(111) reflection shown below, (b) $(\sqrt{3} \times \sqrt{3})$R30°-1CO structure at 88.9 eV for a 0.33 ML coverage of CO, with schematic representation for the $(\sqrt{3} \times \sqrt{3})$R30° reflection shown below and (c) (2×2)-3CO structure at 75.9 eV for a 0.75 ML coverage of CO, with schematic representations for both the p(2×2) reflection along with the incommensurate reflections for the atop and three-fold hollow sites. These are both shown as the complex (2×2)-3CO is associated with both of these LEED patters. 1CO indicates a single CO molecule in the unit cell for the $(\sqrt{3} \times \sqrt{3})$R30°-1CO structure and the 3CO indicating three CO molecules in the unit cell for the (2×2)-3CO structure. Pd(111) crystal surface (blue substrate atoms) with CO molecules (grey-Carbon & red-Oxygen).

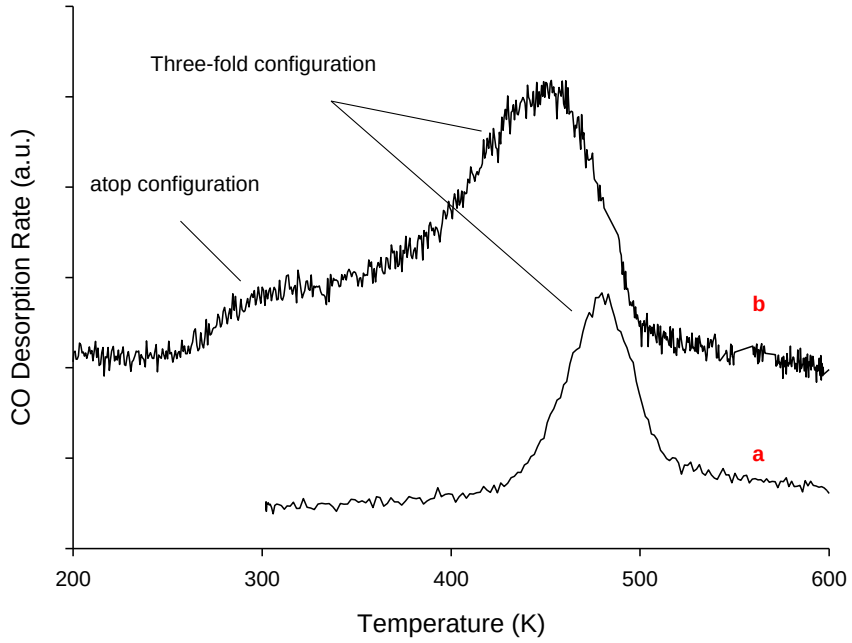

Fig 3.10. TPD of CO from clean Pd(111) at a heating rate (dT/dt) of 2.4 Ks^{-1}, a) 0.33 ML coverage of CO $(\sqrt{3} \times \sqrt{3})$R30°-1CO structure b) saturated 0.75 ML coverage of CO (2×2)-3CO structure

It was found that at a coverage ≤ 0.33 ML the CO molecules preferred to bind to the three-fold hollow site, giving rise to the $(\sqrt{3} \times \sqrt{3})$R30°-1CO structure as shown in the LEED patterns (Figure 3.9 b). When increased to a saturated coverage of 0.75 ML, the molecules were found to occupy both the three-fold hollow and atop sites producing a (2×2)-3CO structure as shown in the LEED patterns (Figure 3.9 c). For the $(\sqrt{3} \times \sqrt{3})$R30°-1CO structure the 1CO signifies a single CO molecule in the unit cell as shown, whereas for the (2×2)-3CO structure there are three CO molecules in the unit cell.

At 0.33 ML coverage of CO only a single peak in the TPD is observed at 481 K (Figure 3.10 a), with a desorption activation energy 1.32 eV (127.1 $kJmol^{-1}$). At the higher coverage of 0.75 ML two combined peaks are observed (Figure 3.10 b) which we attributed to the two different adsorption sites (atop and three-fold configuration). The lowest peak at 320 K corresponds to the atop configuration, having a desorption activation energy 0.9 eV (83 $kJmol^{-1}$), and the highest peak at 451 K corresponding to the

three-fold hollow configuration with a desorption activation energy 1.2 eV (119 kJmol^{-1}). These values were in agreement with those previously observed by Kuhn et al.[77].

For an ideal first-order TPD, the activation energy for desorption E_d should remain consistent regardless of coverage. This was not the case on observation of the TPD peaks in Figure 3.10. At saturation CO coverage of 0.75 ML, the TPD peak appears much broader with an earlier onset and an E_d value 0.12 eV lower, in comparison to the TPD at the lower coverage of 0.33 ML. This we attribute to the strong repulsive lateral interactions between the CO molecules in the compressed (2×2)-3CO structure, where the molecules are much closer, occupying both the atop and three-fold hollow sites. Conversely, in the $(\sqrt{3} \times \sqrt{3})$R30°-1CO configuration, there is less molecular-molecular interaction due to the larger separation between the CO molecules. Whilst both the $(\sqrt{3} \times \sqrt{3})$R30°-1CO and (2×2)-3CO structures were observed in STM studies conducted by Sautet et al.[78] and later Rose et al.[79], other complex structures were also proposed at intermediate CO coverages. At the intermediate coverage of 0.5 ML they proposed two geometric $c(4 \times 2)$ structures; one where the CO molecules occupy both the fcc and hcp three-fold hollow sites and the second where they only occupy the bridge sites. We did not however, observe any of these overlayer structures as our research was mainly focused on low and saturated coverages as opposed to those at the intermediate levels.

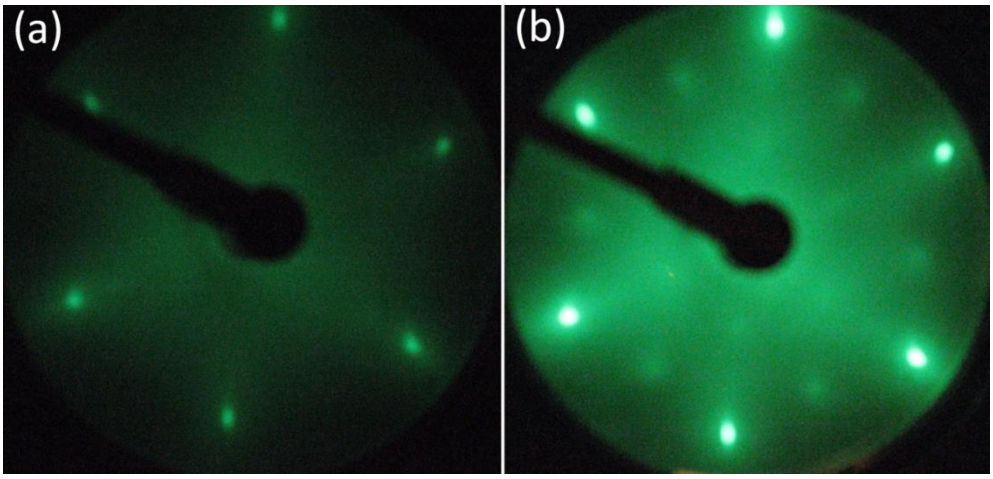

Fig 3.11. LEED images for (a) clean Pd(111) at 89 eV and (b) Pd(111)-(2×2)-O at 91.1 eV dosed at 300 K.

It has been well documented that oxygen adsorbs molecularly on the Pd(111) surface at or below 110 K. Only above 210 K will it dissociate to form a saturated 0.25 ML coverage giving rise to a strong (2×2) LEED pattern after annealing[80,81]. Similarly, we observed dissociative absorption at 300 K with a weak (2×2) LEED pattern as shown in Figure 3.11. The diffuse pattern was a result of the crystal not been annealed to order up the atomic O on the Pd(111) surface.

Whilst one could have expected the Au adatoms to exhibit a much higher density of state (DOS) when alloyed with Pd, the Au remained inert to oxidation at 300 K regardless of the coverage. This is similar to what would be expected on the pure Au crystal surface where the dissociation barrier is too high for any oxidation to occur at these temperatures[82–84].

3.3.4 CO Adsorption on Pd(111) and Au/Pd(111) with 0.2 ML Au alloyed to 700 K

This section details the adsorption of CO at a partial coverage of 0.33 ML on both the 0.2 ML Au covered Au/Pd(111)-alloy (alloyed to 700 K) and the Pd(111) surface. This was carried out specifically to see the effect Au had on the binding energy of the CO molecules as shown in Figure 3.12. As stated, the majority of research done shows that Au when alloyed on the Pd(111) does not have an ordered arrangement[60–62], and we did not observe anything in our LEED patterns (Figure 3.8) to suggest that the Au alloyed on the Pd(111) surface had anything other than a random arrangement. As a result, we present a possible quasi-random alloy structure in Figure 3.13 with a partial coverage of CO bound to all the possible 3-fold hollow sites to compliment the TPD results. When alloyed the Au adatoms remained coplanar with the surface Pd(111) atoms.

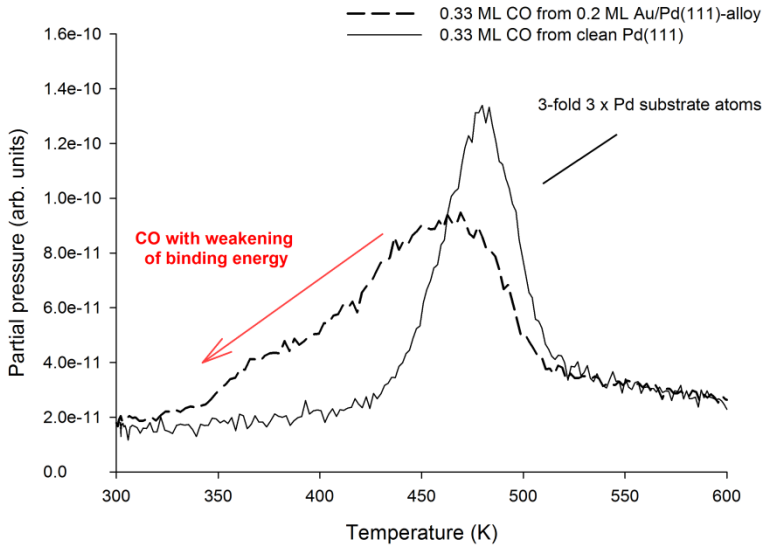

Fig 3.12. TPD of 0.33 ML coverage of CO from the clean Pd(111) (solid line plot) and the 0.20 ML Au/Pd(111)-alloyed surface (dash line plot) at heating rate (dT/dt) of 2.4 Ks^{-1}. The TPD shows that the CO molecules have the lowest binding energy bound to 3 Au atoms increasing in binding energy up to a maximum binding energy for the uncovered Pd(111) surface.

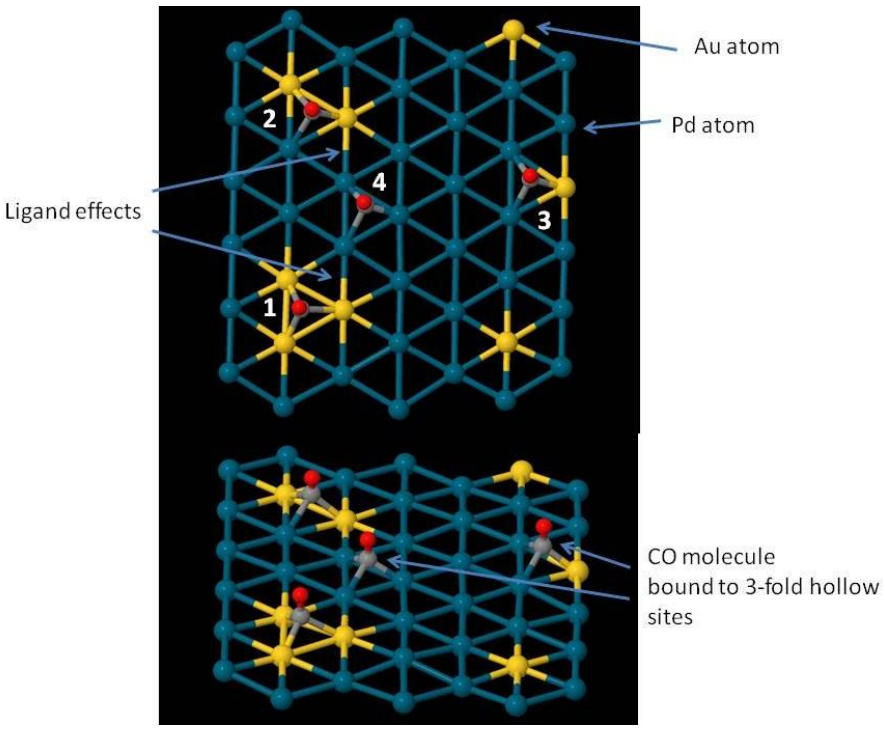

Fig 3.13. Surface structure of Au (yellow atom) alloyed on the Pd(111) crystal surface (blue substrate atoms) with CO molecules (grey-Carbon & red-Oxygen) bound to the 3-fold hollow sites. Position (1), shows CO bound to 3-fold hollow site of 3 Au alloyed atoms; position (2), shows CO bound to 3-fold hollow site of 2 Au alloyed atoms and 1 Pd surface atom; position (3), shows CO bound to 3-fold hollow site of 1 Au alloyed atom and 2 Pd surface atoms and position (4), shows CO bound to 3-fold hollow site of 3 Pd surface atoms.

Based on the LEED patterns and previous work[77,85], it was found at coverage ≤ 0.33 ML that the CO molecules preferred to bind at the three-fold hollow site, giving rise to the $(\sqrt{3} \times \sqrt{3})$R30°-1CO structure. Now assuming the CO was to bind to all three-fold hollow sites including those sites specific to Au (positions 1, 2, & 3 Figure 3.13); Au has a filled d band which means it will form much weaker chemical bonds relative to the pure Pd (position 4, Figure 3.13) which has open d bands. Based on the assumption that the Au/Pd(111)-alloy does form these ensembles as shown in Figure 3.13, the ensembles of a quasi-random alloy structure at this coverage will have small sections of maximum clustering on the Pd(111) crystal as shown at position 1. Here a small portion of the CO molecules desorbing will have a much lower desorption activation energy compared to that of the peak value 1.3 eV (127 kJmol^{-1}) for the clean Pd(111) substrate, calculated from Figure 3.11 (solid line plot). Piccolo et al.[86] reported a desorption activation energy of 0.3 eV (29 kJmol^{-1}) for CO desorbing from the Au(111). This weakening is evident by the shape of the CO desorption plot for the Au/Pd(111)-alloy Figure 3.12 (dash line plot). A large portion of the peak is shifted to lower temperatures, indicating a weakening of the CO with the alloy. We tentatively associate the lower part of the desorption plot to that of the three-fold Au ensemble, also taking into account as stated that the Au atoms will be electronically modified due to bond formation with the surrounding Pd atoms. At this low coverage of Au (0.2 ML), the majority of the surface consists of the Pd substrate atoms with some ensembles of 2Au:1Pd at position 2 reducing to 1Au:2Pd at position 3. These ensembles at positions 2 and 3 should exhibit intermediate binding energies again electronically modified, between that for the three-fold Au up to 1.3 eV (127 kJmol^{-1}) for the pure Pd(111) substrate atoms.

In addition to ensemble effects there are likely to be ligand effects where the Pd surface atoms at position 4 gains d electrons from the two Au atoms at position 1 and 2. This is likely to produce a shift in the d band centre away from the E_f with a resultant weakening of the binding energy of the CO molecule[66]. Recent theoretical calculations demonstrate that the d band for Pd monomers surrounded by Au has a lower DOS than that of the Pd

monolayer in bulk Pd[87]. This would possibly account for the lowering of the maximum binding energy associated with the Au/Pd(111) TPD data in comparison to the maximum binding energy associated with the clean Pd(111) TPD data.

3.3.5 Catalytic oxidation reactions

3.3.5.1 On clean Pd(111)

Although knowledge of the overall kinetics of CO oxidation on Pd(111) and the exact nature of the surface intermediates is still lacking, the fundamental Langmuir-Hinshelwood type mechanism for CO oxidation on the Pd(111) surface is expected to proceed according the following reaction 3.1 – 3.4;

$$CO_{(g)} \rightleftharpoons CO_{(ads)} \tag{3.1}$$

$$O_{2(g)} \rightleftharpoons 2O_{(ads)} \tag{3.2}$$

$$CO_{(ads)} + O_{(ads)} \rightarrow CO_{2(ads)} \tag{3.3}$$

$$CO_{2(ads)} \rightleftharpoons CO_{2(g)} \tag{3.4}$$

The rate at which CO oxidation takes place on the clean Pd(111) surface was found to be dependent on temperature, the pre-coverage of both CO and atomic O and the order in which they were dosed. When dosed above 210 K O_2 will dissociate on the clean Pd(111) surface, saturating at a coverage of 0.25 ML with formation of a (2×2) structure. CO molecules dosed onto this (2×2)-O surface will readily adsorb, forming mixed domains and resulting in relatively facile oxidation, as shown in Figure 3.14 A. Immediately after the CO beam enters the chamber there is an initial CO_2 spike (at t =24 s). This is probably due to CO reacting with atomic O on surrounding areas including the flag. In addition to the CO and atomic O being in close contact within the mixed domains, the pre-adsorbed O atoms are electronegative and will withdraw charge from the Pd surface atoms. This

will also withdraw charge from the neighbouring Pd-CO bonds, weakening the binding energy of CO and hence creating a highly reactive environment for the production of CO_2.

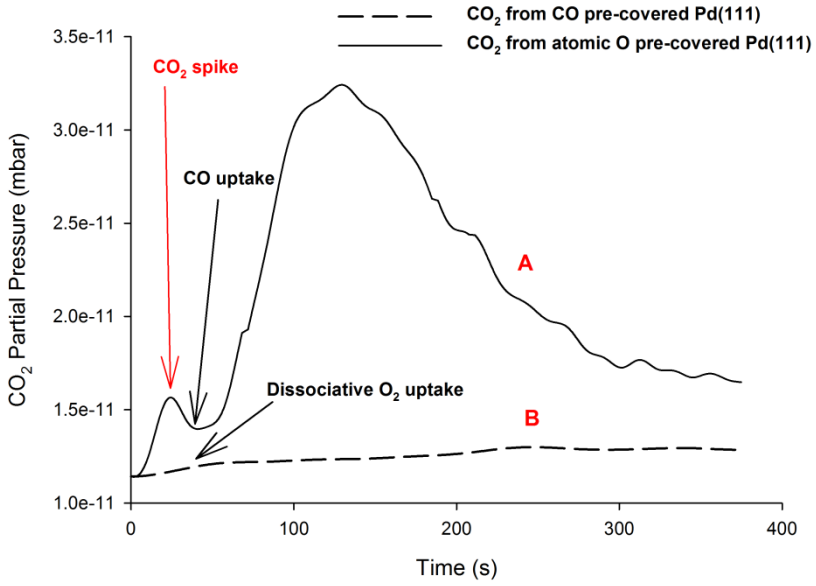

Fig 3.14. The comparative rates of CO_2 being produced from both CO and atomic O pre-covered Pd(111) surfaces at 300 K. Plot (A) corresponds to CO being dosed onto the atomic O (0.2 ML) pre-covered surface with plot (B) corresponding to O_2 being dosed onto the CO (0.20 ML) pre-covered surface. There is an initial CO_2 spike (at t =24 s) immediately after the CO beam enters the chamber; possibly due to CO reacting with atomic O on surrounding areas including the flag.

In contrast, when CO was adsorbed on the Pd(111) surface first, followed by O_2 deposition no oxidation took place. At the saturation coverage of 0.75 ML, the CO molecules were found to occupy both the three-fold hollow and a-top sites. This gave rise to steric hindrance due to the excessive CO coverage and also a lack of neighbouring Pd surface atoms required for the dissociation of O_2. Only when the initial CO coverage was reduced to ≤ 0.37 ML did oxidation occur, as the deposited O_2 was able to dissociate at the CO free areas of Pd(111) substrate. In spite of this, since the O_2 dissociated in separate domains, the oxidation reaction rate remained relatively slow in comparison to when O_2 was dosed first, as shown in Figure 3.14 B. Even taking all of the aforementioned factors into account, a

reduction in the CO binding energy should improve the oxidation reaction rate during the uptake and subsequent dissociation of the O_2 molecules.

3.3.5.2 On Au/Pd(111)

The aim of this chapter was to produce a bimetallic Au/Pd(111) alloy with a view to enhance the activity for CO oxidation with CO pre-dosed on the surface. Even though Au alloyed on the Pd(111) surface appears to possess a quasi-random lattice distribution, the overall effect on the CO is a reduction of the binding energy. This should improve the oxidation reaction rate during the uptake and subsequent dissociation of O_2 on a CO pre-dosed surface. However, Au is inert and incapable of dissociating O_2. Therefore, an intermediate coverage that enables both the dissociation of O_2 and weakening of the CO on the substrate is vital to produce a good catalyst. Any enhancement in the oxidation activity was assessed by comparing the CO_2 production rate of the clean Pd(111) surface with that of the Au/Pd(111) surface. This was done initially by pre-dosing the clean Pd(111) with 0.20 ML of CO, followed by a continuous molecular beam uptake of O_2, and monitoring the amount CO_2 desorbing from the surface at 300 K. The same test was then repeated on various Au covered Pd(111) surfaces annealed to 650, 700 and 750 K. The data obtained represent the average CO_2 production rate from these annealed temperatures.

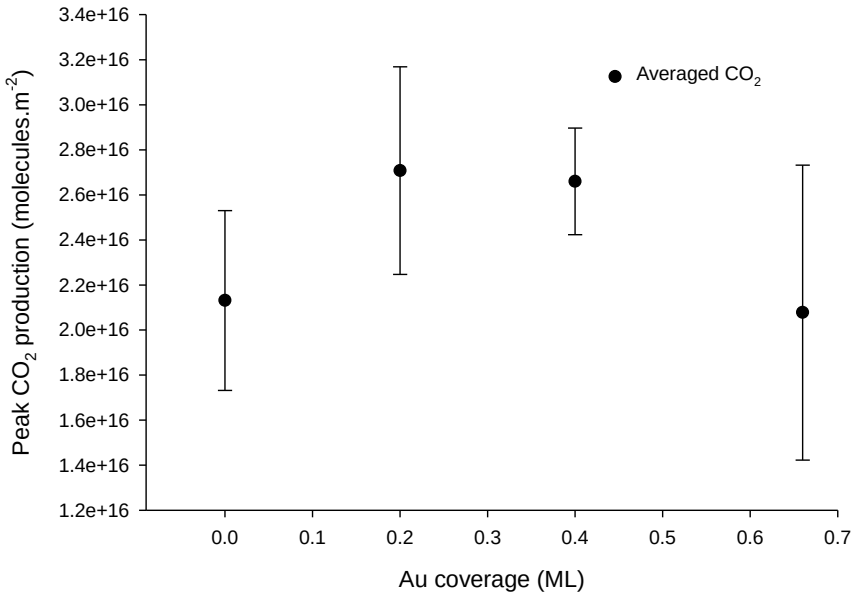

Fig 3.15. Peak spontaneous CO_2 production from deposition of O_2 on the partially CO (0.20 ML) pre-covered Pd(111), and the 0.20, 0.40 and 0.66 ML Au/Pd(111) surfaces at 300 K. Error bars calculation based on $(1.96 \times Standard\ Error/\sqrt{(No.of\ Tests)})$

Figure 3.15 shows the peak CO_2 production rate from O_2 being dosed onto 0.20 ML of CO, for both the clean Pd(111) surface and the Au/Pd(111) alloy. There is a clear increase in the peak CO_2 production rate with an overall increase of 27.0 % for the Au coverages of 0.20 and 0.40 ML. There was however some lack of consistency in the results obtained when annealing from 650 to 750 K. This could have been due to the Au forming a quasi-random lattice on the Pd(111) which would almost certainly create isolated areas with varying activity. Above a 0.40 ML coverage for the Au/Pd(111)-alloy, the peak CO_2 production began to drop off to that of the clean Pd(111) surface, with a further increase in Au coverage deactivating the surface completely. As stated, pre-dosing CO followed by O_2 was found to create separate domains where the bulk of the reaction presumably occurred at the boundary edge.

Having exposed the pre-dosed CO to a continuous molecular beam of O_2 for 6 min, the sample with remaining adsorbates was subjected to a post-TPD. This was done in order to establish the amount of unreacted CO remaining after the spontaneous production of CO_2. Figure 3.16 presents the

post-TPD quantities of CO_2 produced from the 0.20 ML Au/Pd(111)-alloy surfaces annealed to 650, 700 and 750 K. These results show that the bimetallic surface had a greater reactivity pre-TPD, based on the post-TPD producing a larger quantity of CO_2 from the clean Pd(111) compared to that of the Au/Pd(111) alloys. This was for all annealed temperatures, with all surfaces having identical initial CO uptakes. There was however very little difference between that post-TPD quantities of CO_2.

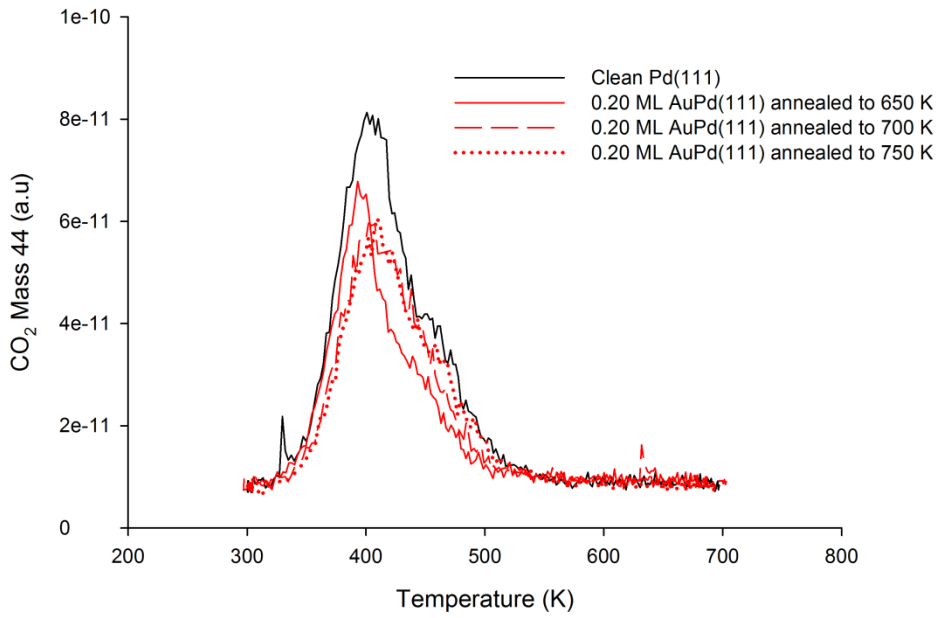

Fig 3.16. Post-TPD CO_2 production from oxidation of CO on the (0.20 ML) pre-covered Pd(111), $Au_{(0.20)}Pd_{(0.80)}$/Pd(111) at (dT/dt) of 2.4 Ks^{-1}

3.4 Discussion and Conclusions

Au/Pd(111) alloys were produced by the sublimation of various coverages of Au onto the Pd(111) substrate crystal. This was followed by flash annealing to 650, 700 and 750 K in order to form the surface alloy. The main aim of this research was to produce the bimetallic Au/Pd(111) alloy and to determine if the activity of CO oxidation is enhanced by pre-dosing CO on the surface followed by O_2. The catalytic activity of these surfaces were then compared to that of the Pd(111) by the pre-dosing with CO on all surfaces followed by

O_2 and monitoring for CO_2 production. Post TPD experiments were then carried out in order to test for any un-reacted CO.

We were able to achieve an enhanced activity with the alloys at 0.2 - 0.4 ML Au coverages followed by annealing to temperatures 650 up to 750 K. Overall, both a combination of ensemble and ligand effects have been responsible for generating this enhanced activity although it has been difficult to ascertain which was directly responsible for enhancing the activity of the surface. Ensemble effects will increase the reactivity of CO by weakening the binding energy in the order 3Au > 2Au:1Pd > 1Au:2Pd. In addition, the ligand effects are primarily associated with the complex exchange of electrons between the Au and the Pd. Although Au has one of the largest electron affinities, in bulk alloys the behaviour is somewhat different depending on the E_f.

Whilst Au remains inert for O_2 dissociation and hence CO oxidation, a DFT study by Yuan et al.[4] showed that a Pd-decorated Au(111) surface, is also highly active for CO oxidation with or without dissociative adsorption of O_2. Their studies focussed on CO oxidation by O_2 (or O) on Pd monomer, dimer, and trimers incorporated into Au(111) surface using first-principles methods.

Although Pd ensembles greater than trimers are required to dissociate O_2, their calculations showed that the CO and O_2 molecules could form an intermediate metastable adsorbate (OOCO). This would easily dissociate into CO_2 gas leaving atomic O on the surface. The remaining atomic O would subsequently react with CO to give rise to more CO_2. The fact that these reactions were not possible on the Au(111) substrate alone due to lack of atomic O and much slower at high Pd coverage further emphasises that alloys of the two metals enhances activity. These intermediate metastable adsorbate (OOCO) are able to form due to the diatomic O_2 binding initially to the atop Pd ensembles. This interaction results in weakening of the O-O bond, increasing its length from 1.36 to ~ 1.70 Å. This weakening and bond stretching is further enhanced by its reaction with CO on adjacent atop or bridge site. Due to the overall lowering in DOS of the Pd atoms by the Au substrate, this will inevitably create weakening of both CO and O_2 species. Hence desorption of CO_2 is inevitable during the formation of the intermediate metastable adsorbate (OOCO) after dissociation of the O-O

bond. These principles could possibly be applied here to similar adsorption sites surrounding the Au ensembles of the Pd(111) substrate.

Gao et al.[1,2] previously looked at CO oxidation on a AuPd(100) single crystal employing polarization-modulation infrared reflection absorption spectroscopy (PM-IRAS). Whilst their experiments also provided evidence that contiguous Pd sites were requires in order to dissociate O_2 prior to oxidation this only occurred at high CO pressures in excess of 0.1 mbar. Whilst pressures of 1×10^{-3} mbar were sufficient to achieve migration of Pd atoms to the surface, pressures of ~0.1 mbar were required for the formation of significant populations in order for oxidation to occur. These pressures produced a surface with ~10% Pd and ~90% Au atoms where the Pd atoms are completely isolated by Au. At UHV pressures, it was not possible to achieve any oxidation reactions due to a lack of Pd sites and extensive Au atoms populating the surface.

As stated, both a combination of ensemble and ligand effects have been responsible for generating the enhanced activity of the bimetallic Au/Pd(111) alloy in comparison to the pure Pd(111) surface. However, because both of these effects operate simultaneously, separating each effect and assessing their relative importance has proved to be extremely difficult. Although we have obtained a detailed understanding of the surface composition by means of characterisation TPD experiments, knowledge of the lateral distribution at atomic level still remains relatively sketchy. In terms of the ensemble effects, with Au being relative inert to oxidation, this would drastically reduce the dissociation probability with increasing coverage of Au coverage. Concomitantly, the increase in ligand effect with increasing Au coverage is only effective in increasing the oxidation rate up to a Au coverage of 0.3 ML as shown in Figure 3.15.

It is a well-known fact that a clear decision on the mechanism of a catalytic reaction cannot be made solely on the basis of the rate laws governing the steady-state kinetics. Instead an investigation of the reaction intermediates in terms of the surface complexes formed and/or the time resolved relaxation behaviour are necessary. Although the detailed reaction mechanism is likely to be quite complex it is obvious that the Pd surface provide the atomic O for the adsorbed CO on both the Au and Pd sites. The necessity for atomic O_2

therefore rules out the possibility of an Eley-Rideal mechanism. As a result one can assume a bifunctional mechanism[88] for oxidation where the dissociated O_2 migrates after dissociation both to neighbouring Pd surface atoms and Au alloyed adatoms. With this being the case one would assume the reaction to proceed by way of the Langmuir-Hinschelwood mechanism. As such the rate-limiting step would be the dissociative chemisorption of O_2. Alternatively, assuming CO_2 production was to coincide with the dissociative chemisorption of O_2, one could assume the reaction would proceed by way of the Hot-atom mechanism as reported by Lahr and Ceyer[89] for oxidation of CO on Au/Ni surface alloys.

Chapter 4

4 Oxidation of CO on Cu(110) at 90 to 170 K

4.1 Introduction

Although Cu is an industrially important catalyst, used essentially in methanol production from CO and H_2; it is very rarely used for the catalytic oxidation of CO. Chemisorbed O_2 has been studied extensively over the last 40 years on Cu, much of the interest focussed on understanding the oxidation of hydrocarbons; e.g. the epoxidation of ethylene to produce ethylene oxide, subsequently used in surfactant chemistry[5,90]. This chapter details the kinetic study of the catalytic oxidation of CO on the Cu(110) substrate focused on the reactivity of chemisorbed atomic O at 90 to 170 K.

This study was done initially by pre-adsorbing O_2 on the Cu(110) substrate surface at various coverage, followed by CO and monitoring for CO_2 production. The crystal was then subjected to a post TPD experiment with both oxidation reactants on the surface again monitoring for CO_2 production. This was then reversed with CO pre-dosed followed by O_2 and again monitoring for CO_2. We thereby obtained information essential for the kinetic, qualitative and quantitative understanding of the CO oxidation reaction.

As stated in the introduction noble metals such as Pt, Pd and Rh have commonly been used for CO oxidation. In contrast the oxidation activity of Cu has remained questionable particularly at higher temperatures around 300 K where the chemisorbed atomic O appears to be less reactive bound as the (2×1)-O reconstruction.

4.1.1 Classification of reaction rates and mechanisms

In any heterogeneous catalysis process, the reaction will proceeds by way of a sequence of steps, including adsorption, surface diffusion and reorganization of the adsorbed intermediates, followed by desorption. Factors

that influence the reaction rates of catalytic chemical reactions include the concentration of reactants, temperature, the physical state of reactants and their dispersion. With heterogeneous catalysis, the reactants and the catalyst are initially in two different phases; therefore collisions between the reactants can only occur at the interfaces between phases. As a result of this, transport between the phases and on the surface plays an essential role in surface reactions.

The most common surface reaction mechanism in heterogeneous catalysis is one in which both the reactants adsorb, migrate on the surface and then collide to form products. This is known as the Langmuir-Hinshelwood (L-H) mechanism[37] as shown in Figure 4.1 and is particularly common during heterogeneous oxidation, as the O_2 molecules have to dissociate prior to reacting with the reductant.

On the other hand, the Eley-Rideal (E-R) mechanism (Figure 4.2), involves a gaseous molecule striking and reacting directly with an adsorbed molecule[15]. This type of mechanism is very unlikely for heterogeneous oxidation reactions due to O_2 being practically un-reactive in its gaseous diatomic state.

An alternative mechanism, known as the Hot Atom (HA) or hot precursor mechanism (Figure 4.3) occurs when one of the reactants pre-adsorbed to the substrate will only react with the other reactant by way of a transient state not fully accommodated to the surface[15]. Assuming that was to happen here, the hot O atom will only react with the pre-adsorbed CO molecule after gaining enough translational kinetic energy during dissociation on the surface to form a mobile precursor state. This type of mechanism has been observed by Mullins et al.[91] when investigating the dynamics of CO oxidation on Pt(111).

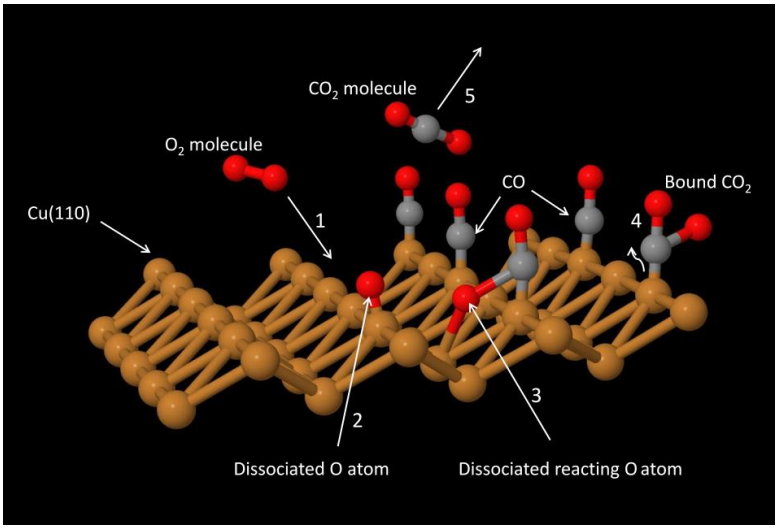

Fig 4.1. Representation of the Langmuir-Hinschelwood mechanism for the oxidation of CO with one of the reactants, CO pre-adsorbed on the Cu(110) substrate surface. The catalytic reaction takes place by way of the following steps as labelled. (1) The incoming diatomic O_2 dissociate when coming into contact with the Cu(110) substrate. (2) This leads to the production of atomic O which migrates on the substrate surface. (3) Some of these dissociated O atoms react to form complexes (4) with the pre-adsorbed CO molecules. (5) These complexes give rise to CO_2, which eventually breaks free to give CO_2 gas.

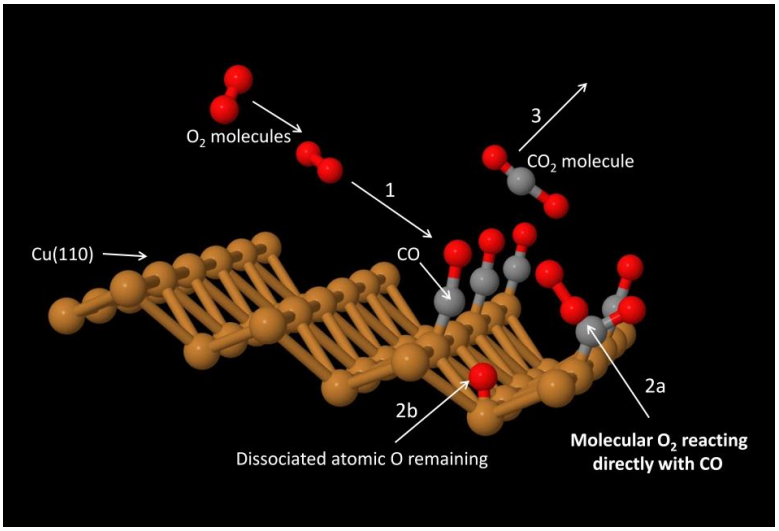

Fig 4.2. Representation of the Eley-Rideal mechanism for the oxidation of CO with one of the reactants, CO pre-adsorbed on the Cu(110) substrate surface. The catalytic reaction takes place by way of the following steps as labelled. (1) The incoming diatomic O_2 reacts directly with the pre-adsorbed CO without coming into contact with the Cu(110) substrate. (2a) This leads to the production of a OOCO-Cu complex which dissociates (2b) leaving atomic O on the Cu(110) substrate and bound CO_2. (3) The bound CO_2 eventually breaks free to give CO_2 gas.

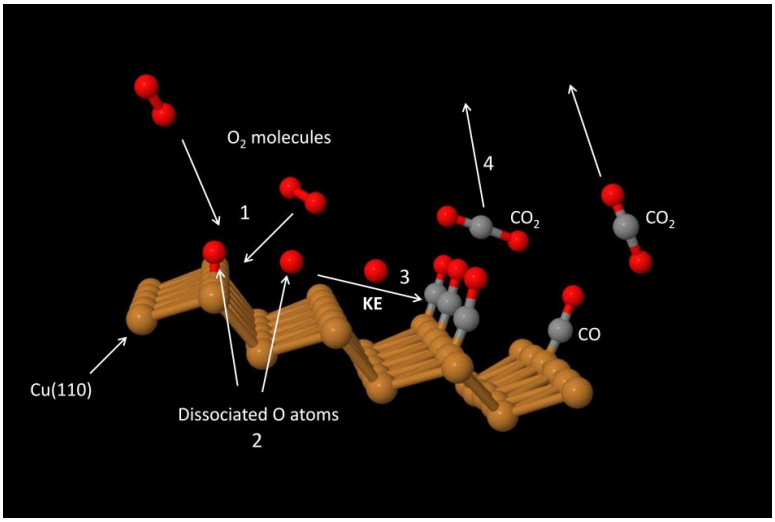

Fig 4.3. Representation of the Hot-atom-mechanism for the oxidation of CO with one of the reactants, CO pre-adsorbed on the Cu(110) substrate surface. The catalytic reaction takes place by way of the following steps as labelled. (1) The incoming diatomic O_2 dissociate when coming into contact with the Cu(110) substrate. (2) This leads to the production of atomic O, one of which remains chemically adsorbed (chemisorbed) to the surface, whilst the other is ejected. (3) The ejected oxygen atom with kinetic energy strikes an adsorbed CO molecule, combining to produce a complex on the substrate. (4) These complexes give rise to CO_2, which eventually breaks free to give CO_2 gas.

4.1.2 A General synopsis of research done on the oxidation of CO on Cu(110)

It has generally been assumed that the oxidation of CO on Cu(110) proceeds by the Langmuir-Hinshelwood (L-H) mechanism between adsorbed species (Reaction 4.1)[28,92,93]. However, contradictory results have been published in studies associated with the adsorption states of oxygenated Cu(110) with no straightforward interpretation of the type of intermediate species adsorbed on the Cu(110) substrate established to date.

$$CO_{(ads)} + O_{(ads)} \rightarrow CO_{2(g)} \tag{4.1}$$

As a result there is a need to extend the research already conducted on the reactivity of O_2 with CO on Cu(110) at low temperatures. In addition, most of the previous work is centred specifically on the reactions of pre-adsorbed O_2 with CO. Hence there is also a need to focus the study on the reactions associated with pre-adsorbed CO as the oxidation mechanism may differ.

Early reports by Schneider & Hirschwald[6] suggest that O_2 adsorbed at 85 K and at 300 K in the Cu(110)-(2 × 1)-O phase does not oxidise coadsorbed CO to produce $CO_{2(g)}$. Instead, they observed adsorbed CO_2^- as a labile species, decomposing at 120 K to give rise to CO, leaving $O^-_{(ads)}$ on the surface. In contrast, research conducted by Sueyoshi et al.[7] suggest that the as exposed (no ordered structure) dissociated O atoms at 100 K, do oxidise CO to form $CO_{2(g)}$. However, they did observe a significant drop in the reactivity of atomic O as the ordered (2 × 1)-O island structures were formed. At the slightly higher temperature of 150 K, Crew & Madix[5] found the short chain Cu-O-Cu (partial ordered structure) formed at this temperature to be equally as un-reactive with CO as the (2 × 1)-O island structure formed at higher temperatures. However, with the temperature elevated to 400 K, the reactivity appeared to increase due to the detachment and subsequent mobility of O atoms from the -Cu-O- chain ends[94].

4.1.3 CO on Cu(110)

In general there are in principle four high symmetry sites where the adsorption of molecular CO is likely to occur as shown schematically in Figure 4.4. The fourfold hollow site (HL) where it is surrounded by four surface Cu atoms, the long-bridge site (LB) where it is equidistant between two surface atoms lying in the [001] direction, the short-bridge site (SB) between two surface atoms lying in the [1$\bar{1}$0] direction and the atop site (TP) directly on top of a surface atom, often referred to as just the top site (T). Other possible locations investigated by Liem et al.[95] are the sites between the long-bridge and the hollow which they referred to as the long-bridge-hollow site (LB-HL), and the pseudo three-fold coordination between the hollow and the short-bridge which they referred to as the near hollow site (NHL). However, there research was focussed solely on the dissociative adsorption of O_2.

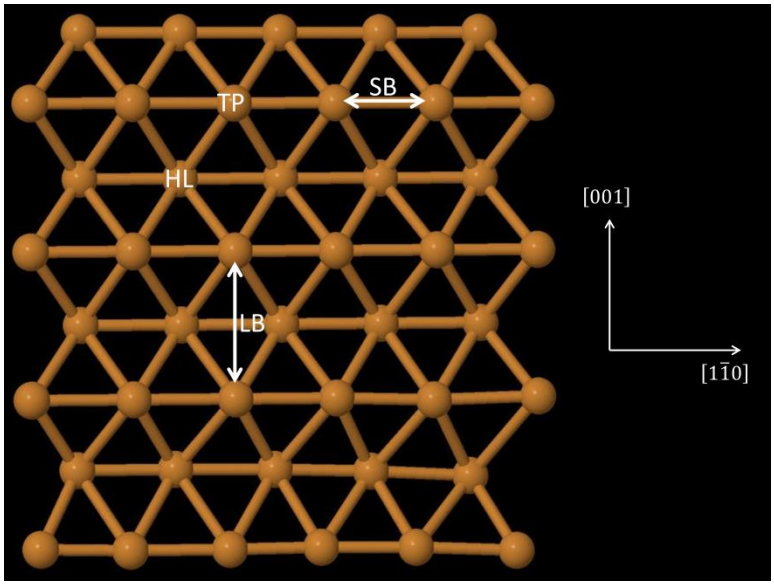

Fig 4.4. Possible adsorption sites on the Cu(110) substrate surface; showing the hollow (HL), long-bridge (LB), short-bridge (SB) and atop (TP) configurations.

According to Schindler et al[96]. and Harendt et al.[97] using various techniques including LEED, TPD and optical differential reflectance, CO adsorbed on the Cu(110) substrate at 110 K will generally bind carbon end down to the atop site at a low surface coverage 0.4 < θ < 0.5. At these coverages the structure formed gives rise to a diffuse (1×1) LEED pattern, which was found to convert to a (2×1) when annealed to 170 K and then cooled back to 110 K. At coverages θ > 0.5, the CO molecules rearrange to a compressed structure, finally saturating at 0.8 ML to form a complex $c(5/4 \times 2)$ LEED pattern when again annealed to 170 K and cooled back to 110 K.

A photoelectron diffraction (PhD) study of CO on Cu(110) by Hofmann et al.[98] showed that at low coverages (θ ≤ 0.2), CO adsorbs to the atop site with a normal orientation, isolated from nearest neighbours by adsorbate-adsorbate repulsion. With an increase in coverage (0.2 ≤ θ < 0.5), pairs of neighbouring CO molecules along the $[1\bar{1}0]$ azimuth were found to tilt due to increased adsorbate-adsorbate interactions. According to Ahner et al.[99] at coverages (θ = 0.5), the CO molecules were found to aggregate and form chains of at least four CO molecules along the $[1\bar{1}0]$ azimuth with a staggered arrangement as shown in Figure 4.5. Here the central CO molecules are slightly tilted in the $[001]$ direction, with the end molecules

tilting 16° towards the empty adjacent sites. These slight changes in the lateral arrangements of the CO molecules with increasing coverage were found to have an effect on the thermal desorption spectra. At low to intermediate coverages ($0.2 \leq \theta < 0.5$), CO was found to desorb from the Cu(110) surface with a peak maxima of 210 K. However, this peak maxima was found to shift to a slightly lower temperature with increasing coverage ($0.5 < \theta \leq 0.8$) due to repulsive adsorbate interactions[6,100,101].

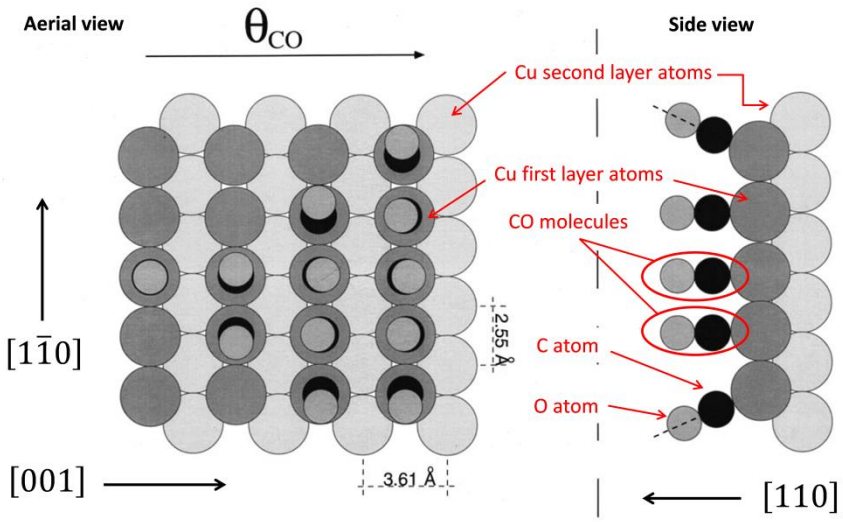

Fig 4.5. Schematic proposed linear chain model for the adsorption of CO on Cu(110) showing increasing coverage moving from left to right.
Reproduced (Adapted) with permission from Dynamics and structure of chemisorbed CO on Cu(110): An electron stimulated desorption ion angular distribution study, J. Vac. Sci. Technol. A 14(3), May/Jun 1996. Ahner et al. Copyright [1996], American Vacuum Society."

A DFT study conducted by Zuo et al.[102] looking at all the possible adsorption sites, calculated that it is possible for CO to bind to either the atop, short bridge or the long bridge site, forming three different surface structures as shown in Figure 4.6. All of these structures having exothermic chemisorption energies, indicating CO chemisorption on the Cu (110) substrate to be thermodynamically favourable. They calculated the most stable chemisorbed structure to be the short bridge with an adsorption energy of -1.13 eV (-109.0 $kJmol^{-1}$), whilst the atop and the long bridge sites are less stable with adsorption energy -1.09 eV (-105.2 $kJmol^{-1}$) and -0.66 eV (-63.7 $kJmol^{-1}$) respectively.

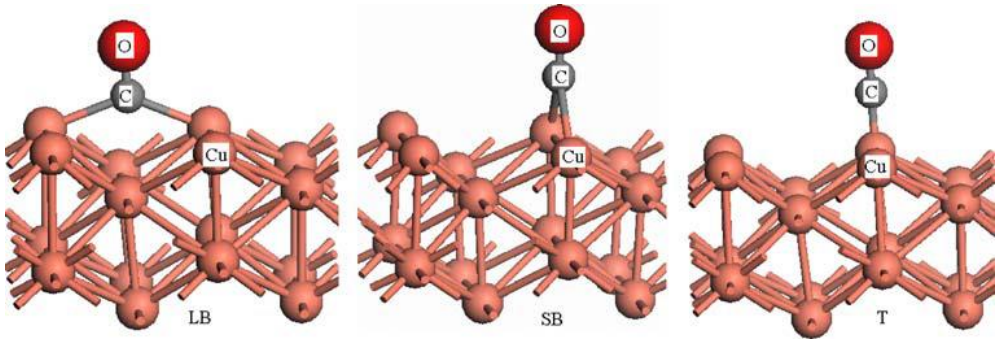

Fig. 4.6. Structures of chemisorbed CO on Cu (110). Adsorption sites: T Top site, LB long bridge, SB short bridge, J. Mol Model (2009) Volume 15, Issue 9:1079–1083/ Adsorption of CO on Cu (110) and (100) surfaces using COSMO-based DFT, Zuo, Huang, Han & Li ; with kind permission from Springer Science and Business Media"

4.1.4 CO_2 on Cu(110)

There is a degree of controversy in early research conducted by Schneider et al.[103] as to whether or not CO_2 will dissociate on the Cu(110) surface at temperatures below 80 K. However, at surface temperatures between $81 < T_s \leq 85$ K, CO_2 was found to adsorb intact and also desorbs in its molecular state at a peak temperature of 100 K. Similar results confirming molecular adsorption/desorption within this temperature range ($81 < T_s \leq 85$ K) were also confirmed by Ernst et al.[104] however, they did not observe dissociation when CO_2 was adsorbed at temperatures ~ 45 K. As shown in Figure 4.7, the TPD spectra recorded for various CO_2 coverages suggest first order desorption kinetics with a binding energy of 21 kJ/mol.

All of the tests reported in this chapter were conducted at surface temperatures $90 \leq T_s \leq 170$ K, therefore it was not possible to calibrate any of the result against pure CO_2. As will be explained later in the experimental section, the amount of CO_2 produced from the TPD experiments was calibrated using formic acid.

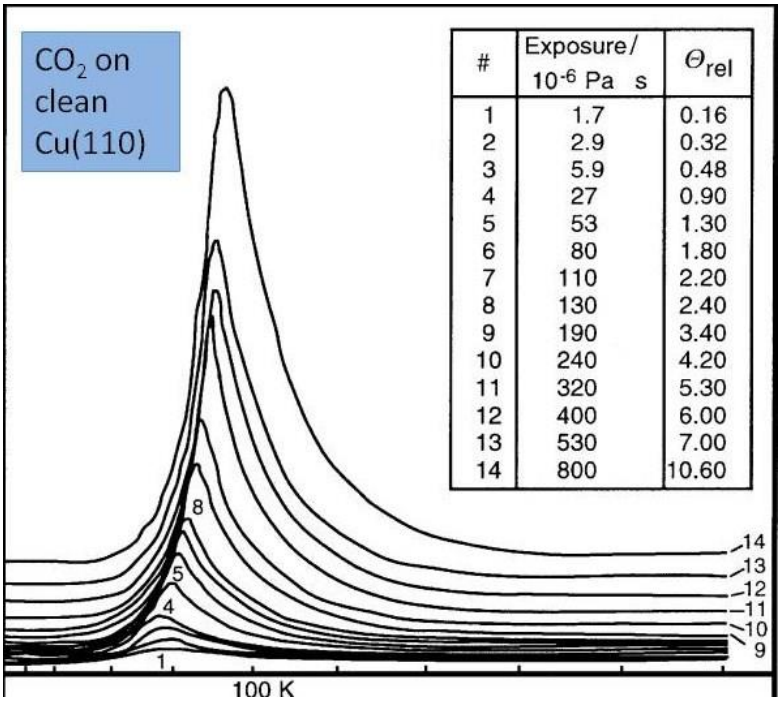

Fig 4.7. A series of TPD spectra (mass: 44), after adsorption of increasing amounts of carbon dioxide on the clean Cu(110) surface. For the sake of clarity, the baselines of the spectra are shifted upwards with increasing exposure, because some of the curves overlap at the leading edge. The major tick lines on the temperature scale equate to 10 K intervals. Adapted from, Ernst et al. Adsorption of carbon dioxide on Cu(110) and on hydrogen and oxygen covered Cu(110) surfaces. *Phys. Chem. Chem. Phys.* **1,** 4105–4112 (1999), with permission of the PCCP Owner Societies.

4.1.5 Adsorption and Dissociation of O_2 at low temperatures on Cu(110) required for oxidation of CO molecules

The formation of CO_2 from the reaction of CO with atomic O is thermodynamically favourable, with an exothermic free energy of formation, as will be detailed in the next section. However, in the gaseous phase this reaction is prohibited due to the high activation energy required to dissociate O_2. When both reactants, CO and O_2 are exposed to the Cu(110) surface the activation energy is lowered sufficiently in order to actively dissociate the diatomic oxygen, leaving atomic O available to react with the CO to produce CO_2.

It has been well established in early experimental studies by Spitzer and Lüth[105] that O_2 adsorbs dissociatively on the Cu(110) surface at room temperature. However, there has been a degree of controversy and

conflicting work published with regards to the exact adsorption state of O_2 at low surface temperatures $4 \leq T_s \leq 140$ K.

Early research by Mundenar et al.[106] using EELS and UPS showed that O_2 adsorbs dissociatively on Cu(110) after exposure at 100 K, albeit with limited long-range order of the atomic O. They went on to conclude that the EELS features previously observed in earlier research by Prabhakaran et al.[107] were probably due to either CO or H_2O contamination, ruling out the existence of a chemisorbed molecular state.

Hodgson et al.[108] later studied the dissociative chemisorption of O_2 on Cu(110) using molecular beam experiments, where they observed two competing dissociation channels according to Equation 4.1.

$$O_{2(g)} \rightleftharpoons O_{2(phys)} \longrightarrow \left[O_{2(ads)}\right] \rightarrow 2O_{(ads)} \tag{4.1}$$

At low translational energies and low temperatures, they observed a trapping-desorption channel associated with a weakly bound physisorbed molecular state. They also observed at molecular translational energies greater than 50 eV, an activated dissociative chemisorption channel. Here, it was assumed that dissociation occurred directly or through a short lived chemisorbed molecular state. By increasing the translational energy above 50 eV, approaching 400 eV, any steric requirements for dissociation were removed completely which gave rise to facile dissociation. Regardless of these findings, their paper casts doubt over the existence of a chemisorbed molecular state, due to a lack of previous theoretical or experimental evidence. A later STM study by Briner et al.[109] confirmed the possibility of both weakly bound, “trapped” molecular O_2, in addition to atomic O adsorbed at 4 K. These findings were later supported in DFT calculations by Liem et al.[110] looking at the dissociative pathways for O_2 on the Cu(110) surface.

4.1.6 Aim of project

As outlined in the introduction section in this project we aim to assess the catalytic activity and the kinetic mechanism of CO oxidation on Cu(110) at temperatures 90 to 170 K. A schematic diagram of the overall process is shown in Figure 4.8, where there are three activated steps. These are; E2 the dissociation of O_2, E5 the transfer and hence reaction of the chemisorbed atomic $O_{(ads)}$ to the (reductant) chemisorbed $CO_{(ads)}$, which will inevitably be determined by the binding energy of the atomic $O_{(ads)}$ with the substrate, and E6 the desorption of CO_2. On an ideal catalyst all of these activation steps are fast. However, in reality this is never the case as no metal is ideal in both the dissociation of oxygen and the reaction of the chemisorbed atomic $O_{(ads)}$ with the chemisorbed $CO_{(ads)}$. Thus the overall reaction rate will be determined by the slowest of these activation steps.

Typically a poor metal catalyst will have a high O-substrate binding energy in the region of 4.5 eV. Catalysts for oxidation reactions on the other hand tend to form weaker bonds in the region of 2.2 eV, e.g Pt and Rh, which are widely used for automotive pollution abatement. On Cu(110) the binding energy ranges from 1.60 – 2.00 eV, decreasing almost linearly with O coverage indicating a gradual build-up of repulsive interactions between the adsorbed O atoms[38].

The schematic energy level diagram shown suggests that CO oxidation is a thermodynamically favourable process, with the production CO_2 having an exothermic free energy of formation. However, it is a non-spontaneous and kinetically unfavourable reaction due to the dissociation of O_2 being the rate determining step in addition to the migration of CO and atomic O assuming dissociation of O_2. Here we investigate the kinetics in order to ascertain whether the reaction proceeds by way of the L-H, the chemically induced E-R or the HA mechanism. Hopefully this will enable us to model a reaction rate mechanism in the process. The L-H mechanism would proceed by way of all of the combined energy steps laid out in Figure 4.8, with both the E-R and HA mechanisms proceeding by way of combined energy steps E2, E5 & E6, with part of the E3 energy step associated only with the HA mechanism.

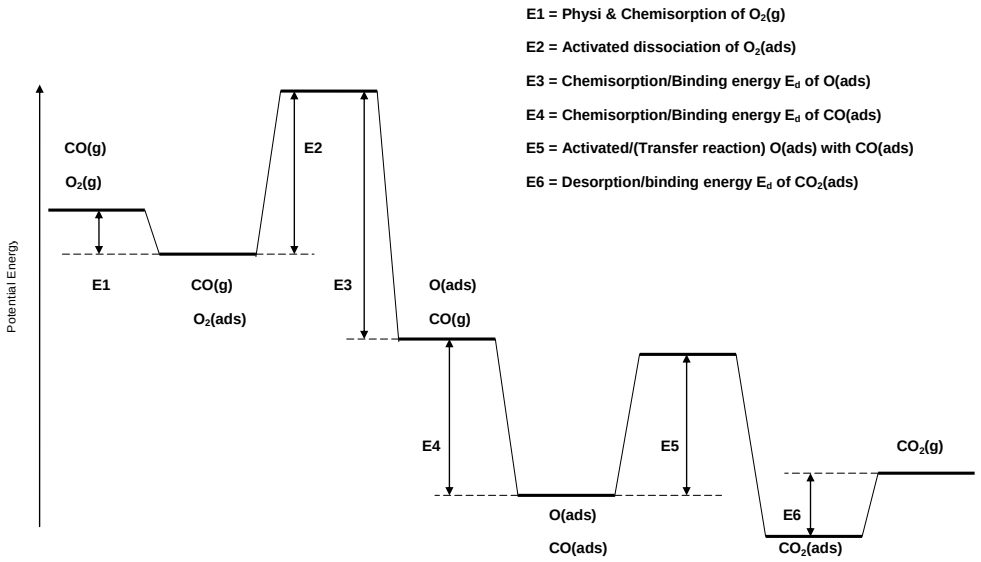

Fig. 4.8. Schematic energy level diagram for the overall CO oxidation process on Cu(110)

4.2 Experimental

A Cu(110) crystal, cut and polished with an accuracy of ~ 0.25°, was used throughout the entirety of this study. All experiments were performed in an Ultra High Vacuum (UHV) chamber, operated at base pressures $< 10^{-10}$ mbar. As detailed in the experimental section, each stage of the UHV chamber was pumped independently by diffusion pumps, all backed by rotary oil pumps, running in combination with a liquid nitrogen cooled titanium sublimation pump. The polished Cu(110) crystal was cleaned by prolonged Ar^+ ion sputtering cycles of 15-20 minutes at a drain current of 2 – 5 μA (500 eV) at room temperature prior to each experiment. This was performed in order to remove surface contaminants such as carbon, oxygen and sulphur, followed by annealing to 823 K. The surface order prior to analysis was assessed by LEED to obtain a bright (1×1) pattern. The crystal was mounted by the use of 0.2 – 0.5 mm Ta-wires on Ta-rods on a rotatable manipulator that could be moved horizontally in the x, y-plane and vertically along the z-axis. The manipulator was also equipped with an electrical feed-through to enable resistive heating and the temperature was monitored by the use of a thermocouple mounted to the side of the crystal.

All Temperature-Programmed Desorption (TPD) and uptake sticking coefficient experiments were measured by means of a Quadrupole Mass Spectrometer (QMS). A heating rate (dT/dt) of 2.7 Ks^{-1} was used throughout for the TPD measurements.

Oxygen (99.5 % O_2 high purity supplied by BOC, CAS No: 7782-44-7) and carbon monoxide (99.0 % CO, supplied by Aldrich, CAS 680-08-0) were dosed by means of a two stage collimated effusive beam. The first stage pumped to a base pressure of 2.6×10^{-6} mbar and the second to 3.0×10^{-9} mbar. Each beam was introduced into the chamber at an in line pressure of 1.0 ± 0.05 mmHg (~1.33 mbar or 1.00 Torr) through a glass nozzle with a 1 mm inner diameter. Exiting the nozzle the beam entered the first stage, then through a 1 mm skimmer prior to entering the second stage and finally entering the chamber through a 5 mm collimation orifice. The effusive molecular beam is incident on a metal flag shielding it from the crystal which could be opened and closed during molecular beam dosing.

For these experiments O_2 was initially dosed at coverages of 0.125, 0.25 and 0.50 ML separately at temperatures 90, 130, 150, and 170 K, followed by a saturated uptake of CO. In order to test for CO_2 production, mass 44 was monitored using the QMS during the CO uptake. To assess for any CO_2 production on the surface the crystal was subsequently heated to desorb any products, while monitoring for both CO_2 mass 44 and unreacted CO (mass 28). Experiments were then carried out by dosing CO at coverages of 0.2, 0.4 and 0.8 ML separately at temperatures 90, 130 150 and 170 K, followed by a saturated uptake of O_2. Again, any CO_2 production during uptakes and TPDs was monitored throughout. The partially ordered O_2 (as exposed) overlayers at 0.125 and 0.25 ML were calibrated against the saturation p(2 × 1) coverage of 0.50 ML. The CO overlayer at 0.2 and 0.4 ML were calibrated against the saturated streaky c(5/4 × 2) structure at CO coverage 0.8 ML. Quantitative analysis of CO_2 produced throughout was calibrated using Formic acid (96 % A. C. S Reagent supplied by Aldrich, CAS No: 64-18-6) adsorption on the clean Cu(110) surface, subsequently giving rise to a formate layer which was thermally decomposed to give carbon dioxide.

The activation energy for CO desorption E_d was estimated using the following equation;

$$E_d = R.T_p\left[In\left(\frac{A.T_p}{\beta}\right) - 3.46\right]$$

where R = the universal gas constant (8.314 $Jmol^{-1}K^{-1}$), T_p = desorption peak max, A = pre-exponential factor (see below for values 10^{13} and 10^{18} s^{-1}) and β= heating rate (dT/dt) = 2.7 Ks^{-1}.

The desorption of CO can be well described by the first-order desorption kinetics as detailed in Chapter 2 (Section 2.5.1.2). As detailed in the introduction (Section 4.1.3), CO adsorbed on the Cu(110) substrate at a low surface coverage (0.4 < θ < 0.5) will gives rise to a diffuse (1×1) structure, converting to the (2×1) when annealed to 170 K followed by cooling back to 110 K. At coverages θ > 0.5, the CO molecules rearrange to the compressed structure, saturating at 0.8 ML to form a complex $c(5/4 \times 2)$ LEED pattern. In accordance with previous research, at the lower surface coverage (θ ≤ 0.5), the activation energy for desorption E_d was estimated using a pre-exponential factor 10^{18} s^{-1}. At the higher surface coverage (0.5 ≤ θ ≤ 08), a pre-exponential factor 10^{13} s^{-1} was used. Different pre-exponential factors were used due to the fact that repulsive CO-CO interactions set in around θ ~ 0.4 – 0.5 ML, due to the formation of the close-packed $c(5/4 \times 2)$ structure[101,111–113].

The turnover frequency (TOF) of the Cu(110) crystal for CO oxidation which is the number of molecules of CO_2 produced per unit time was calculated using the following equation.

$$TOF = \frac{Number\ of\ product\ molecules}{Number\ of\ active\ sites\ \times time} = \frac{1}{s}\frac{dn}{dt}$$

These TOF tests were all conducted at 170 K by first dosing a saturated coverage of CO followed by O_2, monitoring for CO_2 during the O_2 uptake. The main purpose of this TOF test was to evaluate the activity of the Cu(110) crystal after repeated uptakes of both CO followed by O_2 both in the absence

of any cleaning and with only a brief anneal between uptakes. Initially the TOF was conducted repeatedly without any cleaning. The crystal was then cleaned as detailed earlier in this section and the TOF tests repeated with only a brief 1 min anneal up to 773 K between each set of uptakes[114,115].

4.3 Results and Discussion

4.3.1 Quantitative analysis of CO_2

The amount of CO_2 produced during the experiments was quantified by the decomposition of formate, monitoring the CO_2 produced by the QMS (mass 44) TPD signal. Formic acid was used as opposed to CO_2 due to the fact that the lowest working temperature used in these experiments were too high to stabilise CO_2 on the Cu(110) surface[103,104]. Formic acid adsorbed on the clean Cu(110) surface at 340 K produced formate $\left(HCOO^{-}_{(ads)}\right)$ and atomic hydrogen $\left(H^{+}_{(a)}\right)$ by way of the dissociation reaction (Figure 4.9 & Reaction 4.2)[104].

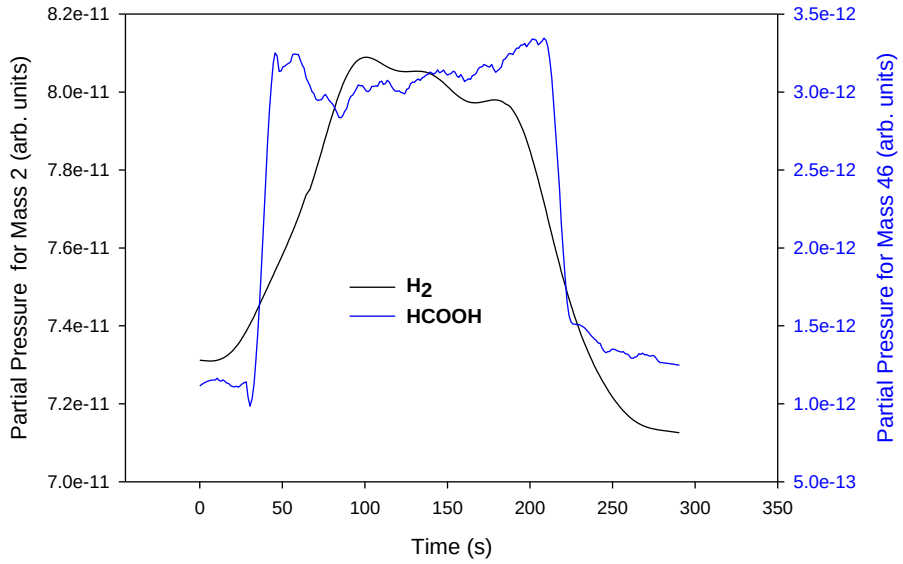

Fig. 4.9. The uptake of formic acid (blue uptake plot) on the clean Cu(110) surface at 340 K, dissociating into atomic H which desorbs recombinately into H_2(g) (black desorption plot) depositing a formate ($HCOO_a^-$) layer on the surface.

$$2HCOOH + 2e^- \rightarrow 2HCOO^-_{(ads)} + H_{2(g)} \quad (4.2)$$

A temperature of 340 K was set conveniently above the desorption temperature of H_2 but below the desorption temperature of formate to enable the formation of a dense monolayer with a coverage of 0.5 ML which is equivalent to 3.62×10^{14} molecules cm^{-2}. This value was confirmed previously in several studies using XPS[116], which showed that the formate was bound to the surface through both equivalent oxygens as shown in Figure 4.10.

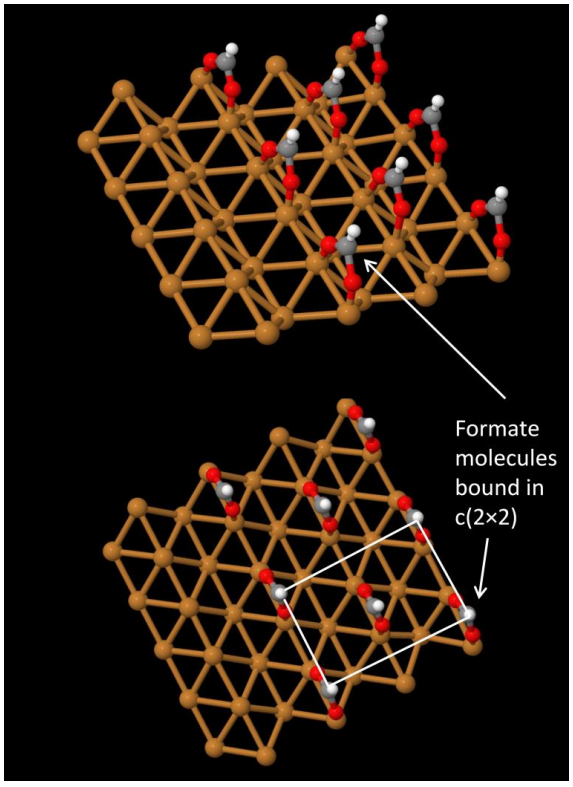

Fig. 4.10. Formate molecules (red-Oxygen, grey-Carbon & white-Hydrogen) bound to Cu(110) crystal surface (brown substrate atoms) in a $c(2 \times 2)$ arrangement, equating to a coverage of 0.5 ML.

This was followed by a TPD where the formate decomposed at 470 K into $H_{2(g)}$ and $CO_{2(g)}$ stoichiometrically (Figure 4.11 & Reaction 4.3).

$$2HCOO_{(ads)} \rightarrow H_{2(g)} + CO_{2(g)} \quad (4.3)$$

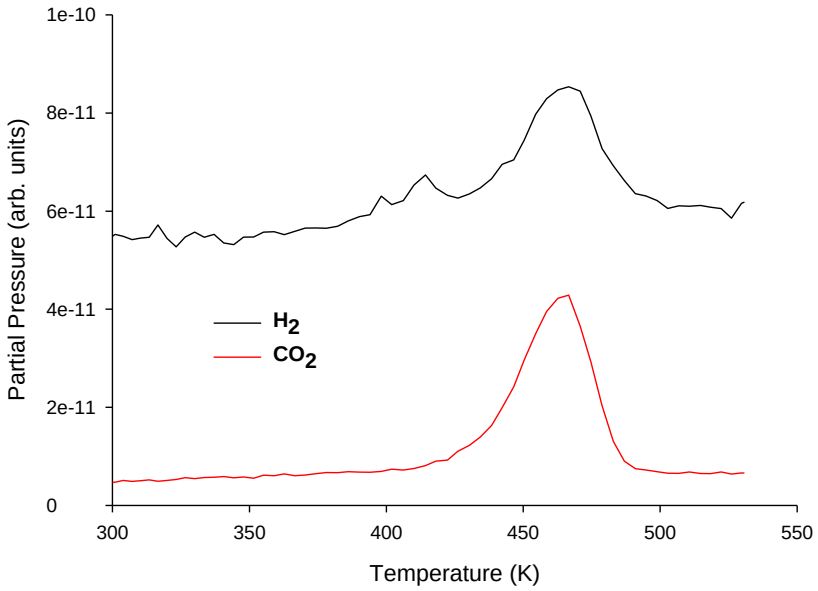

Fig. 4.11. TPD spectra for formate decomposition from clean Cu(110) at 470 K, showing dissociation into H_2(g) and CO_2(g).

The CO_2 signal was calibrated with the equivalent coverage of 0.5 ML which equates to 3.62×10^{14} molecules cm^{-1}. This was then used to calculate the amount of CO_2 produced during the oxidation reactions[104,117–119].

4.3.2 Oxidation on the atomic O pre-covered Cu(110) surface

This section details the oxidation results obtained from CO being dosed onto the atomic O pre-covered Cu(110) surface, monitoring throughout for CO_2 during the uptake of CO and the following TPD. As detailed in the introduction section, there is a degree of controversy and conflicting work published with regards to the exact adsorption state of O_2 at low

temperatures. As a result of this, I have referred to the adsorption state as atomic O throughout the following figures. In addition, this makes practical sense as O_2 in its molecular state will not react with gaseous or bound CO prior to being dissociated.

O_2 was initially dosed at coverages of 0.125, 0.25 and 0.50 ML separately on the clean Cu(110) surface at temperatures 90, 130, 150, and 170 K. This was then followed by a saturated uptake of CO, whilst monitoring continuous for the production of CO_2 (mass 44) throughout the duration of the uptake. Following the CO uptake the crystal was heated whilst concurrently monitoring for both activated CO_2 production (mass 44), in addition to mass 28 for any un-reacted CO as shown in Figure 4.12. All CO oxidation experiments were conducted from the lowest attainable temperature of 90 K, up to the onset desorption temperature of 170 K for CO as shown in Figure 4.13.

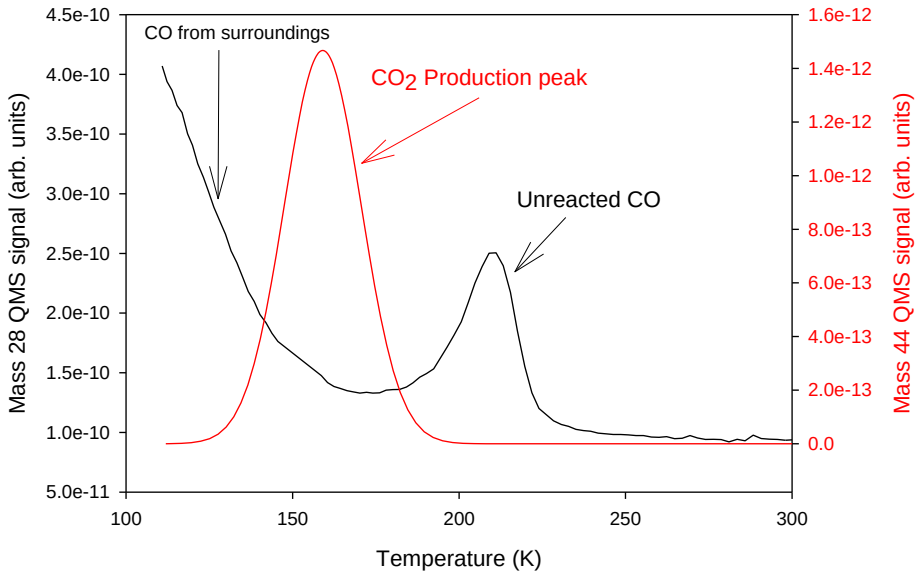

Fig. 4.12. TPD spectra for CO_2 produced along with unreacted CO, after heating the crystal from 0.25 ML of atomic O and a saturated coverage of CO. The uptake of both of the oxidation reactants was carried out at 90 K prior to the TPD.

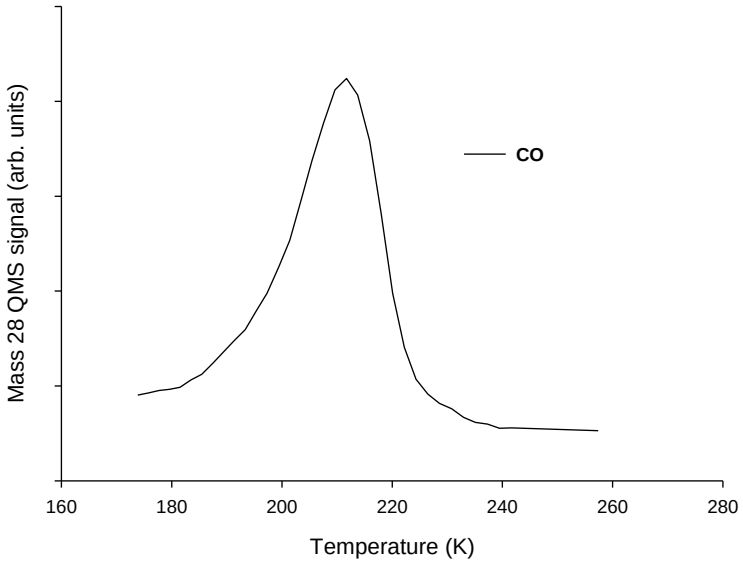

Fig. 4.13. TPD spectra for a monolayer of CO desorbing from the clean Cu(110) surface with an onset at 170 K and peak maximum at 212 K. This full monolayer coverage corresponds to the saturated c(5/4 × 2) structure which has a coverage of 0.8 ML.

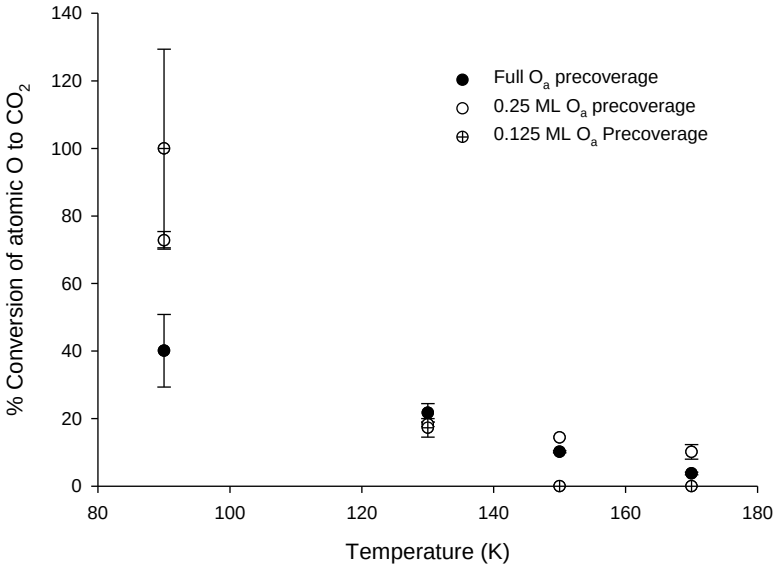

Fig. 4.14. The percentage conversion of atomic O (at pre-coverage 0.125, 0.25 and full 0.5 ML) to CO_2 after heating the crystal following a saturated CO uptake. The pre-coverage uptakes were all carried out separately at 90, 130, 150 and 170 K.

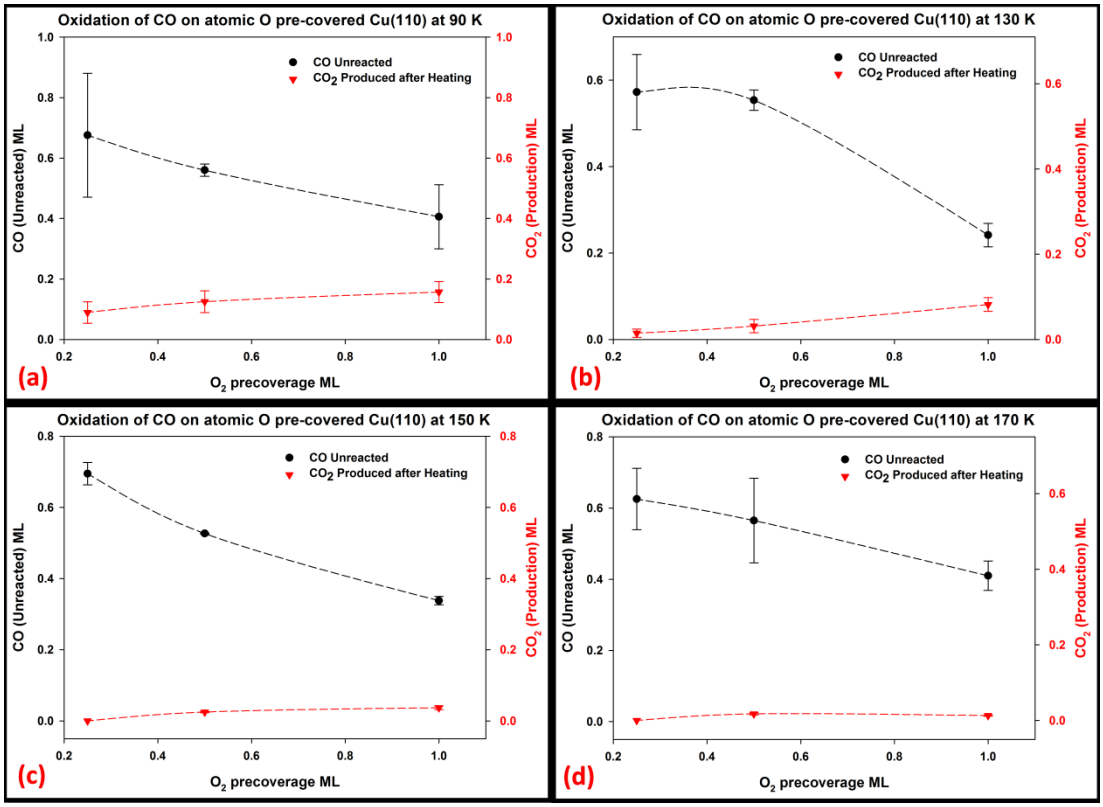

Fig. 4.15. The amounts of CO_2 produced along with any unreacted CO after heating the crystal with both atomic O and CO on the surface, at uptake temperatures of (a) 90 K. (b) 130 K, (c) 150 K and (d) 170 K. A relative coverage of 1 ML was used for each; equating to 0.5 ML for atomic O, 0.8 ML for CO and 0.3 ML for CO_2. These results are based on the average of a series of TPDs with the errors based on (1.96 × Stdev ÷ No. of experiments).

Figure 4.14 shows the % conversion of atomic O to CO_2 after heating the crystal with both O_2 and CO dosed on the surface at 90, 130, 150 and 170 K. Clearly when dosed at 90 K there is a significant amount of CO_2 being produced during the TPD, which steadily decreased as the uptake temperature was increased up to 170 K. The individual breakdown of each product, CO_2 and unreacted CO is presented in Figure 4.15 at each uptake temperature (a) 90 K. (b) 130 K, (c) 150 K and (d) 170 K.

Whilst Sueyoshi et al.[7] observed oxidation of CO occurring at 100 K, no oxidation of CO has previously been reported at temperatures as low as 90 K. Assuming O_2 did dissociate at 90 K with CO present on the surface, it is unlikely at this temperatures there are ordered overlayer structures formed i.e. the (2×1)-O, (2×1)-CO or $c(5/4 \times 2)$-CO. As a result the oxidation could be attributed to both atomic O and CO diffusing during annealing and reacting whilst moving to their favourable sites. This Langmuir-Hinschelwood

mechanism, as observed by Sueyoshi et al.[7], would only be possible prior to the formation of the stable (2×1)-O reconstruction which would explain the reduction in oxidation with increasing temperatures.

Although Mundenar et al.[106] found O_2 adsorbs dissociatively on exposure at 100 K, there is very little evidence to suggest that it does not remain in a physisorbed state at 90 K. If this was the case, dissociation of O_2 would inevitably occur during heating, again giving rise to mobile atomic O and CO reacting similarly as before resulting in oxidation.

Additionally, some late transition and noble metals can stabilize molecular adsorbed O_2 at these low temperatures as $O^{2-}_{(ads)}$, peroxo $O^{2-}_{2(ads)}$ and superoxo $O^{-}_{2(ads)}$ transition states[39]. The formation of these transient states can be explained by the following processes from diatomic oxygen in the gaseous state, becoming physisorbed (phys) and then forming various transient (trans) states according to Reactions 4.4 - 4.6, 4.7 and/or 4.9.

$$O_{2(g)} \rightleftharpoons O_{2(phys)} \tag{4.4}$$

$$O_{2(phys)} + e^- \rightarrow O^-_{2(trans)} \tag{4.5}$$

$$\boldsymbol{O^-_{2(trans)} + e^- \rightarrow O^{2-}_{2(trans)} \rightarrow O^{2-}_{2(ads)}} \tag{4.6}$$

and/or

$$O_{2(g)} \rightleftharpoons O_{2(phys)} \tag{4.4}$$

$$O_{2(phys)} + e^- \rightarrow O^-_{2(trans)} \tag{4.5}$$

$$\boldsymbol{O^-_{2(trans)} \rightarrow O^-_{2(ads)}} \tag{4.7}$$

and/or

$$O_{2(g)} \rightleftharpoons O_{2(phys)} \tag{4.4}$$

$$O_{2(phys)} + e^- \rightarrow O^-_{2(trans)} \tag{4.5}$$

$$O^-_{2(trans)} + e^- \rightarrow 2O^-_{(trans)} \tag{4.8}$$

$$\boldsymbol{O^-_{(trans)} + e^- \rightarrow O^{2-}_{(ads)}} \tag{4.9}$$

These transient states will have a much higher reactivity up until the point they react with any Cu atoms migrating on terraces and from the step edges. It is also known that dissociation in this way leaves the dissociated fragments energetically excited[5]. These factors would certainly explain the reactions of physisorbed oxygen with CO at 90 K where the highly reactive transient states produced during the TPD were able to react directly with the chemisorbed CO. At the higher temperatures of 150 and 170 K oxygen when pre-adsorbed will react directly with any migrating surface Cu atoms to form small immobile –Cu-O- units, unable to react with any subsequent uptake of CO.

Whether the oxygen existed as mobile atomic O, in the physisorbed transient state, there was still a significant difference in the amount of CO being converted to CO_2 particularly at 90 K. At the lowest atomic O pre-coverage of 0.125 ML, a 100 % yield of CO_2 was obtained which could probably be attributed to the fact that at such a low coverage the excess CO dominates, surrounding the O adatoms. With this being the case one would expect a high yield during the TPD. Although still in excess at the saturated atomic O coverage, the yield dropped off significantly to 40 %, due to oxidation occurring only at the boundaries of the atomic O islands prior to the O adatoms forming stable –Cu-O- units during the TPD.

It is important to note here that at no point was any CO_2 observed desorbing spontaneously during the subsequent uptake of CO on the oxygen pre-covered surface. All CO_2 production occurred only during the TPD stage of the experiments which would suggest a transient state mechanism, akin to that of an Eley-Rideal mechanism.

Even at the highest O_2 uptake and subsequent atomic O coverage, the Cu substrate was able to accommodate adequate quantities of CO in order for the oxidation reaction to proceed according to the stoichiometric Reaction 4.1. This is significant in order to obtain a true % conversion at all O coverages and temperatures. The excess CO was evident by the quantitative amounts of unreactive CO observed throughout all of the experiments as shown in Figure 4.16. Although there was no direct correlation between the amount of unreacted CO and CO_2 produced, there was however a precipitous drop in line with the increase in atomic O (O_2 uptake) coverage.

With reference to the fact that atomic O forms a full coverage of 0.5 ML, assuming this to have a relative value of 1 ML according to Figure 4.15; the average amount of unreacted CO throughout all the temperatures 90, 130, 150 and 170 K was 0.35 ML ± 0.07. At the lowest relative atomic O coverage of 0.25 ML the average amount of unreacted CO throughout all the temperatures was 0.64 ML ± 0.05 and 0.55 ML ± 0.01 at the intermediate relative atomic O coverage of 0.5 ML.

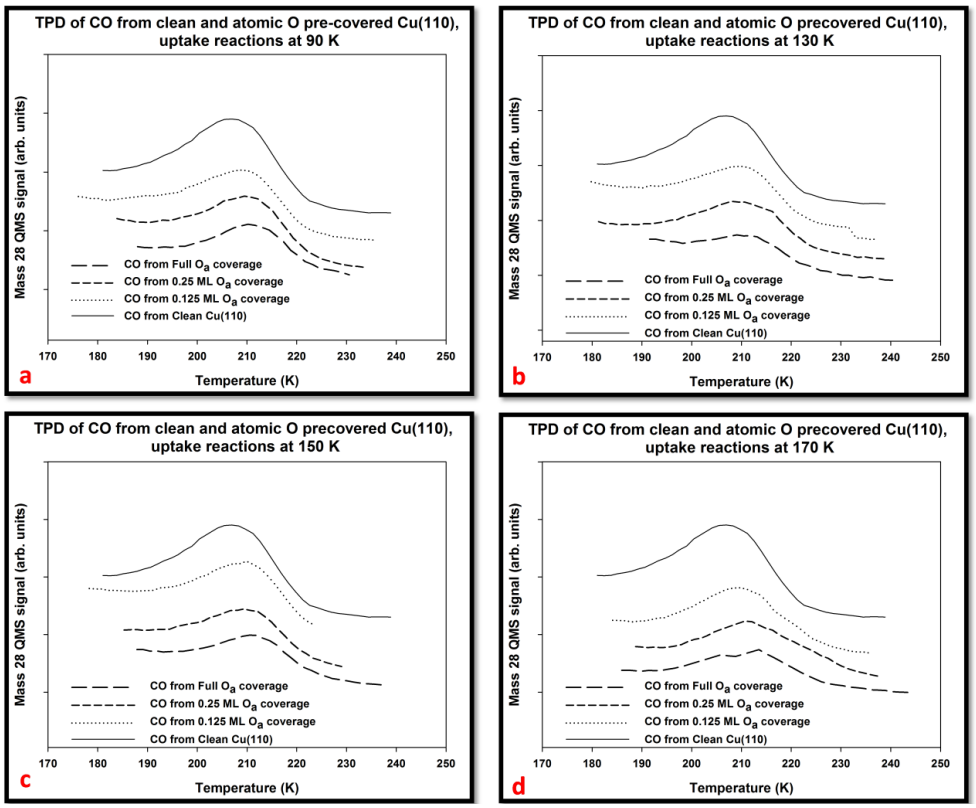

Fig. 4.16. The TPD spectra for unreacted CO from the clean Cu(110) and atomic O pre-covered Cu(110) surface at 0.125, 0.25, and 0.5 ML for oxidation reaction at (a) 90 K. (b) 130 K, (c) 150 K and (d) 170 K, with a heating rate dT/dt = 2.7 Ks^{-1}

As stated in the introduction (Section 4.1.3) at low coverages (θ ≤ 0.2), CO adsorbs to the atop site with a normal orientation, isolated from nearest neighbours by adsorbate-adsorbate repulsion[98]. With increased coverages the molecules were found to aggregate and form chains of at least four CO molecules along the $[1\bar{1}0]$ azimuth with a staggered arrangement[99]. At this coverage the central CO molecules were found to be slightly tilted in the $[001]$ direction, with the end molecules tilting 16° towards the empty adjacent sites. These slight changes in the lateral arrangements of the CO

molecules with increasing coverage were found to have an effect on the thermal desorption spectra. At these intermediate coverages ($0.2 \leq \theta < 0.5$ ML), the CO was found to desorb from the Cu(110) surface with a peak maximum of 210 K, shifting to a slightly lower temperature with increasing coverage ($0.5 < \theta \leq 0.8$ ML) due to repulsive adsorbate interactions[6,99,101].

With the addition of atomic O on the surface at 0.125, 0.25 and 0.5 ML, the unreacted CO was found to have an increased binding energy; 0.32 $kJmol^{-1}$ higher than the binding energy when adsorbed on the clean Cu(110) surface; values all calculated from the TPD peak temperatures as detailed in the experimental section. Although relatively small, these differences are probably due to the mixed domains of the two adsorbates with the atomic O separating the CO molecules hence reducing the lateral repulsive adsorbate-adsorbate interactions between the CO molecules[7]. With the increasing temperature the atomic O adatoms formed stable –Cu-O- units and were found to be relatively unreactive even when the oxidation reaction was repeated with further doses of CO. Alternatively, according to Feng et al. the chemisorption characteristics of CO on the (2×1)-O surface was found to be most stable when adsorbed to Cu adatoms attached to –Cu-O- chains. Using first-principles calculations they attributed this extraordinary chemisorption behaviour to the lifting of the host Cu adatoms from the surface by ~ 1 Å to enhance the bonding and reduce the repulsive interaction with the substrate. This structural distortion allowed short-range intermolecular dipole-dipole attraction between the molecules[120].

4.3.3 Oxidation on the CO pre-covered Cu(110) surface

CO was initially dosed at coverages of 0.2, 0.4 and 0.8 ML separately on the clean Cu(110) surface at temperatures 90, 130, 150, and 170 K. This was followed by a saturated coverage of O_2 whilst monitoring for the production of CO_2 (mass 44) during the uptake. To test for any activated production of CO_2 on the surface, the crystal was heated after each uptake monitoring again for both CO_2 (mass 44) in addition to mass 28 for any un-reacted pre-adsorbed CO.

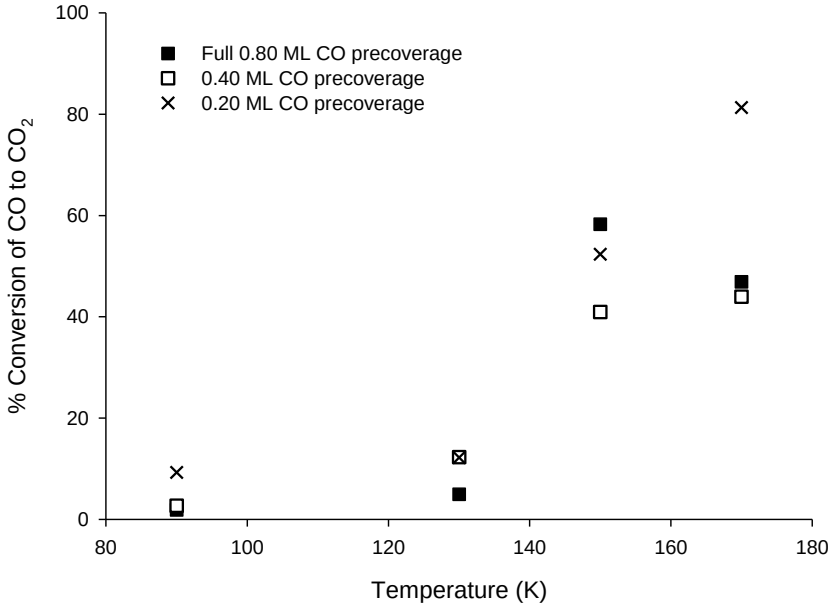

Fig 4.17. The percentage conversion of CO at pre-coverages of 0.2, 0.4 and 0.8 ML to CO_2 by spontaneous desorption reacting with a saturated coverage of atomic O. The pre-coverage uptakes were all carried out separately at 90, 130, 150 and 170 K.

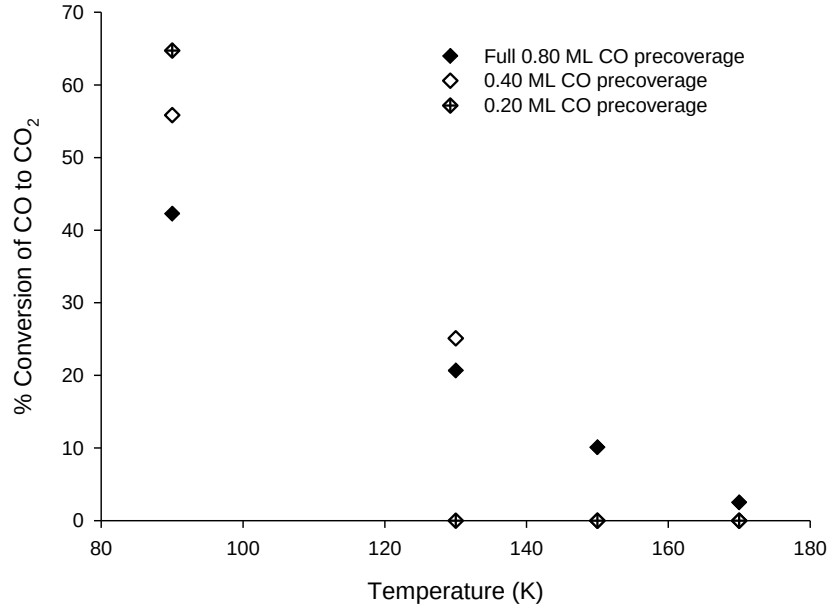

Fig 4.18. The percentage conversion of CO at pre-coverages of 0.2, 0.4 and 0.8 ML to CO_2 after heating the crystal following a saturated uptake coverage of atomic O. The pre-coverage uptakes were all carried out separately at 90, 130, 150 and 170 K.

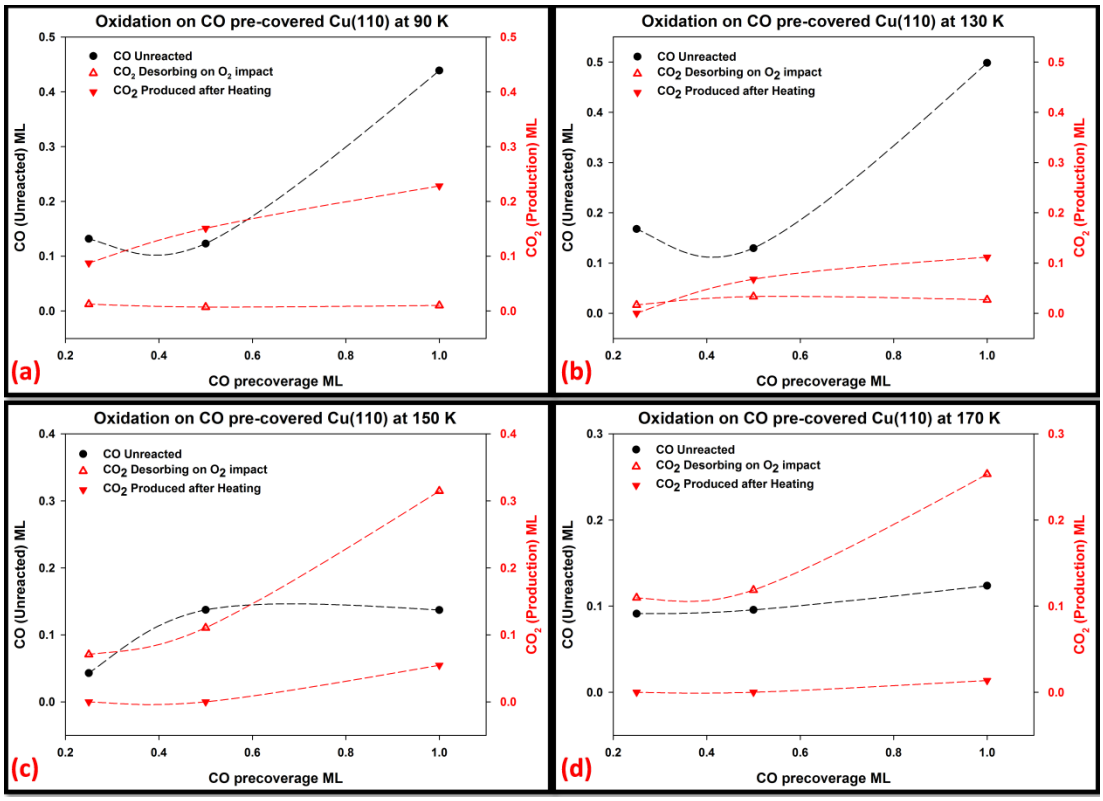

Fig. 4.19. The amounts of CO_2 produced along with any unreacted CO during the molecular uptake of O_2 and after heating the crystal with both atomic O and CO on the surface. Each experiment was carried out separately at uptake temperatures (a) 90 K. (b) 130 K, (c) 150 K and (d) 170 K. A relative coverage of 1 ML was used for each; equating to 0.5 ML for atomic O, 0.8 ML for CO and 0.3 ML for CO_2.

With the previous set of experiments (Section 4.3.2), no CO_2 was produced spontaneously when O_2 was pre-dosed onto the surface followed by CO. Any CO_2 produced occurred only when activated during the TPD experiments. However, with CO pre-dosed on the surface followed by O_2, spontaneous desorption of CO_2 occurred both during the uptake of O_2 and during the activated TPD experiments.

Figure 4.17 shows the % conversion of CO to CO_2 desorbing during the uptake of O_2 onto the 0.2, 0.4 and 0.8 ML CO pre-covered surface at the set temperatures of 90, 130, 150 and 170 K. Looking at the percent conversion at 90 K, as with the previous set of experiments (Section 4.3.2) O_2 adsorbed

in a similar physisorbed or transition state. This was evident by the fact that the majority of CO_2 was produced during the TPD experiments (Figure 4.18), with only a small conversion occurring during the uptake of O_2. A combined view of the CO_2 produced along with any unreacted CO during the molecular uptake of O_2 and after heating the crystal with both atomic O and CO on the surface is shown in Figure 4.19.

The 10 % conversion that occurred at the 0.2 ML CO coverage (Figure 4.17) is clearly due to small amounts of O_2 dissociating on impact. Any dissociation occurring would certainly be reduced, significantly, with larger coverages of CO, due to a lack of vacant Cu sites required for O_2 dissociation. This would probably account for only the 3 and 2 % conversion occurring at the higher coverages of 0.4 and 0.8 ML of CO respectively. In addition, Briner et al.[109] also confirmed the possibility of both weakly bound, physisorbed molecular O_2, in addition to atomic adsorbed O existing simultaneously, albeit at the much lower temperature of 4 K. If this was the case at 90 K, then this would possibly account for the small amount of oxidation occurring during the O_2 uptakes.

Why oxidation was seen to occur with CO pre-dosed followed by uptakes of O_2, but not when O_2 was pre-adsorbed followed by uptakes of CO is down to the state of the atomic O. Any atomic O produced from pre-dosed O_2, would bind to the surface in a stable adsorption site, and only react with CO during the TPD when activated by heat. However, with CO pre-dosed on the surface any atomic O produced was able to react instantaneously whilst in a transient mobile state or some other high energy state.

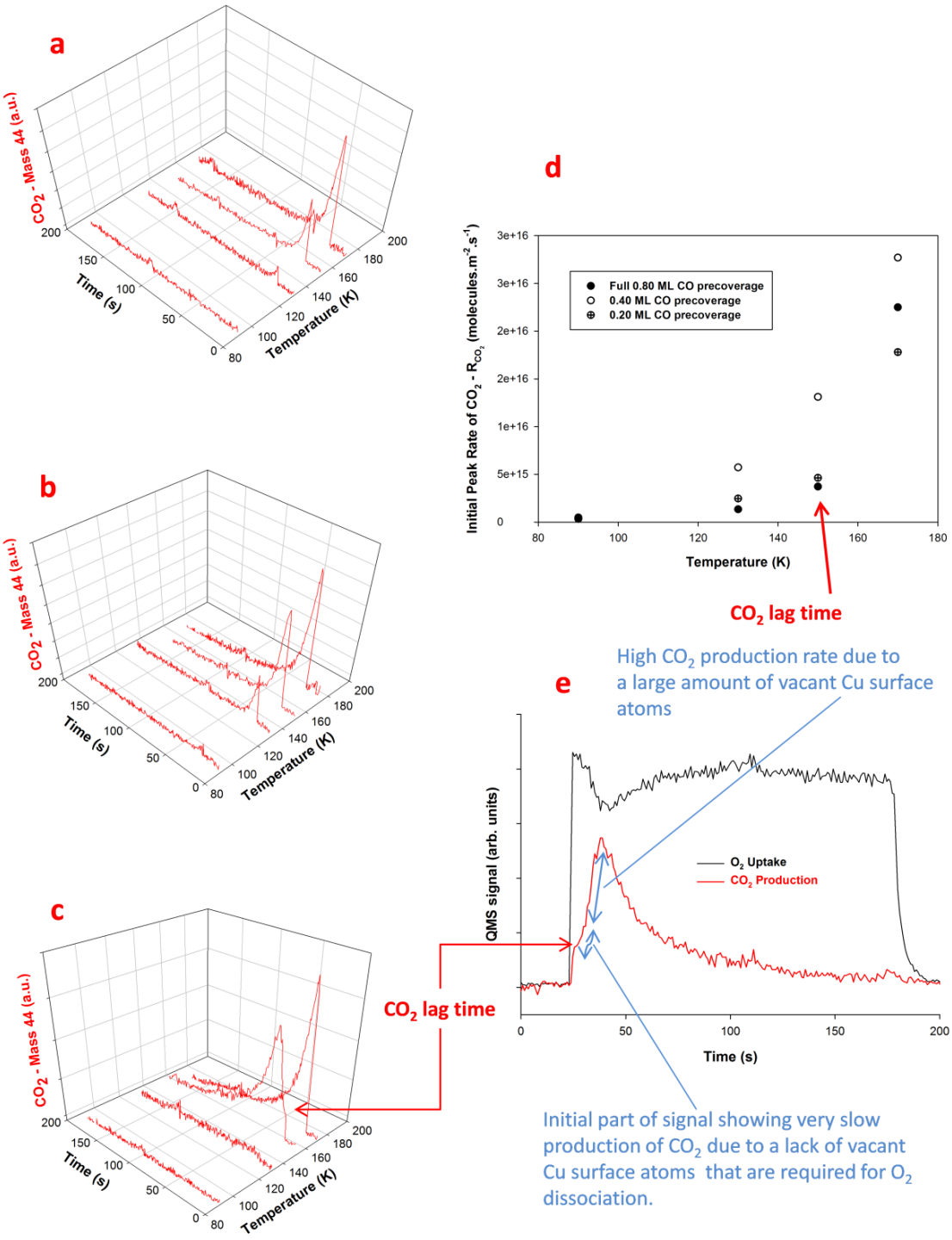

Fig. 4.20. Spontaneous CO_2 desorbing as O_2 is dosed on the (a) 0.20 ML, (b) 0.40 ML and (c) 0.80 ML CO pre-covered Cu(110) surface at temperatures 90, 130, 150 and 170 K. Graph (d) shows the combined initial peak rate for CO_2 production as a function of temperature at all CO pre-coverages with the saturated 0.80 ML CO coverage displaying a lag in the initial reaction time, shown in the expanded view (e).

The degree of activated dissociation increased when the temperature was increased to 130 K, giving rise to a slightly higher percent conversion of spontaneous CO_2. Likewise with less oxygen being in the physisorbed state, the % conversion of CO_2 during the TPD was sequentially reduced throughout. Similar patterns were observed when dosing O_2 at 150 and 170 K. At these higher temperatures virtually all of the dosed O_2 dissociated on impact, reacting and desorbing spontaneously to give high yields of CO_2.

With this being the case there was nonetheless a clear lag time before the oxidation reaction accelerated as shown in Figure 4.20 at 150 K, for the saturated 0.80 ML CO pre-coverage. Clearly, the CO pre-coverage (or alternatively the vacant Cu atom sites), are a major controlling factor of the reaction rate, specifically at low temperatures where activated dissociation is less likely to happen. To be more specific, on a surface with high or saturated CO coverage, it is difficult for the incoming O_2 to find an open space for dissociative adsorption where clearly neighbouring Cu atoms are required. Only after the initial slow desorption of CO_2 do vacant sites appear giving rise to the abrupt rise in the reaction rate.

There was a slight drop in the observed CO_2 production at 170 K for the higher coverages of CO at 0.4 and 0.8 ML. This drop could be attributed to a slight loss in the adsorbed CO, due to this uptake temperature (170 K) being very close to that of the onset desorption temperature for CO from the clean Cu(110) surface. As mentioned earlier this drop will be more pronounced at the higher coverage of $0.5 \leq \theta \leq 0.8$ ML due to the CO-CO lateral repulsions in the compressed c(5/4 × 2) overlayer. At the lower coverage of $\theta \leq 0.5$ ML, the CO-CO lateral repulsions are much lower in the (2×1) overlayer structure.

Systematically breaking down these observations in terms of the amounts of CO_2 produced at each temperature; it is clear that very little CO_2 was produced at 90 K unless activated during the TPD experiments. This was probably due to the O_2 being in a physisorbed or transient state. Additionally, no reaction occurred when O_2 was dissociated and chemisorbed on the Cu(110) surface at 170 K. Reactions only took place during the TPDs of the physisorbed complexes ($90 \leq T_s \leq 130$ K) or during activated dissociation at higher temperatures ($150 \leq T_s \leq 170$ K). This is significant as it tells us that

only transitory mobile atomic oxygen is able to react with chemisorbed CO to produce CO_2, once the atomic O is chemisorbed the reaction ceases. The transition of O_2 from the molecular physisorbed state to the atomic chemisorbed state requires activation that is obtainable only by way of TPD below 140 K. During this activated transition it has a limited period with which to react with any chemisorbed CO before entering a chemisorbed state with a potential energy well too deep to react with any chemisorbed CO.

The activated dissociation of O_2 by means of the TPD experiments produced significant quantities of CO_2, as shown in Figures 4.14 and 4.18. However, the initial reaction rate was relatively low in comparison to that of the CO_2 produced during the uptake of O_2 on the CO pre-covered surfaces at temperatures 130 to 170 K as shown in Figure 4.20. This presents compelling evidence that the catalytic reaction of O_2 being dosed onto the CO pre-covered surface at temperatures $130 \leq T_s \leq 170$ occurred by the hot atom mechanism. This is due to the high exothermicity associated with this dissociation process.[121] With this being the case on Cu(110) the binding energy for atomic O ranges from 1.6 – 2.0 eV, much lower than that of the bond energy of 5.1 eV associated with diatomic O_2. As a result, from a thermodynamic perspective, the dissociative abstraction process would most likely occur with the O_2 molecule oriented perpendicular to the Cu surface, as opposed to parallel. Although the dissociation barrier is slightly higher when oriented perpendicular, the sticking probability is higher when oriented parallel to the surface which would significantly reduce any abstraction of the O adatoms as hot atoms[121–123].

The intrinsic activity of the Cu(110) surface was found drop off precipitously with repeated uptakes of CO followed by O_2 due to the formation of –Cu-O- units inactivating the surface at 170 K as shown in Figure 4.21. Only after a brief anneal up to 773 K for a period of 1 min did the surface gain a degree of activity due to some of the atomic O diffusing on the surface and to a lesser extent into the Cu bulk[124,125]. Lacunas are normally present on the (2×1) added row -Cu-O- chains at both terrace edges and in the middle of terraces[126]. Thermal annealing has been found to induce surface rearrangement by way of dissociation of the -Cu-O- units, refilling these lacunas with the restoration of flat surface terraces. After thermal

annealing of the surface up to 773 K followed by cooling to 170 K, the -Cu-O- units either reattach to the (2×1) added row chains or dissociate, with the Cu adatoms inducing lattice terrace growth according to Reaction 4.10.

$$[Cu - O]_{(fluid)} + Cu_{(solid)} \leftrightarrow [Cu - Cu]_{(solid)} + O_{(ads)} \quad (4.10)$$

The release of the atomic O could result in re-abstraction of Cu adatoms or recombinative desorption of O_2 according to Reaction 4.11.

$$O_{(ads)} + O_{(ads)} \rightarrow O_{2(g)} \quad (4.11)$$

This recombinative desorption of O_2 in addition to the production and restoration of flat surface terraces reactivated the surface for additional oxidation reactions. In the absence of annealing the surface remained relatively inactive due to the (2×1) added row -Cu-O- chains. Although annealing created open spaces on the surface, the activity dropped continuously due to eventual overcrowding; however, never completely to zero over the course of these five experiments.

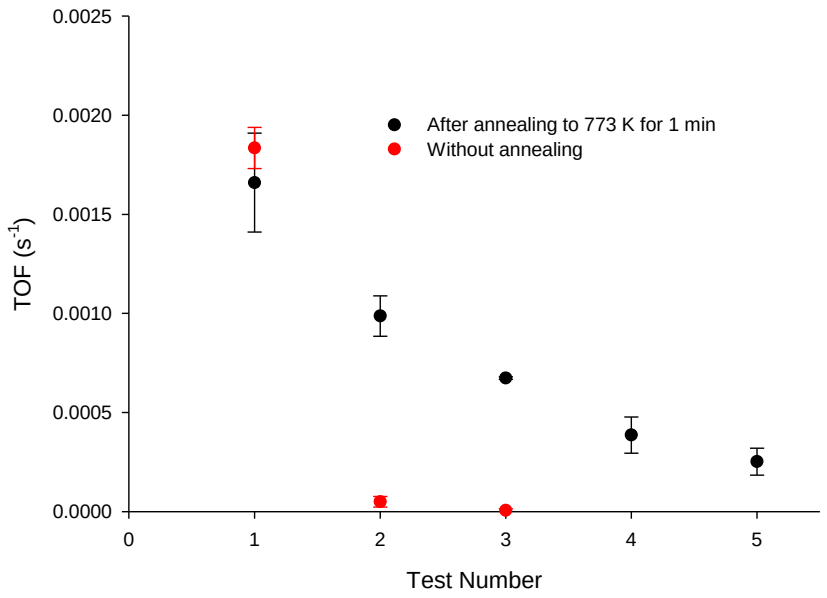

Fig. 4.21. Turnover frequency (TOF) for oxidation of CO at 170K, with and without annealing between each oxidation test.

4.4 Conclusions

We investigated the reactivity of O_2 with CO on the Cu(110) surface at low temperatures 90 to 170 K. This process of oxidation, by means of the coadsorption of CO and O_2 on the Cu(110) surface was found to be extremely complex. This was due to the strong interaction of atomic O with the Cu(110) surface at temperatures ≥ 130 K, in addition to the possible transient states existing below this temperature.

The oxidation process was found to proceed by separate mechanisms dependent on temperature and the order that the reactants were pre-adsorbed on the surface. With O_2 pre-adsorbed on the surface followed by uptakes of CO, oxidation only occurred at 90 K by induced thermal molecular dissociation, gradually dropping off at the higher surface temperatures of 130 – 170 K. This progressive drop was due to the O_2 dissociating and forming strong immobile –Cu-O- units. With CO pre-adsorbed on the surface followed by adsorption of O_2, oxidation occurred spontaneously by the Hot-Atom mechanism with a significant yield (above 40 %) of CO_2 only above 130 K. Below this temperature the O_2 appeared to adsorb physically in the molecular form or transient state and only reacted by induced thermal molecular dissociation with the O atoms remaining in a reactive transient state by the Eley-Rideal mechanism.

In addition to the reaction temperature the CO coverage was a major factor in terms of slowing down the reaction rate. At 130 K the oxidation reaction by the Hot-atom mechanism was unhindered at surface coverages of CO ≤ 0.4 ML as shown Figure 4.20. However, at a saturated coverage the reaction rate dropped off significantly due to a lack of open space. Only at the higher temperature of 150 K does the reaction propagate after the initial lag time. Spontaneous oxidation occurs at all coverages at the highest temperature of 170 K as discussed due to weakening at the onset temperature and facile dissociation of the O_2. Partial reactivation of the surface was achieved by way of thermal annealing up to 773 K. The restored Cu terraces were produced by surface rearrangement of -Cu-O- units splitting away from the (2×1)-O added row reconstruction and diffusing into the lacunas.

Chapter 5

5 Water on Clean and Oxygen pre-covered Cu(110)

5.1 Introduction

Water on metal surfaces has been one of the most studied adsorption systems since the establishment of modern surface science some 28 years ago[9,49]. However, there is a degree of uncertainty as to how exactly a study conducted under UHV conditions will correlate to those reactions occurring at or close to ambient conditions. This uncertainty occurs because under ambient conditions the majority of solid surfaces are covered with both oxygen and water. The study of water at interfacial surfaces also has importance in terms of understanding redox reactions associated with electrochemistry, heterogeneous catalysis and corrosion. In electrochemistry interfacial studies are important in understanding the characteristics of the molecules at the surface of the electrode as they play a key role in the electrochemical reactions, as opposed to those of the bulk solution[9]. Similarly, in heterogeneous catalysis, where reactions occur at the surface, interfacial studies on water are important to understand reactions involving water as a reactant or product, an example of this is seen in the water-gas-shift[29] where hydrogen is produced (Equation 5.1);

$$H_2O_{(ads)} + CO_{(ads)} \rightarrow CO_{2(g)} + H_{2(g)} \qquad (5.1)$$

In this chapter we report results investigating the formation, composition and stability of mixed structures formed from both water and oxygen at elevated temperatures and pressures. In order to provide the starting point for our study, in this section we detail previous work done at both UHV and elevated pressures and temperatures, which we have used in order to understand our findings.

5.1.1 Fundamentals of the H_2O & H_2O-OH structure on Cu(110) surfaces

The structure of the water network on metal substrates is determined by the interplay between the intermolecular and water–substrate interactions, in addition to the barriers towards both diffusion and dissociation. In other words, it is determined by a combination of the interaction of Hydrogen bonded (H-Bonded) water-water (H_2O-H_2O), water-hydroxyl (H_2O-OH), hydroxyl-substrate (OH-substrate) and water-substrate (H_2O-substrate) interactions[127]. The dimensions and properties of the water network formed, be it 1 dimensional (1D), 2D or 3D, (partially) dissociated, intact, wetting adsorption or non-wetting, is determined by the lattice parameter, surface symmetry and reactivity of the metal[8].

Water will form monomers or clusters when adsorbed on the Cu(110) surface at low temperatures (ca. 40 K) due to a lack of thermal energy which would otherwise give rise to surface diffusion. Whilst these structures are thermodynamically unstable, they are kinetically stable, converting to larger clusters with an increase in temperature and coverage. Increasing the surface temperature to 80-140 K may give rise to either 1 or 2D ordered extended H-bonded structures, depending on the coverage, as the water becomes mobile. Because the binding energy of intact H_2O on Cu(110) is relatively weak and comparable to that of the hydrogen bond itself (0.20 - 0.36 eV/ H_2O)[128], this gives rise to a delicate balance between the bonding to both the adsorbate and substrate. The formation of these structures may of course be dependent on the initial coverage of H_2O, with 1D H-bonded networks sometimes forming at low initial coverages and 2D/3D extended H-bonded networks at higher coverages. Further increases in temperature will give rise to direct desorption or partial dissociation of H_2O to form H_2O-OH structures, depending on the background pressure. Whilst dissociation is activated, it can be initiated by step edges or pre-adsorbed atomic oxygen O, as detailed later. In contrast to the weak adsorption energies of pure H_2O on the Cu metal surface, significantly higher adsorption energies are found for the mixed H_2O-OH phases.

The formation of H_2O-OH wetting layers has been studied on different Cu metal surfaces for decades. Only recently, however, have researchers established a clear picture of the structures formed at molecular level on any well-defined metal surface, including Cu. The wetting properties of Cu have attracted significant attention due its borderline nature between being hydrophobic and hydrophilic, depending on the surface symmetry of the face being studied. In the absence of pre-adsorbed atomic O, Cu(111) remains inert to H_2O (hydrophobic) at background pressures of 1.333 mbar (1 Torr) and surface temperature T_s 200 – 300 K, whilst under similar conditions water adsorbed on the Cu(110) surface will dissociate giving rise to H_2O-OH structures with or without the presence of pre-adsorbed oxygen [10,129]. Mixed, H_2O-OH structures can, however be produced at much lower temperatures as a result of electron bombardment damage which will be expanded on later in Section 5.1.4. This sensitivity to atomic O or electron exposure has been responsible for a number of misleading reports in earlier studies of H_2O on Cu(110), as will be comprehensively detailed later.

5.1.2 Molecular H_2O growth on Cu(110)

According to first-principles electronic structure calculations conducted by Ren & Meng [50,130] the most stable position for the H_2O monomer to adsorb at the Cu surface was found to be on the atop site (0.375 eV), in a flat-lying geometry with its molecular structure deformed very little from that in the gaseous phase. Diffusion allowed cluster formation at temperatures as low as 20 K, along both the $[1\bar{1}0]$ and $[001]$ azimuths. Directional diffusion along the $[1\bar{1}0]$ azimuth was found to be much more favourable due to its lower diffusion barrier of 0.12 eV, as opposed to 0.23 eV along the $[001]$ azimuth.

Recent studies by Kumagai et. al.[72,131] on the donor-acceptor interchange growth of water on Cu(110) by STM at 12-20 K, confirmed that monomer diffusion is favoured along neighbouring Cu atoms of the $[1\bar{1}0]$ closed packed rows to form dimers, followed by trimers. Alternatively, trimers could also be formed by the diffusion of dimers along the $[1\bar{1}0]$ azimuth, subsequently bonding with monomers on adjacent $[1\bar{1}0]$ rows. Two trimer

conformations were observed, with one having all three H_2O molecules bonded at neighbouring atoms along the $[1\bar{1}0]$ azimuth (Figure 5.1B(i)) and the other being a metastable conformation with two H_2O molecules bonded atop across the $[001]$ azimuth trough and the third attached to the end as an acceptor (Figure 5.1B(ii)). The metastable trimers were found to arise from dimers and monomers on adjacent rows and would eventually transform into the more stable conformation along the $[1\bar{1}0]$ row. This was not by any means a static arrangement, as the H-bond orientation of the donor and acceptor molecules exchange by means of concerted rotation through quantum tunnelling for both dimers and trimers[132,133].

Although cyclic trimers are stable in the gaseous phase, due to maximization of H-bonding, this structure was never observed on the Cu(110) surface. According to DFT studies conducted by Michaelides[134], cyclic trimers were found to be stable on the Cu(111) surface (Figure 5.1A). Both of the cyclic trimers, where each H_2O donates and accepts a single H-bond and the trimer conformation where one water molecule donates two hydrogen bonds, were found to be commensurate and stable on the Cu(111) surface, but not on the Cu(110) surface, as shown in Figure 5.1. This difference was primarily due to the fact that the symmetry of the closed-packed (111) template is closely matched to that of hexagonal bulk ice films. When simulated, it was found to be geometrically unfavourable on the (110) template, despite maximizing the H-bonding. This reaffirmed that water structures require optimum Cu adsorption sites so that the overall stabilization from H_2O-H_2O and H_2O-Cu interactions is maximized.

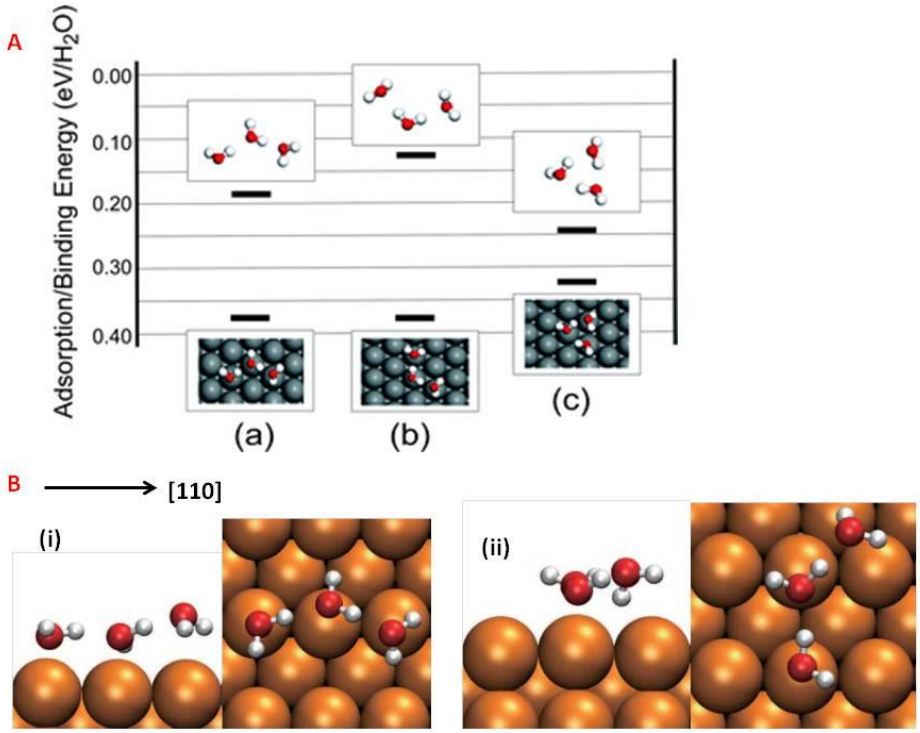

Fig. 5.1. A. Relative energies and structures of three gas phase and adsorbed H_2O trimers. Adsorption and binding energies on Cu(111) and binding energies are relative to isolated gas phase H_2O molecules. Adapted from Michaelides, A.[134] Simulating ice nucleation, one molecule at a time, with the 'DFT microscope Faraday Discuss. 136, 287–297 (2007), with permission of The Royal Society of Chemistry. B. (i) The structure of the $(1\bar{1}0)$ chain trimer & (ii) The optimized structure for the second trimer, in which two water molecules are bonded along $[001]$ and another one is attached to the end forming a chainlike structure ($[001]$-chain trimer). Reprinted with permission from Kumagai et al.[131] Water clusters on Cu(110): Chain versus cyclic structures. *J. Chem. Phys.* 134, 024703 (2011). Copyright [2011], AIP Publishing LLC.

Whilst extended chain growth to form tetramers, pentamers, hexamers, etc., could be achieved by STM tip manipulation, it is also possible to produce two additional tetramers by means of an electrical pulse applied directly to a linear tetramer (Figure 5.2a). One of these isomers is thought to have a "Y" shaped structure, with the central molecule acting as a double donor single acceptor (Figure 5.2b), which was found to be degenerate in energy (0.49 eV/H_2O) to that of the chain tetramer structure. The other isomer is the cyclic structure (Figure 5.2c), found to be thermodynamically more stable by 0.015eV/H_2O[131].

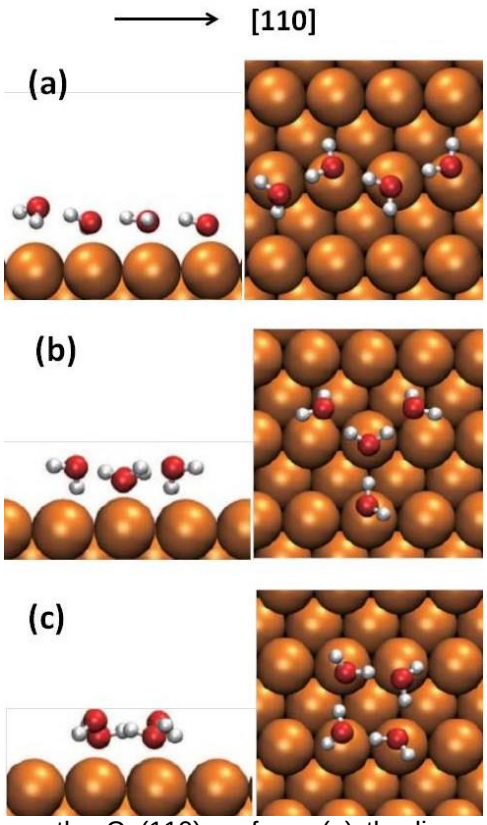

Fig. 5.2. Water tetramers on the Cu(110) surface; (a) the linear tetramer, where the end molecule of single acceptor is most protruded from the surface, (b) the tetrahedral configuration with the center molecule acting as a double donor and single acceptor and (c) the cyclic configuration. Reprinted with permission from Kumagai et al.[131] Water clusters on Cu(110): Chain versus cyclic structures. *J. Chem. Phys.* 134, 024703 (2011). Copyright [2011], AIP Publishing LLC.

5.1.3 Adsorption of H_2O at surface temperatures (78 ≤ Ts ≤ 140 K) on clean Cu(110) at sub-monolayer surface coverage (θ ≤ 0.3 ML)

The dosing of H_2O at sub-monolayer coverage results in the anisotropic growth of 1D chains along the [001] azimuth, as reported by Yamada et al.[135] and later by Lee et al.[136]. These were characterized by STM, where bright zigzagged protrusions were observed running along the [001] direction. These chains were found to be highly reproducible across the temperature range 78 – 140 K. At a coverage > 0.3 ML, across this temperature range (78 - 140 K), the chain growth was found to saturate with the chains spaced 10 Å from each other before subsequently forming a coexisting 2D structure.

Hexagonal ice I_h crystals form six-fold hexagonal plates and columns where the top and bottom faces are basal planes $[0001]$, and the six equivalent side faces are known as the prism faces $[10\bar{1}0]$. One of the common features associated with ice nucleation on metal surfaces is that they are typically interpreted as being built from cyclic hexagons, analogous to the top or bottom basal plane $[0001]$ of ice I_h. Yamada et al.[135] tentatively proposed the 1D chains to have a cyclic hexagon (zigzag) chain structure, but Carrasco et al.[137] recently proposed a more favourable pentagon (zigzag) chain structure. This pentagon chain structure, shown in Figure 5.3, was found to be more favourable than the hexagonal chain structure due to its ability to maximize the H_2O-substrate bonding. This structure allows two thirds of the H_2O molecules to bond in their most favoured site, that being the flat geometry atop Cu, whilst still maintaining a strong H-bonded network. These findings were based on DFT calculations of different hexagonal and pentagonal structures. DFT adsorption energies for the simulated structures (Figure 5.4a-d), based on E_{gas} (H_2O-H_2O) and E_{ads} (H_2O-substrate) show that the pentagonal chain structures have the highest binding energy. The computed IR spectra for the pentagon structure was found to correspond more closely to that of the experimental infrared spectra for the 1D water chains on Cu(110). In addition, the zigzag alternation in intensity observed by STM is replicated for the pentagons but not for hexagons, confirming that these chains were built from pentagons.

This pentagonal structure (Figure 5.4d) consists of 5 H_2O molecules, 4 adsorbed as double donor single acceptors planar and parallel to the surface atop the $[1\bar{1}0]$ row, and a single double acceptor tilted orthogonal to the adjoining 4 molecules situated above the trough[8,137,138]. The chain structures were formed with regular intervals along $[1\bar{1}0]$ direction at sub-monolayer coverages, indicative of a long range dipole-dipole repulsive interaction, inhibiting the formation of denser films. Once the chains were forced to within 10 – 15 Å of each other with increasing coverage, the stability of the 1D chains dropped, giving rise to 2D phase nucleation. This 2D phase eventually gave the extended 2D $[7 \times 8]$ structure detailed in the following section.

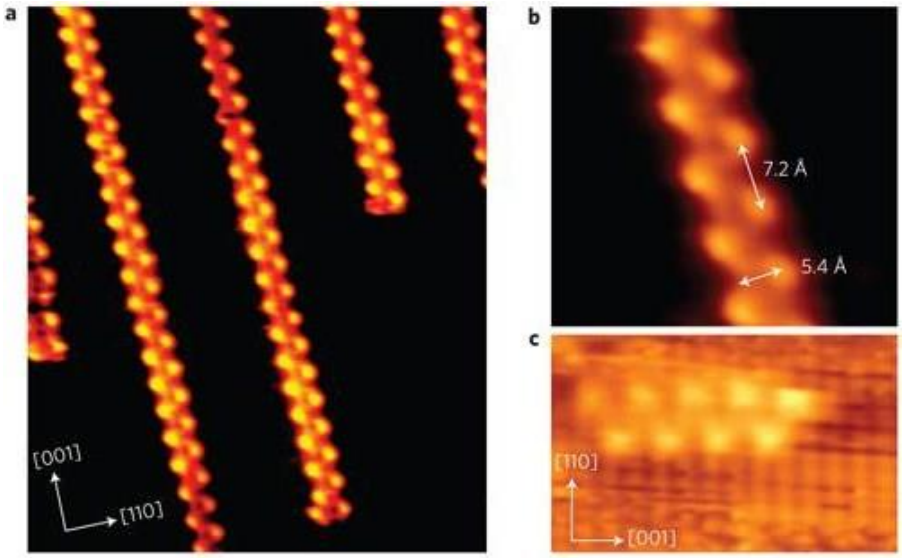

Fig. 5.3. Experimental STM images of water on Cu(110). a) STM image taken at 100 K showing water chains growing along the [001] direction. b) Expansion of (a) showing partial resolution of the water structure within the chain. c) Image showing protrusions residing between the Cu rows in the [001] direction. Reprinted from Nature, Vol 8, Carrasco et al.[137], A one-dimensional ice structure built from pentagons Pages 427-431, Copyright (2009), with permission from nature publishing group (npg).

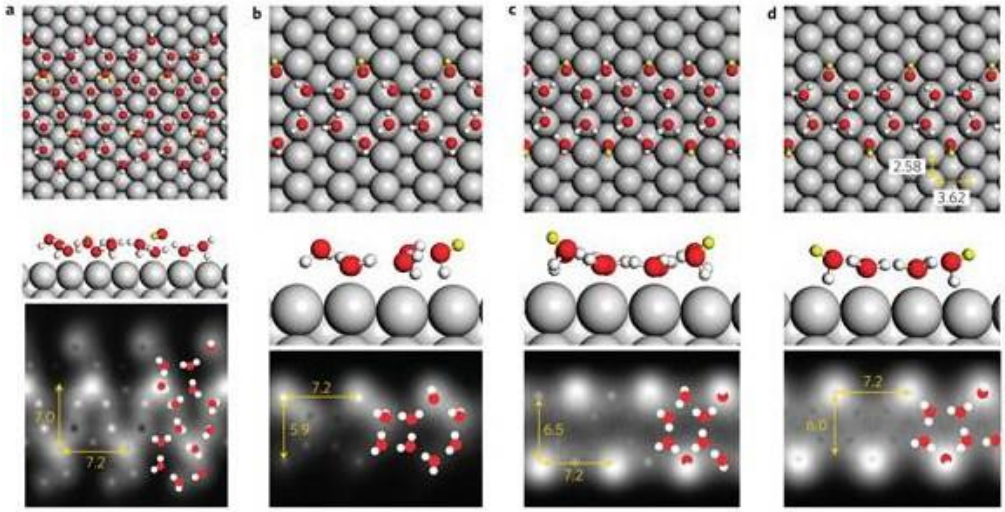

Fig. 5.4. Models for 1D water chains on Cu(110). a–d, Equilibrium geometry and simulated STM images for a selection of structures identified with DFT for water chains on Cu(110). Grey spheres correspond to Cu atoms, red ones to O atoms and small white ones to H atoms. The highest H atoms of each structure, which are responsible for the brightest features in the simulated STM images, are highlighted in yellow. In the simulated STM images, the locations of the water molecules in one surface unit are also shown. The most stable structure and the one we claim is observed in experiment is d, the pentagon-based structure. Distances are in Å. Reprinted from Nature, Vol 8, Carrasco et al.[137], A one-dimensional ice structure built from pentagons Pages 427-431, Copyright (2009), with permission from nature publishing group (npg).

5.1.4 Adsorption of H_2O at surface temperatures (78 ≤ Ts ≤ 140 K) on clean and oxygen-covered Cu(110) at surface coverage > 0.5 ML

Until recently there has been a high degree of uncertainty with regards to the proposed structures formed at high coverage and surface temperatures in the range 78 ≤ Ts ≤ 140 K. Early studies conducted by Bange et al.[139] and later Benndorf and Madey[140] on Ni(110), reported an H-bonded $c(2 \times 2)$ bi-layer structure with the H_2O molecules intact, arranged with a slight asymmetric distortion, as shown in Figure 5.5A. These studies conducted by Bange et al.[139] were carried out at 100 K on the clean and oxygen pre-covered surface using a combination of UPS, TDS and LEED. Similar studies conducted by Benndorf and Madey[140] were carried out at 80 K using a variety of methods including ESDIAD, TDS and LEED.

Although these H-bonded structures, proposed by both Bange et al. and Benndorf and Madey, disputed the earlier reports of a dissociated $c(2 \times 2)$ structure reported by Spitzer and Lüth[141], recent work by Schiros et al.[142] showed that the $c(2 \times 2)$ structure contained dissociated H_2O. This dissociated $c(2 \times 2)$ structure was formed as a result of electron beam damage from LEED, inducing dissociation of the H_2O molecules. This also confirmed that the reported H-bonded $c(2 \times 2)$ bi-layer structure was a misinterpretation of the dissociated $c(2 \times 2)$, as shown by the hypothetical structure in Figure 5.5B. Instead, new work by Foster et al.[46,127] showed that the $c(2 \times 2)$ structure comprised of a mixture of OH and H_2O containing Bjerrum defects.

A Bjerrum defect, which was first put forward by Bjerrum[143] in 1952, is a lattice fault in the crystalline structure of ice caused by thermal excitation. These are either orientation faults, where two neighbouring H_2O molecules become incorrectly orientated, or ionization faults, where ions occur within the crystalline lattice. With the orientation fault sites, two protons may be orientated towards each other (D-type defect) or no protons directly between two oxygen atoms (L-type defect). With ionization fault sites, the ions H_3O^+ or OH^- occur instead or H_2O molecules. Foster et al. calculated that the most stable 2D partially dissociated structures in the $c(2 \times 2)$ unit cell all have

defective H-bonding networks containing D-type Bjerrum defects, with a H_2O:OH ratio of 2:1.

At 140 K, Schiros et al.[142] found that H_2O actually adsorbs on the clean Cu(110) surface to form a complex structure having a (7×8) unit cell. This could only be observed with the use of a microchannel plate (MCP) LEED, which minimised the electron exposure and damage. They found the (7×8) superstructure diffraction order spots disappeared rapidly after electron exposure, giving rise to an intense $c(2 \times 2)$ LEED pattern. They confirmed by means of XPS, XAS, and RAIRS, a mixed H-down and H-up configuration with approximately a third of the H_2O molecules binding H-up. They also found that the (7×8) LEED pattern showed diffuse spots, compared to that of H_2O/Pt(111) and H_2O/Ru(0001), and also a significant background due to diffuse scattering. This suggested that the water structure was not pinned into close registry with the Cu(110) surface, but more likely consisted of a complex H_2O network. The sensitivity of this structure to electron induced dissociation is therefore responsible for the $c(2 \times 2)$ phase, which is the most commonly observed structure.

It is important to also add that the partially dissociated $c(2 \times 2)$ structure will also form above 150 K by means of thermally induced dissociation[46,8,142] and also at lower temperatures by reaction with small amounts of atomic O[139,141,144]. This reaction, along with electron beam damage during LEED, probably accounted for the inaccuracies observed and reported in earlier research.

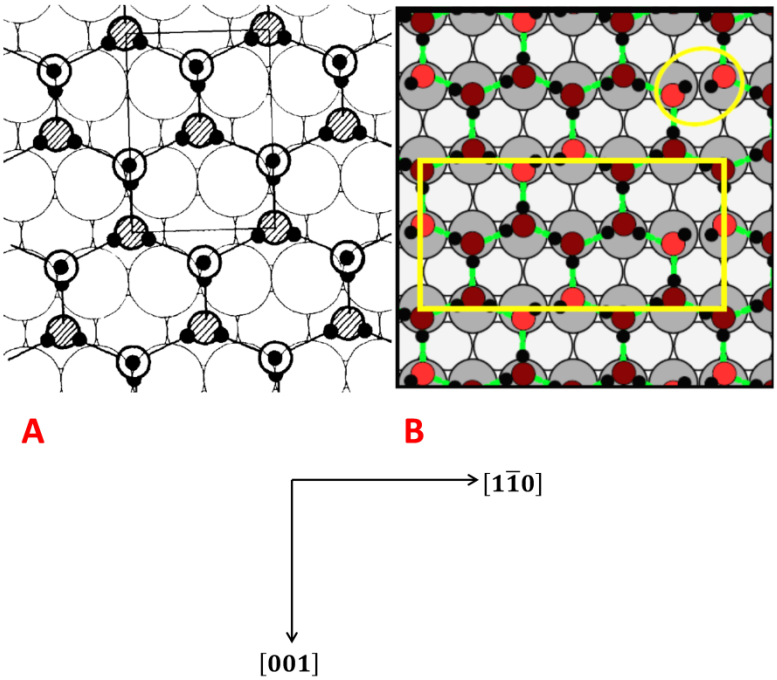

Fig. 5.5. (A) Schematic of the proposed H-bonded $c(2 \times 2)$ bi-layer structure with the H_2O molecules intact, arranged with an asymmetric distortion (LHS) with the unit cell containing four water molecules. Reprinted from Surface Science, Vol 137/Issue1, Bange et al.[139], The surface chemistry of H_2O on clean and oxygen-covered Cu(110) Pages 38–64, Copyright (1984), with permission from Elsevier. (B) Schematic of the proposed calculated structure of the dissociated H-bonded $c(2 \times 2)$ H_2O-OH structure (RHS) with a Bjerrum defect circled and the rectangle indicating the unit cell employed in the calculation. Reproduced (Adapted) from Forster et al.[127], Water-hydroxyl phases on an open metal surface: breaking the ice rules. *Chem. Sci.* **3,** 93–102 (2011) with permission of The Royal Society of Chemistry.

5.1.5 Adsorption of H_2O at surface temperatures (150 ≤ Ts ≤ 270 K) on clean and oxygen-covered Cu(110)

As stated earlier the partially dissociated $c(2 \times 2)$ structure will form above 150 K by means of thermally induced dissociation or with small amounts of atomic O. Dosing with the surface temperature within the range $185 \leq T_s \leq 200$ K, gives rise to the formation or two different chain structures with a H_2O:OH ratio of 1:1. According to Forster et al.[46,127] and Shi et al.[129] these were identified as Pinch (P) and Zigzag (Z) as shown in the STM images and calculated structures in Figure 5.6. As discussed previously in detail, the LEED pattern provides information on the size, symmetry and rotational alignment of the adsorbate unit cell with respect to the substrate unit cell. The fact that steaks may be observed in the diffraction pattern is an indication that the surface structure is 1D disordered.

If a streak in a LEED pattern is observed continuously when changing the electron energy this implies either a 1D object on the surface perpendicular to the streak or, (at higher coverage) partially disordered 2D structures. Arranged in a 2D array, these two P and Z chain structures will have a similar structure to that of the partially dissociated H_2O:OH 2:1 H-bonded structure, which produces a clear $c(2 \times 2)$ LEED pattern. Therefore, in relation to the hydroxyl end groups, these P and Z structures will produce either a $(2 \times n)$ or $(4 \times n)$ LEED pattern exhibiting ½ and ¼ order streaks respectively in the $[001]$ azimuth. The Z chain structure with a $2a_{Cu}$ repeat assigned to the ½ order pattern and the P chain structure with a $4a_{Cu}$ repeat assigned to the ¼ order. Streaking in the $[001]$ direction is an indication of long range disorder along the $[001]$ azimuth, with ordered chain growth in the $[1\bar{1}0]$ direction. Although they were never identified as chain structures at the time, previous work carried out under identical conditions by Spitzer and Lüth[141] also showed LEED patterns exhibiting a $c(2 \times 2)$ transforming into a LEED pattern with ½ and ¼ order streaks in the $[001]$ azimuth at sub monolayer coverages.

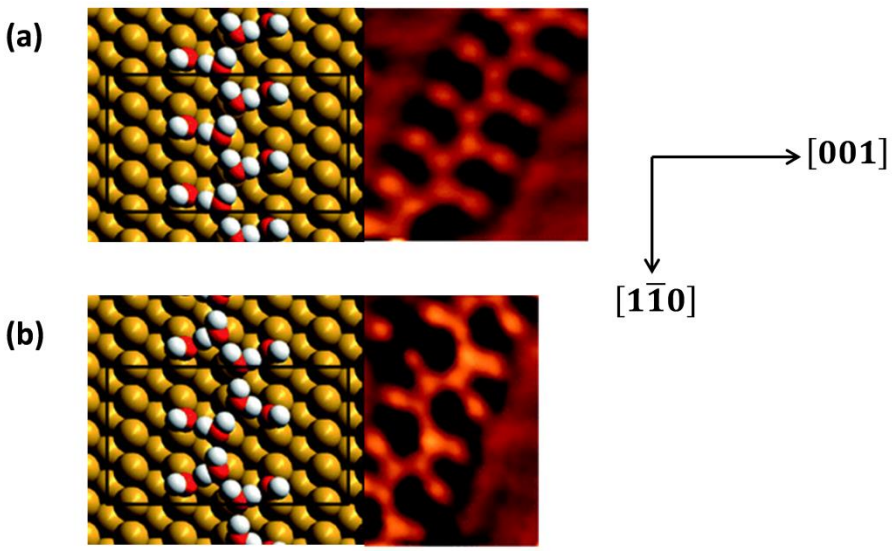

Fig. 5.6. STM and calculated chain structures containing $1H_2O$:1OH for (a) "Z" (zigzag) chain having a $2a_{Cu}$ repeat and (b) "P" (pinch) chain having a $4a_{Cu}$ repeat along the $[1\bar{1}0]$ azimuth. Adapted from Forster et al.[127].

Dosing H_2O in the presence of pre-adsorbed atomic oxygen with the surface temperature within the range 225 ≤ Ts ≤ 240 K, gives rise to the formation of hydroxyl dimers[127]. These were observed as bright features by STM elongated along the $[001]$ azimuth, no closer than $2a_{Cu}$ along the $[1\bar{1}0]$ direction. Analogous to atomic O, these dimers exhibited a (2×1) LEED pattern, but much weaker[141,145] with faint streaking in the $[001]$ direction. This indicated disorder along $[001]$ with relatively ordered growth in the $[1\bar{1}0]$ direction. Although these pure hydroxyl dimers have a weak tendency to associate into chains, they are usually only found as either isolated OH monomers or dimers aligned along the $[001]$ azimuth and no closer than two Cu atoms apart in the $[1\bar{1}0]$ direction[127], giving rise to the (2×1) LEED pattern shown in Figure 5.7. According to Kumagai et al.[146] the monomer has an inclined angle (between the axis and the surface normal) of 62°, flipping by way of quantum-mechanical tunnelling between the $[001]$ or $[00\bar{1}]$ directions at a rate of 10^6 s^{-1}. The dimers have different tilt angles to the surface norm; with the H-bond donor at 78.6° and the H-bond acceptor at 43.4°. This lack of order in the $[001]$ direction gives rise to the streaking observed in the LEED patterns.

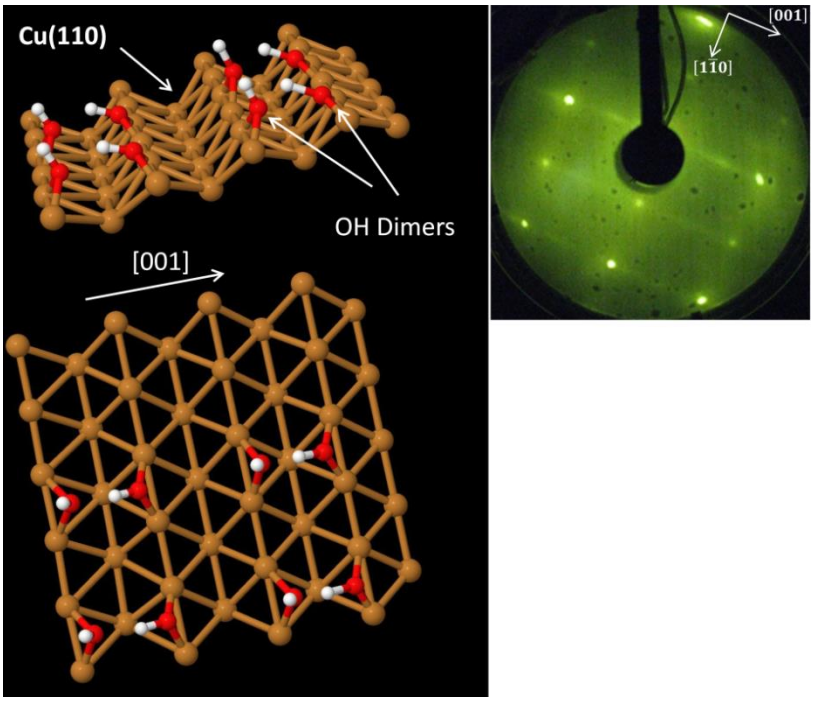

Fig. 5.7. Side and aerial view for adsorbed OH dimers that gives rise to the faint (2×1) LEED pattern, Brown (Cu substrate), Red (Oxygen) and White (Hydrogen).

5.1.6 Summary of the structural transformations with temperature and relative bond energies

Under UHV conditions at temperatures ≤ 150 K, H_2O adsorbs molecularly on Cu(110), initially forming 1D pentagon chains with a face sharing arrangement along the $[001]$ direction, followed by 2D islands at increasing H_2O coverage. These 2D islands eventually give rise to the (7×8) repeat unit cell structure detailed earlier, before desorbing intact at 160 K. Contrary to what was published earlier, H_2O adsorbs intact and will react in the presence of atomic oxygen, or dissociate as result of electron beam radiation damage, giving rise to the mixed OH/H_2O $c(2 \times 2)$ structure detailed earlier.

In the temperature range 185 ≤ Ts ≤ 240 K, and in the presence of atomic oxygen, P and Z chains are formed at sub monolayer coverages below 225 K with hydroxyl dimers forming above this temperature, leaving atomic O on the surface after recombinative desorption above 280 K.

Kinetically there is a competition between thermally induced dissociation and desorption processes which is dependent on the H-bonding and Cu-O bonding between each of the phases. The relative bond energies determine the stability of the observed structures, where the stability decreases in the following order; Cu-O > Cu-OH >> H_2O(donor)-OH(acceptor) > Cu-H_2O ≈ H_2O-H_2O > OH(donor)-H_2O(acceptor)[47].

5.1.7 High pressure studies and aims of project

The main focal point of the research described in this chapter is to gain some insight into the bonding mechanism at elevated water pressures and ambient temperatures, whilst assessing the stability of the water-hydroxyl species. Here we focused on pressures within the range 7.5 x 10^{-12} - 7.5 x 10^{-8} Torr (1.0 x 10^{-11} – 5.0 x 10^{-7} mbar) and temperatures 200 - 300 K. Moreover, there is a need to bridge the gap to studies conducted at low temperature under UHV conditions, as most chemical processes actually take place under ambient conditions. Given that both kinetics and thermodynamics determine

the formation and stability of these surface structures, the wetting dynamics were assessed by keeping a constant temperature and varying the pressure as well as keeping the pressure constant and varying the temperature.

Yamamoto et al.[10] hypothesized that the strong attractive interaction between the mixed OH and H_2O slowed down the desorption kinetics dramatically. This resulted in large quantities of H_2O being adsorbed on the Cu(110) surface at near-ambient conditions, which in their case was a pressure of 1 Torr and a temperature of 295 K. They found that wetting was controlled primarily by the presence of OH groups on the surface, acting as anchors for water adsorption. An earlier XPS study on the H_2O/Cu(110)-system undertaken by Andersson et al.[147] showed that the activation barrier towards dissociation was very close to that of the adsorption/desorption barrier. On the basis of these calculated values, (0.53 - 0.56 eV for dissociation and 0.50 – 0.53 eV for desorption), the equilibrium between adsorption/desorption and dissociation is shifted towards dissociation under ambient conditions.

Recent work by Guillemot and Bobrov[11] addresses the hitherto ignored influence of the surface mobility and chemical state of the hydroxyl species on the H_2O/Cu(110)-system at elevated pressures. Focussing on the surface mobility of the Cu adatoms, they showed by STM that surface transport on Cu(110) significantly modified the hydroxyl reactivity. Having produced hydroxyls by reacting H_2O with pre-adsorbed atomic O above 200 K at pressures 5.0×10^{-9} – 1×10^{-8} mbar, they observed nucleation of 2D Cu islands. These islands were single atomic layer in thickness and formed during abstraction of the (2×1) added row Cu-O chains (Figure 5.8) and were covered by chemisorbed hydroxyl.

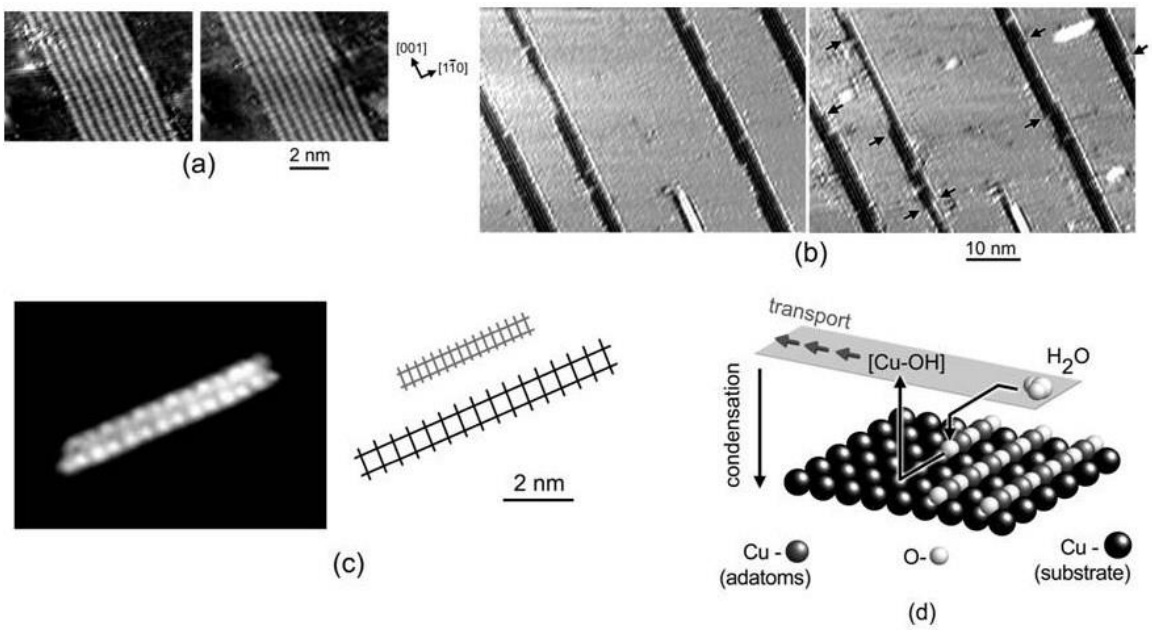

Fig. 5.8. Illustration of the formation and transport of Cu–OH complexes on the Cu(110)-(2 × 1)-O surface under water adsorption at T = 200 K. (a) Single (2 × 1)-O band under water exposure. The STM topographies were recorded consequently at the 0.0048 L (left) and 0.024 L (right) adsorption dose. (b) The (2 × 1)-O superstructure under water exposure. The two STM topographies were recorded consequently for the 18.9 L (left) and 27.5 L (right) adsorption dose. The black arrows mark the abstraction events taking place at the (2 × 1)-O band borders during the elapsed time. (c) Left: Close-up view on a single Cu island (the protrusions in panel b). The image contrast was adjusted to observe fine structure of the adsorbate phase. Right: The grids representing the adsorbate phase (black) and the Cu lattice (gray). (d) Formation and transport of the [Cu–OH] complexes. Reprinted from The Journal of Physical Chemistry C, 115, Guillemot and Bobrov[11], Formation of a Chemisorbed Water-Hydroxyl Phase on Cu(110) Mediated by Surface Transport. Pages 22387–22392, Copyright (2011), with permission from American Chemical Society.

According to their findings the fact that these islands nucleated away from the abstracted added row Cu-O chains indicated long-range transport of both Cu adatoms and OH. Throughout the nucleation process the Cu island was covered by the adsorption phase and at no stage were single hydroxyls detected on the surface. This suggests that the Cu-O bonds remained intact throughout implying the Cu adatoms and hydroxyl species diffused together on the surface.

In conjunction with this, their main finding was that the Cu-OH island growth stabilized a chemisorbed H_2O-OH phase stable up to RT, as shown in Figure 5.9. The research presented in this chapter were conducted to explore the findings of Guillemot and Bobrov, since no structures corresponding to those proposed in Figure 5.9 have previously been observed at UHV or ambient pressures. In addition the H-bonded structures formed by reacting

H_2O with both high and low O_2 coverages needed addressing specifically within this temperature range.

These proposed structures (Figure 5.9) are very unusual, as you would expect such a structure to be neither kinetically nor thermally stable at these temperatures with this structural arrangement. Due to the strong interactions between the H_2O and OH, wetting layers on Cu(110) tend to be formed from a mixture of H_2O and OH with the H_2O adapting the favoured atop site. Although in this proposed structure, the H_2O appears to be arranged and interacting with the substrate at its most favoured site, that being in a flat geometry and atop, it only acts as a single donor and doesn't accept any H-bonds. It is very unusual to have the hydroxyl groups acting as a both donor and acceptor in mixed H_2O-OH structures except during the formation of dimer chain along the [001] direction for trimer, tetramers etc[131] at very low temperature.

In previous observed stable H_2O-OH structures, the hydroxyl acts as a strong H-bond acceptor with the H_2O donating both H-bond in order to optimize the H_2O-OH network. As detailed earlier, hydroxyls in the P and Z chains accept a single H-bond from the H_2O chains with the structures having a $1H_2O$:1OH ratio, whilst accepting two H-bonds at higher coverages in the $c(2 \times 2)$ structure with a $2H_2O$:1OH ratio exhibiting Bjerrum defects[46,127].

Although Kumagai et al.[45] produced similar H_2O-OH complexes; these were produced selectively by manipulating the H_2O molecules in a controlled manner by the STM probe. In addition, their H_2O-OH proposed structure was assembled using a single H_2O molecule attached to a single OH molecule and never assembled into an entire phase.

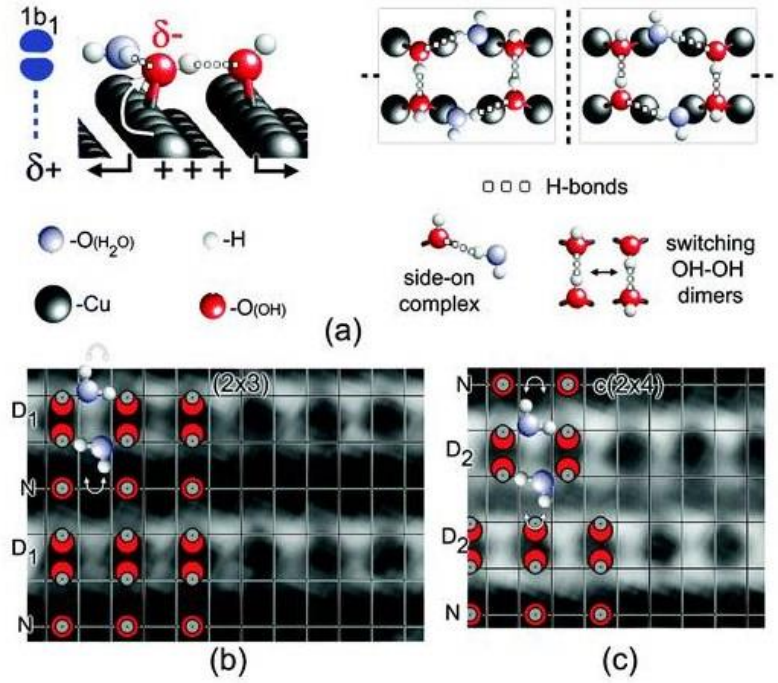

Fig. 5.9. Proposed structure of the water-hydroxyl phase. (a) Left: Schematics of charge transfer (the arrows) in the topmost surface layer. Right: Two mirror configurations of the water-hydroxyl phase (the left and right panels). The two mirror planes are specified (the dashed lines) with configurations of the switching OH–OH dimers and the side-on complex. (b,c) Structural model of the water-hydroxyl phase superimposed on STM topographies of the domain body (b) and the domain boundary (c). The close-packed rows of the Cu substrate are shown by the grid lines. The hydroxyls structures (D1, D2, and N) are simplified and emphasized for clarity. Reprinted from The Journal of Physical Chemistry C, 115, Guillemot and Bobrov[11], Formation of a Chemisorbed Water-Hydroxyl Phase on Cu(110) Mediated by Surface Transport. Pages 22387–22392, Copyright (2011), with permission from American Chemical Society.

5.2 Experimental

A Cu(110) crystal, cut and polished with an accuracy of ~ 0.25°, was used throughout the entirety of this study. All experiments were performed in an Ultra High Vacuum (UHV) chamber, operated at base pressures $< 10^{-10}$ mbar, elevated only for the high background H_2O exposure experiments to pressures from $< 10^{-10}$ up to 5.0×10^{-7} mbar inclusive. As detailed in the experimental section, each stage of the UHV chamber was pumped independently by diffusion pumps, all backed by rotary oil pumps, running in combination with a liquid nitrogen cooled titanium sublimation pump. The polished Cu(110) crystal was cleaned by prolonged Ar^+ ion sputtering cycles of 15-20 minutes at a drain current of 2 – 5 μA (500 eV) at room temperature prior to each experiment. This was performed in order to

remove surface contaminants such as carbon, oxygen and sulphur, followed by annealing to 823 K. The surface order prior to analysis was assessed by LEED to obtain a bright (1×1) pattern. The crystal was mounted by the use of 0.2 – 0.5 mm Ta-wires on Ta-rods on a rotatable manipulator that could be moved horizontally in the x, y-plane and vertically along the z-axis. The manipulator was also equipped with an electrical feed-through to enable resistive heating and the temperature was monitored by the use of a thermocouple mounted to the side of the crystal.

All Temperature-Programmed Desorption (TPD) and sticking coefficient experiments were measured by means of a Quadrupole Mass Spectrometer (QMS). The QMS was also used to monitor the purity of the background water prior to and during dosing for the high background water exposure experiments. A heating rate (dT/dt) of 1 Ks^{-1} was used throughout for the TPD measurements.

Oxygen (99.5 % high purity supplied by BOC, CAS No: 7782-44-7), water (deionised Milli-Q) and deuterium oxide (99.9 % D, Aldrich, CAS 7789-20-0) were dosed by means of a two stage collimated effusive beam. The first stage was pumped to a base pressure of 2.6×10^{-6} mbar and the second to 3.0×10^{-9} mbar. The beam was introduced into the chamber at a source pressure of 1.0 ± 0.05 mmHg (~1.33 mbar or 1.00 Torr) through a glass nozzle with a 1 mm inner diameter. Exiting the nozzle, the beam entered the first stage, and then expanded through a 1 mm aperture prior to entering the second stage and finally entering the chamber through a 5 mm collimation orifice. The effusive molecular beam is incident on a metal flag that shields it from the crystal and could be opened and closed during molecular beam dosing.

Both the Cu(110)-(2×1)-O added row and the Cu(110)-c(6×2)-O reconstructions were obtained following the methods reported by Bobrov & Guillemot[148] and Gruzalski et al.[125,149]. For the Cu(110)-(2×1)-O added row structure, oxygen was dosed at 298 K (RT) to ensure dissociative adsorption, followed by annealing to T_s = 493 K for a period of 1 min. The overlayers at 0.06, 0.32 and 0.50 ML atomic O were calibrated against the saturation uptake which resulted in a coverage of 0.50 ML to give the p(2×1) structure.

The Cu(110)-c(6×2)-O reconstruction was obtained by filling the chamber with oxygen to give an exposure of 1 L (1.33×10^{-8} mbar.s) for a period of 100 seconds at surface temperature T_s = 90 K, followed by a 5 minute anneal to T_S = 430 K. All of the surface reconstructions were subsequently assessed by LEED.

Water adsorption was carried out initially by exposing the clean Cu(110) crystal, the Cu(110)-c(6×2)-O reconstruction and the Cu(110)-(2×1)-O reconstructions to varying background water pressures and temperatures independently. This was done in order to obtain 'LEED phase diagrams' for H_2O on Cu(110) as a function of surface temperature T_s and background H_2O pressure p(H_2O). LEED observations were made whilst varying the background H_2O pressures, starting at 200 K with an initial base chamber pressure of < 10^{-10} mbar, up to 300 K and 1.0×10^{-7} mbar of H_2O. This was done initially at fixed temperature intervals of 20 K by varying the pressure, then at fixed H_2O pressures by increasing the temperature. These experiments were performed to assess the ordered structures formed at a given water-adsorption temperature as a function of H_2O pressure. From this data we would be able provide a clearer picture of the H-bonded surface structures formed at temperatures and pressures approaching ambient conditions. In order to avoid electron beam radiation damage the crystal was moved regularly to observe virgin areas of the overlayer structures during LEED observation.

The final set of experiments involved dosing H_2O and D_2O directly onto the aforementioned Cu-O reconstructions. This was done by means of the two stage collimated molecular effusive beam, monitoring the uptakes, subsequent overlayer structures and reaction products by TPD. This was carried out to obtain a quantitative measurement of the extent of dissociation taking place by means of TPD experiments. Particular attention was given to the hydroxyl intermediates at a given water-oxygen coverage in addition to assessing any relative temperature-dependency. D_2O was used in place of H_2O in these experiments to test for the liberation D_2. The relative H_2O and D_2O coverages and TPDs were calibrated against those obtained from the clean Cu(110) crystal to form a monolayer at $90 \leq T_s \leq 140$ K.

5.3 Results and Discussion

5.3.1 LEED images & two dimensional LEED phase diagrams elevated background H_2O on the Cu(110)

Initially we investigated the interaction of H_2O with the Cu(110) substrate by varying the background H_2O pressures and temperatures independently, recording the LEED images observed throughout. These images were then used in order to obtain 'LEED phase diagrams' for H_2O on Cu(110) as a function of surface temperature T_s and background H_2O pressure $p(H_2O)$.

It should be noted that describing these plots as a "phase diagram" is short hand; in fact kinetic factors also influence the formation of different structures and will limit what phases can form in some circumstances. This is discussed in the relevant places.

Due to the large number of LEED images required to construct these diagrams (Figures 5.15 & 5.16), only a selection of the LEED images obtained are presented here (Figures 5.11 – 5.14). A LEED image of the Cu(110)-(1×1) substrate is provided in Figure 5.10, with schematic representations of the corresponding reflections obtained throughout in order to simplify these interpretations.

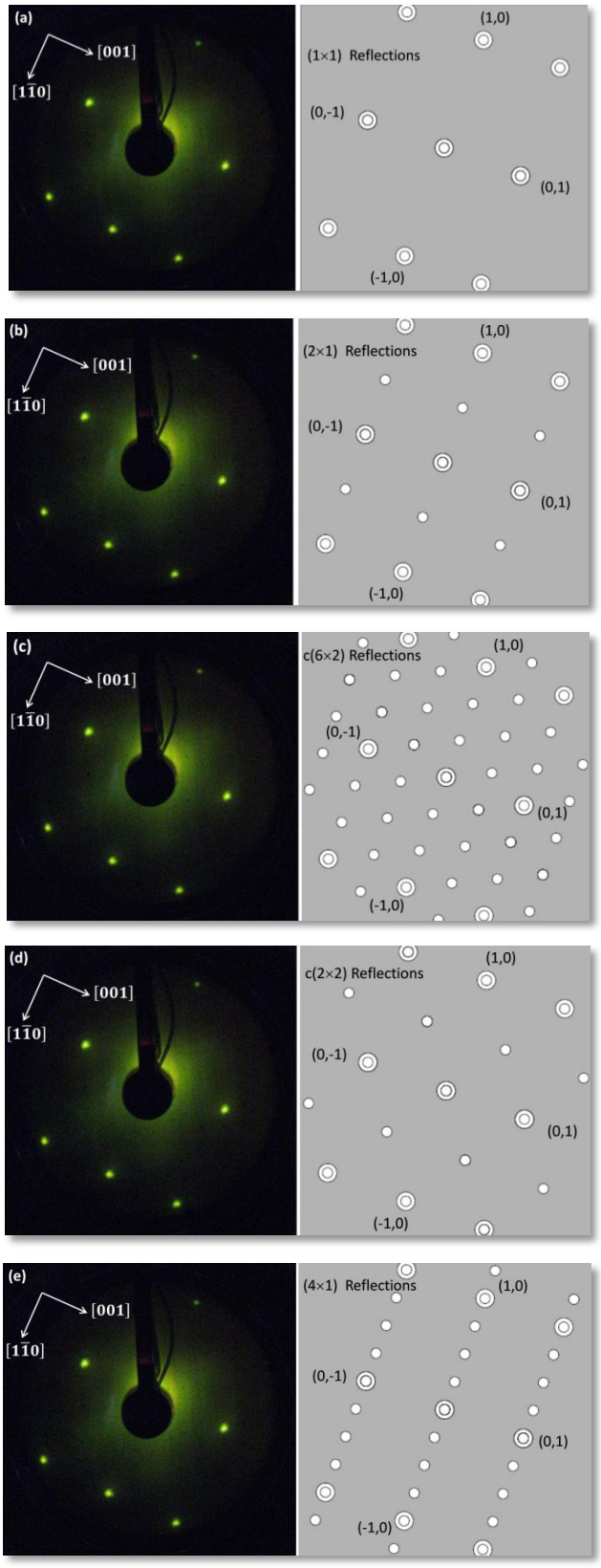

Fig. 5.10. LEED image for Cu(110)-(1×1) at 72 eV alongside schematic representations for (a) (1×1), (b) (2×1), (c) $c(6 \times 2)$, (d) $c(2 \times 2)$ and (e) (4×1) reflections.

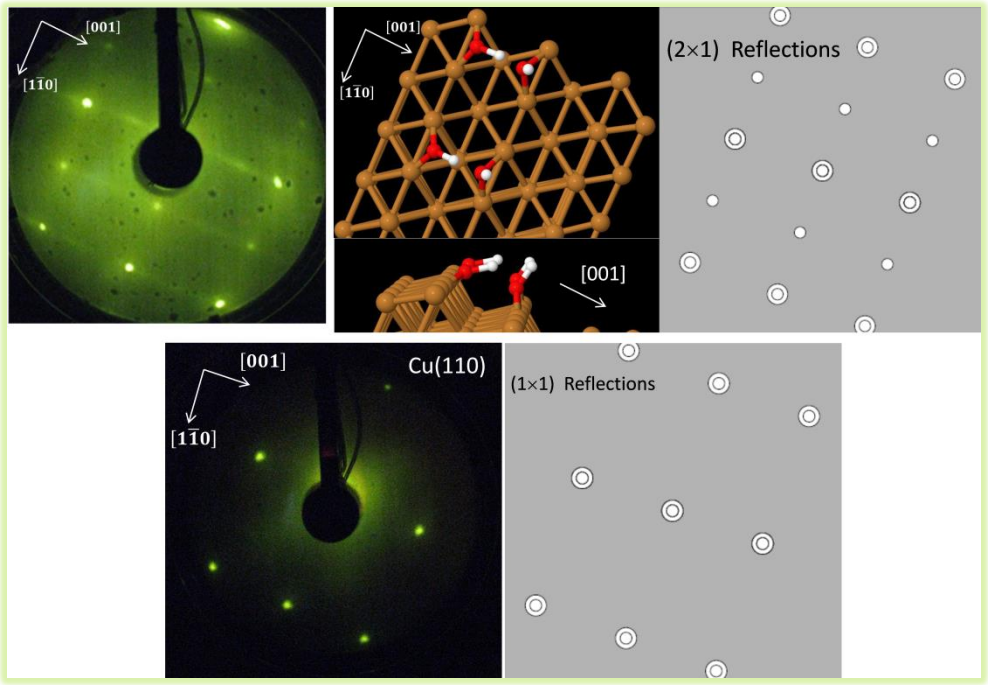

Fig. 5.11. LEED for H_2O adsorption on Cu(110) at 2.0 x 10^{-9} mbar, temperature 200 K, showing a weak (2×1) or $(2 \times n)$ pattern at 73 eV with faint streaking in the $[001]$ azimuth, indication disorder along the $[001]$. This corresponds to discrete H-bonded hydroxyl (OH) dimer chain growth along the $[1\bar{1}0]$ azimuth as illustrated, Brown (Cu substrate), Red (Oxygen) and White (Hydrogen), shown together with the schematic representation for the (2×1) reflection. LEED for Cu(110)-(1×1) at 72 eV. The LEED image for Cu(110)-(1×1) at 72 eV also shown along with the (1×1) reflections. According to Kumagai et al.[146] these dimers have different tilt angles to the surface norm; with the H-bond donor at 78.6° and the H-bond acceptor at 43.4°. The flip tunnelling motion is quenched due to stabilization by H-bonding between the dimmers.

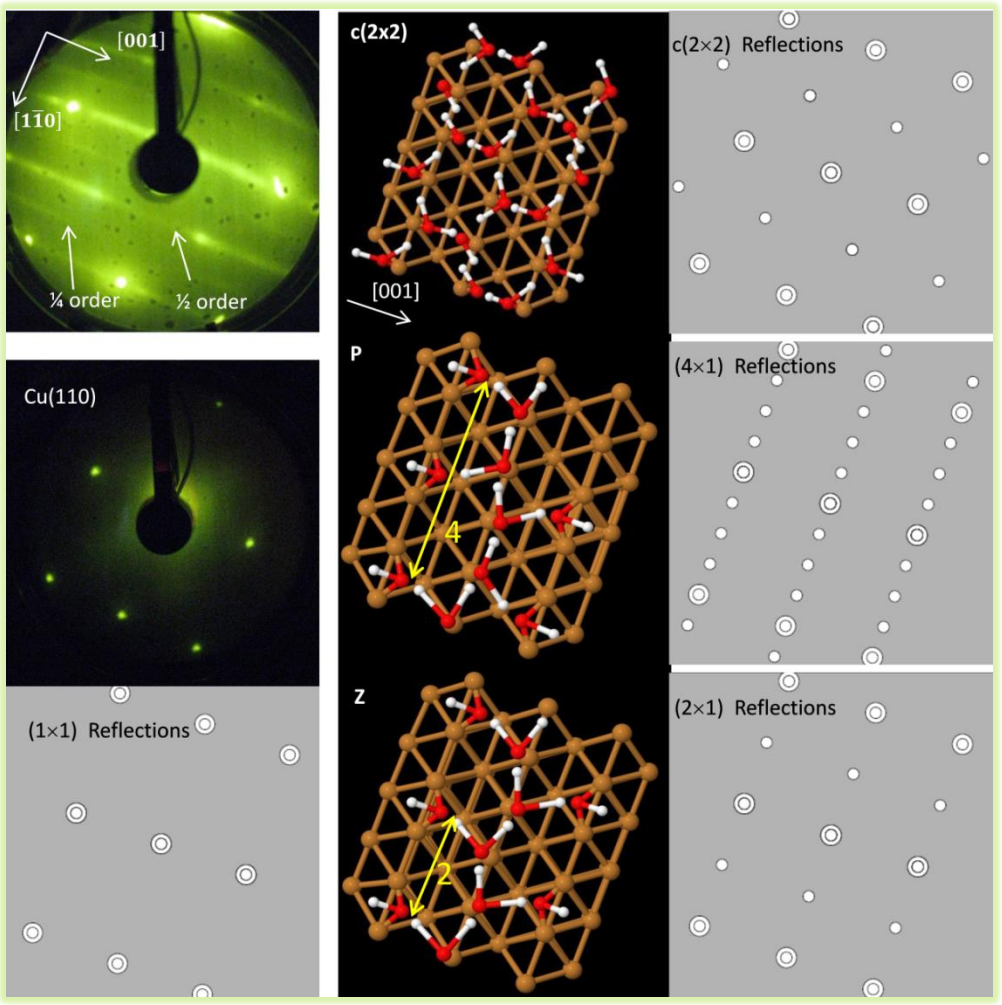

Fig. 5.12. LEED for H_2O adsorption on Cu(110) above 2.0 x 10^{-9} mbar, temperature at 200 K, showing a c(2 × 2) pattern with ½ & faint ¼ order streaking in [001] azimuth at 73 eV, corresponding to the partially dissociated H-bonded structure H_2O:OH 2:1, co-existing with Zig-zag (Z) and Pinch (P) chains growth, as shown along the $[1\bar{1}0]$ azimuth, Brown (Cu substrate), Red (Oxygen) and White (Hydrogen). Schematic representation for the $c(2 \times 2)$, (4×1) and the (2×1) reflections are shown alongside the c(2 × 2), Zig-zag (Z) and Pinch (P) chains respectively with the LEED image for Cu(110)-(1×1) at 72 eV also shown above the (1×1) reflections.

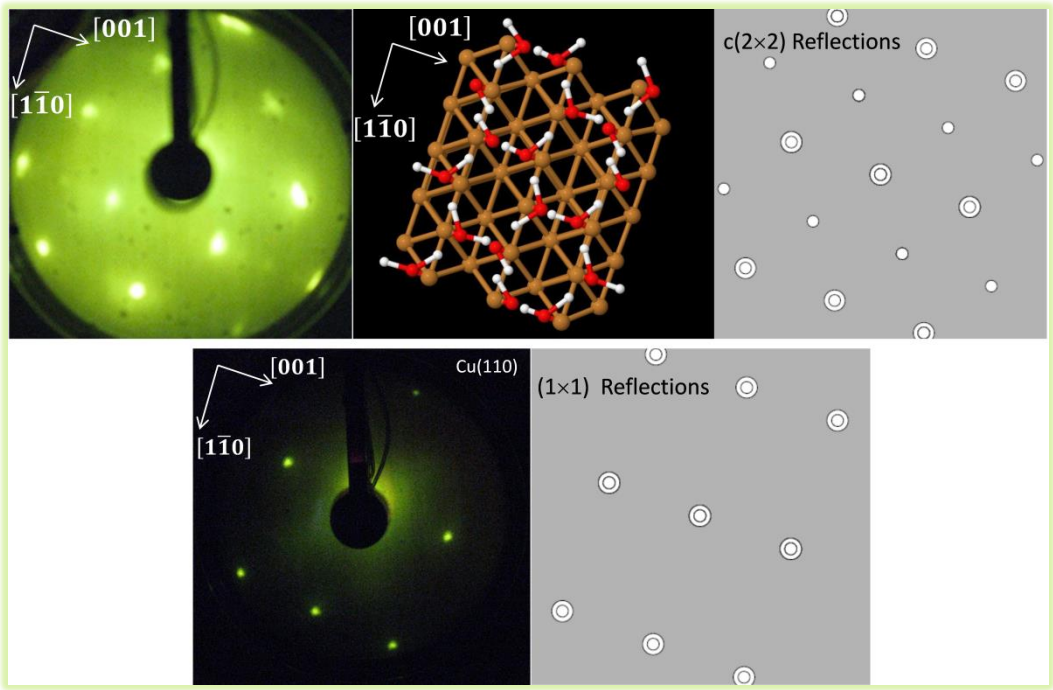

Fig. 5.13. LEED for H_2O adsorption on Cu(110) at 1.0 x 10^{-7} mbar, temperature 200 K, showing a c(2 × 2) pattern at 68 eV. This corresponds to the partially dissociated H-bonded structure H_2O:OH 2:1 as shown with Djerrum defects associated uncoordinated hydroxyl groups, Brown (Cu substrate), Red (Oxygen) and White (Hydrogen) together with the corresponding schematic representation for the $c(2 \times 2)$ reflections. The LEED image for Cu(110)-(1×1) at 72 eV is also shown together with the (1×1) reflections.

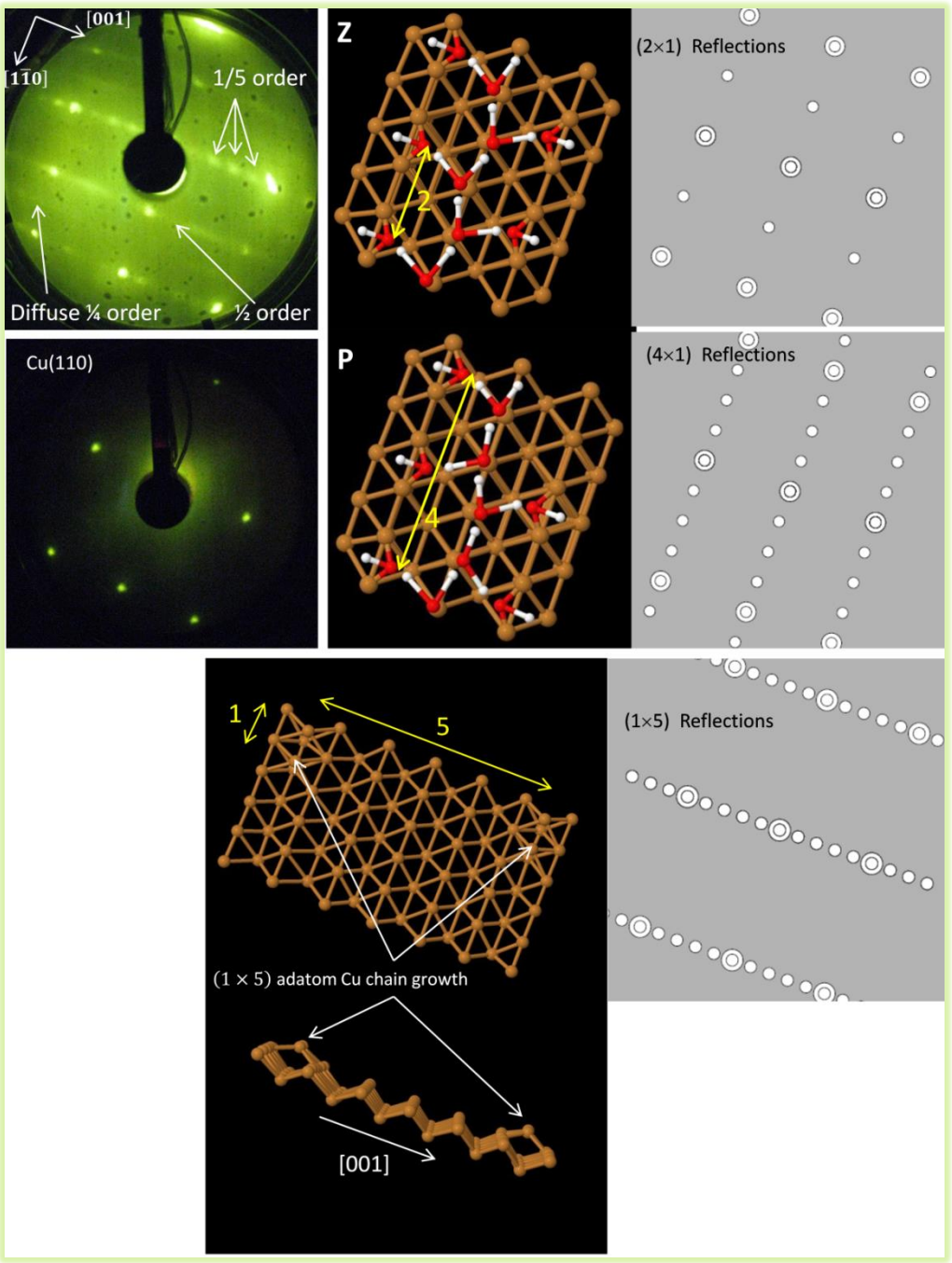

Fig. 5.14. LEED for H_2O adsorption on Cu(110) at 4.0 x 10^{-7} mbar, temperature 260 K, showing a (2 × 1) and diffuse (4 × 1) pattern with streaking in [001] azimuth at 69 eV. The ½ order streaks correspond to the Zig-zag (Z) chains & the diffuse ¼ order streaks correspond to the Pinch (P) chains growing along the $[1\bar{1}0]$ azimuth as illustrated, Brown (Cu substrate), Red (Oxygen) and White (Hydrogen). Schematic representation for (2×1) and (4×1) reflections are shown alongside each structure with the LEED for Cu(110)-(1×1) at 72 eV also shown. A schematic image of the one-dimensional monatomic Cu adatom chain growth is also shown with a $5a_{Cu}$ repeat periodicity alongside the corresponding (1×5) reflections associated with the 1/5 order spots observed in the LEED image.

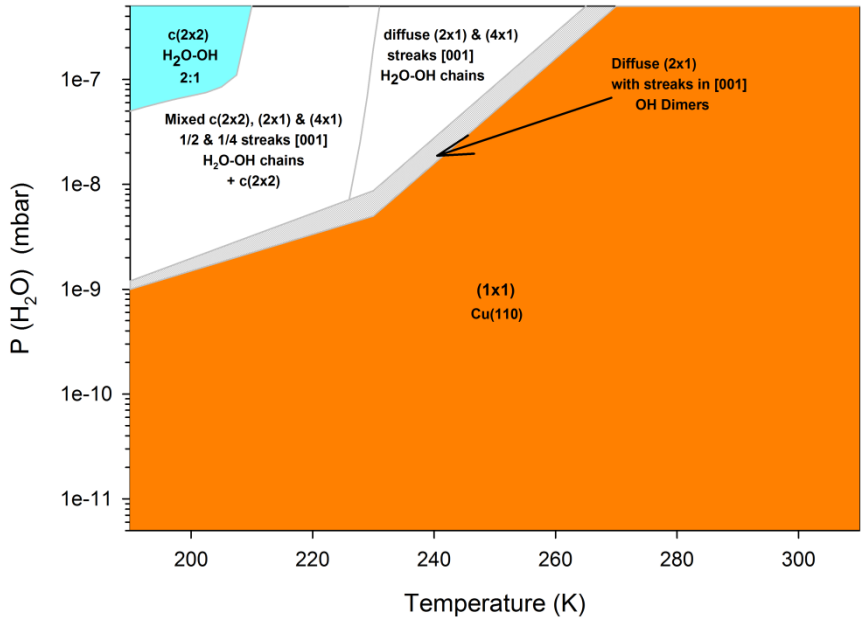

Fig. 5.15. Two dimensional LEED phase diagram for water equilibrium as a function of H_2O pressure P(H_2O) and surface Temperature. The Temperature is kept constant while varying (increasing) the pressure P(H_2O). With regions; (1×1) Cu(110) (orange), $c(2 \times 2)$, (2×1) and (4×1) with ½ & ¼ order streaks in the $[001]$ azimuth - Zigzag (Z), Pinch (P) chains with H-bonded $c(2 \times 2)$ (white), dimers (white dotted) and $c(2 \times 2)$ H_2O-OH (blue).

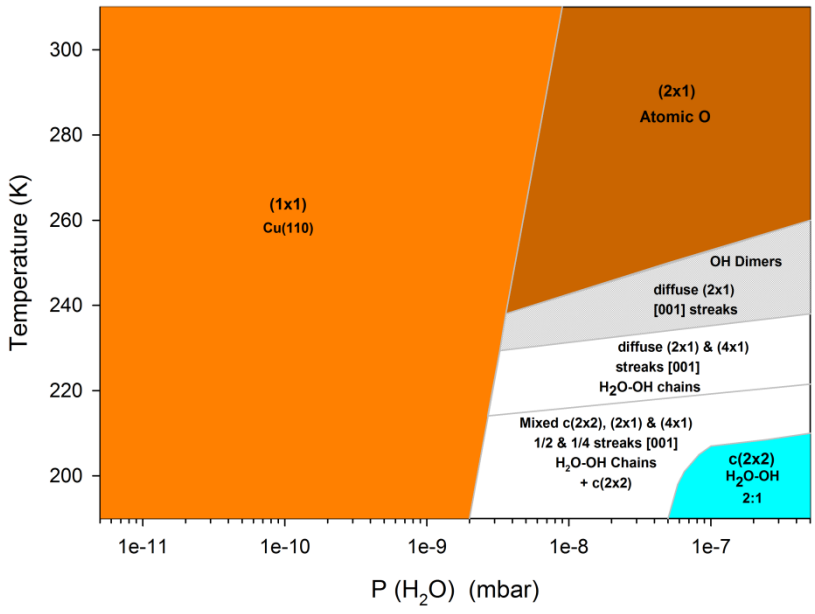

Fig. 5.16. Two dimensional LEED phase diagram for water equilibrium as a function of pressure P(H_2O) and surface Temperature. The pressure P(H_2O) is kept constant while varying (increasing) the Temperature. With regions; (1×1) Cu(110) (orange), (2×1) atomic O light (brown),$c(2 \times 2)$, (2×1) and (4×1) with ½ & ¼ order streaks in the $[001]$ azimuth - Zigzag (Z), Pinch (P) chains with H-bonded $c(2 \times 2)$ (white), dimers (white dotted), and $c(2 \times 2)$ H_2O-OH (blue).

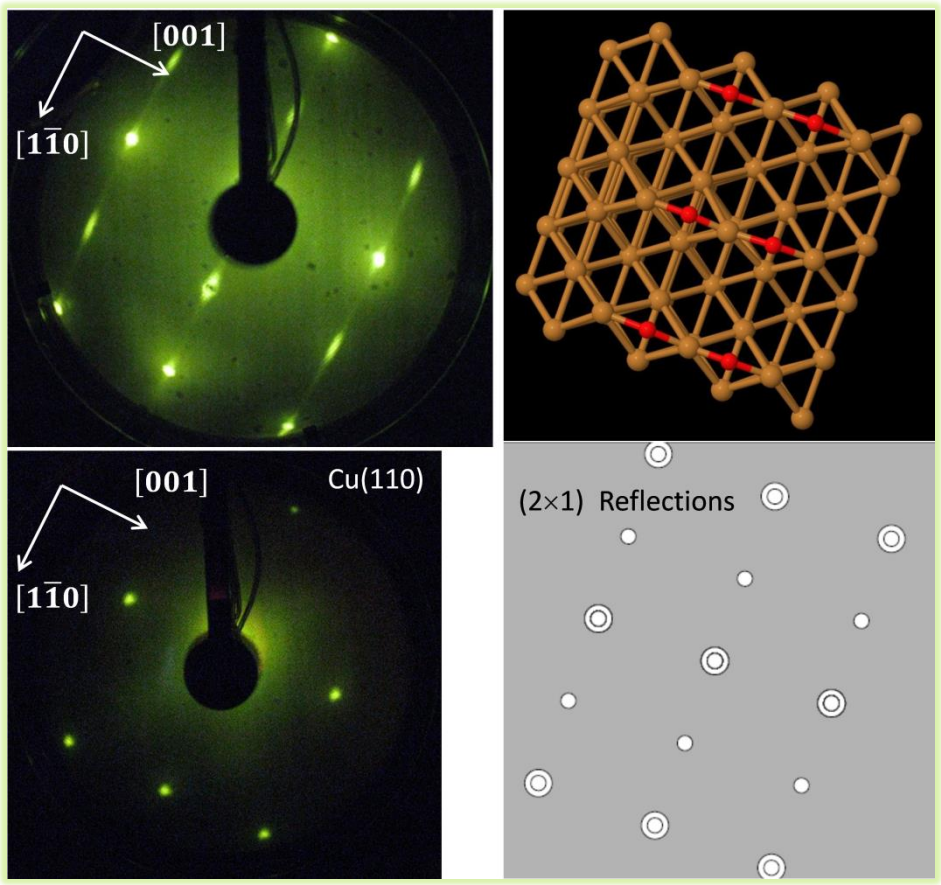

Fig. 5.17. LEED for Cu(110)-(2×1)-O overlayer streaked pattern at 68 eV with an uptake of 0.06 ML of atomic O at T_s 298 K followed by annealing to T_a = 493 K for a period of 1 min. Brown (Cu substrate) and Red (Oxygen). Schematic representation for (2×1) reflection shown below, alongside LEED for Cu(110)-(1×1) at 72 eV.

As detailed in the introduction, it is also well documented that the stability of the H-bonded H_2O-OH complexes shows increasing orders of stability with the ratios of H_2O:OH being 2:1, 1:1 and 0:1[47]. However, the exact mechanism for the formation of these H_2O-OH complexes on the clean Cu(110) at temperatures up to RT and background H_2O pressures up to near ambient conditions is less well understood. The key parameters that control the rate of formation of each of these structures are the activation energy $\left(E_a^{diss}\right)$, associated with the kinetic stability and the free energy (ΔG), associated with the thermodynamic stability of the phases. For this reason,

we present here an interpretation of H_2O/OH structures in two separate 2D LEED phase diagrams constructed between the pressure ranges 7.5 x 10^{-12} - 7.5 x 10^{-8} Torr (1.0 x 10^{-11} – 5.0 x 10^{-7} mbar) and temperatures 200 - 300 K. First the wetting properties were assessed by maintaining a constant temperature whilst increasing the background water pressure (Figure 5.15) and secondly by keeping the background pressure constant and increasing the temperature (Figure 5.16). Note, that the phase diagrams are constructed in accordance with keeping the independent variable on the x-axis.

Before interpretation of the LEED patterns, it is important to set out the variety of surface reaction mechanisms that could occur when H_2O interacts with the Cu(110)-(1×1) substrate. A few of these are considered in the following reaction schemes listed (Reactions 5.2 – 5.7).

5.3.1.1 Reaction mechanisms

$$H_2O_{(g)} \rightarrow H_2O_{(ads)} \tag{5.2}$$

$$H_2O_{(g)} \rightarrow H_2O_{(ads)} \rightarrow H_{(ads)} + OH_{(ads)} \tag{5.3}$$

$$2H_2O_{(g)} \rightarrow 2H_2O_{(ads)} \rightarrow H_{(ads)} + OH_{(ads)} + H_2O_{(ads)} \tag{5.4}$$

$$H_2O_{(g)} + M \rightarrow M - H_2O_{(complex)} \rightarrow M_{(x)}O_{(y)} + /or\ M_{(n)}OH_{(m)} + /or M_{(r)}H_{(s)} \tag{5.5}$$

Autocatalysis;

$$H_2O_{(g)} + O_{(ads)} \rightarrow 2OH_{(ads)} \rightarrow 2H_{(ads)} + 2O_{(ads)} \tag{5.6}$$

or,

$$2H_2O_{(g)} + O_{(ads)} \rightarrow H_2O_{(ads)} + 2OH_{(ads)} \tag{5.7}$$

As detailed in the introduction, at low coverage and temperature, H_2O adsorbs molecularly as monomers, dimers, trimers, etc., on the Cu(110)-(1×1) substrate. These molecules have been found to grow into extended H-bonded 1D, 2D or 3D intact wetting structures, according to Reactions 5.2. At higher temperatures and pressures, the equilibrium between molecular adsorption/desorption and thermal dissociation is shifted towards dissociation (Reaction 5.3). Assuming partial dissociation occurs, this could leave both atomic hydrogen (H) and hydroxyl (OH) on the surface, with the possibility of the OH forming H-bonded dimers. Alternatively, thermally activated partial dissociative adsorption gives rise to 1D, 2D or 3D, (partially) dissociated H-bonded H_2O-OH network structures where the OH stabilises H_2O at higher temperatures. In both cases one would expect atomic H to either remain on the surface or recombine and desorb molecularly above 200 K.

According to a study by Lousada et al.[150], where DFT was used to assess the thermodynamic splitting of H_2O on Cu(110), H_2 desorbs from the surface spontaneously. These DFT calculations were based on experimental results conducted at 298 K. This hypothesis of spontaneous H_2 desorbing after H_2O deposition is further supported by an earlier study conducted by Anger et al.[151]. Here high molecular beam energies were used in order to achieve dissociative adsorption. Following flash desorption, the desorption spectra showed H_2 desorbing from the Cu(110) surface across an extensive range, starting at temperatures c.a. 250 K and peaking at 325 K.

Thermally activated dissociation can also be complete, initiating by way of Reaction 5.3. Here the H_2O dissociates initially into atomic H and OH, with the OH then undergoing further dissociation into atomic H and atomic O. Again, one would expect the atomic H to either remain on the surface or recombine and desorb as molecular H_2. From this, the atomic O would then give rise to the dissociation of molecular H_2O migrating on the surface to set the cycle of autocatalysis, as shown in Reactions 5.6 and 5.7.

A less common reaction, which is much more commonly associated with elements outside of the transition groups VIIIB & IB, is the reaction of H_2O directly with the metal substrate to form stable bulk oxides, hydroxides and/or hydrides (Reaction 5.5).

These surface reaction mechanisms will be used in order assist in the interpretation of the structures presented in the next two sections (5.3.1.2 & 5.3.1.3). Section 5.3.1.2 details a breakdown of the interpretation of structures seen whilst keeping the temperature constant at set intervals between 200 and 300 K and increasing the pressure of H_2O. Section 5.3.1.3 details a breakdown of the interpretation of structures seen whilst keeping the background H_2O pressure constant whilst increasing the temperature.

5.3.1.2 Two dimensional LEED phase diagram for constant temperature varying (increasing) pressure P(H_2O).

Figure 5.15 shows a summary of all of the LEED images taken whilst maintaining a constant temperature at set intervals between 200 and 300 K and increasing the pressure. At the initial temperature of 200 K and a base pressure of < 10^{-10} mbar, the Cu(110) surface retains a (1 x 1) LEED pattern as expected, as shown in Figure 5.10 and Figure 5.15 (orange region). Following the increase of the background water pressure slightly above 10^{-9} mbar, the LEED pattern initially transformed into a faint (2×1) pattern with steaks in the $[001]$ azimuth as shown in Figure 5.11 and Figure 5.15 (white dotted region). As discussed earlier, when streaking in a LEED pattern is continuously observed on changing the electron energy, it corresponds to a 1D object at the surface perpendicular to the streak. Just to reiterate, whilst pure hydroxyl dimers have a weak tendency to associate into chains, they are usually only found either as isolated OH monomers or dimers aligned along the $[001]$ azimuth regularly spaced no closer than $2a_{Cu}$ along the $[1\bar{1}0]$ direction. This gives rise to a $(2 \times n)$ LEED pattern, while the lack of dimer order along the $[001]$ direction gives rise to the streaking observed in the LEED patterns. As a result we can assign the initial diffuse (2×1) LEED pattern to the (formation of) hydroxyl dimers (OH) formed by thermal activated, partial dissociation of H_2O, according to Equation 5.3. Although atomic O forms the well known (2×1)-O reconstruction on the Cu(110) surface, it is very unlikely under these conditions that this faint (2×1) pattern could be attributed to atomic O alone. A partial coverage of atomic O alone

would produce a much stronger (2×1) pattern with streaks perpendicular in the $[1\bar{1}0]$ azimuth as shown in Figure 5.17.

Following the (2×1) streaked LEED pattern the diffraction pattern transformed into a mixed streaked $c(2 \times 2)$, (2×1) and (4×1) as shown in Figure 5.12 the moment the pressure was increased to 2.0 x 10^{-9} mbar. This diffraction pattern showed clear ½ & ¼ order streaks again in the $[001]$ azimuth (white region on Figure 5.15 & Figure 5.12). The initial dissociation of H_2O into hydroxyl dimers greatly enhanced the stabilization of H_2O at this higher pressure forming H_2O-OH units eventually transforming into chains growing along the $[1\bar{1}0]$ with the partially dissociated (H_2O:OH 2:1) H-bonded structure. Similar observations of chain growth were observed by Lee et al.[136] and Ammon et al.[152], at these temperatures. The fact that these chains have irregular branches as illustrated in the surface structural image Figure 5.12 with a $2a_{Cu}$ repeat (periodicity of 5.1 Å) for the Z chain structure and $4a_{Cu}$ repeat (periodicity of 10.2 Å) for the P chain structure, this produces ¼ and ½ order streaks as seen in the $[001]$ azimuth. It is noticeable that these chains coexisted with a partial coverage of the partially dissociated (H_2O:OH 2:1) H-bonded structure due to the appearance of the diffuse $c(2 \times 2)$ LEED image spots.

To summarize, the transformation from a streaked (2×1) diffraction pattern into a streaked $c(2 \times 2)$ (2×1) and (4×1) pattern occurs as a result of the dimers stabilizing the migrating H_2O molecules (Equation 5.4). This causes the production of these two closely related chains, both having a 1:1 H_2O:OH ratio. The streaks are again an indication of long range disorder along the $[001]$ direction due to partial coverage with ordered chain growth in the $[1\bar{1}0]$ direction. The interpretations for these chain structures are also based on findings by Forster et al.[127] and Shi et al.[129], who found similar chain structures by STM and concluded both of these to have similar stability composed of H_2O and OH with a ratio of 1:1. Incidentally, in their research these structures were found within a slightly lower temperature range of 185 to 200 K. This was due to the fact that their research was conducted at UHV conditions and not with the background H_2O in equilibrium with the surface.

As expected clearly the higher pressure pushes the stabilization and formation of structures to higher temperatures.

Both the hydroxyl dimers and the Z chains exhibited diffuse $(2 \times n)$ LEED patterns with streaking in the $[001]$ azimuth. However we were able to make a distinction between these two structures based on the coexistence of the P chains appearing with the Z chains. The two chains structures together always produced a mixed $(2 \times n)$ and $(4 \times n)$ LEED patterns with streaking in the $[001]$ azimuth.

Increasing the pressure to 5.0 x 10^{-8} mbar, the diffuse $c(2 \times 2), (2 \times 1)$ and (4×1) LEED pattern exhibiting ½ & ¼ order streaks transformed into a clear $c(2 \times 2)$ LEED pattern (blue region Figure 5.15), which remained up to 5.0 x 10^{-7} mbar. Here we recognize this to be the partially dissociated H-bonded structure as shown in Figure 5.13. This was formed as a result of the increasing H_2O pressure transforming the 1D chains into a 2D $2H_2O$:1OH H-bonded structure. Although the structures here were exposed to low energy electrons, as stated in the experimental section, observations were carried out on virgin areas of the sample to minimize the effects of electron radiation damage. Furthermore, it was very unlikely that this (7×8) 2D H-bonded structure could exist at these temperatures due to thermal dissociation at temperatures ≥ 150 K[46,8,142,147].

The temperature of the crystal was then increased to 220 K and then subjected to identical pressure increases to the initial temperature of 200 K. With this change in temperature there is a significant change in the thermodynamic stability of the structures. Onset of the partially dissociated hydroxyl dimers (Fig. 5.11) occurs at a higher pressure of 3.0 x 10^{-9} mbar as opposed to just above 10^{-9} mbar at 200 K. Formation of the P and Z chains coexisting with a partial coverage of the partially dissociated H-bonded (H_2O:OH 2:1) structure occurred similarly at the higher pressure of 5×10^{-9} mbar as opposed to 2.0×10^{-9} mbar at 200 K. Clearly with this increase in temperature there was a shift in the free energy of formation for these P and Z chains along with the H-bonded structure. In addition, at this temperature (220 K) it was no longer kinetically stable for the partially dissociated (H_2O:OH 2:1) H-bonded structure to exist completely at the

highest pressure of 5×10^{-7} mbar. Just to reiterate, the stability of these H-bonded H_2O-OH complexes show an increase in stability with the ratios 2:1, 1:1 and 0:1 (H_2O:OH). As a result, the partially dissociated H-bonded $c(2 \times 2)$ structure is not as stable at temperatures ≥ 220 K. This however does not mean the partially dissociated (H_2O:OH 2:1) H-bonded structure would not be kinetically stable at higher H_2O pressures. Although the partially dissociated H-bonded $c(2 \times 2)$ structure has a higher H-bond coordination than the P and Z chain structures (ca. 3 as opposed to 2), formation of this structure gives rise to a loss of the favoured bridge adsorption sites for OH as shown in Figures 5.5 and 5.6. As a result of this the structure has a lower binding energy[127].

Increasing the temperature to 240 K and subjecting the crystal surface to the same pressure increase as before produced yet again a shift in the onset to a slightly higher pressure. At this temperature the onset of partial dissociation for the hydroxyl dimers OH occurred at the higher pressure, 1.7 x 10^{-8} mbar followed by a combination of P and Z chains forming without the partially dissociated (H_2O:OH 2:1) H-bonded structure at the higher pressure of 2.8 x 10^{-8} mbar as shown Figure 5.14.

The shift in the onset persisted at 260 K, with the dimers forming at a higher pressure of 1.6 x 10^{-7} mbar, followed by the formation of both chain structures at 2.6 x 10^{-7} mbar. As shown in Figure 5.14 the distinction was made based on the diffuse (4×1) streaks, labelled as diffuse ¼ order streaking, which corresponded to the P chains. Without these ¼ order streaks, the (2×1) LEED patterns corresponding to the dimers and the Z chains would be indistinguishable. It is also noticeable that there is minor splitting of the streaks, which could be attributed to the formation of chains simultaneously at the step edges and terraces. This was particularly noticeable in STM images taken by Shi et al.[129] where extensive restructuring of the surface was observed accompanied by chain growth. There are numerous studies that clearly show that the Cu(110) substrate has a direct influence on the structure and dissociation of H_2O giving rise to a variety of partially dissociated H-bonded structures. However, there is very little to suggest that these structures can induce restructuring of the Cu(110)

surface. Within a similar temperature range of 180 to 220 K, Shi et al. observed the formation of 1D monatomic Cu chains running along the $[1\bar{1}0]$ azimuth when the surface was covered with similar P and Z chain structures. These 1D monatomic Cu chains (or wires) were not observed however when the Cu(110) crystal was heated under UHV conditions in the absence of H_2O, nor when molecular H_2O alone was present. This indicates that atomic Cu wires form as a result of the interaction with these two partially dissociated P and Z chain structures. It was particularly noticeable that the formation of these wires paralleled with the dissociation of H_2O into H and OH and decreased with H_2O desorption.

As stated the formation of these mixed chain structures produced a mixed $(2 \times 1)/(4 \times 1)$ LEED pattern with streaks in the $[001]$ azimuth corresponding to the $2a_{Cu}$ repeat periodicity for the Z chain structure and $4a_{Cu}$ repeat periodicity for the P chain structure. As a result of this it was very difficult to obtain a strong LEED pattern directly associated with the formation of the monoatomic chains. This was mainly due to the streaking associated with the chain's long range disorder along the $[001]$ azimuth. It is noticeable in Figure 5.14 that there are a few diffuse 1/5 order spots which are probably associated with the monatomic Cu adatoms chains in the (1×5) configuration. According to Shi et al. the monatomic wires were observed by STM at both $5a_{Cu}$ and $2a_{Cu}$ repeat periodicities whereby one would expect to observe LEED patterns of (1×5) and (1×2) respectively. Shi et al. observed a maximum Cu chain growth at around 200 K, which subsequently decreased above 220 K. These findings parallel with our observations for the P and Z chain structures, as no structures were observed when the tests were performed at temperatures above 260 K.

All of the tests conducted at the higher temperatures of 280 and 300 K showed no evidence of any dissociative reactions with the surface maintaining a (1×1) LEED pattern throughout as shown in Figure 5.10. Clearly at these temperatures and pressures it is both kinetically and thermodynamically unfavourable for the formation of any of the H-bonded structures, which also prevents H_2O dissociation.

5.3.1.3 Two dimensional LEED phase diagram for constant pressure P(H_2O) varying (increasing) temperature.

Figure 5.16 shows a summary of all the LEED patters taken whilst maintaining a constant background H_2O pressure and increasing the temperature. At a glance it is clear that within the temperature range 200 – 300 K and pressure range 1.0×10^{-11} – 1.0 x 10^{-9} mbar, there was no observable adsorption or dissociation on the crystal (orange region). Although there is an obvious change in the kinetics with each pressure increase the collision rate and hence the kinetics remains constant at each individual pressure. As a result with no structures forming at the lowest temperature (200 K) within these pressure ranges (pressure range 1.0×10^{-11} – 1.0 x 10^{-9} mbar), it is expected that no structures were likely to develop with the temperature increased to 300 K. Within these pressure and temperature ranges the LEED patterns and structures formed were practically identical to those observed whilst keeping the temperature constant at set intervals and increasing the pressure (Figure 5.15) in section 5.3.1.2.

A visible change in the kinetics occurred with the pressure increased to 2.0 x 10^{-9} mbar. Here, thermally activated partial dissociation occurred with stabilization of the P and Z chains up to 5.0×10^{-8} mbar (white region). This was evident from the mixed diffuse $c(2 \times 2), (2 \times 1)$ and (4×1) LEED pattern exhibiting ½ & ¼ order streaking in the $[001]$ azimuth, similar to that observed in the LEED pattern shown in Figure 5.12. The partially dissociated H-bonded structure (H_2O:OH 2:1) formed when the pressure was increased above 5.0 x 10^{-8} mbar (blue region) was evident from the formation a $c(2 \times 2)$ LEED pattern (Figure 5.11).

As would be expected with an increase in temperature the partially dissociated structure converted initially into P and Z chains coexisting with the partially dissociated H-bonded structure and then completely into P and Z chains (white region). This was due to the increase in temperature destabilizing the excess H_2O, with a further increase in temperature leaving dimers on the surface above 230 K (white dotted region). Increasing the temperature with the dimers on the substrate between 3.7×10^{-9} –

5.0×10^{-7} mbar, resulted in recombinative desorption of H_2O, leaving atomic O on the surface (brown region) detailed by Equation 5.8.

$$OH_{(ads)} + OH_{(ads)} \rightarrow H_2O_{(ads)} + O_{(ads)} \rightarrow H_2O_{(g)} + O_{(ads)} \quad (5.8)$$

This was evident by the LEED pattern changing from a faint (2×1) pattern as shown in Figure 5.11 with the steaks in the $[001]$ azimuth, to a much clearer (2×1) with the streaks perpendicular in the $[1\bar{1}0]$ azimuth as shown in Figure 5.17.

Comparing the two LEED phase diagrams it is clear that the main difference is the formation of atomic oxygen when keeping the background H_2O pressure constant and increasing the temperature (brown region Figure 5.16). This occurred as a result of the extent of dissociation occurring initially at pressures > 3.7×10^{-9} mbar and low temperatures. A subsequent increase in temperature with dissociated structures on the surface resulted in atomic O being left on the surface as the structures destabilize with the loss of H_2O. This did not occur in the results observed whilst keeping the temperature constant and increasing the pressure (Figure 5.15, section 5.3.1.2.) due to the initial difference in coverage of the structures.

Although the strong attractive interaction between the mixed OH and H_2O dramatically slowed down the desorption kinetics, hence increasing the stability of the various water hydroxyl phases, at no point did any of these structures appear to be stable at room temperature from the results obtained on the clean Cu(110) substrate. Based on the LEED phase diagram (Figure 5.16), above 260 K and 5.0×10^{-7} mbar, only atomic O was present on the surface. However, when looking at the region of thermodynamic stability for the hydroxyl dimers at pressures in excess of 5.0×10^{-7} mbar, mixed OH and H_2O may well be stable up to and beyond room temperature. With this being the case, the next section deals with the introduction of atomic oxygen prior to any adsorption of H_2O. This was done to establish whether or not the hydroxyl species produced as a result of the pre-adsorbed atomic oxygen reacting with H_2O was able to stabilize H_2O up to room temperature.

5.3.2 Oxygen reconstructions & the two-dimensional LEED phase diagrams for elevated background H_2O on the oxygen reconstructions.

5.3.2.1 Oxygen reconstructions

Here we give a brief outline of the oxygen reconstructions prepared in the way detailed in the experimental section. We have prepared (as detailed) reconstructions from the well-known (2×1) added-row reconstruction at coverage 0.06, 0.32 & 0.5 ML up to a saturated coverage of 0.66 ML for the $c(6 \times 2)$-O reconstruction.

It has been documented that H_2O when adsorbed with small amounts of pre-adsorbed atomic O will form hydroxyls[142]. However, according to Guillemot and Bobrov[11], the hydroxyl species produced by reaction with pre-adsorbed atomic O has a different reactivity to that produced by direct dissociation of H_2O, while its mobility on the substrate surface enables the formation of H_2O-OH complexes stable up to RT. Hydroxyl species produced by direct dissociation apparently do not have the same mobility on the surface and there are not able to stabilize H_2O-OH complexes stable up to RT. Therefore by varying the atomic O pre-coverage prior to reacting with H_2O, this should provide us with an opportunity to access whether it changes the stability of the complexes formed at higher temperatures. Again, this was assessed by means of LEED in addition to TPD which provided a desorption profile in the range 200 – 300 K.

As shown in Figures 5.18 to 5.20, oxygen chemisorption on the Cu(110) is accompanied by significant restructuring of the surface. This produces the well-known (2×1) added-row reconstruction (AR) (often referred to as the missing-row (MR) reconstruction)[153], illustrated schematically in Figure 5.21. The streaks observed in the $[1\bar{1}0]$ direction for both the 0.32 and 0.06 ML are due to the low coverage of atomic O creating less order in the spacing of the (2×1)-O chains along the $[001]$ azimuth.

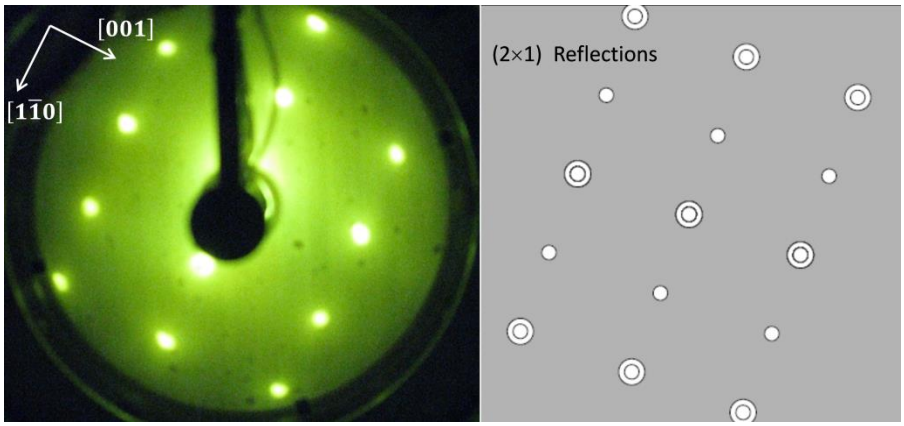

Fig. 5.18. LEED for Cu(110)-(2×1)-O overlayer pattern at 74 eV from saturated coverage 0.5 ML at T_s 298 K followed by annealing to T_a = 493 K for a period of 1 min alongside schematic representation for (2×1) reflections.

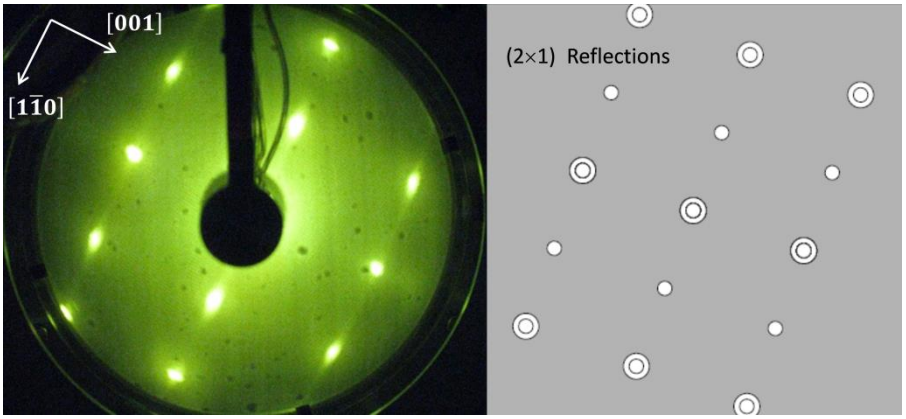

Fig. 5.19. LEED for Cu(110)-(2×1)-O overlayer pattern at 72 eV with an uptake of 0.32 ML at T_s 298 K followed by annealing to T_a = 493 K for a period of 1 min with streaking of ½ order spots along the $[1\bar{1}0]$ alongside schematic representation for (2×1) reflections.

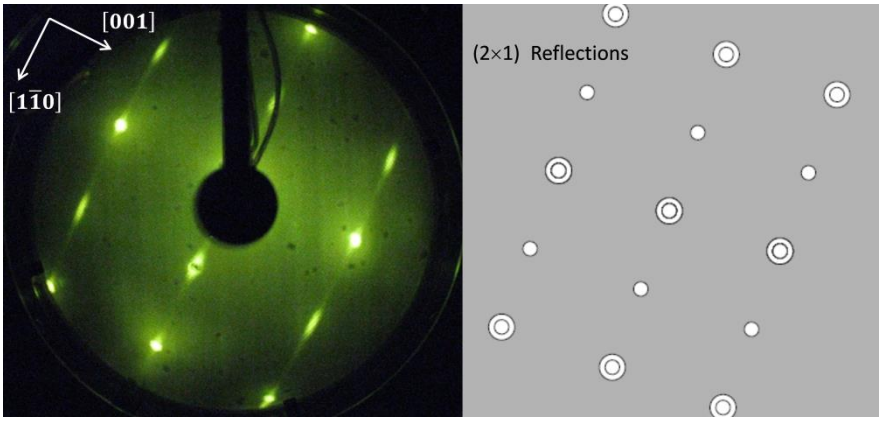

Fig. 5.20. LEED for Cu(110)-(2×1)-O overlayer pattern at 68 eV with an uptake of 0.06 ML at T_s 298 K followed by annealing to T_a = 493 K for a period of 1 min with excessive streaking of ½ order spots along the $[1\bar{1}0]$ alongside schematic representation for (2×1) reflections.

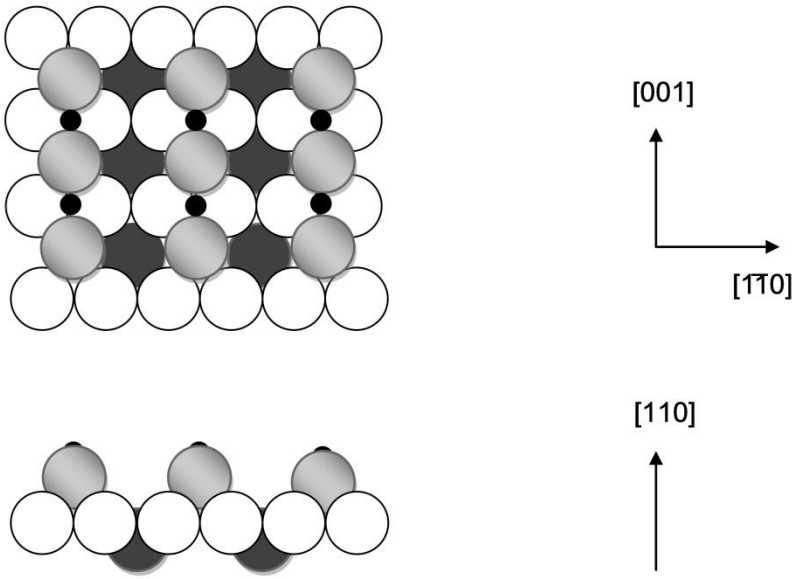

Fig. 5.21. Schematic reconstruction models for Cu(110)-(2×1)-O Added/ Missing-row model. The light grey circles represent the surface copper atoms, the empty circles the atoms beneath the surface and the dark grey the third layer. The small black circles represent the oxygen adatoms.

As with the (2×1) added-row reconstruction the $c(6 \times 2)$ LEED pattern shown in Figure 5.22 is formed by Cu adatoms diffusing from step edges and combining with the O adatoms freely diffusing on the surface. However, due

to the excess of O adatoms, further migration of Cu adatoms gives rise to the formation of a superstructure with an overall three-dimensional structure and coverage of 2/3 ML. As illustrated in Figure 5.23, this superstructure contains two Cu-O-Cu-O chains for every three $[1\bar{1}0]$ lattice spacings as opposed to one Cu-O-Cu-O chain for every two $[1\bar{1}0]$ lattice spacings with the added-row reconstruction[154,155]. This reconstruction was achieved by exposing the crystal to an extremely high background concentration of oxygen (1 L ≡ 1.33 × 10^{-8} mbar.s) for an extended period of 100 s at a surface temperature of T_s = 90 K. Uptake at this temperature is molecular, and much higher than that at 298 K, and subsequent annealing to T_S = 430 K produces dissociation and the formation of the $c(6 \times 2)$-O reconstruction.

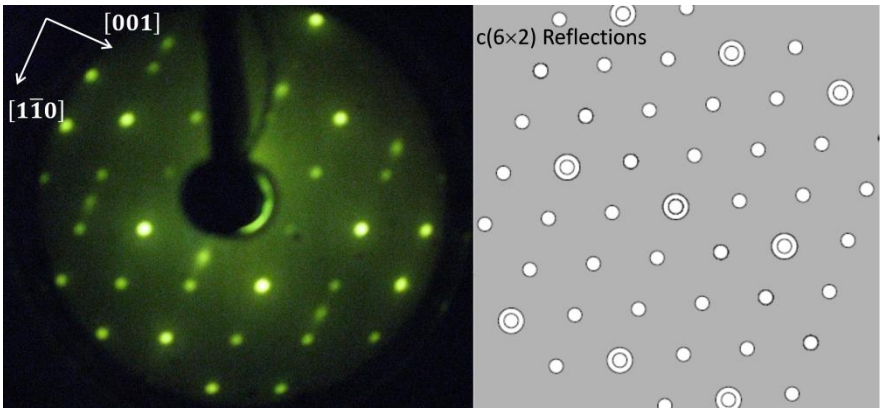

Fig. 5.22. LEED for Cu(110)-$c(6 \times 2)$-O overlayer pattern at 70 eV. Produced with a high background concentration of oxygen of 1 L ≡ 1.33 × 10^{-8} mbar.s for an extended period of 100 s at surface temperature T_s = 90 K followed by annealing to T_a = 430 K for a period of 5 min, alongside schematic representation for c(6×2) reflections.

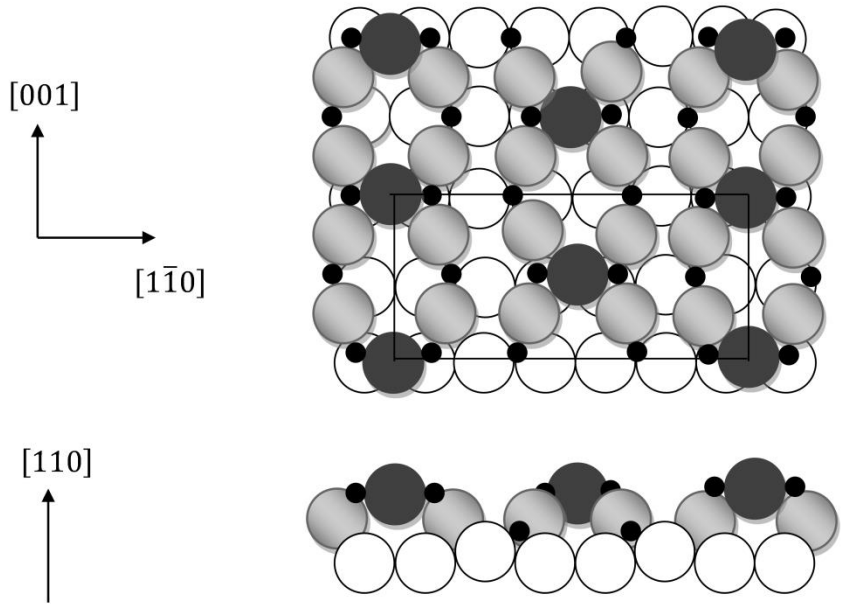

Fig. 5.23. Schematic reconstruction model for Cu(110)-$c(6 \times 2)$-O, with unit cell. The dark grey circles represent the topmost super copper adatoms, the light grey circles the second layer copper atoms and the empty circles the third layer. The small black circles represent the oxygen adatoms.

The following sections details a complete summary, in the form of two dimensional LEED phase tables recorded for all of the LEED images taken on the atomic O pre-covered surfaces reacting with H_2O at elevated pressures from < 10^{-10} up to 5.0×10^{-7} mbar inclusive. Although pre-adsorbed atomic O was found to be reactive with water forming various complexes, the reactivity dropped off significantly with increased surface coverage.

Even though the 0.5 ML reconstruction showed significant reactivity towards H_2O, it was not possible to distinguish the H-bonded complex formed clearly due to the extensive surface coverage of atomic O. The LEED patterns obtained at this coverage (0.5 ML) from the experiments conducted with a constant background H_2O pressure > 1.0×10^{-8} mbar, resulted in extensive reconstruction at temperatures > 230 K. This occurred from the recombinative desorption of H_2O depositing further atomic O on the surface which resulted in the formation of a $c(6 \times 2)$ mixed with a (2×1) diffraction pattern. The saturated 0.66 ML reconstruction was found to be un-reactive with H_2O at all background pressures up to 5.0 x 10^{-7} mbar and temperatures

within the range 200 - 300 K. As a result the summary presented here relates only to the (2×1)-O reconstructions at the 0.06 and 0.32 ML coverage, omitting that of the (2×1)-O reconstruction at 0.50 ML and c(6×2) reconstruction at 0.66 ML.

The main difference between the clean Cu(110), summarised in Figures 5.15 and 5.16, and the atomic O reconstructions shown in the Figures 5.24 and 5.25, was the increased reactivity with H_2O at much lower pressures. The clean surface was found to initially form dimers which subsequently stabilized more H_2O, giving rise to 1:1 H_2O:OH chain structures, followed by partially dissociated 2:1 H_2O:OH H-bonded structures. The surface appeared to be more reactive with H_2O with atomic O on the surface due to the formation of the H-bonded structures at much lower temperatures compared to the clean Cu(110) surface.

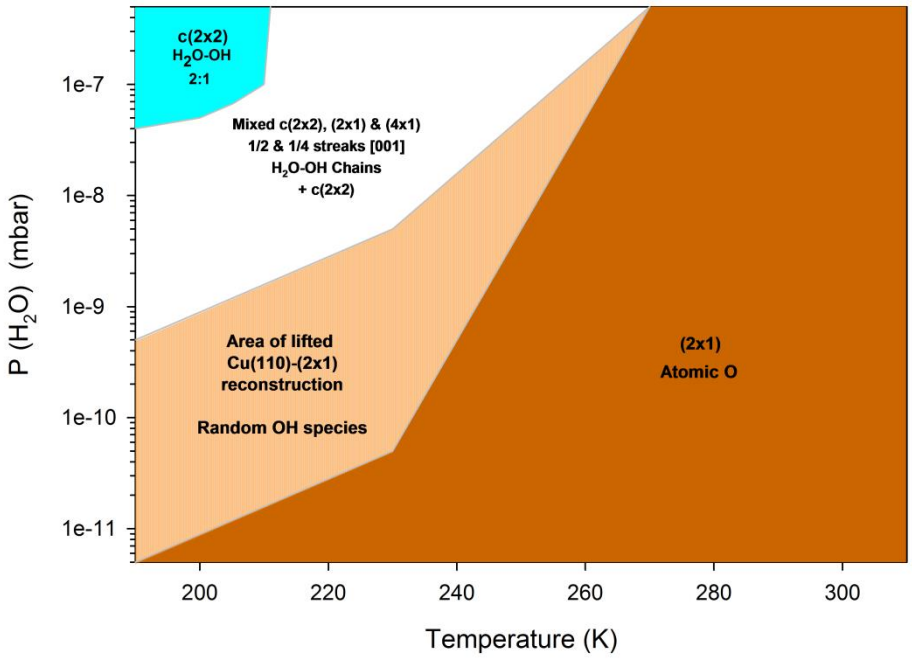

Fig. 5.24. The two dimensional LEED phase diagram for water equilibrium as a function of H_2O pressure P(H_2O) and surface temperature. The temperature is kept constant while increasing the H_2O pressure P(H_2O). With regions; 0.06 and 0.32 ML Cu(110)-(2×1)-O reconstruction (brown), Mixed $c(2 \times 2)$, (2×1) and (4×1) with ½ & ¼ order streaks in the $[001]$ azimuth - Zigzag (Z) & Pinch (P) chains with $c(2 \times 2)$ H-bonded (white), lifted (2×1)-O producing OH species (orange stripe) and $c(2 \times 2)$ H_2O-OH (blue).

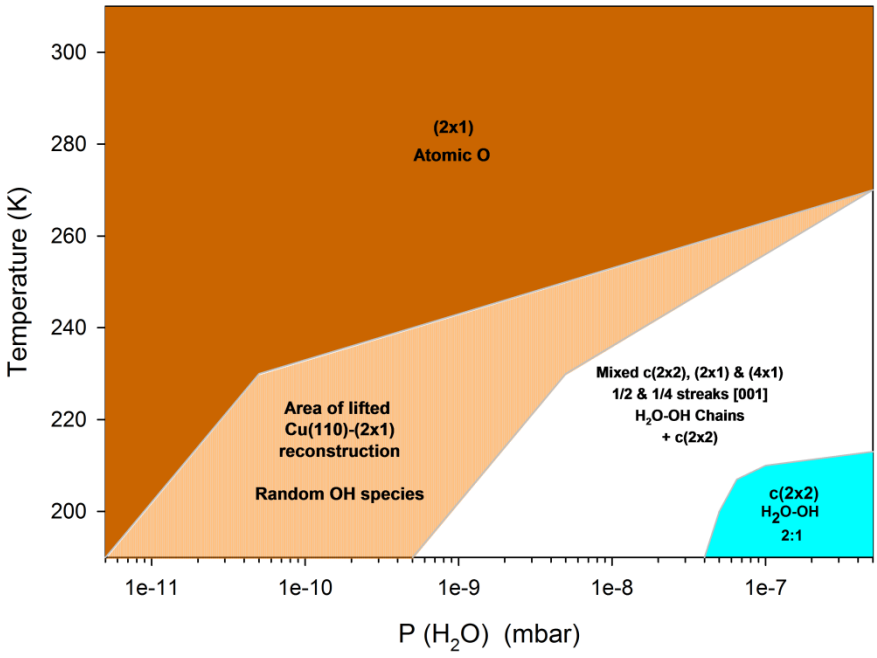

Fig. 5.25. The two dimensional LEED phase diagram for water equilibrium as a function of H_2O pressure $P(H_2O)$ and surface temperature. The pressure is kept constant while increasing the temperature. With regions; 0.06 and 0.32 ML Cu(110)-(2×1)-O reconstruction (brown), Mixed $c(2 \times 2)$, (2×1) and (4×1) with ½ & ¼ order streaks in the $[001]$ azimuth - Zigzag (Z) & Pinch (P) chains with $c(2 \times 2)$ H-bonded (white), lifted (2×1)-O, producing OH species (orange stripe) and $c(2 \times 2)$ H_2O-OH (blue).

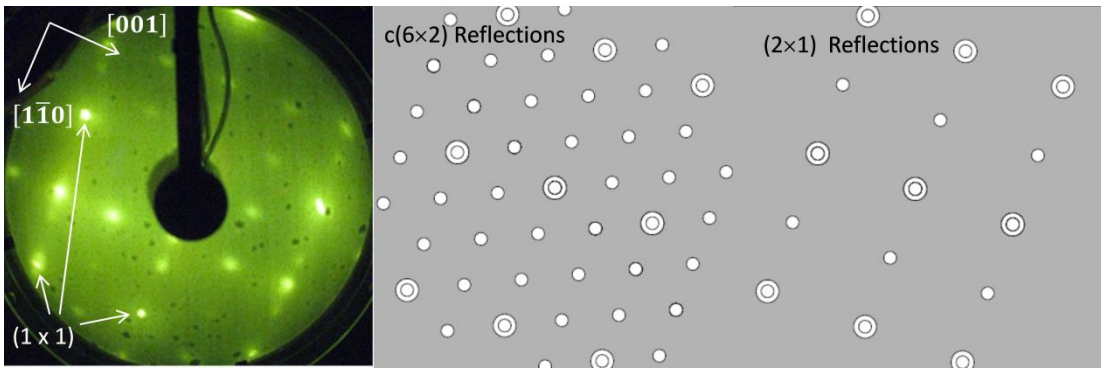

Fig. 5.26. LEED for H_2O adsorption on 0.50 ML Cu(110)-(2×1)-O reconstruction above 240 K and 5.2×10^{-9} mbar, showing a mixed c(6 × 2)/(2 × 1) pattern at 66 eV corresponding to co-existing reconstructions alongside the $c(6 \times 2)$ and (2×1) reflections.

5.3.2.2 Two dimensional LEED phase diagrams on the 0.06 and 0.32 ML Cu(110)-(2×1) oxygen reconstructions, constant temperature varying (increasing) pressure P(H_2O).

With atomic O at coverages 0.06 and 0.32 ML pre-adsorbed on the Cu(110) surface, Figure 5.24 shows a summary of all the LEED patterns recorded whilst keeping the temperature constant at set intervals between 200 and 300 K and increasing the pressure. It is important to note that whilst the experiments for both coverages 0.06 and 0.32 ML were actually conducted separately, the LEED images obtained were virtually identical. As a result of this, a combined summary is presented here in the form a single LEED phase diagram.

With an initial temperature of 200 K, increasing the base pressure above 1.0×10^{-11} mbar produced an immediate reaction with H_2O observed by the disappearance of the streaked (2×1)-O reconstruction. The lifting of the reconstruction (Figure 5.24, orange striped region) was observed merely as a (1×1) LEED pattern analogous to that of the clean Cu(110) surface as shown in Figure 5.10. This lifting of the (2×1)-O reconstruction, which requires a large displacement of Cu adatoms, remained up to 1.0×10^{-9} mbar. Although no ordered structures were formed on this region we attribute this region to the slow formation of hydroxyls. Similar lifting of the (2×1)-O reconstruction was observed by Ammon et al.[152] when studying the low-temperature reactivity of D_2O on an atomic O pre-covered Cu(110) surface, at temperatures ≤ 225 K.

Guillemot and Bobrov[11] looked at the formation and transport of the Cu-OH complexes focussing on the previously ignored influence of the surface mobility and chemical state of the hydroxyl species at elevated pressures. Based on their studies by STM the possible absence of a clear LEED structure could be attributed to the long-range transport of both the Cu adatoms and OH. The nature of the reaction involved H_2O attacking preferentially the unsaturated ends on the Cu-O chain in addition to abstractions taking place along the $[1\bar{1}0]$ direction. The reaction and subsequent lifting of the (2×1)-O could proceed by two different

mechanisms. Either the Cu-O bond dissociated leaving both the Cu adatoms and OH species to migrate independently on the surface or the Cu-O remains intact producing Cu-OH which in turn migrates similarly. Either way the fact that they observed nucleation of two-dimensional Cu islands covered by hydroxyl species suggested long transport of these Cu-OH species away from the original Cu-O chains. The fact that no clear LEED image was observed during this process suggests that the intermediate between abstractions of the Cu-O to the formation of the Cu-OH structures at these temperatures and pressure ranges has no clear defined structure.

Similar long transport of both Ni and Cu adatoms was observed by Ruan et al.[156] for the reaction of H_2S with preadsorbed O on both Ni(110) and Cu(110) respectively. Here the H_2S reacts with the (2×1) added row Cu-O chains to form H_2O, which desorbs at RT leaving chemisorbed S. With atomic O removed the resulting Ni and Cu atoms are very unstable, relaxing and finally accumulating into (1×1) islands with the chemisorbed S.

Above 1.0×10^{-9} mbar, a mixed (2×1) + diffuse (4×1) LEED pattern with ½ and faint ¼ order streaking in the [001] azimuth shown in Figure 5.14 was observed briefly. This was assigned to the P and Z chain structures existing alone before converting to a mixed $c(2 \times 2)$, (2×1) and (4×1) with ½ and faint ¼ order streaking in the [001] azimuth shown in Figure 5.12. This was assigned to the P and Z chain structures coexisting with the partially dissociated $c(2 \times 2)$ (H_2O:OH 2:1) H-bonded structure. These mixed structures remained up to 5.0 x 10^{-8} mbar, transforming into a clear $c(2 \times 2)$ LEED pattern (blue region Figure 5.24) which remained throughout up to 5.0 x 10^{-7} mbar. As with the clean Cu(110) surface (Figure 5.15), we recognized this to be the partially dissociated H-bonded structure as shown in Figure 5.13, corresponding to the 2D $2H_2O$:1OH H-bonded structure.

The lifting of the reconstruction corresponding to the random hydroxyl formation (orange striped region) occurred at the higher pressure of 5.0×10^{-11} mbar at 220 K and 4.0×10^{-10} mbar at 240 K. Likewise the formation of the P and Z chain structures coexisting with the partially dissociated $c(2 \times 2)$ H-bonded structure occurred at higher pressures due to the increased temperatures. At these temperatures it was no longer

kinetically stable to form the complete partially dissociated (H_2O:OH 2:1) H-bonded structure, even at the highest pressures of 5 x 10^{-7} mbar.

With the temperature increased to 260 K, only at pressures above 5 × 10^{-8} mbar were the P and Z chain structures with a fractional coverage of the partially dissociated $c(2 \times 2)$ structure found to be stable. Above this temperature none of the H-bonded structures were found to be kinetically stable.

5.3.2.3 Two dimensional LEED phase diagrams on the 0.06 and 0.32 ML Cu(110)-(2×1) oxygen reconstructions, constant pressure P(H_2O) varying (increasing) temperature.

A summary of the tests conducted with a constant background H_2O pressure whilst increasing the temperature (Figure 5.25) revealed a very similar picture to that observed from a constant temperature with increasing pressure. Whilst there did not appear to be any difference in the stability of the H-bonded structures produced below 240 K, a different picture emerged during the recombinative desorption of the chain structures above this temperature at the saturated coverage of 0.5 ML (***LEED phase diagram not shown***). Here the LEED pattern above 240 K, appeared to show a mixed $c(6 \times 2)$ with a $p(2 \times 1)$ LEED pattern. This was due to the recombinative desorption of H_2O from hydroxyls (produced at lower temperatures) according to Reaction 5.8 depositing further atomic O on the surface which resulted in the reconstruction shown in Figure 5.26. These observations of atomic O being deposited due to the recombinative desorption of H_2O were very similar to when the tests were conducted on the clean surface (Figure 5.14). Here atomic oxygen appeared to be deposited on the surface resulting in a streaked (2×1) LEED pattern.

5.3.3 Wetting properties from molecular beam uptake experiments

This section details the results from a set of experiments where H_2O was dosed directly onto the atomic O structures by means of a molecular beam and the products examined by TPD. TPD plots are presented in Figure 5.27 for H_2O desorbing from the clean Cu(110) surface and in Figures 5.29 to 5.32 for H_2O desorbing from the atomic O pre-covered Cu(110)-(2×1)-O reconstructions. Figure 5.28 presents the TPD for structures associated with H_2O adsorbed on an O (0.1 ML) pre-covered surface adapted from Forster et al.[127]. Quantitative breakdowns of the different peaks presented in Figures 5.29 to 5.32 are displayed in Figures 5.33, 5.34 and 5.35. Particular attention was given to a high temperature H_2O peak desorbing at 285 K very close to that of the dimers desorbing at 269 K, which was not previously observed.

It important to note that after exposure to H_2O the crystal was first cooled 20 K below the uptake temperature prior to TPD experiments to enable a linear ramp for the heating rate. There is a slight but noticeable difference in the desorption temperatures associated with the H-bonded structures in Figures 5.29 and 5.30. This discrepancy was mainly due to the fact that the results were obtained at different times under slightly different conditions due to the maintenance of the chamber and associated analytical attachments. The quantitative breakdown presented in Figures 5.33, 5.34 and 5.35 are based on the average of a series of uptakes and subsequent TPDs with the errors limits calculations based on $\left(1.96 \times Standard \frac{Dev}{\sqrt{No\ of\ tests}}\right)$.

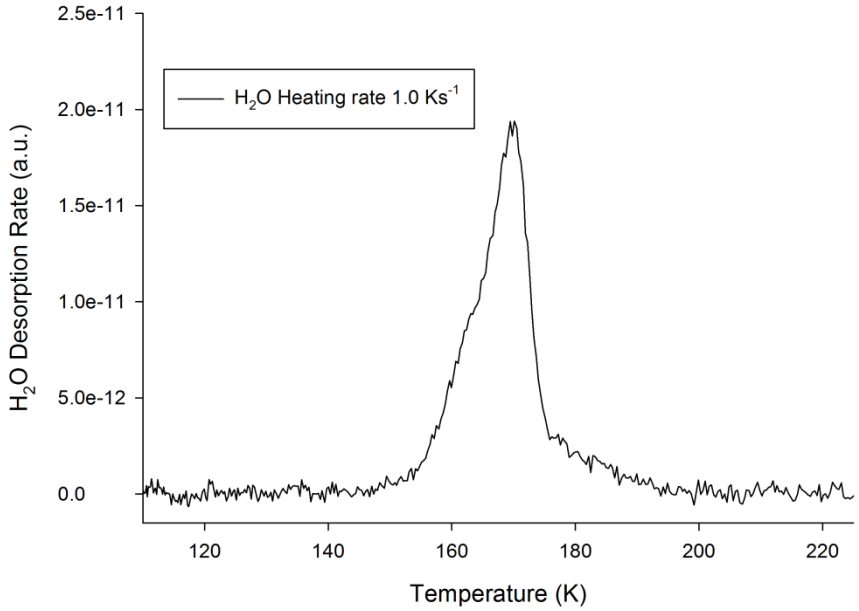

Fig. 5.27. TPD for H_2O desorption from Clean Cu(110) surface (dT/dt) of 1 Ks^{-1} (amount slightly in excess of 1 ML), adsorbed at 90 K

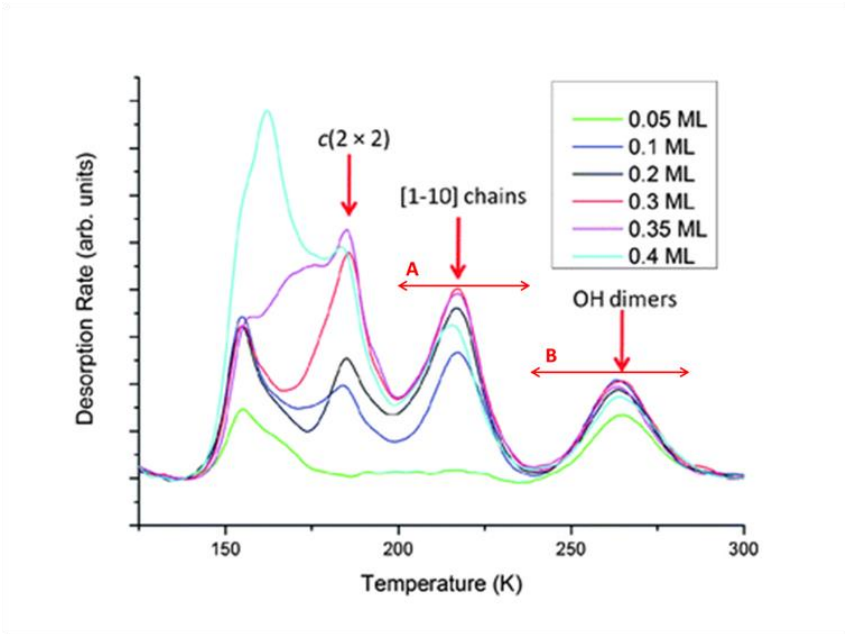

Fig. 5.28. TPD traces for water from an O (0.1 ML) pre-covered surface following adsorption of 0.05–0.4 ML water at 140 K. The 185 K peak is assigned to decomposition of the $c(2 \times 2)$ $2H_2O$:1OH structure, with peaks at (A) 220 K and (B) 260 K from decomposition of the H_2O:OH $[1\bar{1}0]$ chain and OH dimer structures respectively, as marked with a heating rate of 1 Ks^{-1}. Adapted from Forster et al.[127], Water-hydroxyl phases on an open metal surface: breaking the ice rules. Chem. Sci. 3, 93–102 (2011) with permission of The Royal Society of Chemistry.

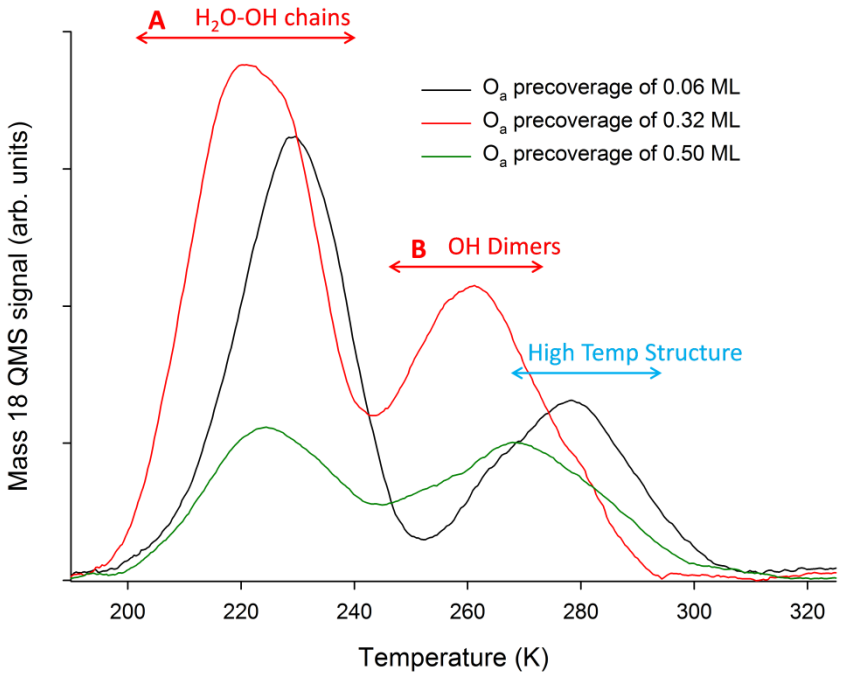

Fig. 5.29. TPD profiles for H_2O desorption from Cu(110)-(2×1)-O reconstructions (dT/dt) of 1 Ks^{-1} at 0.06, 0.32 and 0.5 ML, adsorbed at 200 K (backed up 20 K prior to desorption). The peaks at (A) 230 K are assigned to the decomposition of the H-bonded $1H_2O$:1OH chain structures, those at (B) 269 K assigned to the Hydroxyl OH dimers and at 285 K to an additional high temperature H_2O desorption structure. There is a slight discrepancy between the desorption peak maxima associated with the H_2O-OH chains related to the atomic O precoverage at 0.06 ML in comparison to those related to the atomic precoverages at the higher values of 0.32 and 0.50 ML. This disparity was mainly due to the fact that the results were obtained at different times due to the maintenance of the thermocouple and chamber.

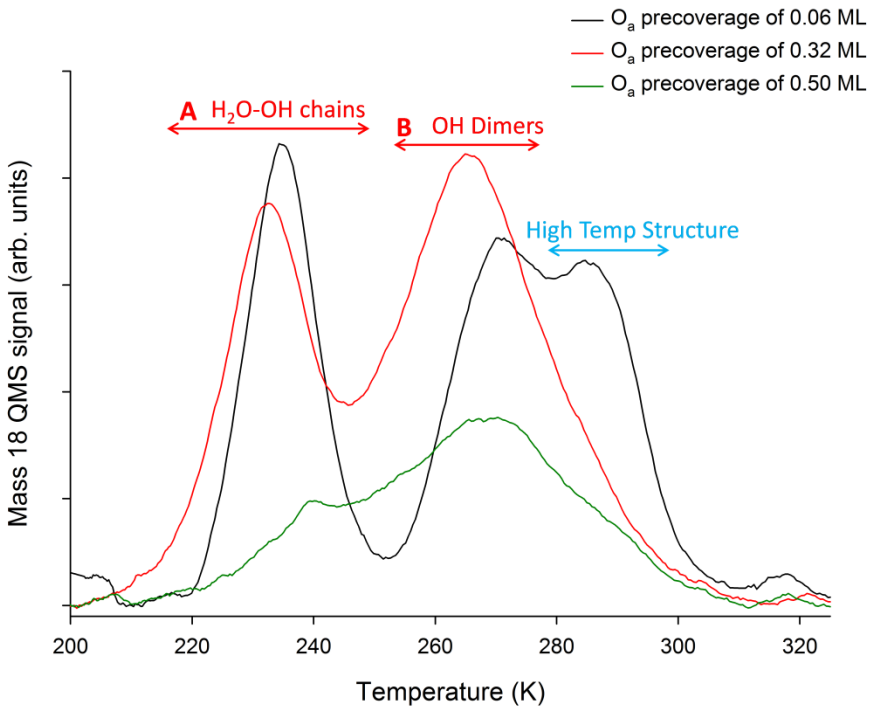

Fig. 5.30. TPD profiles for H_2O desorption from Cu(110)-(2×1)-O reconstructions (dT/dt) of 1 Ks^{-1} at 0.06, 0.32 and 0.5 ML, adsorbed at 220 K (backed up 20 K prior to desorption). The peaks at (A) 230 K are assigned to the decomposition of the H-bonded $1H_2O$:1OH chain structures, those at (B) 269 K assigned to the Hydroxyl OH dimers and at 285 K to an additional high temperature H_2O desorption structure.

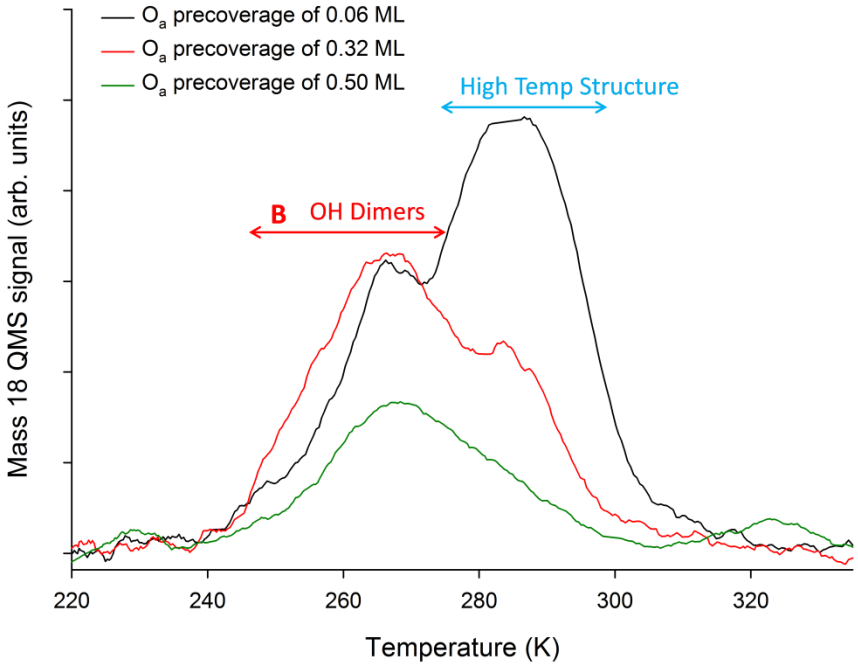

Fig. 5.31. TPD profiles for H_2O desorption from Cu(110)-(2×1)-O reconstructions (dT/dt) of 1 Ks^{-1} at 0.06, 0.32 and 0.5 ML, adsorbed at 240 K (backed up 20 K prior to desorption). The peaks at (B) 269 K assigned to the hydroxyl OH dimers and at 285 K to an additional high temperature H_2O desorption structure.

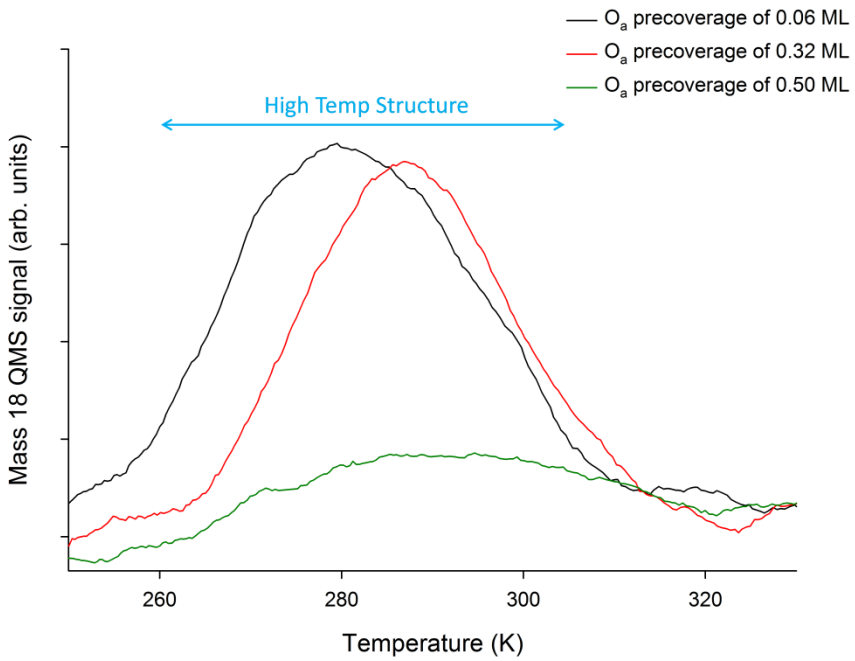

Fig. 5.32. TPD profiles for H_2O desorption from Cu(110)-(2×1)-O reconstructions (dT/dt) of 1 Ks^{-1} at 0.06, 0.32 and 0.5 ML, adsorbed at 260 K (backed up 20 K prior to desorption). These peaks at 285 K are assigned to the additional high temperature H_2O desorption structure.

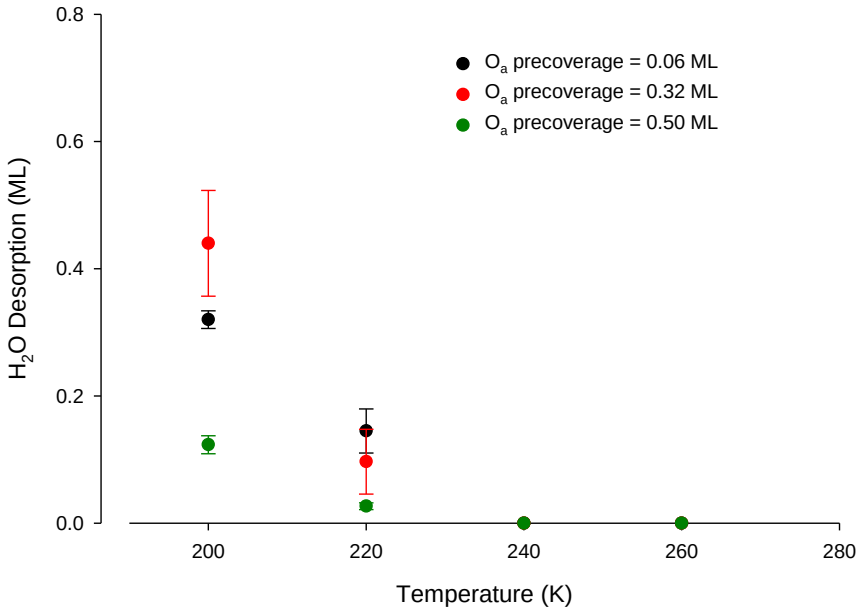

Fig. 5.33. The comparative integrated breakdown of the amount of H_2O associated only with the H-bonded $1H_2O$:1OH chain structures labelled (A) from the TPD peaks shown in Figures 5.29 to 5.32. The total H_2O content was measured relative to a single monolayer of H_2O. The temperatures 200, 220, 240 and 260 K correspond to the actual uptake temperatures on each of the individual Cu(110)-(2×1)-O reconstructions at 0.06, 0.32 and 0.50 ML.

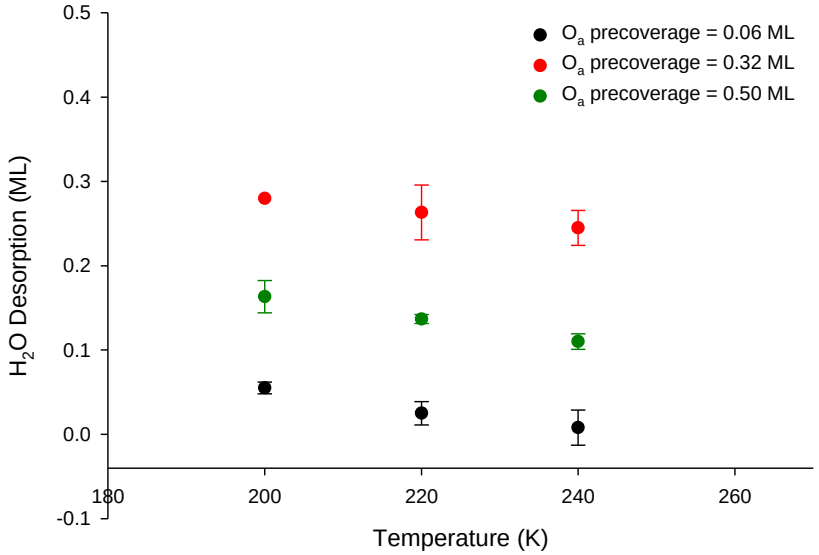

Fig. 5.34. The comparative integrated breakdown of the amount of H_2O associated only with the hydroxyl OH dimers labelled (B) from the TPD peaks shown in Figures 5.29 to 5.32. The total H_2O content was measured relative to a single monolayer of H_2O. The temperatures 200, 220, 240 and 260 K correspond to the actual uptake temperatures on each of the individual Cu(110)-(2×1)-O reconstructions at 0.06, 0.32 and 0.50 ML.

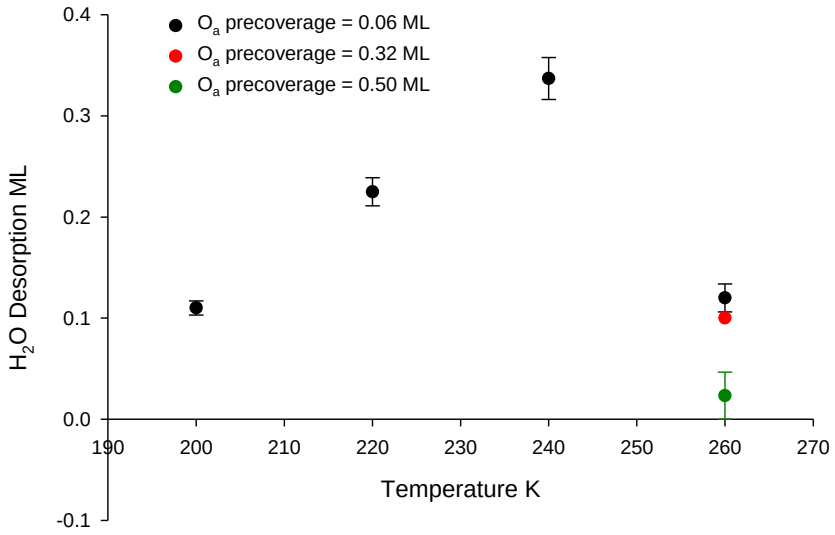

Fig. 5.35. The comparative integrated breakdown of the amount of H_2O associated only with the high temperature structure labelled (BLUE) from the TPD peaks shown in Figures 5.29 to 5.32. The total H_2O content was measured relative to a single monolayer of H_2O. The temperatures 200, 220, 240 and 260 K correspond to the actual uptake temperatures on each of the individual Cu(110)-(2×1)-O reconstructions at 0.06, 0.32 and 0.50 ML.

Figures 5.29 – 5.32 show the recombinative TPD of H_2O from the atomic O pre-covered Cu(110)-(2×1)-O reconstructions at 0.06, 0.32, and 0.50 ML coverages after saturated uptake of H_2O. The uptakes and the subsequent TPD experiments were also conducted on the clean Cu(110) surface along with that of the Cu(110)-$c(6 \times 2)$-O reconstruction. However, desorption signals from these proved to be insignificant and within the baseline noise of the uptake and TPD spectra. This confirmed the two surfaces to be relatively un-reactive towards H_2O at these temperatures, under UHV conditions. In contrast, the clean Cu(110) was actually found to be reactive when the background H_2O pressure was raised > 1.0×10^{-9} mbar within a temperature range of 200 – 300 K as shown in Figures 5.15 and 5.16 section 5.3.1.

5.3.4 Discussion

Initial observation of the TPD data presented in Figures 5.29 and 5.30, where the uptakes were carried out at 200 and 220 K respectively, is consistent with $1H_2O$:1OH chains and OH dimers forming on the surface, as previously reported by Forster et al.[127] for the structures associated with water adsorbed on an O (0.1 ML) pre-covered surface, Figure 5.28. Since the experiments reported here were all conducted at uptake temperatures > 200 K, none of the TPD traces (Figures 5.29 – 5.32) show the $2H_2O$:1OH partially dissociated H-bonded $c(2 \times 2)$ structure at 185 K or the intact H_2O peak at 160 K, both of which appear at low atomic O coverage in experiments conducted below 200 K.

In addition to the previously reported TPD features associated with $1H_2O$:1OH chains and OH dimers, we have observed a new high temperature peak at 285 K associated particularly with low (0.06 ML) atomic O pre-coverage. This peak was initially thought to be a simple hydroxyl peak, however, it became apparent that it was in fact distinct from the feature reported previously, as shown in figures 5.31 and 5.32. Initially, for adsorption at 200 and 220 K, this feature appeared only at low atomic O coverage, but it becomes increasingly prominent as the temperature is increased from 200 to 240 K, as shown in the qualitative breakdown in Figure

5.35. The high temperature feature appeared for 0.32 ML atomic O coverage at 240 K and for all three atomic O coverages at 260 K. This TPD peak appears at a temperature where we expect both the partially dissociated H-bonded $c(2 \times 2)$ and the chain structures to be unstable in the absence of water vapour. Since it is documented that these structures destabilize in the order Cu-H_2O < 2H_2O-OH < H_2O-OH < Cu-OH < Cu-O[47,10,157], it is unclear what causes this desorption feature which could originate from either a kinetic stabilisation of one of these phases or some different structure, such as that reported by Guillemot and Bobrov[11] discussed in detail in the introduction (Figure 5.9) and later in this discussion.

We have shown earlier that in the presence of sufficient H_2O vapour, low quantities of atomic O will react to produce hydroxyls that stabilize H_2O at temperatures up to 270 K, i.e. the P and Z chain structures and partially dissociated H-bonded $c(2 \times 2)$ structure. It therefore seems likely that this high temperature peak is associated with a new hydroxyl or water-hydroxyl phase that is stabilised under high temperature adsorption conditions but does not form at low temperature. Since the high temperature peak appears most strikingly at low atomic O pre-coverage, where significant water dissociation to create OH and H occurs, one possibility is that co-adsorbed H somehow stabilises a different phase. To check this idea the uptake and TPD experiments were repeated with D_2O to look for D_2 formation. However, no D_2 was observed at all throughout, despite the fact that atomic oxygen was left on the surface after TPD experiments, evident from the development of a faint streaked (2×1)-O LEED pattern that became more prominent after several water doses. At temperatures where the new TPD feature appears, D_2 is expected to slowly recombine and desorb from the surface[150,151], indicating that although dissociation is certainly taking place, the D_2 signal was simply too small, and spread out over too long a time to be detected during an adsorption measurement, implying that H/D does not remain on the surface to stabilise OH/H_2O.

As discussed in the introduction (Figure 5.9), the structures proposed by Guillemot & Bobrov[11] are unusual. The structure proposed consists of chains of H-bonded OH dimers in the bridge site, spaced by $2a_o$ along the close

packed direction, with two water molecules in the bridge position between each dimer pair, each having one H-bond to an OH and one other uncoordinated H pointing out of the chain. The authors suggest that this arrangement is stabilised by the final H donating to another OH that does not appear in STM, though OH has been shown to image as a protrusion[146]. All the other mixed H_2O-OH phases reported have water adsorbed atop Cu, not on a Cu site shared by bridge OH. For example, the 1:1 chain structures complete the water H-bond network and have OH in the bridge site and water flat atop Cu, optimising the site and orientation of each species, unlike in Figure 5.9. As seen earlier, even with the H_2O acting as a double H-bond donor and the OH acting as a single bond acceptor the structures reported earlier[46,127,129,136] are not stable up to RT. As a result, it is very unlikely that with H_2O acting as a single H-bond donor these structures would remain stable at temperatures up to and above RT. In the absence of supporting DFT calculations and STM simulations it seems unlikely that the structure shown in Figure 5.9 can be correct.

Although the low temperature STM studies that characterised the pure water chains, the $c(2 \times 2)$ structure and the $1H_2O$:1OH chains saw no evidence for movement of Cu or Cu ad-atoms in these structures, both Guillemot & Bobrov[11] and Shi et al.[129] have found that Cu movement is important at higher temperatures. According to their STM studies at 200 K Guillemot & Bobrov[11] believed that the hydroxyl OH dimers originally produced on the surface were highly mobile Cu–OH complexes. They suggested that these complexes condense, inducing nucleation and growth of Cu islands on the substrate, releasing the hydroxyl species. Nucleation and growth of these nanometer scaled Cu islands significantly enhance the surface reactivity towards H_2O hence producing additional hydroxyls particularly at the island edges. However, those authors interpreted the new structure reported in Figure 5.9 in terms of an un-reconstructed Cu surface without any ad-atoms involved in this phase. Shi et al.[129] also saw Cu movement on the surface when heating $1H_2O$:1OH chain structures to temperatures of 200 K. They found that under these conditions the chains disappeared from the terraces, decomposing to form (2×1)-O islands, while Cu chains form from the step edges and decorate surviving P type

1H_2O:1OH chain structures along $[1\bar{1}0]$. Continuing heating caused these chains to grow up to 15 nm long and order along the step edge, giving regularly spaced chains separated by $2a_o$ similar to the missing row reconstruction. Shi et al.[129] found, during their STM experiments that when heated above 220 K both the 1H_2O:1OH chain structure and the Cu chains to disappear. The appearance of the Cu chains parallels the process of H_2O-OH dissociation, indicating that the two structures are intimately linked to each other and that OH and H play a significant role in the formation of the Cu wires. Since the amount of (2×1)-O islands increases from 180 to 220 K, when the Cu wires have disappeared, Shi et al.[129] concluded that reaction with O atoms is not the mechanism driving the formation of the wires. Since isolated wires are always flanked by water chains it appears that diffusing Cu atoms attach to existing H_2O−OH chains, stabilizing these structures and guiding their subsequent growth.

On this basis of Shi et al.'s results we suggest that the stabilization of water on the surface to form the high temperature 285 K TPD peak is most likely caused by the stabilization of the H_2O:OH chain structure by Cu adatom chains at step edges. These assumptions would need further exploration for better clarification by more experimental data including STM, XPS and DFT.

5.4 Conclusions

We have studied the wetting properties, autocatalytic dissociative adsorption and the reactivity of the hydroxyl species originating from the co-adsorption of water and oxygen on Cu(110) at 200 to 300 K. Experiments were conducted by two separate methods; molecular beam uptakes and by varying the H_2O pressures in conjunction with LEED and TPD.

Dissociated H-bonded complex structures were observed on both the clean and oxygen pre-covered reconstructions, with low atomic O coverages (0.06 – 0.32 ML) providing a more active medium for dissociation by way of

hydrogen abstraction. In contrast the oxygen-saturated coverages at 0.50 to 0.67 ML were found to be relatively un-reactive.

There was a direct comparison between the growth and formation of the dissociated H-bonded complex structures formed by elevated H_2O pressure experiments to those formed by molecular beam experiments. However with the elevated background experiments the H-bonded complexes were found to be far more stable at higher temperatures due to the kinetic effects of the increased background H_2O pressure. This was evident from the partially dissociated H-bonded $c(2 \times 2)$ structure produced at elevated pressures, not present in the molecular uptake decomposition traces. With this being the case, kinetically there is still a clear competition on the clean Cu(110) surface between the thermally induced dissociation and desorption processes. This competition is dependent on the H-bonding and Cu-O bonding between each of the phases. Whilst there were no H-bonded complexes or hydroxyls observed at RT, even at the highest background H_2O pressures, it is clear that the hydroxyl groups are responsible for the stabilization of H_2O molecules with the stability of the observed structures changing in the following order: Cu-O > Cu-OH >> H_2O(H-bond donor)-OH(H-bond acceptor) > Cu-H_2O ≈ H_2O-H_2O > OH(H-bond donor)-H_2O(H-bond acceptor)[47,10,157].

Extensive surface restructuring was observed on both the clean and 0.5 ML covered Cu(110) giving rise to a (2×1)-O and a mixed $c(6 \times 2)/(2 \times 1)$-O reconstruction respectively at pressures above 1.0×10^{-8} mbar and temperatures in excess of 250 K. Having observed and verified this by the LEED phase tables, a re-examination of these trends may suggest that the observed H-bonded structures reported by Guillemot & Bobrov[11] could have occurred under slightly different conditions i.e. slightly lower temperatures. Looking at summary of the LEED data, it may have been possible that the co-existing H-bonded structures i.e. the Zig-zag (Z) and Pinch (P) chains co-existing with hydroxyl observed just below 280 K, contributed to their observations.

We have shown it is thermodynamically more favourable for water to undergo partial dissociation forming strong H_2O(H-bond donor)-OH(H-bond acceptor) structures, than to remain molecularly intact[127,158]. In addition,

these reactions are initiated by the activation barrier for dissociation being lower at atomically rough areas such as steps, terraces, and grain boundaries on the surface. Additionally, whilst the presence of small amounts of atomic oxygen can have profound influence on the surface reactivity, forming H_2O/OH structures up 260 K, at high saturation atomic O coverages the surface was found to be un-reactive. Most of the H-bonded structures were found to desorb recombinatively, depositing only atomic oxygen at RT, with relatively no detectable liberation of deuterium.

We have also found an additional structure desorbing at 285 K very close to that of the hydroxyl complexes which has not been observed in any previous work conducted under similar conditions. This would suggest stabilisation of H_2O at high temperatures with a possible association to the structures observed by Guillemot & Bobrov[11]. With this being the case we have not been able to establish an exact structure for this H-bonded complex.

Alternatively, as mentioned in section 5.3.2.2, the reaction and lifting of the (2×1)-O could proceed by two separate mechanisms. That is where the Cu-O dissociates leaving both Cu adatoms and OH species to migrate independently on the surface as in Equation 5.9, or the Cu-O remains intact producing Cu-OH and OH as in Equation 5.10.

$$[Cu - O]_{(units)} + H_2O_{(ads)} \rightarrow Cu_{(adatom)} + 2OH_{(fluid)} \quad (5.9)$$

$$[Cu - O]_{(units)} + H_2O_{(ads)} \rightarrow Cu - OH_{(fluid)} + OH_{(fluid)} \quad (5.10)$$

There is a possibility that this high temperature structure could be associated specifically to one or other of these mechanisms with autocatalysis according to Equations 5.6 and 5.7 also playing a significant role in the process. Assuming this was the case this would explain why the structure appeared to change in line with the different levels of pre-adsorbed atomic O. The

research of G & B focussed mainly on a well ordered 2D H_2O-OH structure having stability at RT, a structure that has very little correlation to anything observed in any previous research conducted at high temperatures. The fact that their interpretations were based solely on an STM study and ours on both LEED and TPD experiments, both sets need to be carried out under identical conditions with all techniques used.

Chapter 6

6 Summary and further work

This thesis utilizes superior ultra-high vacuum resolving temperature-programmed desorption (TPD) techniques by way of quadrupole mass spectrometry (QMS) together with low energy electron diffraction (LEED) to study the wetting and oxidation of CO on transition metals and bimetallic surfaces. In this thesis we focussed on the interaction of H_2O on Cu(110) and the catalytic oxidation of CO on both Cu(110) and the bimetallic surface alloy of Au/Pd(111). Physical vapour deposition (PVD) was used in order to sublime the Au onto the Pd(111) surface with the Au/Pd(111) surface alloy formed by annealing to the required temperature.

6.1 Summary

In summary, we showed that the alloying of Au on the Pd(111) crystal surface enhanced the CO catalytic oxidation activity in comparison to that of the pure Pd(111) surface. This overall enhancement termed promotion occurred as a result of the charge transfer from the Au to the Pd. This charge transfer occurred due to the fact that the electrons associated with the Au were at a higher Fermi energy (E_f) level than the electrons associated the Pd. This resulted in a rise in the E_f away from the Pd d band centre which resulted in an overall weakening towards the reactants CO and O. This subsequent weakening gave rise to an enhancement in the oxidation activity in comparison with the pure Pd(111) crystal.

This enhancement in the oxidation activity was assessed by comparing the CO_2 production rate of the clean Pd(111) surface with that of the Au/Pd(111) surface alloy. Overall there was a clear increase of 27.0 % in the peak CO_2 production rate for Au coverages of 0.20 to 0.40 ML in conjunction with flash annealing to ~ 700 K. Above a coverage of 0.40 ML the peak CO_2 production began to drop off, with further increases deactivating the surface completely.

It is fairly clear from our studies that both ensemble and ligand effects played a significant role in the enhancement of the oxidation reaction. Where the ensemble effects are the arrangement of the active atoms and the ligand effects are the electronic modifications or charge transfer associated with these active atoms. However with this, it was extremely difficult to deduce whether the enhancement was due primarily to the ensembles of Au on Pd or to the transfer of electrons between the two metals. This was particularly difficult with this system, due to the fact that the alloy formed was quasi-random.

The catalytic oxidation of CO along with kinetic mechanism was investigated on the Cu(110) surface between 90 and 170 K. This study was carried out initially by pre-dosing O_2 on the Cu(110) substrate surface at various coverage followed by CO and then reversed with CO pre-dosed followed by O_2. During each experiment any production of CO_2 was monitoring during the uptake of the second reactant and then with both reactants on the surface by way of a TPD experiment.

In any heterogeneous catalysis process, the reaction will proceeds by way of a sequence of steps, including adsorption, surface diffusion and reorganization of the adsorbed intermediates, followed by desorption. The most common surface reaction mechanism in heterogeneous catalysis is the Langmuir-Hinshelwood mechanism where both of the reactants adsorb, migrate on the surface and then collide to form products. Research on the catalytic oxidation of CO has always suggested the reaction proceeds by way of the Langmuir-Hinshelwood mechanism on most transitions metals including Cu. Our research suggests that the reaction is significantly more complex on the Cu(110) substrate. The results obtained show that the mechanism is dependent on temperature, the order the reactants CO and O_2 are pre-dosed on the Cu(110) substrate and the coverage of the initial pre-dosed reactant.

With O_2 pre-dosed on the Cu(110) substrate, no CO_2 was observed desorbing spontaneously during the subsequent uptake of CO. All of the CO_2 produced occurred only during the subsequent TPD which indicated a transient state mechanism similar to that of the Eley-Rideal mechanism. Typically the Eley-Rideal mechanism occurs when the gaseous reactant

strikes and reacts directly with the adsorbed reactant with the subsequent product then desorbing from the surface. However these transient states only occurred ≤ 130 K as very little CO_2 was produced above this temperature due to the pre-adsorbed O_2 dissociating and forming stable –Cu-O- units at the higher temperatures.

With CO pre-dosed on the surface followed by O_2 a significant amount of oxidation occurred spontaneously, specifically ≥ 150 K. Although spontaneous oxidation of CO occurred below this temperature, the conversion was well below 20 % in comparison to > 40 % above 150 K. Due to the spontaneity of this mechanism in conjunction with the high exothermicity associated with the dissociation of O_2, we attributed this mechanism to the hot precursor or hot atom mechanism. At temperatures below 130 K with both reactants on the substrate the main bulk in terms of % conversion took place by means of thermally induced dissociation during the subsequent TPD. This indicated a transient state mechanism similar to that of the Eley-Rideal mechanism comparable to when O_2 was pre-dosed followed by CO at these temperatures. Fractional reactivation of the Cu(110) was achieved by flash annealing to 773 K due to surface rearrangement by way of dissociation of the -Cu-O- units. This would eventually decline however due to eventual overcrowding.

We have studied the wetting properties, originating from the co-adsorption of H_2O and O_2 on Cu(110) at 200 to 300 K. Experiments were conducted by molecular beam uptakes and by varying the background H_2O pressures in combination with LEED and TPD. We observed dissociated H-bonded complex structures on both the clean and low pre-covered atomic O reconstructions of 0.06 and 0.32 ML. In contrast the high and saturated pre-covered atomic O reconstructions of 0.50 to 0.67 ML were found to be relatively un-reactive. We establish that kinetic effects associated with increased background H_2O pressures produced far more stable H-bonded complexes in comparison to the complexes produced by means of the molecular beam experiments.

What determines the adsorbed H_2O structures and their stabilities at low temperatures are the two fundamental forces at the interfaces; the H_2O-Cu interaction, which occurs predominantly in the H_2O-Cu contact layer and the

H-bonding between the H_2O molecules. The strength of the H-bonding between the H_2O molecules may be modified by the presence of the Cu substrates. On most metal surfaces, these two interactions turn out to be comparable in strength where their competition results in a rich class of adsorbed structures especially at sub-monolayer coverages. However, at higher temperatures the forces are a lot more complex due to partial dissociation and the formation of the OH species. At the highest background H_2O pressures it was clear that the OH groups were responsible for the stabilization of H_2O molecules with the stability of the observed structures changing in the following order: Cu-O > Cu-OH >> H_2O(H-bond donor)-OH(H-bond acceptor) > Cu-H_2O ≈ H_2O-H_2O > OH(H-bond donor)-H_2O(H-bond acceptor)

It has been documented that the strong attractive interaction between mixed OH and H_2O produced at elevated H_2O pressures slows down the desorption kinetics of H_2O dramatically to produce stable H_2O-OH structures up to RT. With this being the case we have found a new structure formed by the reaction of H_2O with low coverages of atomic O. The structure became increasingly prominent when the uptake temperature was increased from 200 up to 240 K and remained stable on the surface up to 320 K. Assignment of the high temperature structure to a partially dissociated H_2O-OH phase is supported by previously observed chain structures, although more extensive research would be required in order to ascertain a definitive structure. Alternatively, it is possible that this high temperature structure could be associated specifically to the mechanisms associated with the formation of the OH species. That is, where the Cu-O dissociates leaving both Cu adatoms and OH species to migrate independently on the surface or the Cu-O remains intact producing Cu-OH and OH.

Extensive restructuring of the Cu surface was observed accompanied by partially dissociated chain growth at elevated H_2O pressures ~ 2.8×10^{-8} mbar and temperatures 240 to 260 K. This was evident by the formation of monatomic Cu chains as a result of interaction with the partially dissociated P and Z chain structures.

6.2 Further work

There has been an immense growth over the last thirty years in the understanding of bimetallic surface chemistry, particularly with the advent of UHV surface analytical techniques in addition to the development of efficient methods for surface preparation. This has allowed researchers to develop a realistic predictive understanding of the surface structures resulting when alloying different metals under controlled UHV conditions. As a result there has also been a related increase in the study of catalytic reactions on these types of surfaces.

As a precious noble metal, solitary Au has until recently been considered a useless catalyst due to its' inert characteristics. The Au/Pd results presented in this thesis should contribute to a better understanding of catalytic reaction. We were unable to establish exactly the extent that ensemble and ligand effects had on the enhancement of the oxidation reaction. This was predominantly due to the fact that the alloy formed was quasi-random. However, on carefully prepared bimetallics with well-defined surfaces using additional alternative analytical techniques such as STM, RAIRS and LEISS, it should be possible to determine the individual effects of each. In particular the ensemble effects should be assessed carefully as O_2 dissociation on will only take place on the more active metal, i.e. the Pd surface atoms as opposed to the Au adatoms.

As a consequent of the insight obtained from the research presented in this thesis, we feel this will inspire more researchers to study bimetallic surfaces for oxidation of CO particularly at ambient temperatures. This research is also significant as it only complements the practice of reserving resources for future generations without any harm to the nature and other components of it.

As a cheaper noble metal, Cu has been considered as an alternative for the catalytic oxidation of CO in place of the more expensive metals such as Pt, Pd and Rh. Based on the results presented in this thesis it may be possible to develop new catalytic material at a much lower cost than those presently produced.

With oxidation occurring rapidly on the Cu surface during the dissociation of O_2, as a functional catalyst, Cu would be better suited to temperatures where the Cu adatom density on the surface is low. This not only prolongs the life of the dissociated O but also slows down the formation of the surface oxide, which when formed completely deactivates the surface. The ideal conditions for low temperature CO oxidation would be 150 to 300 K in a CO rich environment in order to prevent oxidation of the Cu substrate during dissociation of O_2. Alternatively, for high temperature CO oxidation, temperatures in excess of 400 K, where the detachment of atomic O from the (2×1)-O reconstruction occurred. In this thesis we attributed the spontaneous oxidation to that of the hot precursor or hot atom mechanism. Theoretical calculations are currently ongoing in order to complement this assumption.

While our studies for the interaction of H_2O on clean and atomic O pre-covered Cu(110) have provided important for H_2O structural transformations; there were still some unanswered questions worth pursuing. We were not able to determine a definitive structure related to the high temperature TPD peak at 285 K. The fact that our interpretations were based solely on LEED and TPD experiments, further exploration using STM, XPS and DFT would be required to clarify a structure.

The partial dissociation of H_2O gave rise to P and Z chains above 220 K accompanied by 1D monatomic Cu chains running along the $[1\bar{1}0]$ azimuth. Although previously observed by Shi et al.,[129] a better understanding of these chains would be crucial in terms of understanding the significant impact it will have on Cu surface reconstruction in the presence on H_2O and atomic O.

Chapter 6

List of publications and conference contributions

Papers:

1. Forster, M., Massey, A., McBride, F., Taylor, M.S., Darling G. R., Raval R. & Hodgson, A.
   Nanoscale wetting and hydration of bitartrate on Cu(110)
   (In manuscript)

2. The SnPd surface Alloy: catalytic and structural properties determined by electronic behaviour
   Massey, A., Taylor, M.S., Darling, G.R. & Hodgson, A.
   (In manuscript)

Author's contribution
In paper 1, I obtained the LEED images required for the structural analysis and in paper 2, I also took part in obtaining the LEED IV images in addition to the data analysis of the IV curves required for the theoretical calculations.

Conference contributions (poster presentation):

Taylor, M. S., Massey, A., Haq, S. & Hodgson, A.
Heterogeneous Catalytic activity of Cu(110) for Carbon monoxide (CO) Oxidation

ECOSS 30th European Conference on Surface Science
31st August – 5th September, 2014, Antalya, Turkey

Bibliography

1. Gao, F., Wang, Y. & Goodman, D. W. CO Oxidation over AuPd(100) from Ultrahigh Vacuum to Near-Atmospheric Pressures: The Critical Role of Contiguous Pd Atoms. *J. Am. Chem. Soc.* **131,** 5734–5735 (2009).
2. Gao, F., Wang, Y. & Goodman, D. W. CO Oxidation over AuPd(100) from Ultrahigh Vacuum to Near-Atmospheric Pressures: CO Adsorption-Induced Surface Segregation and Reaction Kinetics. *J. Phys. Chem. C* **113,** 14993–15000 (2009).
3. Gao, F., Wang, Y. & Goodman, D. W. Reaction Kinetics and Polarization-Modulation Infrared Reflection Absorption Spectroscopy (PM-IRAS) Investigation of CO Oxidation over Supported Pd−Au Alloy Catalysts. *J. Phys. Chem. C* **114,** 4036–4043 (2010).
4. Yuan, D. W., Liu, Z. R. & Chen, J. H. Catalytic Activity of Pd Ensembles over Au(111) Surface for CO Oxidation: A First-principles Study. *J. Chem. Phys.* **134,** 054704 (2011).
5. Crew, W. W. & Madix, R. J. CO Adsorption and Oxidation on Oxygen Pre-covered Cu(110) at 150 K: Reactivity of two types of Adsorbed Atomic Oxygen Determined by Scanning Tunnelling Microscopy. *Surf. Sci.* **356,** 1–18 (1996).
6. Schneider, T. & Hirschwald, W. Adsorption States of Carbon Monoxide on Oxygenated Cu(110) faces. *Catal. Lett.* **16,** 335–343 (1992).
7. Sueyoshi, T., Sasaki, T. & Iwasawa, Y. Reactive Oxygen Atoms on Cu(110) formed at 100 K: Vibrational Spectra and CO Oxidation. *Surf. Sci.* **343,** 1–16 (1995).
8. Hodgson, A. & Haq, S. Water Adsorption and the Wetting of Metal Surfaces. *Surf. Sci. Rep.* **64,** 381–451 (2009).
9. Thiel, P. A. & Madey, T. E. The Interaction of Water with Solid Surfaces: Fundamental Aspects. *Surf. Sci. Rep.* **7,** 211–385 (1987).
10. Yamamoto, S. *et al.* Hydroxyl-Induced Wetting of Metals by Water at Near-Ambient Conditions. *J. Phys. Chem. C* **111,** 7848–7850 (2007).

11. Guillemot, L. & Bobrov, K. Formation of a Chemisorbed Water-Hydroxyl Phase on Cu(110) Mediated by Surface Transport. *J. Phys. Chem. C* **115,** 22387–22392 (2011).
12. Atkins, P. W. & De Paula, J. *Elements of Physical Chemistry*. (Oxford : Oxford University Press, 2009., 2009).
13. Somorjai, G. A. & Li, Y. *Introduction to Surface Chemistry and Catalysis*, 2nd Edition (2010).
14. Vannice, M. A. in *Kinetics of Catalytic Reactions* 38–86 (Springer US, 2005).
15. Kolasinski, K. K. & Kolasinski, K. W. *Surface Science: Foundations of Catalysis and Nanoscience*. (John Wiley & Sons, 2012).
16. Wachs, I. E. & Madix R. J. The Oxidation of H_2CO on a Copper(110) Surface. *Surf. Sci.* **84,** 375–386 (1979).
17. Dowden, D. A. Heterogeneous Catalysis. Part I. Theoretical Basis. *J. Chem. Soc. Resumed* 242–265 (1950).
18. Drexler, E. J. & Field, K. W. An NMR Study of Keto-Enol Tautomerism in β[beta]-Dicarbonyl Compounds. *J. Chem. Educ.* **53,** 392 (1976).
19. Kluger, R. Decarboxylation, CO_2 and the Reversion Problem. *Acc. Chem. Res.* **48,** 2843–2849 (2015).
20. Cleland, W. W. Mechanisms of Enzymatic Oxidative Decarboxylation. *Acc. Chem. Res.* **32,** 862–868 (1999).
21. Cleland, W. W., Frey, P. A. & Gerlt, J. A. The Low Barrier Hydrogen Bond in Enzymatic Catalysis. *J. Biol. Chem.* **273,** 25529–25532 (1998).
22. Liu, W. & Flytzani-Stephanopoulos, F. Total Oxidation of Carbon Monoxide and Methane Over Transition Metal-Fluorite Oxide Composite Catalysts. I. Catalyst Composition and Activity. *J. Catal.* **153,** (1995).
23. Taylor, K. C. *Catalysis* (eds. Anderson, D. J. R. & Boudart, P. M.) 119-170 (Springer Berlin Heidelberg, (1984)).
24. Bagot, P. A. J. Fundamental surface science studies of automobile exhaust catalysis. *Mater. Sci. Technol.* **20,** 679–694 (2004).
25. Briner, E. *Ozone Chemistry and Technology* **21,** 1–6 American Chemical Society, (1959).
26. Crawford, J. H. *et al.* Evidence for Photochemical Production of Ozone at the South Pole Surface. *Geophys. Res. Lett.* **28,** 3641–3644 (2001).

27. Schnell, R. C. *et al.* Rapid Photochemical Production of Ozone at High Concentrations in a Rural site during Winter. *Nat. Geosci.* **2,** 120–122 (2009).
28. Domagala, M. E. & Campbell, C. T. The Mechanism of CO Oxidation over Cu(110): Effect of CO Gas Energy. *Catal. Lett.* **9,** 65–70 (1991).
29. Flaherty, D. W., Yu, W.Y., Pozun, Z. D., Henkelman, G. & Mullins, C. B. Mechanism for the Water–Gas Shift Reaction on Mono-functional Platinum and cause of Catalyst Deactivation. *J. Catal.* **282,** 278–288 (2011).
30. Schumacher, N. *et al.* Trends in Low-temperature Water–Gas Shift Reactivity on Transition Metals. *J. Catal.* **229,** 265–275 (2005).
31. Lewis, B. & Elbe, G. Von. *Combustion, Flames and Explosions of Gases*. (Elsevier, 2012).
32. Jaworska-Galas, Z., Mista, W., Wrzyszcz, J. & Zawadzki, M. Thermal Stability Improvement of Hopcalite Catalyst. *Catal. Lett.* **24,** 133–139 (1994).
33. Royer, S. & Duprez, D. Catalytic Oxidation of Carbon Monoxide over Transition Metal Oxides. *ChemCatChem* **3,** 24–65 (2011).
34. Blyholder, G. Molecular Orbital View of Chemisorbed Carbon Monoxide. *J. Phys. Chem.* **68,** 2772–2777 (1964).
35. Sung, S. S. & Hoffmann, R. How Carbon Monoxide Bonds to Metal Surfaces. *J. Am. Chem. Soc.* **107,** 578–584 (1985).
36. Andreoni, W. & Varma, C. M. Binding and Dissociation of CO on Transition-Metal Surfaces. *Phys. Rev. B* **23,** 437–444 (1981).
37. Hinshelwood C. N. *The Kinetics Of Chemical Change*. The Clarendon Press, (1940).
38. Duan, X., Warschkow, O., Soon, A., Delley, B. & Stampfl, C. Density Functional Study of Oxygen on Cu(100) and Cu(110) Surfaces. *Phys. Rev. B* **81,** 075430 (2010).
39. Campbell, C. T. Bimetallic Surface Chemistry. *Annu. Rev. Phys. Chem.* **41,** 775–837 (1990).
40. Gao, F. & Goodman, D. Model Catalysts: Simulating the Complexities of Heterogeneous Catalysts. *Annu. Rev. Phys. Chem. VOL 63* **63,** 265-286 (2012).

41. Gao, F. & Goodman, D. W. Pd-Au Bimetallic Catalysts: Understanding Alloy Effects from Planar Models and (supported) Nanoparticles. *Chem. Soc. Rev.* **41,** 8009–8020 (2012).
42. Xue, L. *et al.* Implementation of a Silver Iodide Cloud-Seeding Parameterization in WRF. Part II: 3D Simulations of Actual Seeding Events and Sensitivity Tests. *J. Appl. Meteorol. Climatol.* **52,** 1458–1476 (2013).
43. Xue, L. *et al.* Implementation of a Silver Iodide Cloud-Seeding Parameterization in WRF. Part I: Model Description and Idealized 2D Sensitivity Tests. *J. Appl. Meteorol. Climatol.* **52,** 1433–1457 (2013).
44. Leung, L. W. H. & Goodman, D. W. Modeling the Metal-solution Interface under Ultrahigh Vacuum: Vibrational Studies of the Coadsorption of Water and Carbon Monoxide on Rhodium(100). *Langmuir* **7,** 493–496 (1991).
45. Kumagai, T. *et al.* Symmetric Hydrogen Bond in a Water-hydroxyl Complex on Cu(110). *Phys. Rev. B* **81,** 045402 (2010).
46. Forster, M., Raval, R., Hodgson, A., Carrasco, J. & Michaelides, A. c(2×2) Water-hydroxyl Layer on Cu(110): A Wetting Layer Stabilized by Bjerrum Defects. *Phys. Rev. Lett.* **106,** (2011).
47. Schiros, T. *et al.* Cooperativity in Surface Bonding and Hydrogen Bonding of Water and Hydroxyl at Metal Surfaces. *J. Phys. Chem. C* **114,** 10240–10248 (2010).
48. Michaelides, A., Ranea, V. A., de Andres, P. L. & King, D. A. General Model for Water Monomer Adsorption on Close-Packed Transition and Noble Metal Surfaces. *Phys. Rev. Lett.* **90,** 216102 (2003).
49. Henderson, M. A. The Interaction of Water with Solid Surfaces: Fundamental Aspects revisited. *Surf. Sci. Rep.* **46,** 1–308 (2002).
50. Ren, J. & Meng, S. Atomic Structure and Bonding of Water Overlayer on Cu(110): The Borderline for Intact and Dissociative Adsorption. *J. Am. Chem. Soc.* **128,** 9282–9283 (2006).
51. Bagus, P. S., Hermann, K. & Charles, W. B. Jr., On the Nature of the Bonding of Lone Pair Ligands to a Transition Metal. *J. Chem. Phys.* **81,** 1966–1974 (1984).

52. Zuleta, E. C., Baena, L., Rios, L. A. & Calderón, J. A. The Oxidative Stability of Biodiesel and its Impact on the Deterioration of Metallic and Polymeric Materials: A Review. *J. Braz. Chem. Soc.* **23,** 2159–2175 (2012).
53. Chambers, A., Fitch, R. K. & Halliday, B. S. *Basic Vacuum Technology*. (Bristol, England ; Institute of Physics Pub, (1989).
54. Attard, G. A. & Barnes, C. *Surfaces*. Oxford University Press, (1998).
55. Zangwill, A. *Physics at Surfaces.* Cambridge University Press, (1988).
56. Oura, K. *Surface science : An Introduction*. Berlin ; Springer, (2003).
57. Suzuki, M. & Suzuki, I. S. A Proper Understanding of the Davisson and Germer Experiments for Undergraduate Modern Physics Course. *Phys.* (2013).
58. King, D. A. & Wells, M. G. Molecular Beam Investigation of Adsorption Kinetics on Bulk Metal Targets: Nitrogen on Tungsten. *Surf. Sci.* **29,** 454–482 (1972).
59. Kisliuk, P. The Sticking Probabilities of Gases Chemisorbed on the Surfaces of Solids. *J. Phys. Chem. Solids* **3,** 95–101 (1957).
60. Baddeley, C., Tikhov, M., Hardacre, C., Lomas, J. & Lambert, R. Ensemble Effects in the Coupling of Acetylene to Benzene on a Bimetallic Surface: A Study with Pd(111)/Au. *J. Phys. Chem.* **100,** 2189-2194 (1996).
61. Calaza, F., Gao, F., Li, Z. & Tysoe, W. T. The Adsorption of Ethylene on Au/Pd(111) Alloy Surfaces. *Surf. Sci.* **601,** 714–722 (2007).
62. Li, Z. *et al.* Formation and Characterization of Au/Pd Surface Alloys on Pd(1 1 1). *Surf. Sci.* **601,** 1898–1908 (2007).
63. Lee, J. D. *Concise Inorganic Chemistry*. London : Chapman & Hall, (1991).
64. Rogers, D. L. & Fong, C. Y. The Electronic Band Structure and Density of States of Palladium. *Phys. Lett. A* **39,** 345–346 (1972).
65. Lee, A. F. *et al.* Structural and Catalytic Properties of Novel Au/Pd Bimetallic Colloid Particles: EXAFS, XRD, and Acetylene Coupling. *J. Phys. Chem.* **99,** 6096–6102 (1995).
66. Liu, P. & Nørskov, J. K. Ligand and Ensemble effects in Adsorption on Alloy Surfaces. *Phys. Chem. Chem. Phys.* **3,** 3814–3818 (2001).

67. Yi, C. W., Luo, K., Wei, T. & Goodman, D. W. The Composition and Structure of Pd-Au Surfaces. *J. Phys. Chem. B* **109,** 18535–18540 (2005).
68. Sárkány, A., Geszti, O. & Sáfrán, G. Preparation of Pdshell–Aucore/SiO_2 Catalyst and Catalytic Activity for Acetylene Hydrogenation. *Appl. Catal. Gen.* **350,** 157–163 (2008).
69. Ponec, V. Alloy Catalysts: The Concepts. *Appl. Catal. -Gen.* **222,** 31–45 (2001).
70. Corem, G. *et al.* Ordered H_2O Structures on a Weakly Interacting Surface: A Helium Diffraction Study of H_2O/Au(111). *J. Phys. Chem. C* **117,** 23657–23663 (2013).
71. Okuyama, H. & Hamada, I. Hydrogen-bond Imaging and Engineering with a Scanning Tunnelling Microscope. *J. Phys. Appl. Phys.* **44,** 464004 (2011).
72. Kumagai, T. *et al.* Water Monomer and Dimer on Cu(110) Studied Using a Scanning Tunneling Microscope. *E-J. Surf. Sci. Nanotechnol.* **6,** 296-300 (2008).
73. Stuve, E. M., Jorgensen, S. W. & Madix, R. J. The Adsorption of H_2O on Clean and Oxygen-covered Pd(100): Formation and Reaction of OH groups. *Surf. Sci.* **146,** 179–198 (1984).
74. Paffett, M. T., Campbell, C. T. & Taylor, T. N. Surface Chemical Properties of Silver/Platinum(111): Comparisons between Electrochemistry and Surface Science. *Langmuir* **1,** 741–747 (1985).
75. Paffett, M., Campbell, C., Taylor, T. & Srinivasan, S. Cu Adsorption on Pt(111) and its Effects on Chemisorption - A Comparison with Electrochemistry. *Surf. Sci.* **154,** 284–302 (1985).
76. Blyholder, G. Molecular Orbital View of Chemisorbed Carbon Monoxide. *J. Phys. Chem.* **68,** 2772–2777 (1964).
77. Kuhn, W. K., Szanyi, J. & Goodman, D. W. CO Adsorption on Pd(111): The Effects of Temperature and Pressure. *Surf. Sci.* **274,** L611–L618 (1992).
78. Sautet, P., Rose, M. K., Dunphy, J. C., Behler, S. & Salmeron, M. Adsorption and Energetics of Isolated CO Molecules on Pd(111). *Surf. Sci.* **453,** 25–31 (2000).

79. Rose, M. K. *et al.* Ordered Structures of CO on Pd(111) Studied by STM. *Surf. Sci.* **512,** 48–60 (2002).
80. Clay, C., Cummings, L. & Hodgson, A. Mixed Water/OH Structures on Pd(111). *Surf. Sci.* **601,** 562–568 (2007).
81. Zheng, G. & Altman, E. I. The Oxidation of Pd(111). *Surf. Sci.* **462,** 151-168 (2000).
82. Yotsuhashi, S. *et al.* Dissociative Adsorption of O_2 on Pt and Au surfaces: Potential-energy surfaces and electronic states. *Phys. Rev. B* **77,** 115413 (2008).
83. Okazaki-Maeda, K. & Kohyama, M. Atomic Oxygen Adsorption on Au(100) and Au(111): Effects of Coverage. *Chem. Phys. Lett.* **492,** 266-271 (2010).
84. Ji, M., Hao, C., Xie, Z., Liu, S. & Qiu, J. Theoretical Study of Oxygen Chemisorption on Pd (111), Au (111) and Pd-Au (111) Alloy Surfaces. *J. Comput. Theor. Nanosci.* **9,** 394–400 (2012).
85. Conrad, H., Ertl, G., Koch, J. & Latta, E. E. Adsorption of CO on Pd Single Crystal Surfaces. *Surf. Sci.* **43,** 462–480 (1974).
86. Piccolo, L. *et al.* The Adsorption of CO on Au(111) at Elevated Pressures Studied by STM, RAIRS and DFT calculations. *Surf. Sci.* **566–568, Part 2,** 995–1000 (2004).
87. Yuan, D., Gong, X. & Wu, R. Origin of High Activity and Selectivity of PdAu(001) Bimetallic Surfaces toward Vinyl Acetate Synthesis. *J. Phys. Chem. C* **112,** 1539–1543 (2008).
88. Xu, J. *et al.* Biphasic Pd-Au Alloy Catalyst for Low-Temperature CO Oxidation. *J. Am. Chem. Soc.* **132,** 10398–10406 (2010).
89. Lahr, D. L. & Ceyer, S. T. Catalyzed CO Oxidation at 70 K on an Extended Au/Ni Surface Alloy. *J. Am. Chem. Soc.* **128,** 1800–1801 (2006).
90. Özbek, M. O. & Santen, R. A. Van. The Mechanism of Ethylene Epoxidation Catalysis. *Catal. Lett.* **143,** 131–141 (2013).
91. Mullins, C. B., Rettner, C. T. & Auerbach, D. J. Dynamics of the Oxidation of CO on Pt(111) by an Atomic Oxygen Beam. *J. Chem. Phys.* **95,** 8649–8651 (1991).

92. Habraken, F. H. P. M., Bootsma, G. A., Hofmann, P., Hachicha, S. & Bradshaw, A. M. The Adsorption and Incorporation of Oxygen on Cu(110) and its Reaction with Carbon Monoxide. *Surf. Sci.* **88,** 285–298 (1979).
93. Habraken, F. H. P. M. G. A. B. The Kinetics of the Interactions of O_2 and N_2O with a Cu(110) Surface and of the Reaction of CO with Adsorbed Oxygen Studied by means of Ellipsometry, AES and LEED. *Surf. Sci.* **87,** (1979).
94. Crew, W. W. & Madix, R. J. A Scanning Tunnelling Microscopy Study of the Oxidation of CO on Cu(110) at 400 K: Site Specificity and Reaction Kinetics. *Surf. Sci.* **349,** 275–293 (1996).
95. Liem, S. Y., Kresse, G. & Clarke, J. H. R. First Principles Calculation of Oxygen Adsorption and Reconstruction of Cu(110) Surface. *Surf. Sci.* **415,** 194–211 (1998).
96. Schindler, K. M. *et al.* Experimental Demonstrations of Direct Adsorbate Site Identification using Photoelectron Diffraction. *Phys. Rev. Lett.* **71,** 2054–2057 (1993).
97. Harendt, C., Goschnick, J. & Hirschwald, W. The Interaction of CO with Copper (110) Studied by TDS and LEED. *Surf. Sci.* **152–153, Part 1,** 453–462 (1985).
98. Hofmann, P. *et al.* A Photoelectron Diffraction Study of the Structure of the Cu(110)-(2 × 1)-CO System. *Surf. Sci.* **337,** 169–176 (1995).
99. Ahner, J., Mocuta, D., Ramsier, R. D. & Yates, J. T. Jr. Dynamics and Structure of Chemisorbed CO on Cu(110): An Electron-stimulated Desorption Ion Angular Distribution Study. *J. Vac. Sci. Technol. A* **14,** 1583–1587 (1996).
100. Ahner, J., Yates, J. T. Jr., Mocuta, D. & Ramsier, R. D. Dynamics and Structure of Chemisorbed CO on Cu(110): An Electron-stimulated Desorption Ion Angular Distribution Study. *J. Vac. Sci. Technol. Vac. Surf. Films* **14,** 1583–1587 (1996).
101. Ahner, J., Mocuta, D., Ramsier, R. D. & Yates, J. T. Adsorbate–adsorbate Repulsions - the Coverage Dependence of the Adsorption Structure of CO on Cu(110) as Studied by Electron-stimulated Desorption Ion Angular Distribution. *J. Chem. Phys.* **105,** 6553 (1996).

102. Zuo, Z., Huang, W., Han, P. & Li, Z. Adsorption of CO on Cu (110) and (100) Surfaces using COSMO-based DFT. *J. Mol. Model.* **15,** 1079–1083 (2009).
103. Schneider, T. & Hirschwald, W. Interaction of Carbon Dioxide with Clean and Oxygenated Cu(110) Surfaces. *Catal. Lett.* **14,** 197–205 (1992).
104. Ernst, K. H., Schlatterbeck, D. & Christmann, K. Adsorption of Carbon Dioxide on Cu(110) and on Hydrogen and Oxygen covered Cu(110) Surfaces. *Phys. Chem. Chem. Phys.* **1,** 4105–4112 (1999).
105. Spitzer, A. & Lüth, H. The Adsorption of Oxygen on Copper Surfaces: I. Cu(100) and Cu(110). *Surf. Sci.* **118,** 121–135 (1982).
106. Mundenar, J. M. *et al.* Oxygen Chemisorption on Copper (110). *Surf. Sci.* **188,** 15–31 (1987).
107. Prabhakaran, K., Sen, P. & Rao, C. N. R. Studies of Molecular Oxygen Adsorbed on Cu Surfaces. *Surf. Sci. Lett.* **177,** L971–L977 (1986).
108. Hodgson, A., Lewin, A. K. & Nesbitt, A. Dissociative Chemisorption of O_2 on Cu(110). *Surf. Sci.* **293,** 211–226 (1993).
109. Briner, B. G., Doering, M., Rust, H. P. & Bradshaw, A. M. Mobility and Trapping of Molecules During Oxygen Adsorption on Cu(110). *Phys. Rev. Lett.* **78,** 1516–1519 (1997).
110. Liem, S. Y., Clarke, J. H. R. & Kresse, G. Dissociation Pathways of Oxygen on Copper (110) Surface: A First Principles Study. *Comput. Mater. Sci.* **17,** 133–140 (2000).
111. Jin, X. F., Mao, M. Y., Ko, S. & Shen, Y. R. Adsorption and Desorption Kinetics of CO on Cu(110) Studied by Optical Differential Reflectance. *Phys. Rev. B* **54,** 7701–7704 (1996).
112. Vollmer, S., Witte, G. & Wöll, C. Determination of Site Specific Adsorption Energies of CO on Copper. *Catal. Lett.* **77,** 97–101 (2001).
113. Sueyoshi, T., Sasaki, T. & Iwasawa, Y. Catalytic CO Oxidation on Unreconstructed Cu(110) Observed at Low Temperatures. *Chem. Phys. Lett.* **241,** 189–194 (1995).
114. Spivey, J. J., Roberts, G. W., Goodwin, J. G. Jr., Kim, S. & Rhodes, W. D. in *Turnover Frequencies in Metal Catalysis: Meanings, Functionalities and Relationships* (2004).

115. Boudart, M. Turnover Rates in Heterogeneous Catalysis. *Chem. Rev.* **95,** 661–666 (1995).
116. Bowker, M. & Madix, R. J. XPS, UPS and Thermal Desorption Studies of the Reactions of Formaldehyde and Formic Acid with the Cu(110) Surface. *Surf. Sci.* **102,** 542–565 (1981).
117. Haq, S. & Leibsle, F. M. Formic Acid Oxidation on Cu(110) Surfaces as Studied by STM: Reaction Trends and Surface Structure. *Surf. Sci.* **375,** 81–90 (1997).
118. Silva, S. L., Pham, T. M., Patel, A. A., Haq, S. & Leibsle, F. M. STM and FTIR Studies of Methoxy and Acetate on Cu(110) Surfaces Resulting from Reactions with Methyl Acetate and Preadsorbed Oxygen. *Surf. Sci.* **452,** 79–94 (2000).
119. Bowker, M., Rowbotham, E., Leibsle, F. M. & Haq, S. The Adsorption and Decomposition of Formic Acid on Cu (110). *Surf. Sci.* **349,** 97–110 (1996).
120. Feng, M. *et al.* Orthogonal Interactions of CO Molecules on a One-Dimensional Substrate. *ACS Nano* **5,** 8877–8883 (2011).
121. Komrowski, A. J. *et al.* Oxygen Abstraction from Dioxygen on the Al(111) Surface. *Phys. Rev. Lett.* **87,** 246103 (2001).
122. Kurahashi, M. & Yamauchi, Y. Steric Effect in O_2 Sticking on Al(111): Preference for Parallel Geometry. *Phys. Rev. Lett.* **110,** 246102 (2013).
123. Kurahashi, M. & Yamauchi, Y. Huge Steric Effects in Surface Oxidation of Si(100). *Phys. Rev. B* **85,** 161302 (2012).
124. Kurahashi, M. & Yamauchi, Y. Huge Steric Effects in Surface Oxidation of Si(100). *Phys. Rev. B* **85,** 161302 (2012).
125. Gruzalski, G. R., Zehner, D. M., Wendelken, J. F. & Hathcock, R. S. LEED Observations of Oxygen Ordering on Cu(110). *Surf. Sci.* **151,** 430–446 (1985).
126. Guillemot, L. & Bobrov, K. Morphological Instability of the Cu(110)-(2 × 1)-O Surface Under Thermal Annealing. *Phys. Rev. B* **83,** 075409 (2011).
127. Forster, M., Raval, R., Carrasco, J., Michaelides, A. & Hodgson, A. Water-hydroxyl Phases on an Open Metal Surface: Breaking the Ice Rules. *Chem. Sci.* **3,** 93–102 (2011).

128. Vinogradov, S. N. & Linnell, R. H. *Hydrogen bonding*. New York: Van Nostrand Reinhold. (1971).
129. Shi, Y., Choi, B. Y. & Salmeron, M. Water Chains Guide the Growth of Monoatomic Copper Wires on Cu(110). *J. Phys. Chem. C* **117,** 17119–17122 (2013).
130. Ren, J. & Meng, S. First-principles Study of Water on Copper and Noble Metal (110) Surfaces. *Phys. Rev. B - Condens. Matter Mater. Phys.* **77,** (2008).
131. Kumagai, T., Okuyama, H., Hatta, S., Aruga, T. & Hamada, I. Water Clusters on Cu(110): Chain versus Cyclic Structures. *J. Chem. Phys.* **134,** 024703 (2011).
132. Kumagai, T. *et al.* Direct Observation of Hydrogen-bond Exchange within a Single Water Dimer. *Phys. Rev. Lett.* **100,** (2008).
133. Walsh, T. R. & Wales, D. J. Rearrangements of the Water Trimer. *J. Chem. Soc. Faraday Trans.* **92,** 2505–2517 (1996).
134. Michaelides, A. Simulating Ice Nucleation, One Molecule at a time, with the 'DFT Microscope'. *Faraday Discuss.* **136,** 287–297 (2007).
135. Yamada, T., Tamamori, S., Okuyama, H. & Aruga, T. Anisotropic Water Chain Growth on Cu(110) Observed with Scanning Tunneling Microscopy. *Phys. Rev. Lett.* **96,** 036105 (2006).
136. Lee, J., Sorescu, D. C., Jordan, K. D. & Yates, J. T. Hydroxyl Chain Formation on the Cu(110) Surface: Watching Water Dissociation. *J. Phys. Chem. C* **112,** 17672–17677 (2008).
137. Carrasco, J. *et al.* A One-dimensional Ice Structure Built from Pentagons. *Nat. Mater.* **8,** 427–431 (2009).
138. Carrasco, J., Klimeš, J., Michaelides, A. & Santra, B. To Wet or Not to Wet? Dispersion Forces Tip the Balance for Water Ice on Metals. *Phys. Rev. Lett.* **106,** (2011).
139. Bange, K., Grider, D. E., Madey, T. E. & Sass, J. K. The Surface Chemistry of H_2O on Clean and Oxygen-covered Cu(110). *Surf. Sci.* **137,** 38–64 (1984).
140. Benndorf, C. & Madey, T. E. Adsorption of H_2O on Clean and Oxygen-preposed Ni(110). *Surf. Sci.* **194,** 63–91 (1988).

141. Spitzer, A. & Lüth, H. The Adsorption of Water on Clean and Oxygen Covered Cu(110). *Surf. Sci.* **120,** 376–388 (1982).
142. Schiros, T. *et al.* Structure of Water Adsorbed on the Open Cu(110) Surface: H-up, H-down, or Both? *Chem. Phys. Lett.* **429,** 415–419 (2006).
143. Bjerrum, N. Structure and Properties of Ice. *Science* **115,** 385–390 (1952).
144. Spitzer, A. & Lüth, H. An XPS Study of the Water Adsorption on Cu(110). *Surf. Sci.* **160,** 353–361 (1985).
145. Polak, M. On the Structure and Bonding of H_2O Adsorbed on Cu(110). *Surf. Sci.* **321,** 249–260 (1994).
146. Kumagai, T. *et al.* Tunneling Dynamics of a Hydroxyl Group Adsorbed on Cu(110). *Phys. Rev. B* **79,** 035423 (2009).
147. Andersson, K. *et al.* Molecularly Intact and Dissociative Adsorption of Water on Clean Cu(110): A Comparison with the Water/Ru(001) System. *Surf. Sci.* **585,** L183–L189 (2005).
148. Bobrov, K. & Guillemot, L. Autocatalytic Effect of Cu Nano-islands on the Reaction of Water with the Oxygen Covered Cu(110) Surface. *Surf. Sci.* (2013).
149. Gruzalski, G. R., Zehner, D. M. & Wendelken, J. F. Two Adsorbate Densities for Cu(110)c(6 × 2)-O. *Surf. Sci. Lett.* **147,** L623–L629 (1984).
150. Lousada, C. M., Johansson, A. J. & Korzhavyi, P. A. Thermodynamics of H_2O Splitting and H_2 Formation at the Cu(110)–Water Interface. *J. Phys. Chem. C* **119,** 14102–14113 (2015).
151. Anger, G., Winkler, A. & Rendulic, K. D. Adsorption and Desorption Kinetics in the Systems H_2/Cu(111), H_2/Cu(110) and H_2/Cu(100). *Surf. Sci.* **220,** 1–17 (1989).
152. Ammon, C., Bayer, A., Steinrück, H. P. & Held, G. Low-temperature Partial Dissociation of Water on Cu(110). *Chem. Phys. Lett.* **377,** 163-169 (2003).
153. Sun, L. D., Hohage, M., Denk, R. & Zeppenfeld, P. Oxygen Adsorption on Cu(110) at Low Temperature. *Phys. Rev. B* **76,** 245412 (2007).

154. Sun, L. D., Hohage, M. & Zeppenfeld, P. Oxygen-induced Reconstructions of Cu(110) Studied by Reflectance Difference Spectroscopy. *Phys. Rev. B* **69,** 045407 (2004).
155. Feidenhans'l, R. *et al.* Oxygen Chemisorption on Cu(110): A Model for the c(6x2) Structure. *Phys. Rev. Lett.* **65,** 2027–2030 (1990).
156. Ruan, L., Besenbacher, F., Stensgaard, I. & Laegsgaard, E. Atom-resolved studies of the reaction between H_2S and O on Ni(110). *Phys. Rev. Lett.* **69,** 3523–3526 (1992).
157. Andersson, K. *et al.* Bridging the Pressure Gap in Water and Hydroxyl Chemistry on Metal Surfaces: The Cu(110) Case. *J. Phys. Chem. C* **111,** 14493–14499 (2007).
158. Andersson, K. *et al.* Autocatalytic Water Dissociation on Cu(110) at Near Ambient Conditions. *J. Am. Chem. Soc.* (2009).

Appendix

Appendix A: List of Acronyms

AES	Auger electron spectroscopy
DFT	Density functional theory
DOS	Density of state
EELS	Electron energy loss spectroscopy
E_f	Fermi level
E-R	Eley-Rideal
HA	Hot Atom
HOMO	Highest occupied molecular orbital
IR	Infrared
LEED	Low energy electron diffraction
L-H	Langmuir-Hinshelwood
LUMO	Lowest unoccupied molecular orbital
MCP-LEED	Micro-channel-low energy electron diffraction
ML	Monolayer
MO	Molecular orbital
PM-IRAS	Polarization-modulation IR absorption spectroscopy
PVD	Physical vapour deposition
QMS	Quadrupole mass spectrometer
RAIRS	Reflection-absorption IR spectroscopy
RCS	Rate-controlling steps
SEM	Secondary electron multiplier
TDS	Thermal desorption spectroscopy
TPD	Temperature-programmed desorption
TSP	Titanium sublimation pump
UHV	Ultra high vacuum
UPS	Ultraviolet photoelectron spectroscopy
WGSR	Water-gas shift reaction
XAS	X-ray absorption spectroscopy
XPS	X-ray photoelectron spectroscopy

Appendix B: List of Figures